Potential effect in the interaction of highly charged ions with materials using Kobe EBIS

Nishida, Naofumi

(Degree)
博士（理学）

(Date of Degree)
2020-03-25

(Date of Publication)
2021-03-01

(Resource Type)
doctoral thesis

(Report Number)
甲第7701号

(URL)
https://hdl.handle.net/20.500.14094/D1007701

Doctoral Dissertation

Potential effect in the interaction of highly charged ions with materials using Kobe EBIS

(Kobe EBIS を用いた多価イオンと物質の相互作用における
ポテンシャル効果に関する研究)

January 2020

Graduate School of Science, Kobe University

Naofumi Nishida

Abstract

A highly charged ion (HCI) has large potential energy increasing with its charge state. In order to remove electrons from an atom, it is necessary to give an energy equal to its binding energy, so a HCI produced after removal of many electrons has a large potential energy which is the sum of binding energy for each ionization step. Since the binding energy increases as the shell becomes deep one, the potential energy increases exponentially as the valence increases, and its value is approximately proportional to the 2.8th power of the valence. The interaction between a HCI and the surface results in emission of photons in the range of visible to X-ray, hundreds of secondary electrons, sputtering of secondary ions and the modification of the surface structure in the nanometer scale. The effects of HCI on the surface are different from those of singly charged ion (SCI), since SCI deposits only its kinetic energy. The effect characteristic to the potential energy deposition is called as 'potential effect'. Many experiments of irradiating materials with HCIs have been performed. However, the fluence (number of irradiated ions per unit area, expressed as ~ ions/cm^2) of HCI employed in most of the experiments is relatively small (~10^{11} ions/cm^2). In the present study, the interaction of HCI (Ar^{8+} ~ Ar^{16+}) with surfaces and the potential effect on various materials were evaluated at an experimental condition of relatively high fluence up to 10^{14} ions/cm^2.

In the present study, HCIs were produced with an electron beam ion source called Kobe EBIS. Kobe EBIS, which has been developed at the Kobe University, is an electron beam ion source (EBIS)-type ion source of HCIs with higher ion beam intensity than existent similar type ion sources. Kobe EBIS uses a focused electron beam to remove electrons around an atom to generate HCIs. The Kobe EBIS consists of four parts; an electron gun, drift tubes, an electron collector and a magnet. In the Kobe EBIS the drift tubes are at room temperature during operation. The magnet is a commercially available superconducting magnet which is cooled by a closed cycle refrigerator. The magnet has Helmholz coils in order to expand the flat region of magnetic field strength (3 T along the electron beam axis).

Recent machine study on the Kobe EBIS revealed that periodic intermission of electron beam improves charge state distribution of extracted ions. This finding is useful for studying potential effect in the interaction of HCI with surfaces because the

potential effect is emphasized for the irradiation with HCI in higher charge state. The period of intermission is in the order of 100 ms, and the width of beam - off time is 1 ms or less. This operation makes it possible to produce Ar^{15+} to Ar^{17+} effectively, whereas the charge is limited less than 14+ under the ordinary operational mode with DC electron beam. A spike of HCIs with a peak current in the order of nA is also produced at each moment of electron beam off. The measurement on the time evolution of the intensity of Ar^{16+} around the timing of mode changes revealed that the intensity of extracted Ar^{16+} changes slowly after mode change with a time constant of few seconds, whereas Ar^{16+} is created rapidly within a few tens ms after switching on. This means that it needs several seconds to reach equilibrium charge state distribution of extracted ions after the operational mode is changed.

The purposes of the present study are to investigate the effects of HCI irradiation by conducting various studies in the region of experimental condition with high ion dose by utilizing the advantages of Kobe EBIS.

Carbon based materials such as carbon nanotube (CNT) are promising materials for nanodevices and circuits. Investigations on the modification of structural and electric/magnetic properties of carbon based materials by the irradiation with HCIs are expected to provide valuable information for applying HCIs to such nanotechnology as well as understanding the interaction of HCIs with the materials. Several experiments which exhibit the potential effect in various irradiation phenomena, such as modifications on structural, electric, and magnetic properties, and photon emission, was performed in this study with carbon based materials.

Structural modification of multi-walled carbon nanotubes (MWCNTs) irradiated with HCIs has been analyzed using a transmission electron microscope (TEM) and Raman spectroscopy. It has been thought to be difficult to observe the identical place on the nanometer scale because samples were transferred between irradiation at Kobe EBIS and observation with TEM. However, we have established a procedure for observing the same location in the sample before and after irradiation for accurate comparisons. We investigated the difference of TEM images at the identical position between samples before and after irradiation with HCIs. TEM images of MWCNTs irradiated with Ar^{14+} exhibit uneven surfaces at the fluence of 6×10^{13} ions/cm^2. Outer diameters are decreased, outlines of surfaces become uneven and hollow regions disappeared by the irradiation. These results are different from the case of irradiation

with SCIs. It is considered that potential sputtering occurred on the surfaces of MWCNTs. From Raman spectroscopy, there is no outstanding dependence on charge state. Since the D/G ratio increases as the fluence of HCIs increases, it is considered that many defects are introduced due to the kinetic energy of HCIs. It is considered that the number of defects is increased by irradiation. The Raman spectrum is considered to show the result of the average information about the defect of MWCNTs due to the beam size of the laser used. Therefore, the contribution of kinetic energy is large in Raman spectroscopy. On the other hand, since a fine structure in atomic scale can be observed by TEM observation, it is considered that the potential effect of HCI is observable.

Irradiation effects on the resistivity of single MWCNT supported on micrometer scale bridge pattern was also measured. The as-prepared MWCNTs were dispersed onto a Si substrate. The source/drain contacts were patterned by depositing 30 nm of Pd followed by 10 nm of Au. The resistance between the contacts was measured using a DC two-terminal method. The resistance was ~10 kΩ at room temperature in most of the MWCNT channels before the irradiation. We evaluated the electric characteristics of MWCNTs irradiated with the HCIs of Ar^{8+}, Ar^{11+}, and Ar^{14+}. Each MWCNT located on the high dope Si substrate had a source/drain contact, forming a back-gate FET configuration. The source to drain resistance of the MWCNT channel tended to increase with increasing fluence and charge state of the HCIs. The current-voltage curves were nonlinear at low temperatures for the irradiated samples, and Coulomb oscillations were observed in the gate voltage dependence of the drain current. At a cryogenic temperature (1.6 K), Coulomb diamonds and periodic Coulomb oscillations were observed, and it is suggested that a single quantum dot (QD) was formed. Fabrication of QD with HCI irradiation is an epochal achievement. This result is full-scale nanotechnology research using atomic physics techniques such as HCI irradiation, which has not been realized before the present research.

We have measured magnetic structure of highly oriented pyrolytic graphite (HOPG) samples irradiated with HCIs using electron spin resonance (ESR) at low temperature. HOPG samples were irradiated with Ar^{8+} and Ar^{14+}. There are two resonance lines in the spectra at low temperatures. A Dysonian line (D1 line) was observed in lower resonance field. A Lorentzian line (L1 line) appeared at low temperatures in higher resonance field. The L1 line was not observed in unirradiated

HOPG sample. This line is considered to be caused by dangling bonds produced by irradiation with HCIs. The L1 line intensity of Ar^{14+} is larger than that of Ar^{8+} at the same fluence of 1×10^{14} ions/cm^2. This is because of the effect of the potential energy of HCIs. The L1 line intensity increases almost proportional to the fluence. Therefore, it is suggested that the defects of HOPG responsible for the magnetization is roughly proportional to the fluence of HCIs and increases with the charge state. Potential effects on the interaction of HCI with the surface are observed. The detection of ESR peak due to HCI irradiation is limited to our research group which uses Kobe EBIS.

For photon emission measurements, we observed spatial and spectral distribution of visible light emission from the surface during irradiation with HCIs. Wavelength distribution for the range of 420–670 nm and spatial distribution of horizontal direction were measured from the two-dimensional CCD image. From the emission spectra, it is suggested that these peaks are not derived from irradiated ions or samples since three emitted light lines appear in common. The analysis of ions produced by irradiation with HCIs was performed using a QMS to identify the origin of the light emission. From these results, it seems that emitted light lines observed by spectroscopic measurements come from H and Na, i.e. Balmer series (H_α and H_β) and the resonance line of Na (D line). The origin of luminescence was identified as hydrogen atom as the main light emission species from the spectroscopic measurement and SIMS. To investigate the nature of Balmer light produced by the injection of HCIs, the emission intensities at the 656 ± 5 nm region (H_α) were evaluated for various experimental conditions. The emission intensity of Balmer light increases with the charge state of HCIs and decreases as the irradiation continues. The Balmer light emission is strongest near the surface irradiated with HCIs. In addition, temporal change in the Balmer light emission of the ABS resin irradiated with HCIs showed that H contained in the chemical composition of the ABS resin did not contribute significantly to the Balmer light than H derived from water or hydrogen. Our observation of Balmer light emitted from excited hydrogen atoms produced by the interaction of HCI with the surface is also a unique achievement in the world.

Chapter 1 Introduction

In the present study, the interaction between highly charged ions (HCIs) and materials was investigated. HCIs have the large potential energy. The interaction of HCIs with materials has various unique properties such as many secondary electron emissions, X-ray emissions, and structural changes over the area in the order of nanometers. The effects of HCI on the surface are different from those of singly charged ion (SCI), since SCI deposits only its kinetic energy. The effect characteristic to the potential energy deposition is called as potential effect. Many kinds of experiments have been performed to exhibit various potential effects, such as the secondary ion emission with high efficiency, or production of nanostructure whose size increases with the potential energy of incident HCIs. For the structural observation of irradiation traces, which is the majority of research subject concerning the interaction of HCIs with the surface, the target material has been limited to bulk crystals, irradiation is conducted at relatively low fluence (~ 10^{11} ions/cm^2), and mostly measured using scanning tunneling microscopy (STM) and atomic force microscopy (AFM). In order to research unexplored fields, we have developed an electron beam ion source (Kobe EBIS) with higher ion beam intensity than existent similar type ion sources.

The purposes of the present study are to investigate the effects of HCI irradiation by conducting various studies in the region of experimental condition with high ion dose by utilizing the advantages of Kobe EBIS. Figure 1.1 shows the comparison of scanning tunneling microscope (STM) images at lower fluence (~10^{11} ions/cm^2) and higher fluence (~10^{13} ions/cm^2). The left image is irradiation traces of I^{30+} ions on the surface of highly oriented pyrolytic graphite (HOPG) surface [1], and the right image is that of Ar^{11+} ions on HOPG surface [2]. The former image was measured at the University of Electro-communications where an ion source ' Tokyo EBIT ' [3] which produces HCI of very high charge state is installed, and the latter image was obtained with the Kobe EBIS.

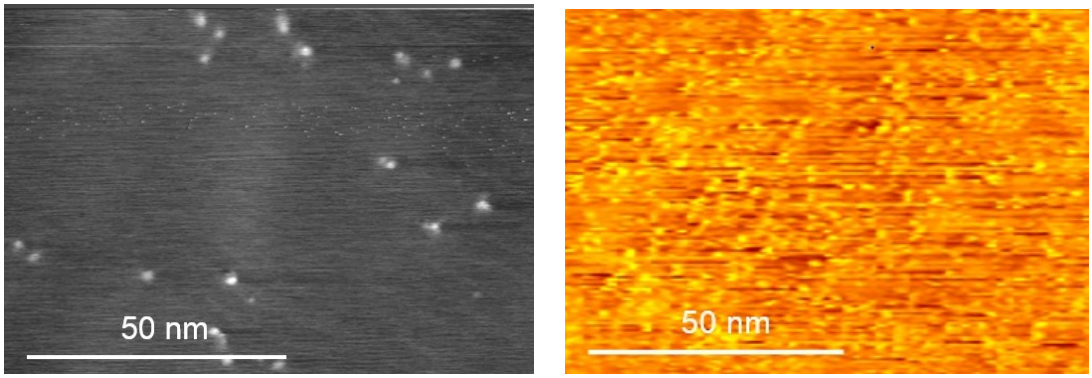

Fig. 1.1. STM images of irradiation traces of HOPG surface at lower fluence (left, ~10^{11} ions/cm^2) [1] and higher fluence (right, ~10^{13} ions/cm^2) [2].

If the fluence become higher than the order of 10^{13} ions/cm^2, irradiated area can be discriminated from unirradiated area by scanning electron microscope (SEM) or even visible light microscope with much lower magnification than that used in STM. Figure 1.2 shows SEM images of HOPG and Si surfaces covered with Cu mesh (#200) irradiated with Ar^{11+}. For HOPG surface irradiation makes the contrast of SEM brighter, while irradiation makes the contrast darker for Si surface. Thus the purpose of the present study is explore the field of researches on the irradiation effect of materials irradiated with HCI at high fluence using Kobe EBIS. Irradiation with high fluence opens up availability of various analysis methods such as SEM, electric resistance measurement, electron spin resonance and visible light detection, which were not useful for irradiation with low dose.

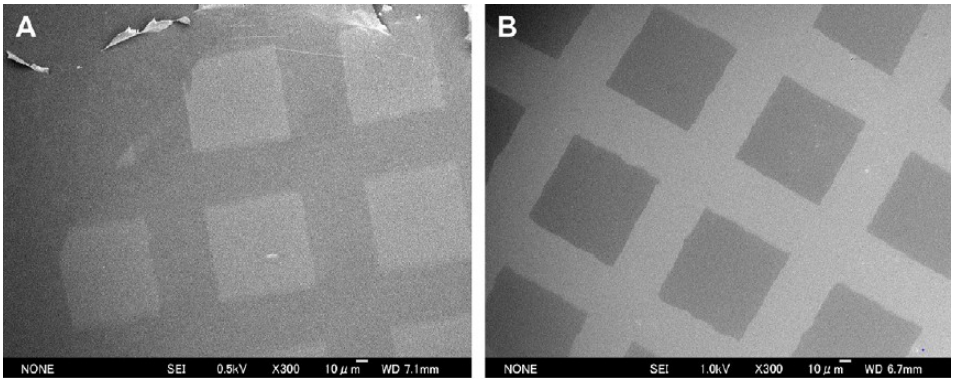

Fig. 1.2. SEM images of HCI irradiated (A) HOPG and (B) Si surfaces covered with Cu mesh (#200). Accelerating voltages of the primary electron beam for (A) and (B) are 0.5 kV and 1 kV, respectively [4].

1.1 Highly charged ion

A positive ion with two or more electrons removed from an atom is called a highly charged ion (HCI).

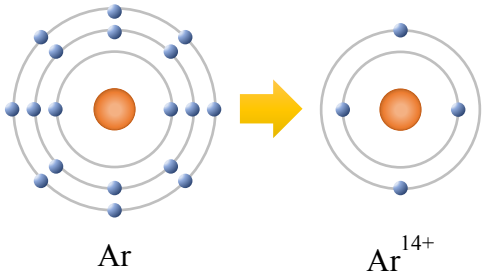

Fig. 1.3. Schematic diagram of highly charged ion.

In order to remove electrons from an atom, it is necessary to give an energy equal to its binding energy, so a HCI with many electrons removed has a large potential energy which is the sum of binding energy for each ionization step. Since the binding energy increases as the shell becomes deep one, the potential energy increases exponentially as the valence increases, and its value is approximately proportional to the 2.8th power of the valence. Figure 1.4 shows the charge state dependence of potential energy for rare gas elements and uranium. The potential energy of bare uranium is as high as 800 keV.

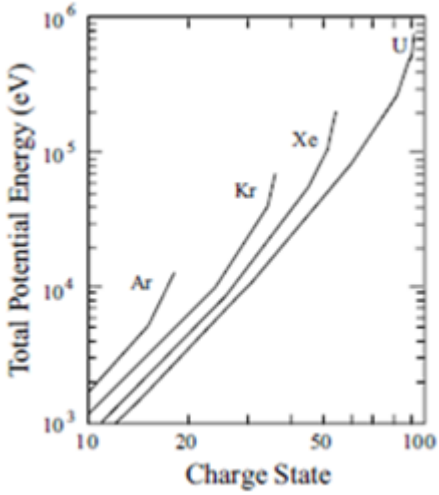

Fig. 1.4. Potential energy of highly charged ions.

HCIs exist in high-temperature plasmas such as solar corona and fusion reactors. Electrons and HCIs collide frequently in the plasma, and ionization, recombination, and excitation processes occur constantly. For this reason, abundant X-rays from the HCIs in the excited state are observed in the plasma, and the identification of HCI species and the study of the electronic state are possible from the X-ray spectrum.

Full-scale research on the behavior of HCIs in plasma (atomic processes) or their atomic spectroscopy has not been completed until the study of high-temperature plasma aimed at nuclear fusion. In fusion plasma, various atoms sputtered from the vacuum vessel wall are mixed into the plasma and ionized to become HCIs. Among these impurity atoms, polyvalent ions of high Z elements such as iron and tungsten do not become fully ionized ions reduce the temperature of the plasma by radiative cooling, while abundant X-rays emitted from these HCIs have been applied to plasma diagnostics.

Spectroscopy on HCI has several characteristics peculiar to HCI. Since the radiation emitted by the transition in a HCI comes under X-ray region, the transition probability becomes higher compared to visible region and the probability of forbidden transitions reaches that of allowed transitions. The relativistic effect and quantum electrodynamic (QED) effect in the energy and transition probability of the X-ray are also significant.

On the other hand, interaction between HCI and atom or molecule, that is, collision experiment between HCI and atom/molecule using a HCI beam as a projectile has provided interesting research field in atomic physics. The most important process is charge exchange; electrons in atom/molecule transfer to HCI. The cross section is as high as the order of 10^{-14} cm^2.

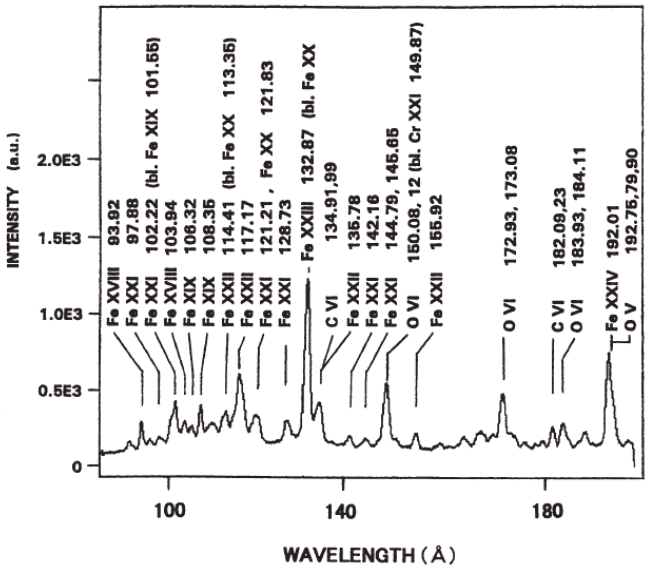

Fig. 1.5. Highly charged ion spectrum observed in LHD plasma with central electron temperature of 1.5 keV [5].

1.2 Interaction between highly charged ions and solid surfaces

When slow HCIs are incident on the solid surface, they behave differently from singly charged ions and neutral atoms. Figure 1.6 shows conceptual diagram of interaction between three types of incident ions and solid.

When slow singly charged ions (SCIs) are incident on the surface, the energy loss is dominated by nuclear inhibition. This energy transfer to the target atom causes the atom to be ejected and collide with other atoms in cascade while exciting surrounding electrons. Subsequently, when fast atomic ions are incident, the energy loss is dominated by ionization around the incident ion trajectory. In addition, the region where electron excitation and ionization occur due to the electrons emitted by inner-shell ionization of target atoms expands. When slow HCIs are incident on the solid surface, energy is transferred to the target electron system through the Auger process.

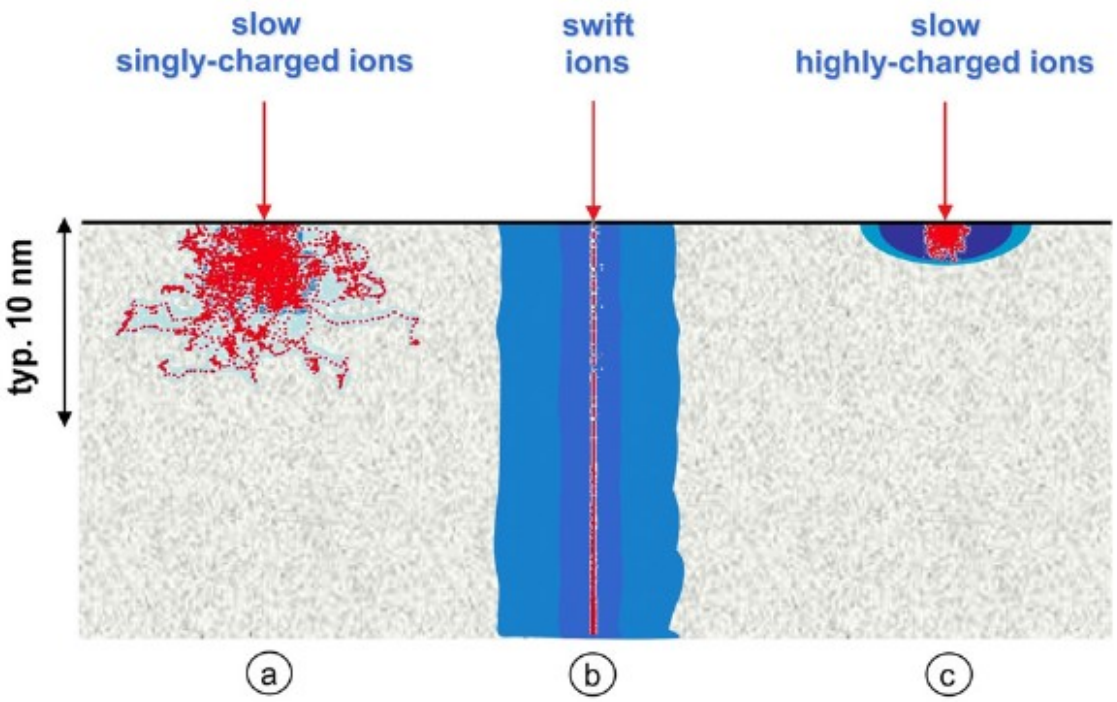

Fig. 1.6. Conceptual diagram of interaction between incident ions and solid [6].

1.3 Multi-electron transfer process

Let's take a closer look at the case of Fig. 1.6(c). When a HCI approaches the target surface, many electrons move from the target surface to the HCI, which is called a multi-electron transfer process. The interaction between HCIs and the solid surface is mainly due to this multi-electron transfer process. The multi-electron transfer process is explained by COB (Classical Over the Barrier model [7])

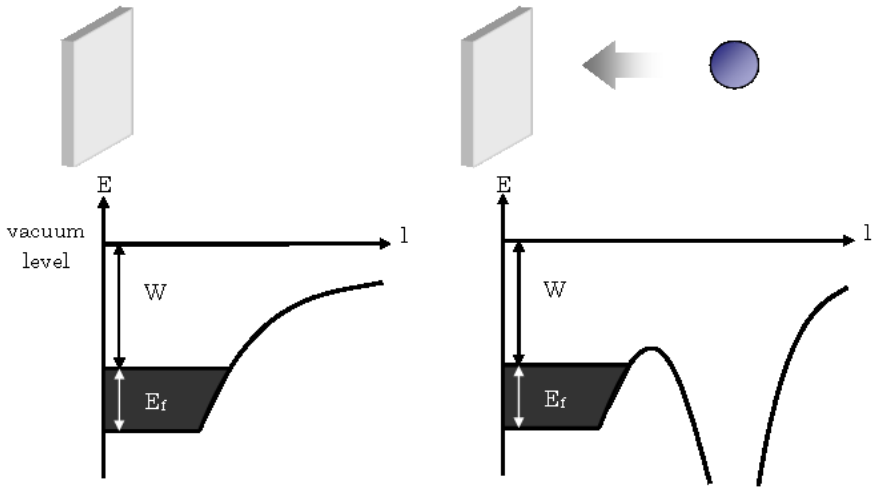

Fig. 1.7. Images of multi-electron transfer process classical over the barrier model.

Electrons in the solid exist so as to satisfy Fermi energy E_f. When a HCI approaches the solid surface, the potential barrier between the solid surface and HCI is lowered by the Coulomb field of the HCI. Many electron transfer occurs when approaching the critical distance R_c expressed by the following formula (electron transfer occurs by tunneling before approaching R_c, but the probability is very small).

$$R_c = \frac{\sqrt{2q}}{W}$$

Where q is the valence of the electron and W is the work function of the solid surface. The electrons in the solid resonantly transfer only those coinciding with the orbits of multiply charged ions (Resonant Neutralization). Since the saddle point of the potential barrier becomes lower as the HCI approaches, the electrons transferred from the solid go into the Rydberg orbit of the HCIs. Therefore, in the initial stage of the multi-electron transfer process, the inner shell of the ion is empty and only the outer shell is filled (hollow atom). There are two types of deexcitation processes for hollow atoms when an electron at the excited level falls to a lower level. One is Auger decay process, in which another electron at the excited level gains the same energy as the first electron loses and ionizes (autoionization). The other is radiative decay process that emits X-ray with the energy equal to the energy difference between the excited level and the lower level.

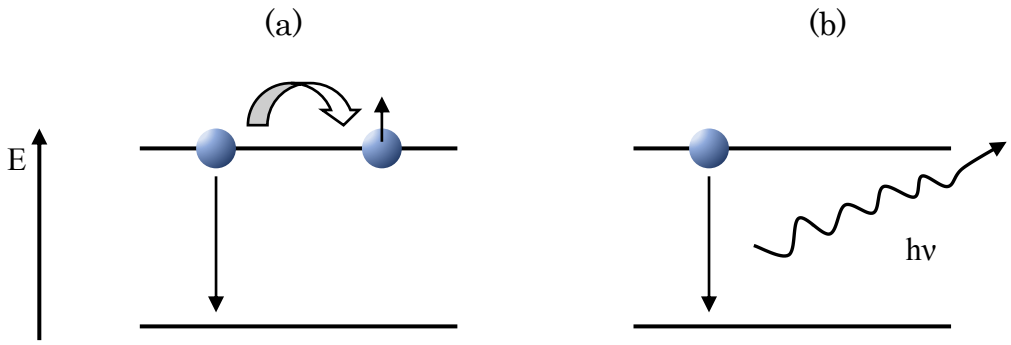

Fig. 1.8. Deexcitation process of highly charged ions ((a) Auger decay, (b) radiative decay).

Some electrons in solids transit to an energy level of HCI which is lower than their initial energy level. In this case, a valence electron fall into the energy level of HCI, which gives the energy to another valence electron and the electron is ejected from the solid surface (Auger neutralization), similar to the autoionization that occurs in hollow atoms.

1.4 Surface modification effect of HCIs

When a HCI approaches to solid surface, the HCI is neutralized accompanied with secondary electron emission. The number of secondary electrons emitted from the surface as a consequence of neutralization processes mentioned above is much more than the number of charge state of the incident HCI. Charge state dependence of secondary electron yield for Xe and Th HCIs is shown in Fig. 1.9 [8]. Since secondary electron is released to vacuum before the incident HCI enters the surface and the interaction time between HCI and surface for charge transfer process is longer when the incident HCI is slower, the number of secondary electron is more for slower HCI.

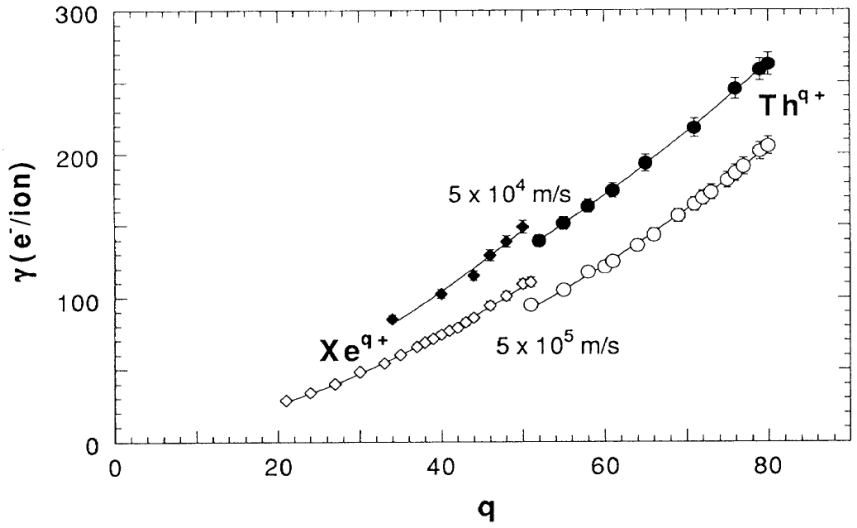

Fig. 1.9. Charge state dependence of secondary electron yield [8].

The solid surface emits a large number of electrons, but the subsequent effect differs depending on the constituent atoms and structure of the surface, especially whether neutralization by supplying electrons to the irradiated region is performed quickly or not. If not enough electrons are supplied to the irradiated area, the irradiated

area will be locally positively charged. Positively charged surface atoms repel each other by Coulomb force and are released into the space as secondary ions. This is called potential sputtering as illustrated in Fig. 1.10, and crater-like depressions and bumps are generated in the irradiated area.

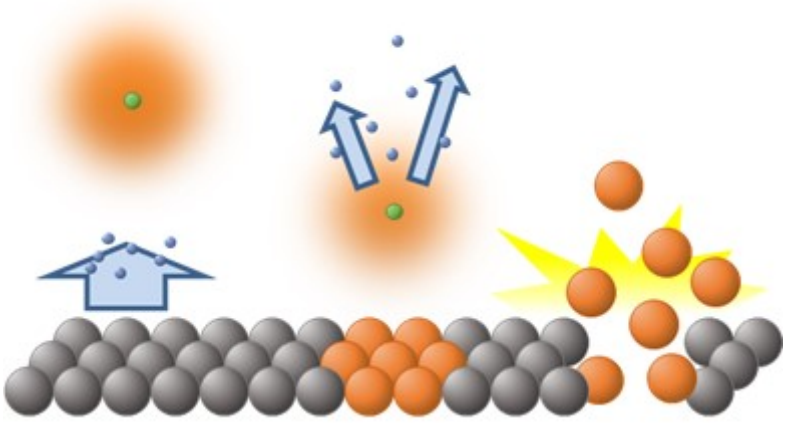

Fig. 1.10. Conceptual diagram of potential sputtering.

Scanning tunneling microscope (STM) images of metal, semiconductor and insulator surfaces irradiated with HCIs are shown in Fig. 1.11 [9].

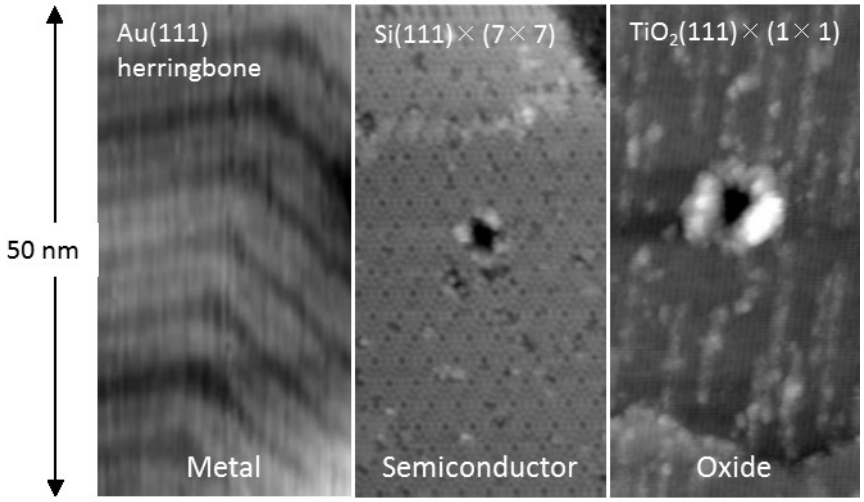

Fig. 1.11. STM images of Au(111), Si(111), and TiO2(110) surfaces irradiated with I^{50+} [9].

The effects of irradiation are more pronounced on semiconductors and insulators than on metals with their high conductivity. The effect of sputtering caused by single ion impact for clean Si surface spreads over several nanometer area in the surface parallel direction and several tenth of nanometers in the vertical direction, depending on

the valence of multiply charged ions, as shown in Fig. 1.12 [10].

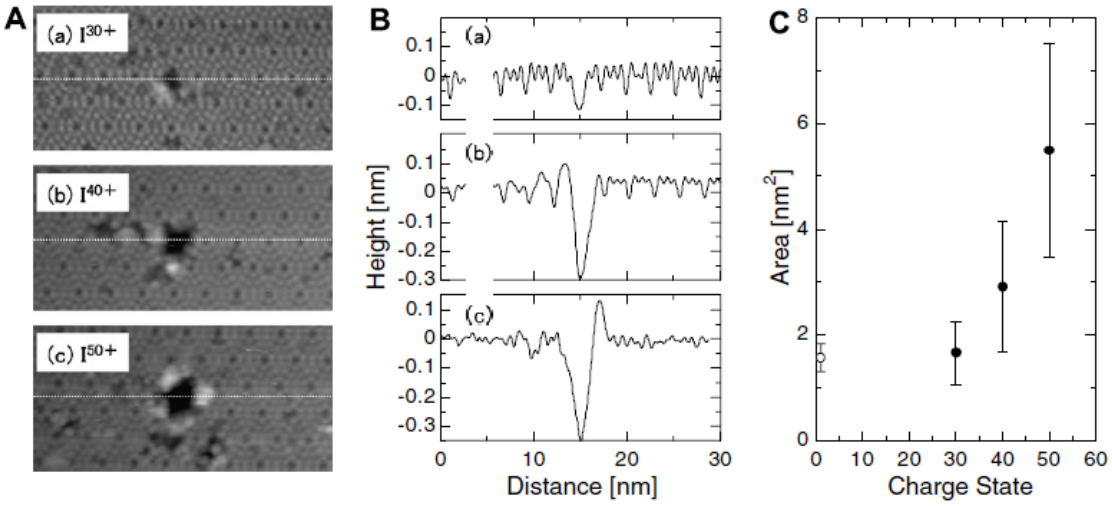

Fig. 1.12. (A) Typical close-up images around impact sites with I^{q+}-bombardment (q = 30, 40 and 50). (B) Depth profiles obtained along the dashed lines in the corresponding STM images of (A). (C) The area of the missing topmost layer of the crater as a function of the incident ion charge q. Error bars represent the standard deviation of the measurements. The open circle plotted at q = 1 represents the area for the Ar^{+} impact [10].

For the surface of highly oriented pyrolytic graphite (HOPG) as well as that of mica and CaF_2, irradiation trace exhibits nanohillock structure [11 - 13]. STM image of HOPG surface irradiated HCIs is shown in Fig. 1.13 [12].

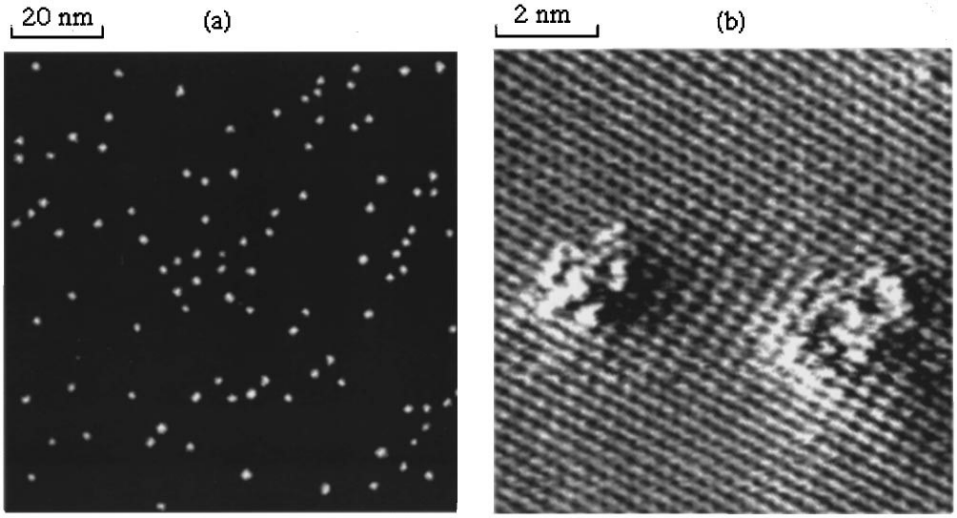

Fig. 1.13. STM image of HOPG irradiated with Ar^{8+} [12].

It has been reported that the number of secondary ion emission events and the number of dot structures created by HCI irradiation on the HOPG surface are almost one-to-one correspondence [14]. That is, when one HCI is implanted, one irradiation trace is formed.

Irradiation effect on HOPG surface has been also studied by Raman spectroscopy. The Raman spectrum of pristine surface has only single peak (G peak) in the Raman shift range between 1200 and 1800 cm^{-1}. However the Raman spectrum of irradiated surface has additional peak (D peak). Figure 1.14(B) is Raman spectrum of HOPG irradiated with Xe^{44+} at the fluence of 3×10^{11} ions/cm^2 [15].

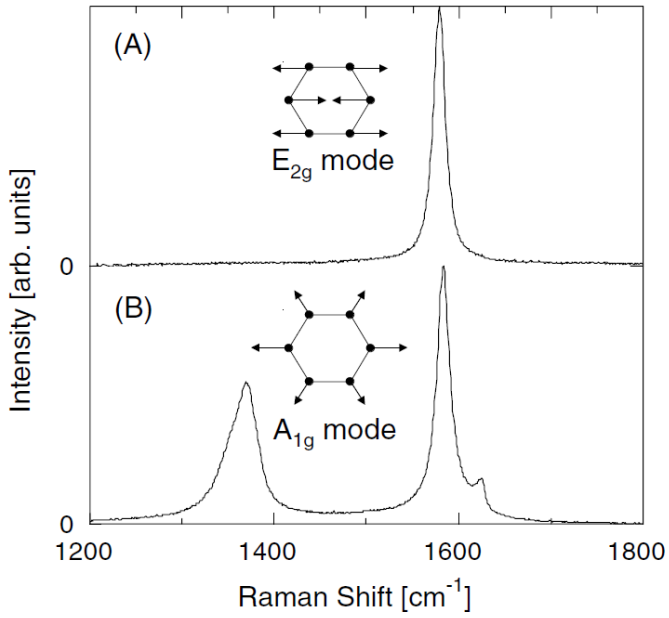

Fig. 1.14. Raman spectra from (A) unirradiated and (B) Xe^{44+}-irradiated HOPG surfaces [15].

In response to the increase of the size of sputtered area due to the impact of single HCI, number of sputtered particles increases as the charge state or potential energy of incident HCI increases. The potential energy dependence of secondary ion yield for the surface of SiO_2/Si and Si-H irradiated with iodine HCI (Fig. 1.15 [16]).

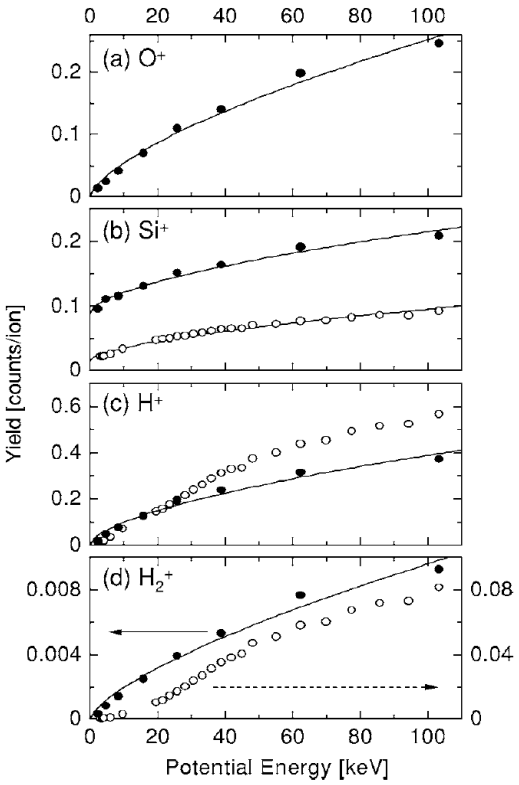

Fig. 1.15. Secondary ion yields as a function of the potential energy. Open and filled circles correspond to the result from Si-H and SiO_2, respectively [16].

When proton sputtering yields of 1 × 1 and 2 × 1 structures are compared in hydrogen-terminated silicon Si (100) -H, the proton sputtering yield is higher for the coarser 1 × 1 structure at the atomic level [17].

Since the potential sputtering effect is concentrated at topmost surface layers secondary particles are released mainly by the potential energy of incident HCI. However, kinetic energy sputtering occurs at the same time, because HCI is accelerated with the potential of ion source multiplied by its charge state. This is a phenomenon in which atoms shed in cascade are released from the surface as shown in Fig. 1.6(a). Sputtering yield depends on kinetic energy and ion incidence angle. The potential sputtering caused by the impact of HCI exhibits high secondary ion yield and no selectivity of element, while secondary ion yield of kinetic sputtering is relatively low and varies over several orders of magnitude with element. The relative sputtering yield of various elementary solids irradiated with singly charged oxygen ion is shown in Fig. 1.16 [18].

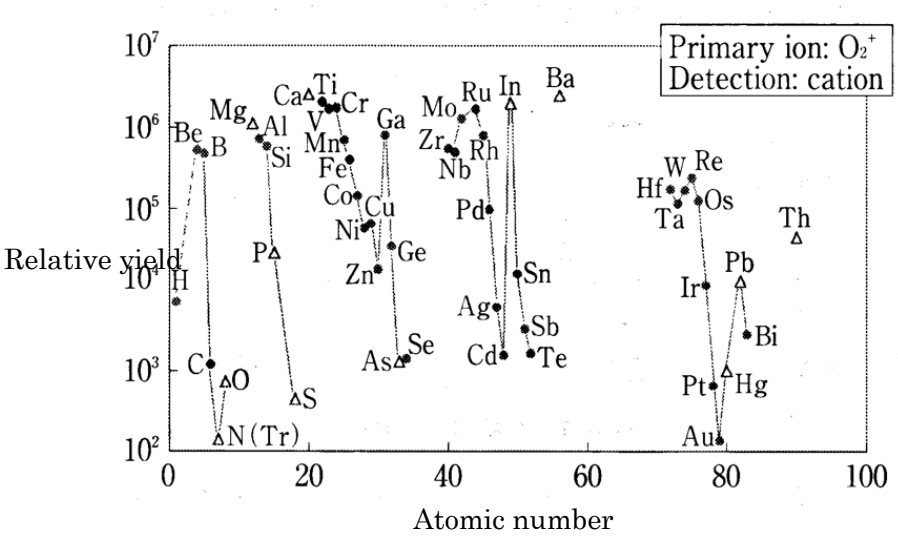

Fig. 1.16. Atomic number dependence of secondary ion yield for singly charged ion bombardment [18].

For oxygen element which is likely to be released as negative ion, the yield of positive oxygen ion sputtered by singly charged ion is very low. The yield, however, increases as the charge state of incident HCI increases as shown in Fig. 1.17. For the case of very high charge states the ratio of secondary ion yields between O^+ and Ti^+ approaches stoichiometric ratio [19].

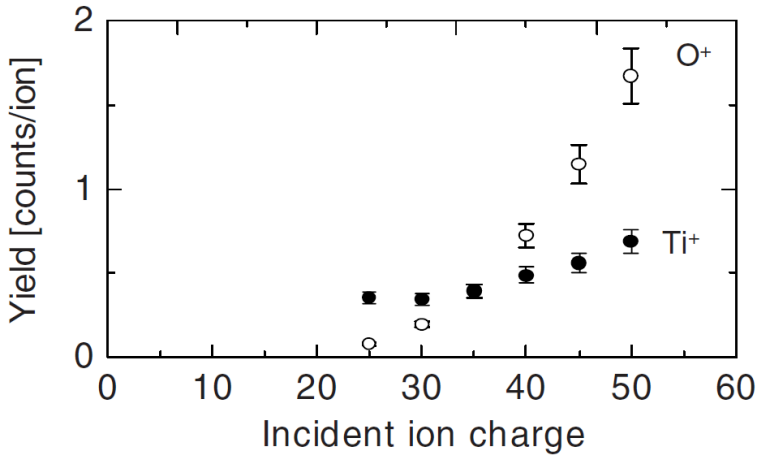

Fig. 1.17. Charge state dependence of secondary ion yield in TiO_2 [19].

When a HCI approaches the solid surface, deexcitation of hollow atom state produced by the electron transfer process between the HCI and surface atoms leads to emission of either an Auger electron or a photon. For HCI of heavy element in very high charge state, hard X ray emitted by this deexcitation process before the HCI hits the

surface is observed. X-ray emission yields from incident I^{q+} ions as a function of charge state q is shown in Fig. 1.18 [20]. Circles are K x rays, squares L x rays, and diamonds M x rays. X-ray emission yield is photon counts emitted into a full solid angle by an incident ion.

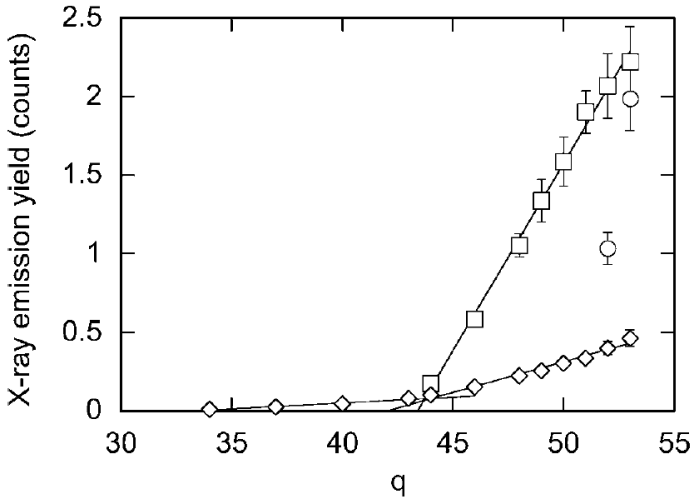

Fig. 1.18. X-ray emission yields from incident I^{q+} ions as a function of q [20].

References

[1] M. Sakurai, M. Tona, S. Takahashi, H. Watanabe, N. Nakamura, N. Yoshiyasu, C. Yamada, S. Ohtani, H. A. Sakaue, Y. Kawase, K. Mitsumori, T. Terui, and S. Mashiko, Nucl. Instr. and Meth. in Phys. Res. B 257 (2007) 297.

[2] M. Sakurai, M. Tona, H. Watanabe, N. Nakamura, S. Ohtani, T. Terui, S. Mashiko, and H. A. Sakaue, J. Phys. Conf. Ser. 163 (2009) 012115.

[3] F. J. Currell, J. Asada, K. Ishii, A. Minoh, K. Motohashi, N. Nakamura, K. Nishizawa, S. Ohtani, K. Okazaki, M. Sakurai, H. Shiraishi, S. Tsurubuchi, and H. Watanabe, J. Phys. Soc. Jpn. 65 (1996) 3186.

[4] M. Sakurai, H. Onishi, K. Asakura, M. Tona, H. Watanabe, N. Nakamura, S. Ohtani, T. Terui, S. Mashiko, and H. A. Sakaue, Vacuum 84 (2010) 530.

[5] M. Fujiwara *et al.*, Nucl. Fusion 40 (2000) 1157.

[6] F. Aumayr and H. P. Winter, Nucl. Instr. and Meth. in Phys. Res. B 233 (2005) 111.

[7] J. Burgdorfer, P. Lerner, and F. W. Meyer, Phys. Rev. A 44 (1991) 5674.

[8] F. Aumayr, H. Kurz, D. Schneider, M. A. Briere, J. W. McDonald, C. E. Cunningham, and H. P. Winter, Phys. Rev. Lett.71 (1993) 1943.

[9] M. Tona and S. Ohtani, J. Phys. Conf. Ser. 185 (2009) 012046.

[10] M. Tona, H. Watanabe, S. Takahashi, H. Nakamura, N. Yoshiyasu, M. Sakurai, T. Terui, S. Mashiko, C. Yamada, and S. Ohtani, Surface Sci. 601 (2007) 723.

[11] D. Schneider, M. A. Briere, M. W. Clark, J. McDonald, J. Biersack, and W. Siekhaus, Surface Sci. 294 (1993) 403.

[12] K. Mochiji, S. Yamamoto, H. Shimizu, S. Ohtani, T. Seguchi, and N. Kobayashi, J. Appl. Phys. 82 (1997) 6037.

[13] A. S. El-Said, R. Heller, W. Meissl, R. Ritter, S. Facsko, C. Lemell, B. Solleder, I. C. Gebeshuber, G. Betz, M. Toulemonde, W. Moller, J. Burgdorfer, and F. Aumayr, Phys. Rev. Lett. 100 (2008) 237601.

[14] N. Yoshiyasu S. Takahashi, M. Shibata, H. Shimizu, K. Nagata, N. Nakamura, M. Tona, M. Sakurai, C. Yamada, and S. Ohtani, Jpn. J. Appl. Phys. 45 (2006) 995.

[15] Y. Baba, K. Nagata, S. Takahashi, H. Nakamura, N. Yoshiyasu, M. Sakurai, C. Yamada, S. Ohtani, and M. Tona, Surface Sci. 599 (2005) 248.

[16] M. Tona, S. Takahashi, K. Nagata, N. Yoshiyasu, C. Yamada, H. Nakamura, S. Ohtani, and M. Sakurai, Appl. Phys. Lett. 87 (2005) 224102.

[17] K. Kuroki, N. Okabayashi, H. Torii, K. Komaki, and Y. Yamazaki, Appl. Phys. Lett. 81 (2002) 3561.

[18] H. A. Storms, K. F. Brown, and J. D. Stein, Anal. Chem, 49 (1977) 2023.

[19] M. Tona, Y. Fujita, C. Yamada, and S. Ohtani, Phys. Rev. B 77 (2008) 155427.

[20] H. Watanabe, S. Takahashi, M. Tona, N. Yoshiyasu, H. Nakamura, M. Sakurai, C. Yamada, and S. Ohtani, Phys. Rev. A 74 (2006) 042901.

Chapter 2 Experimental Equipment

2.1 Kobe EBIS

As shown in Fig. 2.1, the HCI irradiation system consists of three sections; an electron beam ion source (Kobe EBIS [1, 2]), a transport section, and an irradiation section.

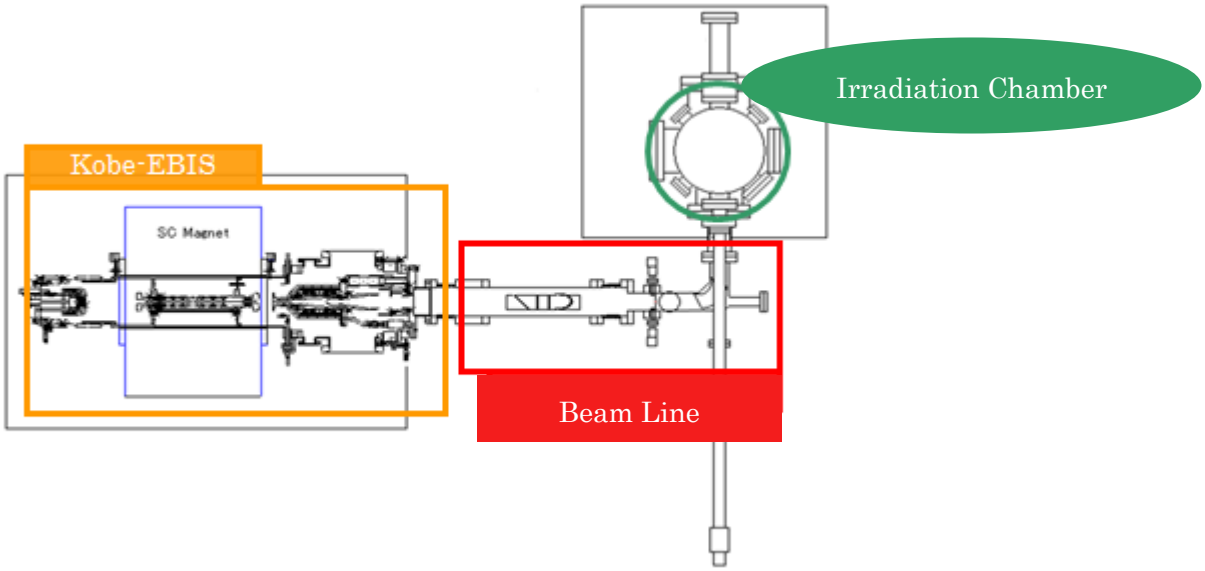

Fig. 2.1. Overall view of highly charged ion irradiation equipment.

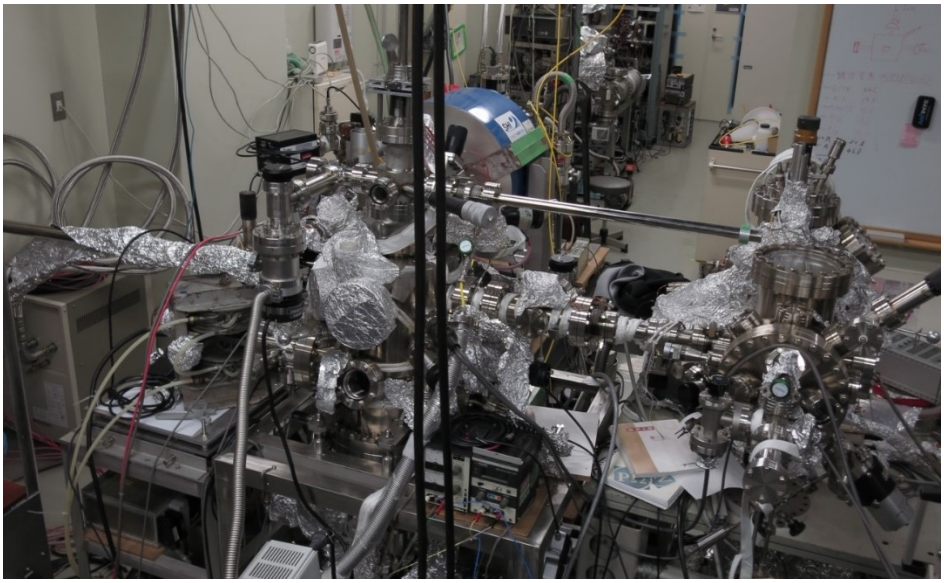

Fig. 2.2. EBIS overview.

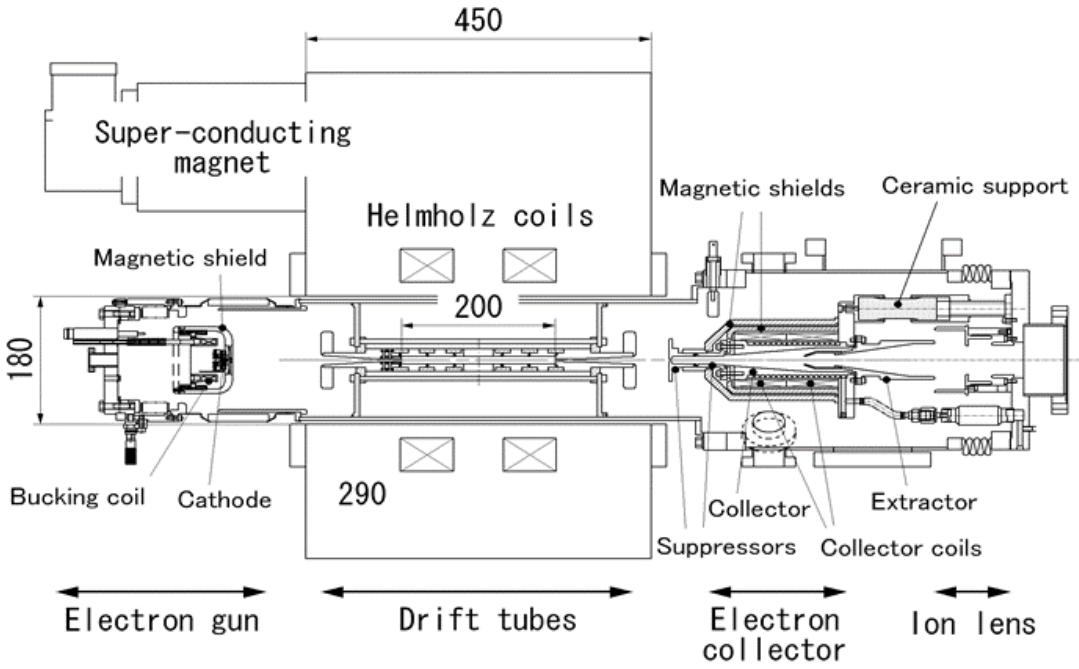

Fig. 2.3. Electron beam ion source (Kobe-EBIS) [2].

Electron beam ion source (EBIS) was developed in early 1980s to produce HCI with high current density electron beam by compressing electron beam using strong magnetic field (~1 T) over the length (~1 m) of drift tube [3, 4]. EBIS consists of four parts; an electron gun, drift tubes, an electron collector and a magnet. Electron beam ion trap (EBIT) that produces HCIs in very high charge states was developed afterwards, where the length of drift tube was made shorter (~3 cm) to avoid the instability of trapped HCIs [5 - 7]. In the Kobe EBIS the length of trap region of drift tubes is 20 cm that are at room temperature during operation. The magnet is a commercial superconducting magnet which is cooled by a closed cycle refrigerator. The magnet has Helmholz coils in order to expand the flat region of magnetic field strength (3 T at maximum). Figure 2.4 shows the comparison of magnetic field distribution between solenoid coil and Helmholz coils. The electron gun, the drift tubes and the electron collector are installed in a vacuum chamber which is inserted in the bore (180 mmϕ) of the magnet. The design of the shapes of electrodes was determined with the simulation of the distribution of electric and magnetic field and the electron beam trajectories using a commercial simulation program (TriComp 5.0). Figure 2.5 shows an example of electron beam trajectory at electron gun, drift tube and collector regions. Horizontal and vertical scales are different for three figures as indicated with values at both ends of axes in mm unit.

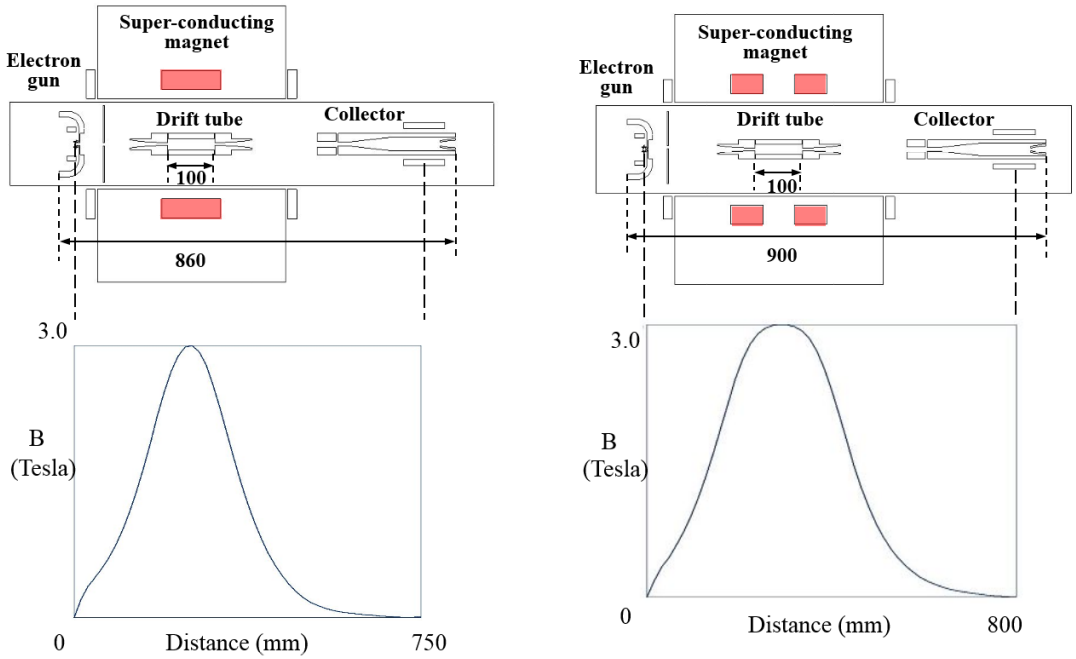

(a) Solenoid coil (b) Helmholz Coils

Fig. 2.4. Comparison of magnetic field distribution.

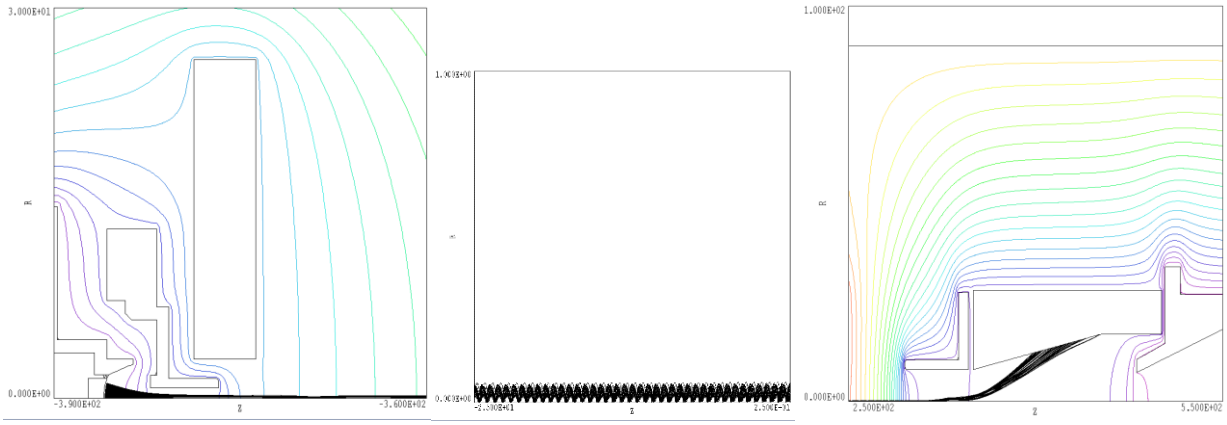

Electron gun drift tubes collector

Fig. 2.5. Simulation of electron beam trajectories.

Electron gun part

The electron gun has a cathode that emits electrons, a filament that heats the cathode and emits electrons, an anode that draws electrons from the cathode, a focus that prevents electrons from diffusing, a snout that accelerates electrons, a magnetic shield that reduces magnetic field of the superconducting magnet, and a backing coil that cancels the magnetic field at the cathode surface (Fig. 2.6). For the cathode we used a

dispenser cathode. The diameter of the emitting surface is 3 mm. In order to create a highly compressed electron beam with a current density in the order of 1000 A/cm^2 at the drift tube region where the magnetic field is high (3 T in Kobe EBIS), it is necessary to make the magnetic field strength nearly zero at the cathode surface and the field increase with the distance from cathode in parabolic manner. The design of the magnetic shield was optimized to fulfil this requirement under specific magnetic field strength of the bucking coil. The operating condition in the present study is that the electron gun part is floating at a negative potential of -10 kV, so that the electrons receive an acceleration potential of 10 kV with respect to the ground potential.

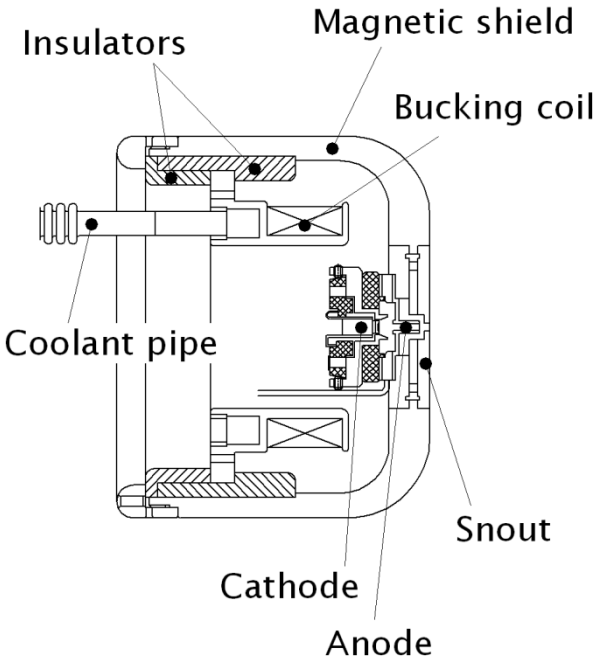

Fig. 2.6. Electron gun and names of each part.

Drift tube part

The drift tube is divided into seven parts so that potential can be applied independently as shown in Fig. 2.7. A small amount of Ar gas is supplied inside the drift tube, and Ar atoms are ionized by a high current density electron beam constricted by the superconducting coil. Once ionized, Ar ions are trapped in a square-well potential formed by the drift tube applying higher potential to DT1 and DT7 than others. The length of potential well (DT2 to DT6) is 200 mm. HCIs are generated by repetitive ionization processes on the identical ion with an intense electron beam. The electric potential at the end of the drift tubes on the collector side are slightly higher than that

of potential well, and some of the HCIs escape from the trap (leak mode). Since the base potential of drift tubes is 3 kV in the preset operation of Kobe EBIS, the HCIs extracted from the ion source have kinetic energy of $q \times 3$ keV (q is the valence), but this can be decelerated by applying a retarding potential to the sample stage.

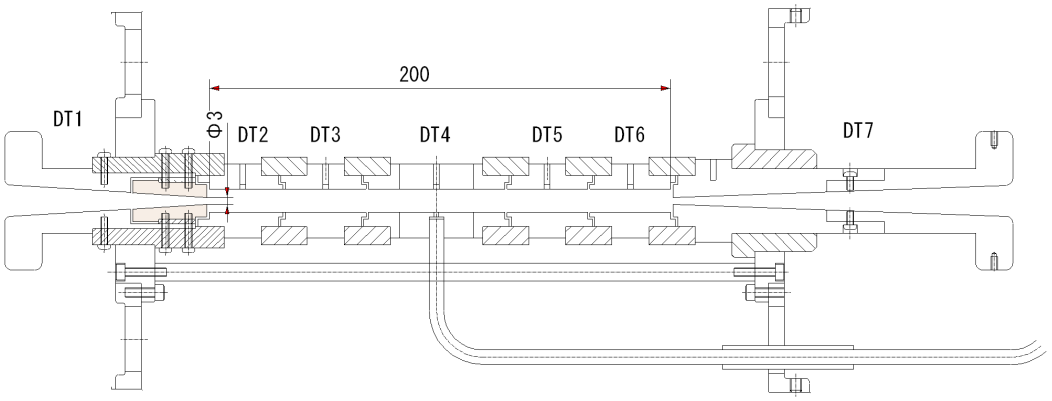

Fig. 2.7. Drift tube and potential and magnetic field during ion production.

Collector part

The collector part is the part that collects the electron beam. The potential is about 1.5 kV higher than the cathode of electron gun under the present operational condition. Therefore, it becomes a negative potential of 10 kV or more with respect to ground. The design of the collector section is shown in Fig. 2.8. It consists of a collector that receives electrons, a suppressor and extractor that prevent electrons from leaking upstream and downstream from the collector, a magnetic shield that prevents the magnetic field of the superconducting coil affecting electron trajectory, and a collector coil that cancels the magnetic field which arises from imperfect action of the magnetic shield.

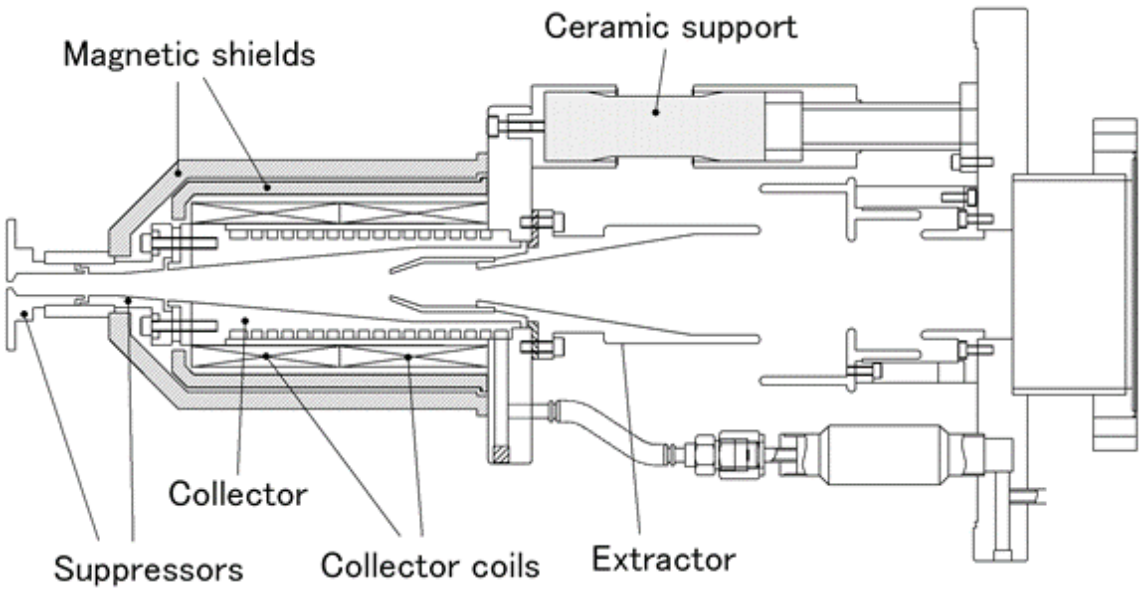

Fig. 2.8. The design of the collector section.

In the collector, it is necessary to collect electrons safely on the ion exit side. The electrons not collected here return to the electron gun again and flow into the anode and snout, which are heated by collision of electrons and damaged in the worst case because a higher voltage is applied than the cathode. In addition, when the electron gun is heated, the characteristics of the electron beam deteriorate (that is degradation of current density of the electron beam) and HCIs cannot be obtained. Therefore, it is necessary to counteract the magnetic field of the superconducting coil to minimize the influence of the magnetic field while forming an electric field that prevent leakage of electrons from the collector.

The bucking coil and collector electrode are cooled by cooling fluid using alternative freon (Vertrel XF, Chemours-Mitsui Fluoloproducts Co., Ltd.), and this fluid is cooled by water via an oil cooler, because they have the heat load coming from Joule heat (~ 10 W) of the bucking coil and the heater of filament and the heat from electron beam bombardment which amount to 150 W at the electron beam current of 100 mA and acceleration potential of 1.5 kV. The alternative freon meets the requirement for the cooling fluid that is electrical insulation property and high vapor pressure which is necessary to evacuate the fluid from whole pass of piping in the Kobe EBIS at the bake out procedure.

The ultrahigh vacuum (UHV) of the Kobe EBIS was established by bake out of the vacuum system of Kobe EBIS which was extracted from the superconducting magnet

for several days at 200~250 ℃ (Fig. 2.9), and by the discharge cleaning around drift tube region at high voltage (3 kV) under the strong magnetic field (3 T).

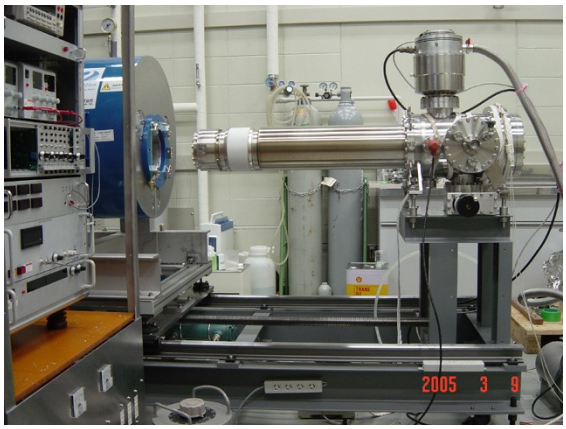

(a) During bake-out procedure

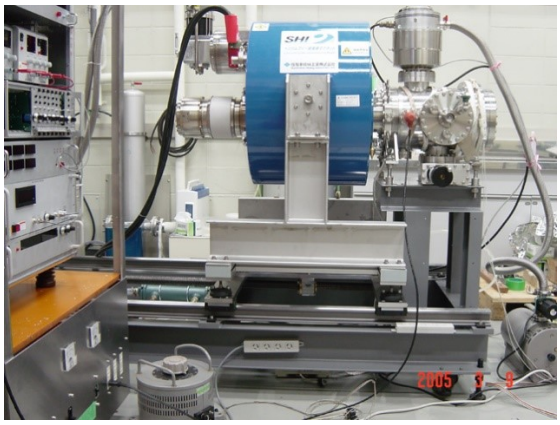

(b) Normal position

Fig. 2.9. Positions of movable magnet.

The vacuum system of the Kobe EBIS consists of a turbo-molecular pump (TMP), a sputter-ion pump (SIP) and a titanium getter pump (TGP). During the bake out process and discharge cleaning the EBIS was evacuated with TMP and after the system reached UHV region the vacuum pump was switched to SIP and TGP. The ultimate pressure of the Kobe EBIS is under 1×10^{-8} Pa. In the presence of electron beam, the pressure increases into 10^{-8} Pa region due to the electron stimulated desorption at collector electrodes and thermal outgassing from the electron gun which is heated by the hot filament of cathode.

Operation of Kobe EBIS

In order to study the potential effect of HCI interacting with materials, it is essential to minimize the kinetic energy of HCI which is given by the potential difference between drift tube electrodes and sample. On the other hand the potential difference between electron gun and drift tube must be high to secure enough kinetic energy of electron beam sufficient for ionization of higher charge state. Thus the electric potential of electron gun and collector is on negative high voltage, while drift tubes are minimum high voltage (+3 kV) necessary to extract HCI with sufficient intensity. Floating of collector is due to the demand for minimizing heat load to the collector from electron beam incidence. Overall potential distribution in the Kobe EBIS is shown in Fig. 2.10.

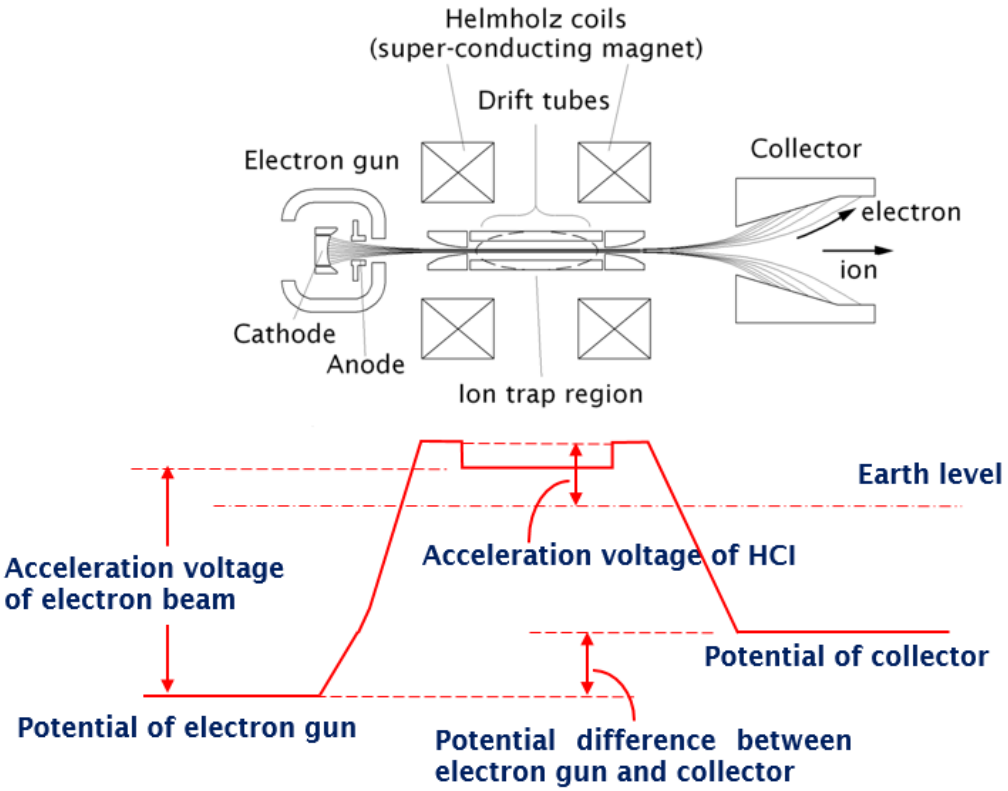

Fig. 2.10. Potential distribution of Kobe EBIS.

Therefore power supplies for giving electric potential to each electrode and current to coil are on floating potential as shown in Fig. 2.11. The capacity of current and voltage of each power supply is also noted in the figure. Power supplies for electron gun and collector are on negative high voltage power supply (max. -30 kV), and power supplies for drift tube electrodes are on positive high voltage (max. +10 kV).

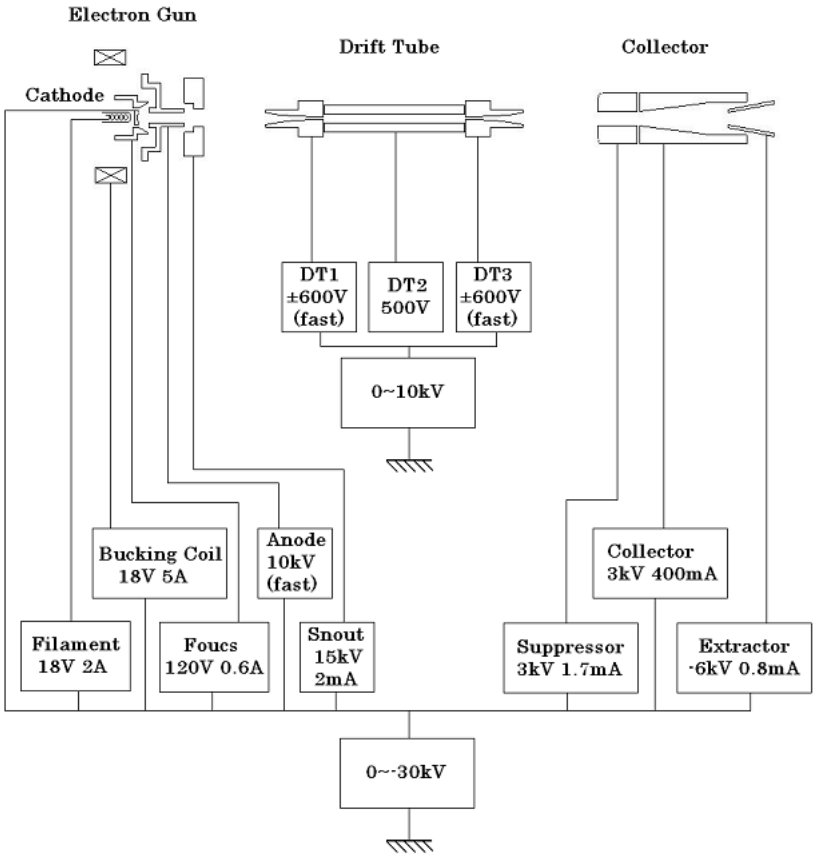

Fig. 2.11. Construction of power supplies.

Power supplies on floating potentials are controllable by PC using interface electronics as shown in Fig. 2.12. Some power supplies indicated as '(fast)' in Fig. 2.11 and 'Fast PS' in Fig. 2.12 can be controlled with fast response time (~100 us). The output of fast high voltage amplifier is switched between two different values that are set by two values of DACs. The output voltage or current of power supplies for all the electrodes and coils is also set by DAC controlled with three digital signals while switching timing of fast power supply is transmitted with an independent digital signal. Output monitor signal (analog voltage) provided by the power supply is converted to digital pulse train whose frequency is proportional to the analog voltage and the pulse is read by a counter board (PCI-6106, Interface Corp.) installed in the PC. Three digital signals for DAC control are produced by PPI board (PCI-2746C, Interface Corp.), and the timing signal by bus-master DIO board (PCI-2472C, Interface Corp.).

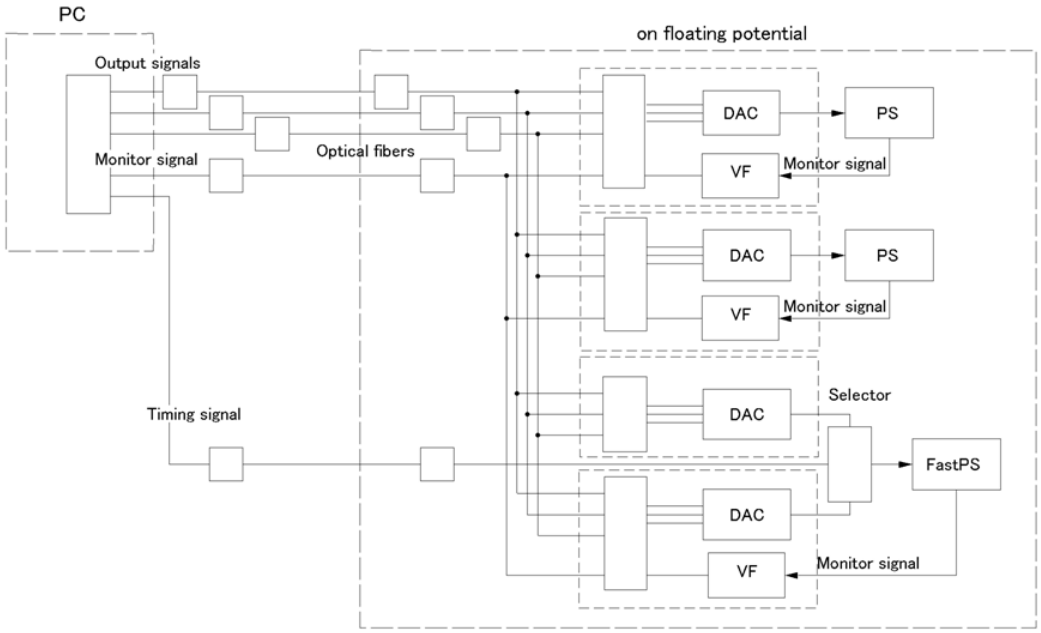

Fig. 2.12. Control of floating power supplies.

The typical operational condition of Kobe EBIS is listed in Table 2.1.

Table 2.1. Typical operational condition of Kobe EBIS.

Electron gun base potential	-10 kV
Drift tube base potential	+3 kV
Collector relative to cathode	+1.5 kV
Anode relative to cathode	+3 kV
Snout relative to cathode	+9 kV
Focus relative to cathode	-150 V
DT1 relative to DT base	250 V
Suppressor 1 relative to cathode	2 kV
Suppressor 2 relative to cathode	2 kV
Extractor relative to cathode	-2 kV
Filament current	0.6 A
Bucking coil current	0.8 A
Collector coil current	~ 0 A
Superconducting magnet current	137 A (3 T)

Transport section

The HCI extracted from Kobe EBIS is transmitted to transport section which consist of beam line with an einzel lens coupled with deflectors and an analyzing magnet with entrance and exit slits. Beam monitor is also installed in this section. Figure 2.13 shows the schematic diagram of transport section.

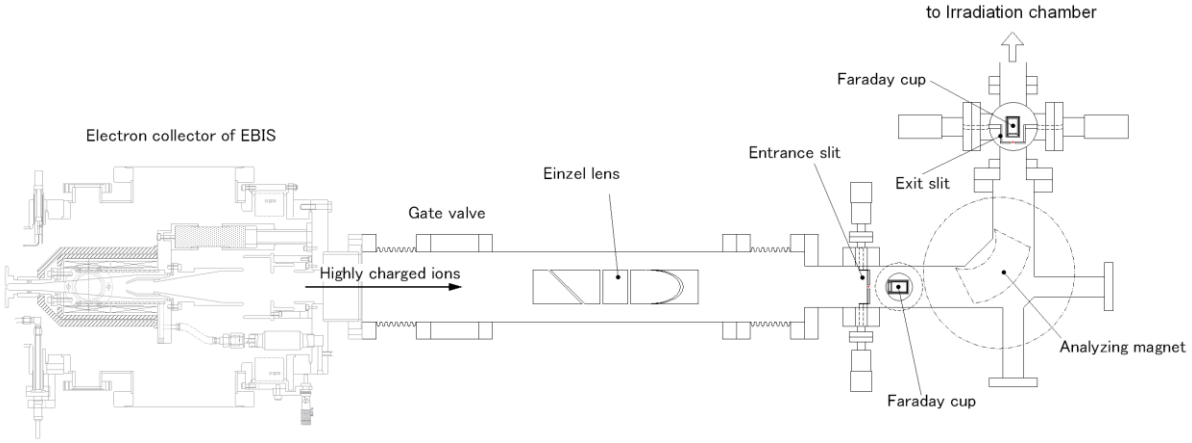

Fig. 2.13. Schematic diagram of transport section.

Analyzing magnet

The extracted ions from Kobe EBIS have various charge states, including those ions derived from elements other than Ar. In order to select the target ions, it is necessary to perform charge state selection, which is performed using an analyzing magnet on the beam line as shown in Fig. 2.13. When the beam focused by the einzel lens is focused at the entrance slit and incident on a magnetic field generated by the analyzing magnet, the ions receive a Lorentz force according to velocity and charge, and draw an arc with a certain curvature. The radius r of this arc is determined by the balance between the centrifugal force and Lorentz force acting on the ions (Fig. 2.14).

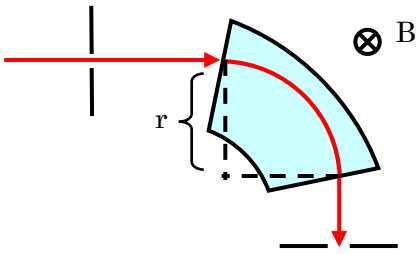

Fig. 2.14 Ion analysis part.

If the ion valence is q, the velocity is v, the mass is M, and the magnetic field strength is B, the condition is expressed as follows;

$$qvB = \frac{Mv^2}{r}.$$

Using the relation between the acceleration potential V and velocity

$$qV = \frac{1}{2}Mv^2,$$

the mass to charge ratio M/q of selected ions is expressed as follows;

$$\frac{M}{q} = \frac{(rB)^2}{2V}.$$

However, ions with similar M/q ratios, such as O^{4+} and Ar^{10+}, cannot be selected because their M/q ratios coincide (4.0). Therefore, these ions should be avoided in irradiation experiments. The entrance and exit plane of pole pieces of analyzing magnet is tilted by 27° in order to focus the ion beam that expands from the entrance slit at the distance of $2r$ from the entrance plane on the exit slit at the distance of $2r$ from the exit plane.

Irradiation section

Irradiation section comprises irradiation chamber equipped with load-lock chamber and sample preparation chamber (Fig. 2.15) [8]. The vacuum of these chambers are isolated by gate valves and evacuated with turbo molecular pumps independently. The irradiation chamber is evacuated also by sputter ion pump and titanium getter pump. A two-step load-lock system at the load-lock chamber makes it possible to transport the sample from the atmosphere into the irradiation chamber

within 1 hour. After the charge state of HCI has been selected through the transport section, the HCI is focused through ion lens installed in the irradiation chamber and the sample is irradiated with HCIs. In order to adjust the sample holder, 5-axes manipulator for XYZ translation, long travel in vertical direction (Z direction) and rotation around Z axis is installed on the bottom of the irradiation chamber (Fig. 2.16) [9]. Secondary ions and visible photons emitted from the sample surface during the irradiation can be detected using a quadrupole mass spectrometer (QMS) and a liquid nitrogen cooled CCD detector, respectively. The QMS is modified from original design so that the ion source is removed and an ion lens is attached instead. The ultimate pressure in the irradiation chamber is approximately 5×10^{-8} Pa. Behind the sample it is equipped with a Faraday cup for beam intensity measurement and a micro channel plate for beam shape observation. The sample preparation chamber has an ion gun to sputter the sample surface. A retarding voltage can be applied to the sample stage in order to decelerate ions and adjust the kinetic energy of incident ions to the sample.

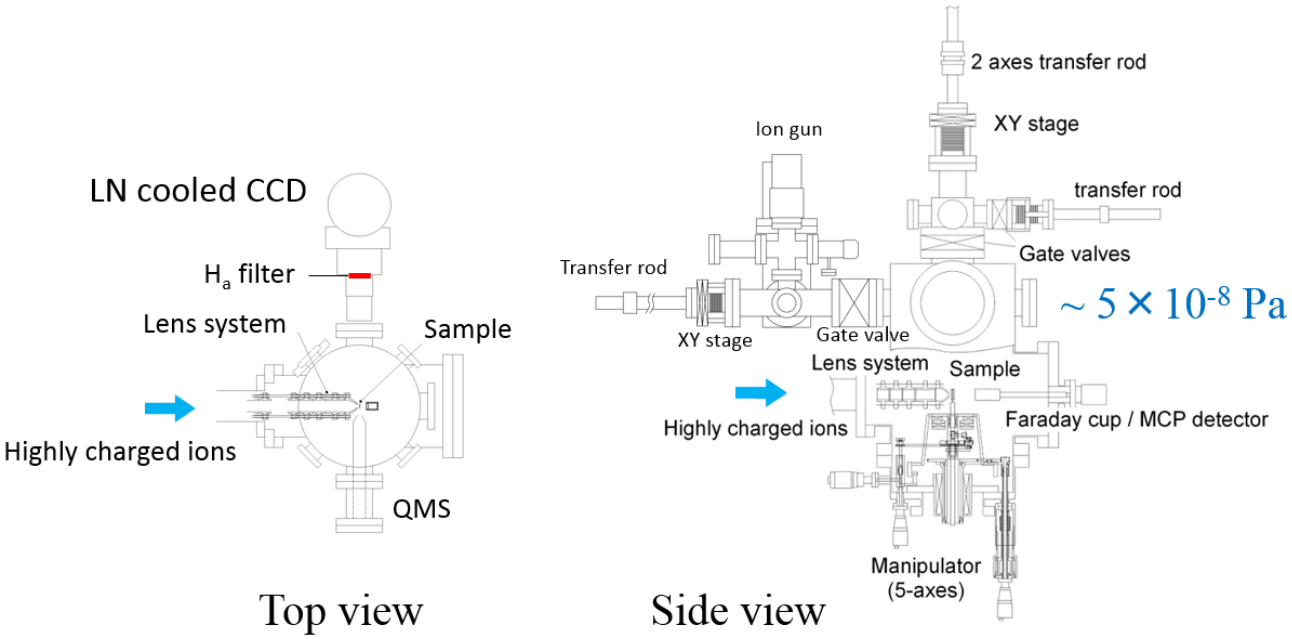

Fig. 2.15. Schematic drawing of irradiation chamber.

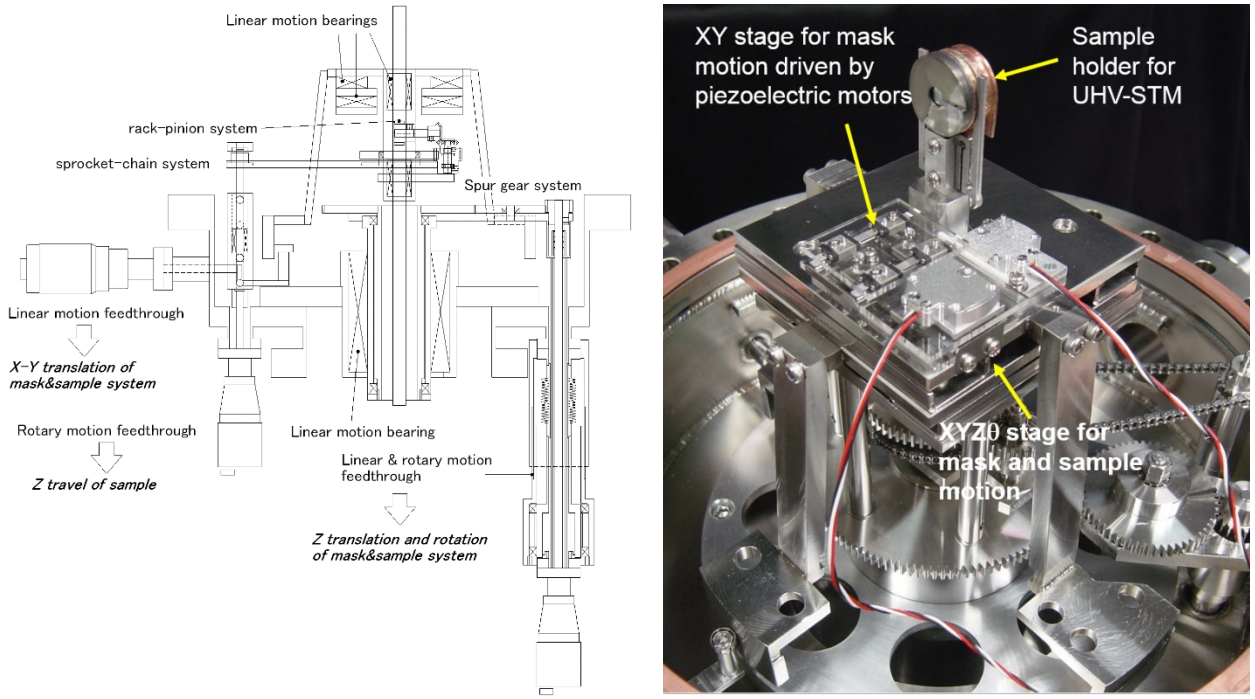

Fig. 2.16. Schematic drawing and photo of 5-axes manipulator [4].

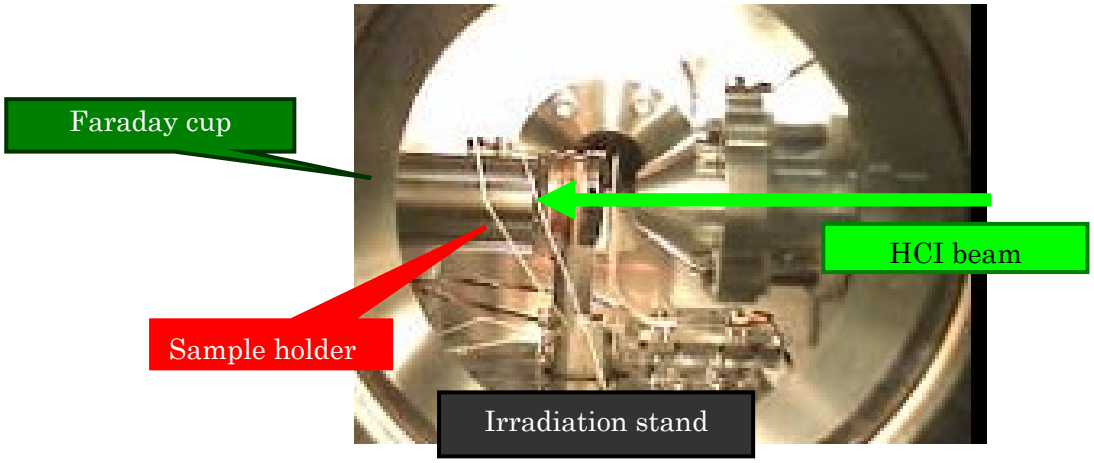

Fig. 2.17. Irradiation chamber.

Measurement of ion dose

HCI beam current is measured with a Faraday cup. When HCIs are incident on an electrode, many secondary electrons are emitted and the measured ion current through the electrode is larger than the actual ion current if the secondary electrons escape to vacuum. Therefore, the Faraday cup has a cup structure that can capture the emitted secondary electrons.

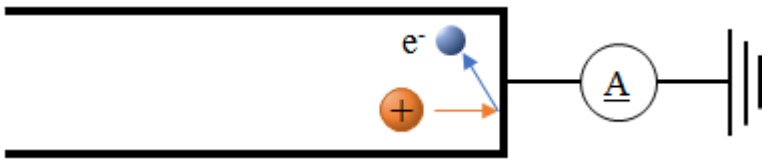

Fig. 2.18. Outline of Faraday cup.

2.2 Transmission electron microscopy

When an electron accelerated at high speed collides with a solid material, an interaction occurs between the electron and the material, and an electromagnetic wave and a secondary electron are generated. When the material is thin, most of the electrons do not change anything. There are other electrons that pass through (transmission electrons), but are scattered without changing the energy (elastically scattered electrons), and electrons that lose some energy and are scattered (inelastically scattered electrons). An image is obtained by enlarging the transmitted electrons, elastically scattered electrons, or their interference waves generated as a result of the interaction with the material. Electrons from the electron source pass through the focusing lens and then collide with the sample. The generated transmitted electrons and elastically scattered electrons pass through the objective lens, intermediate lens and projection lens and form an image on the fluorescent screen. In an electron microscope the lens is not a glass lens used in optical microscopes, but a magnetic-type electron lens, which is a thin copper wire wound in a coil. When an electron beam passes through the magnetic field in this coil, receiving Lorentz force, it rotates and refracts, and the electron beam converges to a single point so that an image can be seen.

In addition, the imaging system has an image observation mode and a diffraction image mode. In the diffraction image mode, a diffraction image can be obtained from the target area of the sample by limiting the field of view. By using this diffraction pattern the surface spacing of lattice planes can be obtained.

$$d_{hkl} = \frac{\lambda L}{R}$$

d_{hkl}: Surface distance, λL: Camera length, R: Distance from center

From this spacing, the crystal structure and orientation of the sample can be identified.

In the present study, we used the TEM in the Department of Instrumental Analysis, Kobe University Research Center. The TEM device was JEM2100F from JEOL Ltd., which is a field emission that provides high-brightness, high coherence, and high stability. Equipped with an electron gun (FEG), it has the feature that it is easy to observe and analyze ultra-high resolution images on the nanoscale order. Table 3.2 shows the TEM measurement conditions used in the present study.

Table 3.2. Measurement conditions.

Model number	JEM-2100F
Vacuum	$\times 10^{-8}$ Pa
Acceleration voltage	80 kV, 100 kV, 200 kV
Magnification	× 8000～250000

References

[1] M. Sakurai, F. Nakajama, T. Fukumoto, N. Nakamura, S. Ohtani, and S. Mashiko, Shinku 48 (2005) 317 (in Japanese).

[2] M. Sakurai, H. A. Sakaue, H. Watanabe, N. Nakamura, S. Ohtani, Y. Kawase, K Mitsumori, T. Terui, and S. Mashiko, Shinku 50 (2007) 390 (in Japanese).

[3] E. D. Donets and V. P. Ovsyannikov, JETP 53 (1981) 466.

[4] T. Iwai, Y. Kaneko, M. Kimura, N. Kobayashi, S. Ohtani, K. Okuno, S. Takagi, H. Tawara, and S. Tsurubuchi, Phys. Rev. A 26 (1982) 105.

[5] R. E. Marrs, M. A. Levine, D. A. Knapp, and J. R. Henderson, Phys. Rev. Lett. 60 (1988) 1715.

[6] F. J. Currell, J. Asada, K. Ishii, A. Minoh, K. Motohashi, N. Nakamura, K. Nishizawa, S. Ohtani, K. Okazaki, M. Sakurai, H. Shiraishi, S. Tsurubuchi, and H. Watanabe, J. Phys. Soc. Jpn. 10 (1996) 3186.

[7] J. R. Crespo Lopez-Urrutia, A. Dorn, R. Moshammer, and J. Ullrich, Physica Scr., T80B (1999) 502.

[8] M. Sakurai, T. Miyamoto, K. Sasaki, D. Kato, and H. A. Sakaue, J. Vac. Soc. Jpn. 50 (2015) 147 (in Japanese).

[9] M. Sakurai, M. Tona, S. Takahashi, H. Watanabe, N. Nakamura, N. Yoshiyasu, C. Yamada, S. Ohtani, H. A. Sakaue, Y. Kawase, K. Mitsumori, T. Terui, and S. Mashiko, Nucl. Instr. and Meth. in Phys. Res. B 257 (2007) 297.

Chapter 3 Pulse operation

3.1 Introduction

Interaction of highly charged ions (HCIs) with solid surfaces causes modification of structure over the nanometer scale region of surface as well as emission of secondary particles and photons[1, 2] as a consequence of potential energy release from HCI to surface (potential effect). Electron beam ion source (EBIS) has been developed to produce HCIs since around 1980 [3, 4]. The Kobe EBIS was developed to perform modification of surfaces using HCIs at the Kobe University, Japan [5]. We have revealed that the irradiation of various surface with HCIs brings electric and magnetic modification, and emission of Balmer light from a hydrogen atom desorbed from the surface [6, 7]. For most phenomena, degree of influence of potential energy increases with the charge state of incident HCI, for example, the intensity of Balmer light changes with the fourth power of the charge state. Recent machine study on the Kobe EBIS revealed that periodic intermission of electron beam improves charge state distribution of extracted ions [8, 9]. This finding is useful for studying potential effect in the interaction of HCI with surfaces because the potential effect is emphasized for the irradiation with HCI in higher charge state. In the present paper, this operation is named as “pulse mode” and ordinary operation as “DC mode,” and we will describe characteristics and advantage of pulse mode in detail.

3.2 Experimental

The performance of the Kobe EBIS was improved by the modulation of electron beam emission. The modulation is periodic repetition of on/off of electron beam, which is realized by on/off of anode voltage; the period is in the order of 0.1 s, and the width of beam off time is around 1 ms. The response time of switching is ~100 μs using a fast high voltage amplifier (Matsusada Precision HEOPS - 10P2). The method of fast control of anode potential is described in chapter 2. The emission current of 100 mA is obtained at the anode voltage of 4 kV relative to cathode, which is at −10 kV from the ground level. The collector is at 1.5 kV relative to cathode. In the present experiment,

data were obtained with the potential of DT7 at 0 V relative to the common potential of drift tubes (3 kV) except special cases (Fig. 3.4) where DT7 potential was switched rapidly between certain voltage and zero, whereas DT1 is 200 V and DT2 to DT6 are 0 V through entire experiments. Because the duty ratio of modulation is almost 1, the intensity of HCI beam extracted from the EBIS can be monitored as DC current with an ordinary electrometer. On the other hand, time structure of each charge state in the ms range exhibits the evolution of charge state distribution. Then we observed the variation of the intensity of specific charge state at the time resolution of ~30 μs. In this time response measurement, ion beam current amplified by the MCP detector (gain is ~380) was converted to voltage using a current preamplifier (DL instruments 1211) at the conversion gain of 10^6 V/A and measured with an oscilloscope (Tektronix TDS3032B).

3.3 Results and discussion

The charge state distributions of the extracted ions are shown in Fig. 3.1 for both modes: (a) DC mode and (b) pulse mode [8].

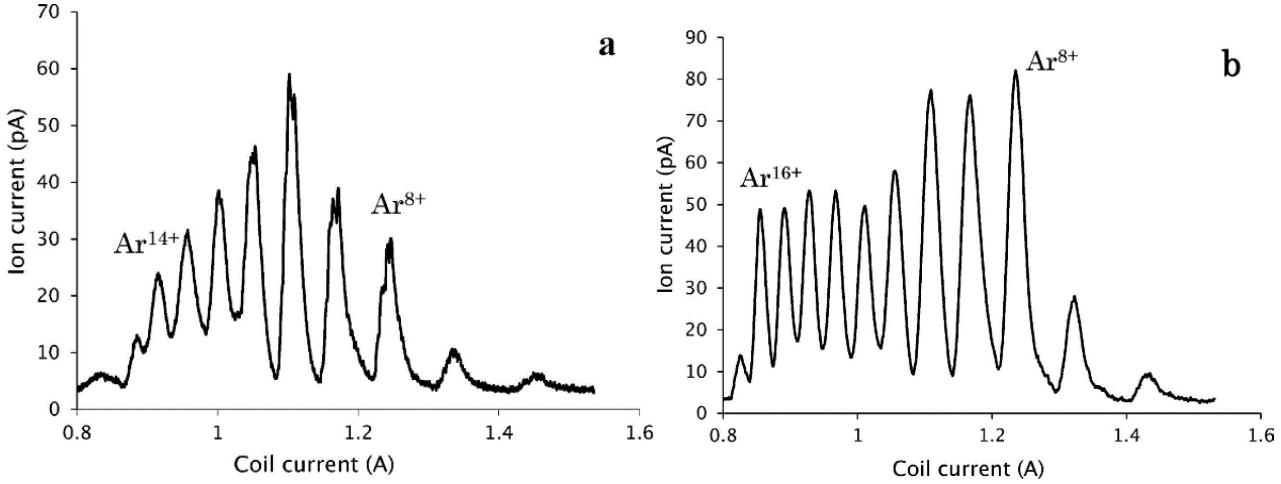

Fig. 3.1. Mass spectra of highly charged ions extracted from the Kobe EBIS for different operational modes: (a) DC mode and (b) pulse mode.

The partial pressure of introduced Ar is 1×10^{-8} Pa. At the DC mode, the ion current of higher charge state decreases with the charge number and diminishes for the charge states larger than 15+ (the peak around Ar^{15+} coincides with O^{6+} signal, which was observed for the mass spectrum measured before introducing Ar gas). For the pulse

mode, higher charge states up to Ar^{16+} are obtained, and Ar^{17+} is also identified. The period of modulation is 400 ms, and the time width of electron beam off is 1 ms for the Fig. 3.2(b). The time response of the intensity of extracted HCI beam of specific charge state (Ar^{16+}) is demonstrated in Fig. 3.2.

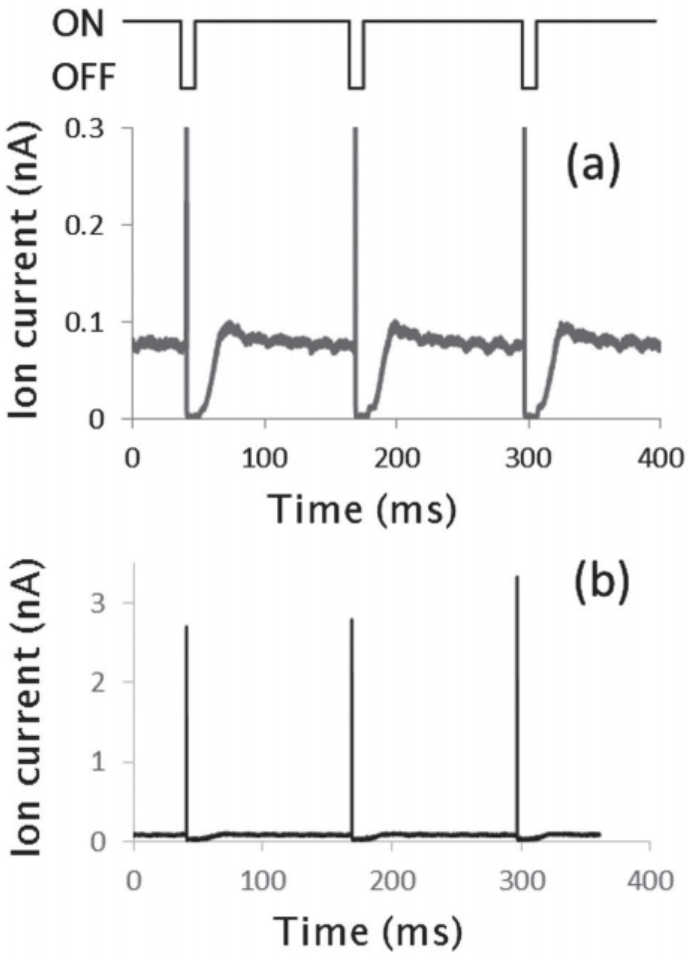

Fig. 3.2. Time evolution of the ion current of Ar^{16+} during pulse mode operation. (a) and (b) are drawn for the same data with the same horizontal scale and different vertical scale.

When the electron beam is turned off a strong spike appears, and the ion beam disappears immediately after the electron beam is turned off. After the electron beam is turned on, the intensity of Ar^{16+} gradually increases with the response time of ~10 ms and saturates toward an almost constant value (viz., DC component). Figure 3.2(b) compares the intensities of the spikes and the DC component; the peak heights of spikes are ~40 times higher than the DC component. The width of the spike is ~100 μs, which

is close to the response time of the high voltage amplifier applied to the anode. The spike indicates that the ions trapped by space charge potential of electron beam are released at once. Such burst signal has been observed in electron cyclotron resonance ion sources due to a similar mechanism; strong ion pulse with the width of 0.1~1 ms is generated when rf is turned off [10, 11]. Figure 3.3 shows the time response of the intensity of Ar^{16+} after switching the operational mode to the other one: Fig. 3.3(a) for DC mode to pulse mode and Fig. 3.3(b) for pulse mode to DC mode.

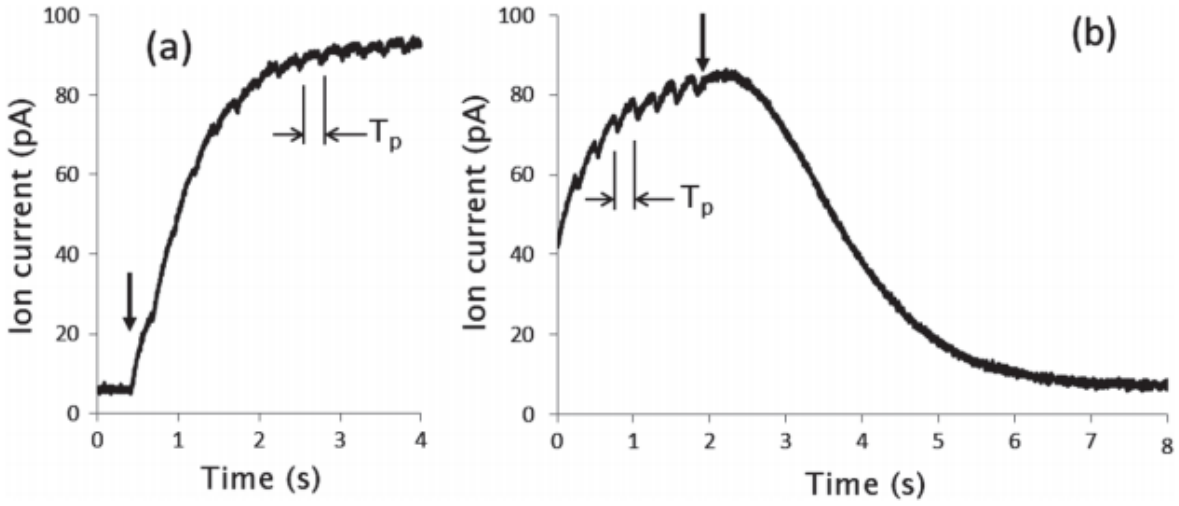

Fig. 3.3. Time response of the intensity of Ar^{16+} after switching the operational mode to the other one. (a) DC mode to pulse mode and (b) pulse mode to DC mode.

In Fig. 3.3, the arrows indicate the timing of mode change and Tp represents the period of repetitive modulation (250 ms). Ion current steeply rises at the moment of beam - off and absolutely stays zero during beam - off time (~1 ms), then the rapid change of ion current will make upward/downward spike at each beam on/off timing as shown in Fig. 3.2; however, such structures are smeared out in Fig. 3.3 due to the limited time response of the electrometer. As shown in Fig. 3.2, the response time for the creation of Ar^{16+} is in the order of 10 ms; however, the fraction of Ar^{16+} among the HCIs stored in and extracted from the drift tube region changes over several seconds. This long time constant in transient response at the mode change suggests that it needs several second to reach equilibrium charge state distribution of trapped HCIs. It seems that some kind of memory effect works for this transient phenomena. The memory

might be ions trapped by the magnetic field, which remain in the drift tube region even in the absence of electron beam. We performed another experiment to observe pulsed ions released by abrupt changing of DT7 potential. Figure 3.4(a) is time response of extracted Ar^{16+} similar to Fig. 3.2(a) for various values of DT7. DC component decreases with the height of DT7 while transition time to reach maximum value increases with DT7. This phenomena may reflect that the capacity of ion trap in the drift tube region increases with DT7 value and the time necessary for the charge state distribution reaching equilibrium condition in the trap increases with the trap capacity. In this experiment, DT7 and anode potentials were controlled as schematically shown in Fig. 3.4(b). The potential barrier is set to zero for 1 ms, and electron beam is turned off at 0.25 ms after the recovery of the potential barrier. The electron beam remains off for 0.75 ms. The spike at the turning off of electron beam is observed only for DT7 = 0, that is, when the potential barrier is turned off the ions escaped from the drift tubes include those ions trapped by the space charge of electron beam.

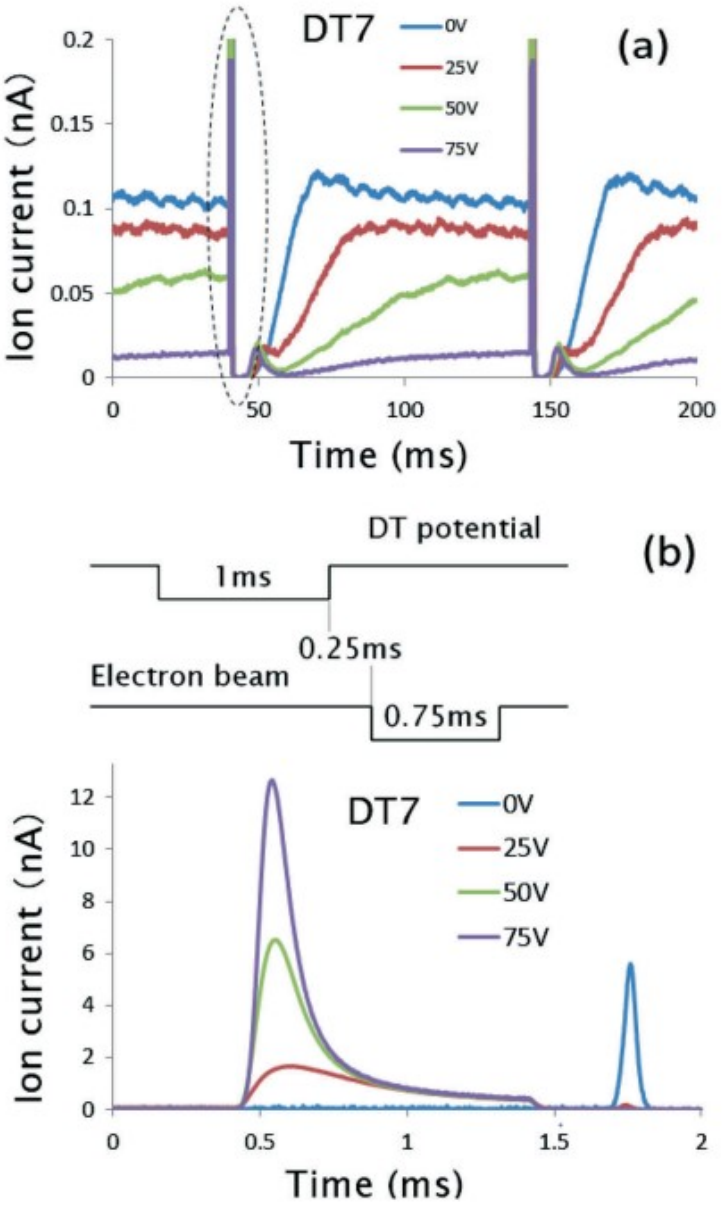

Fig. 3.4. Time evolution of the ion current of Ar^{16+} during pulse mode operation for various DT7 values, (a) is for the time span over several periods, and (b) is near the switching time of DT7 and anode voltage corresponding the moment indicated with a broken ellipse in (a).

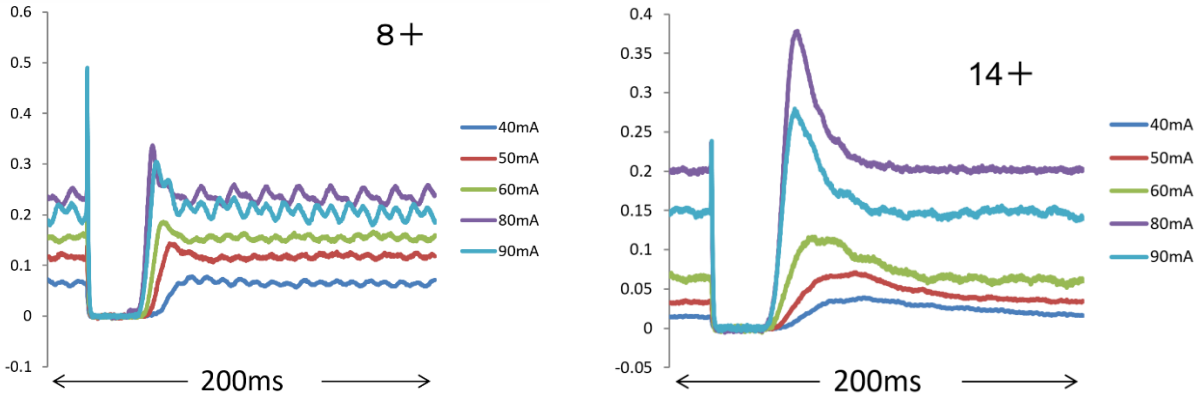

Fig. 3.5. Dependence of time evolution of extracted HCI on the electron beam current for Ar^{8+} and Ar^{14+}.

Figure 3.5 shows time evolution of extracted HCI (Ar^{8+} and Ar^{14+}) for various electron beam current. The extracted ion current increases with the electron beam current. However when the electron beam current was 90 mA ion current became lower than that when the electron beam current was 80 mA. This is due to the degradation of cathode. After the exchange of cathode ion current increases with the electron beam current upto 140 mA as shown in Fig. 3.6. When the electron beam is turned on the ion current starts to increase and reaches maximum value after a specific transition time, and the ion current decreases after the transition time. This is because that the charge state is promoted to higher charge states. The transition time decreases with the electron beam current since higher electron beam current creates HCI faster.

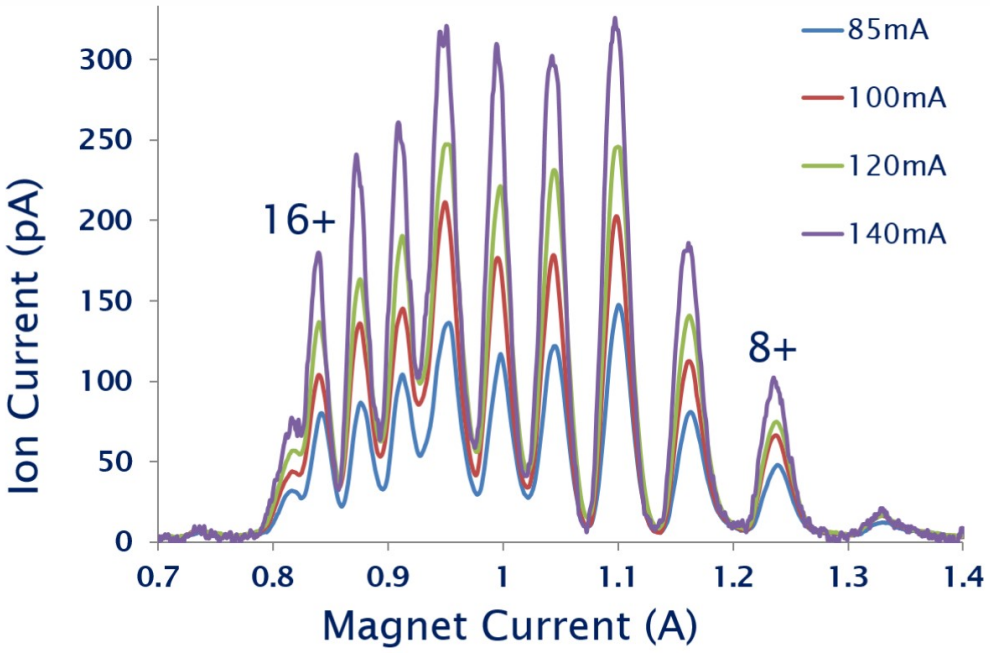

Fig. 3.6. Mass spectra extracted from Kobe EBIS under the pulse mode operation after cathode exchange procedure.

Ion current of higher charge states is improved under pulse mode as shown in Fig. 3.1. This effect depends on the width and poriod of modulation of electron beam. Dependence of extracted HCI intensity on the width and interval of electron beam off is shown in Fig. 3.7. It is noted that the width of beam off more than 0.5 ms is necessary for obtaining sufficient Ar^{16+} intensity while the width of 0.2 ms is enough for Ar^{12+}. On the other hand the ion current of higher charge state (Ar^{16+}) depends also on the period of electron beam modulation (interval of beam off timing). There exist suitable range of period between 0.1 ~ 1 s. Pulse mode operation with a longer period means that the situation approaches to DC mode, then the ion current decreases at the period more than 1 s.

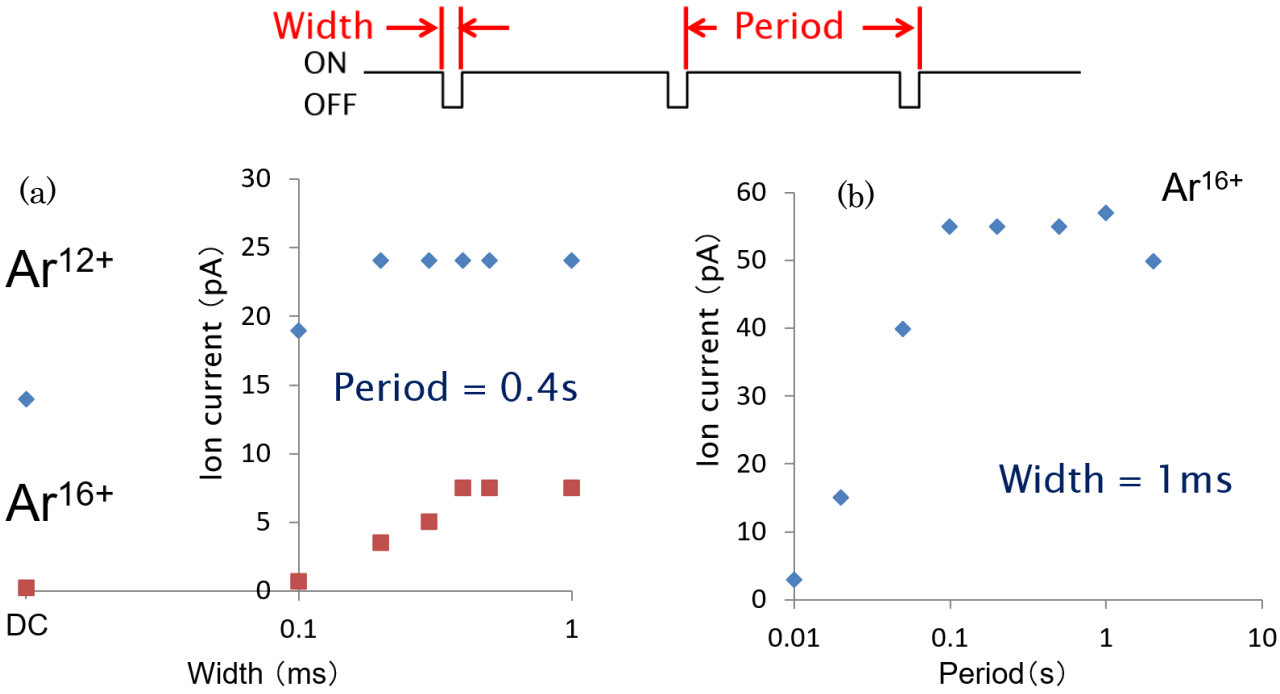

Fig. 3.7. Dependence of extracted HCI intensity on the width (a) and period (b) of electron beam off.

Charge state distribution of Kr HCI is also improved by pulse operation. Figure 3.8 shows mass spectra for Kr HCI obtained by introducing Kr gas instead of Ar inside the drift tube under pulse mode operation. Dark blue line in Fig. 3.8 is the mass spectrum before introducing Kr. Due to the residual gas in the drift tube region there are many peaks of light elements originated from CO, CO_2, and N_2 molecules. In the mass spectrum with Kr gas, intensities of peaks of residual elements are comparable to those of Kr. Figure 3.9 shows the comparison of mass spectra between under pulse mode operation and DC mode operation. The intensity for higher charge states (Kr^{25+} ~ Kr^{31+}) under pulse mode is higher than that under DC mode, while the intensity for lower charge states does not show any difference between pulse mode and DC mode. The peaks of Kr HCI may include the signal of HCIs of residual element as imagined from Fig. 3.8. However, it is assumed that the fraction of intensity originated from residual element is much less than that of Kr in the spectrum with Kr dose. This is justified by observing time structure of the intensity of each charge state. Figure 3.10 shows time evolution of Kr HCI (Kr^{28+} ~ Kr^{31+}). Except the signal of Kr^{29+} there are narrow peaks around several tens of ms after the electron beam is turned on. They are ascribed to the

signal arisen from residual elements. In the spectrum for Kr^{29+} there is no narrow peak because there is no HCI of residual element with same m/q value as that of Kr^{29+}. The slowly rising signal after the tail of the peak of residual element comes from Kr HCI that has longer ionization time. This indicates that the content of ions trapped in the drift tube region changes from HCI of residual element to that of Kr as the ionization time elapses. It is also observable that the time constant of the rising of Kr signal is larger for higher charge state.

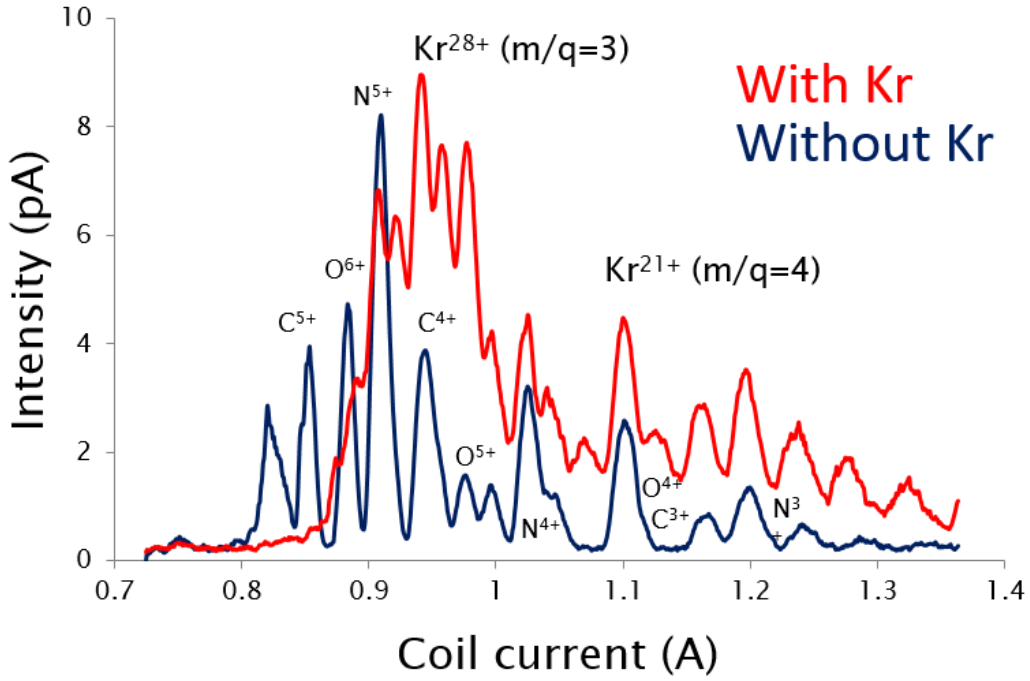

Fig. 3.8. Mass spectra for Kr HCI and residual elements obtained with Kobe EBIS.

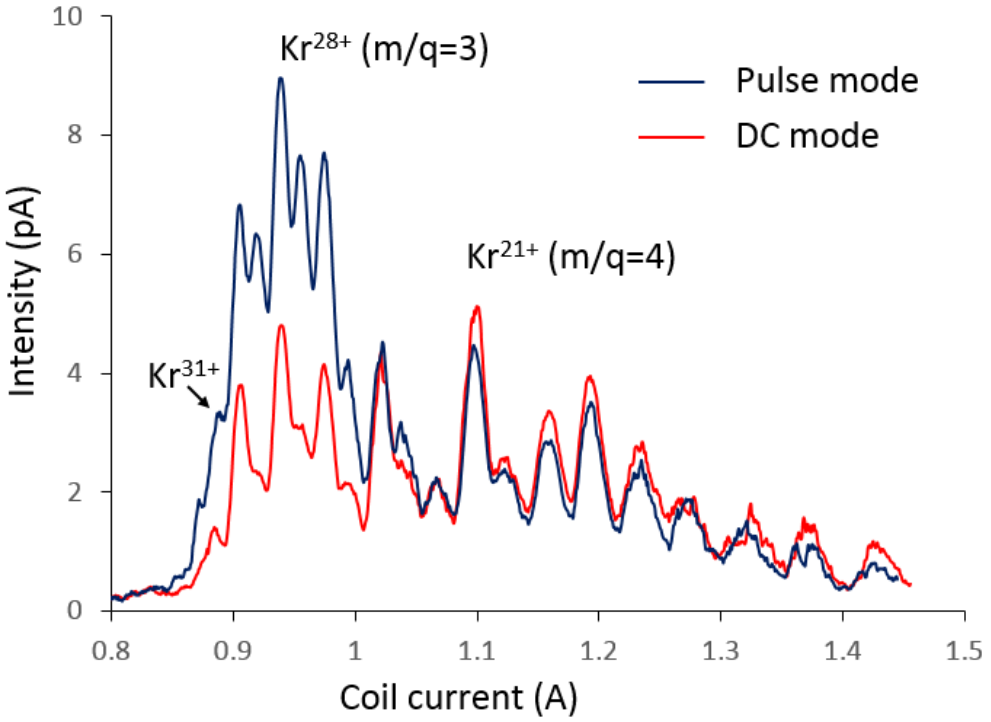

Fig. 3.9. Mass spectra for Kr HCI under pulse mode and DC mode.

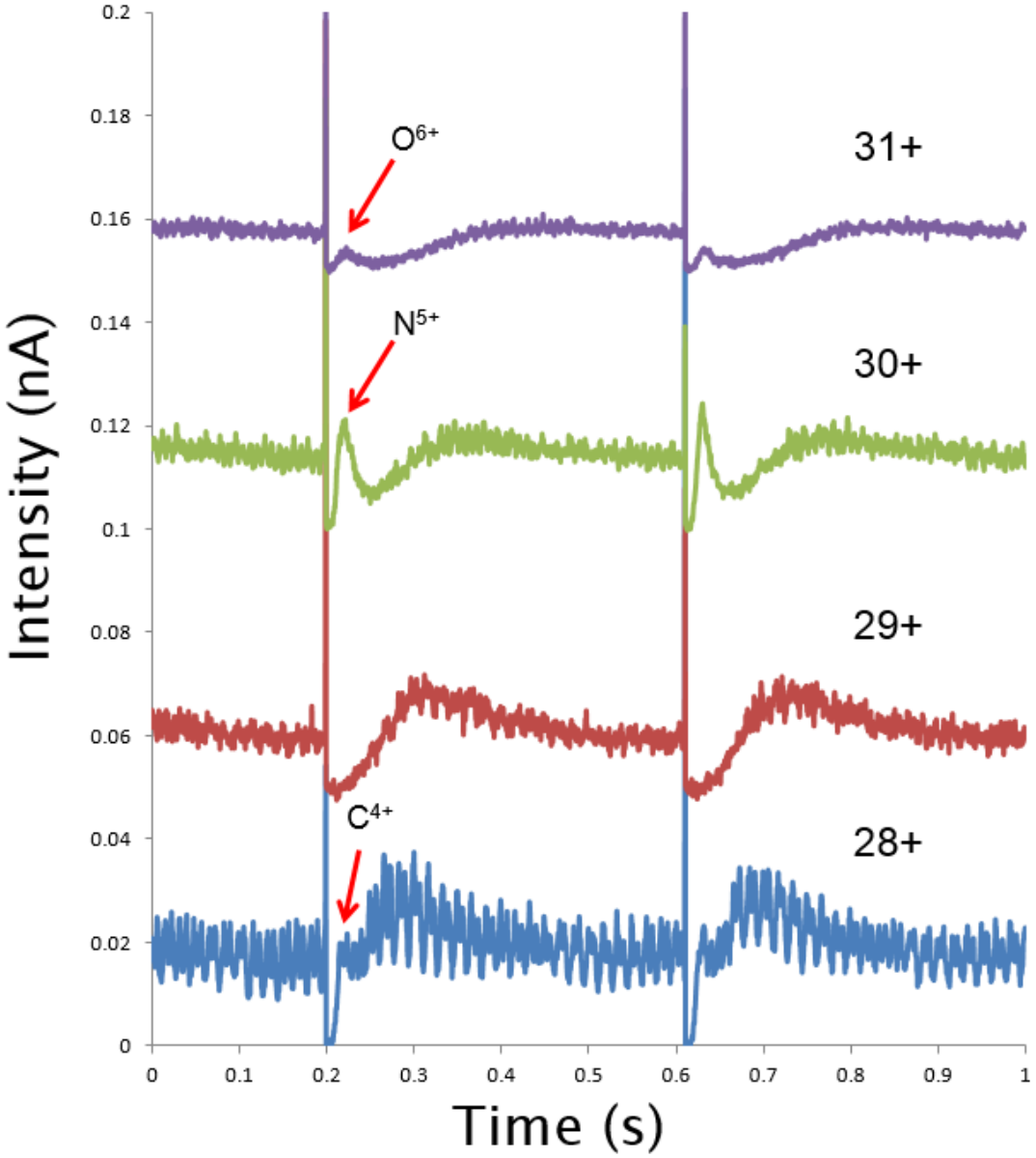

Fig. 3.10. Time evolution of Kr HCI extracted from Kobe EBIS under pulse mode operation.

3.4 Summary

Recent study on the performance of the Kobe EBIS revealed that periodic intermission of electron beam improves charge state distribution of extracted ions. The period of intermission is in the order of 100 ms, and the width of beam - off time is 1 ms or less. This operation makes it possible to produce Ar^{15+} to Ar^{17+} effectively, whereas the charge is limited less than 14+ under the ordinary operational mode with DC electron beam. A spike of HCIs with a peak current in the order of nA is also produced at each

moment of electron beam off. The measurement on the time evolution of the intensity of Ar^{16+} around the timing of mode changes revealed that the intensity of extracted Ar^{16+} changes slowly after mode change with a time constant of few seconds, whereas Ar^{16+} is created rapidly within a few tens ms after switching on. This means that it needs several seconds to reach equilibrium charge state distribution of extracted ions after the operational mode is changed.

References

[1] T. Schenkel, A.V. Hamza, A. V. Barnes, and D. H. Schneider, Prog. Surface Sci. 61 (1999) 23.

[2] F. Aumayr, S. Facsko, A. S. El-Said, C. Trautmann, and M. Schleberger, J. Phys. Condens. Matter 23 (2011) 393001.

[3] E. D. Donets and V. P. Ovsyannikov, JETP 53 (1981) 466.

[4] T. Iwai, Y. Kaneko, M. Kimura, N. Kobayashi, S. Ohtani, K. Okuno, S. Takagi, H. Tawara, and S. Tsurubuchi, Phys. Rev. A 26 (1982) 105.

[5] M. Sakurai, H. Onishi, K. Asakura, M. Tona, H. Watanabe, N. Nakamura, S. Ohtani, T. Terui, S. Mashiko, and H. A. Sakaue, Vacuum 84 (2010) 530.

[6] M. Sakurai, K. Sasaki, T. Miyamoto, D. Kato, and H. A. Sakaue, e-J. Surf. Sci. Nanotech. 14 (2016) 1.

[7] N. Nishida, K. Betsumiya, M. Sakurai, T. Sakurai, T. Terui, and S. Honda, e-J. Surf. Sci. Nanotech. 16 (2018) 356.

[8] M. Sakurai, S. Ohtani, and H. A. Sakaue, J.Vac. Soc. Jpn. 55 (2012) 180 (in Japanese).

[9] N. Nishida, Y. Hori, A. Yamauchi, M. Sakurai, H. A. Sakaue, and D. Kato, X-Ray Spectrometry 49 (2020) 74.

[10] G. Melin, F. Bourg, P. Briand, M. Delaunay, G. Gaudart, A. Girarad, D. Hitz, J. P. Klein, P. Ludwig, T. K. Nguyen, M. Pontonnier, and Y. Su, Rev. Sci. Instrum. 65 (1994) 1051.

[11] C. Mühle, U. Ratzinger, W. Bleuel, G. Jöst, K. Leible, S. Schennach, and B. H. Wolf, Rev. Sci. Instrum. 65 (1994) 1078.

Chapter 4 Structural Modification of Multi-Walled Carbon Nanotube Irradiated by Highly Charged Ions

4.1 Introduction

Nanocarbon materials such as carbon nanotubes (CNT), graphene, and fullerene are noteworthy materials in various fields of nanotechnology. CNT is one of the allotropes of carbon and has a honeycomb structure composed of only carbon atoms. Its diameter is several nm to several hundred nm, and its length is about several μm [1]. CNT with single tube is called as single-walled CNT (SWCNT) and CNT with multiple tubes is called as multi-walled CNT (MWCNT). CNT is a one-dimensional carbon material with a very large aspect ratio and CNT is flexible. It attracts attention as a new functional material due to its high elasticity, it has 10 times as high as that of thermal conductivity of copper, and 100 times the mechanical strength of steel. Controlling one CNT for a quantum device, networked CNT for a gas sensor, vertically aligned CNT for an electron emitter and supercapacitor electrode, vertically aligned high-density CNT for LSI wiring, etc. are expected as applications [2 - 5]. However, in order to realize these, it is necessary to control the form of CNTs according to each application.

By controlling the chirality, it is possible to fabricate CNTs with semiconductor properties and metal properties by winding the graphene sheet. In the form control during synthesis, the diameter and length can be controlled by changing the conditions during the synthesis of the nanocarbon material, and the orientation can be controlled by the substrate. By introducing defects into carbon materials, not only structural changes but also the unique properties of nanocarbon materials can be produced.

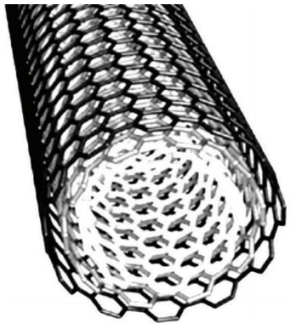

Fig. 4.1. Schematic image of CNT (MWCNT) [6].

The means for introducing defects are ion/electron beam and X-ray irradiation. Researches for device applications have been conducted to control the structure and characteristics of devices by irradiating nanocarbon materials with ions and electron beams. Ions used for the irradiation have large potential energy and kinetic energy compared to electron beams and X-rays, so it has a large effect on materials. In particular, HCIs, have a much larger potential energy than monovalent ions, and give this to a limited area of the target surface in a very short time of several fs. This is not seen in other charged particles. This is a unique feature of the interaction between HCI and surface. However, the influence of the potential energy of HCIs on nanocarbon materials has not been elucidated.

Ion irradiation effect

Defect generation by SCI irradiation as one of the effects of ion irradiation has been observed and its mechanism has been studied [7 - 10]. When ions are irradiated onto a solid, the ions collide with atoms and electrons in the solid. At that time, the energy of the ions moves, and the collided atoms and electrons collide with another particle. By repeating such collisions, defects are generated in the crystal. As shown in Fig. 4.2, the types of defects include single vacancies (SV), double vacancies (DV), and adsorbed atoms (adatom) adsorbed between carbon network lattices. Regarding defects in carbon materials, it is known that DV aggregates to form five- and eight-membered rings, and SV and adatoms form Stone-Wales (SW) defects. SW defects are structures formed by pairs of five- and seven-membered rings in a six-membered ring network. This is a defect that occurs in the reaction process in which two fullerenes are fused or in the reaction process in which two SWCNTs are fused. In addition, the activation energy required for structural deformation is as high as 7 eV, and the energy after formation rises by more than 2 eV, so it rarely occurs under normal conditions. As the process of defect generation, when ions irradiated from the ion source travel through the crystal, the energy of the ions moves to the atoms and electrons in the crystal, so that interstitial atoms or vacancies are formed. Most point defects disappear mainly when the displaced atoms are buried, but some remain in the crystal.

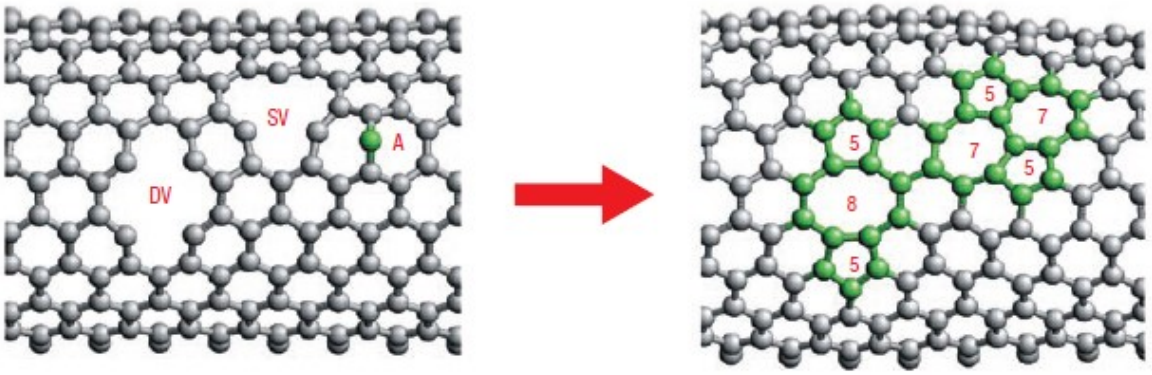

Fig. 4.2. A double vacancy (DV) transforms to an agglomeration of five- and eight-membered rings. A single vacancy (SV) and an adatom may form a metastable Stone–Wales (5–7–7–5) defect [7].

If CNT is irradiated with ions at high fluence (> 10^{15} ions/cm^2) swelling of outer diameter occurs and hollow structure disappears [11]. The TEM image of MWCNT irradiated with Ar^+ at the fluence of 1×10^{16} ions/cm^2 is shown in Fig. 4.3 and mean diameters of the MWCNTs as a function of Ar^+ ion fluence is shown in Fig. 4.4.

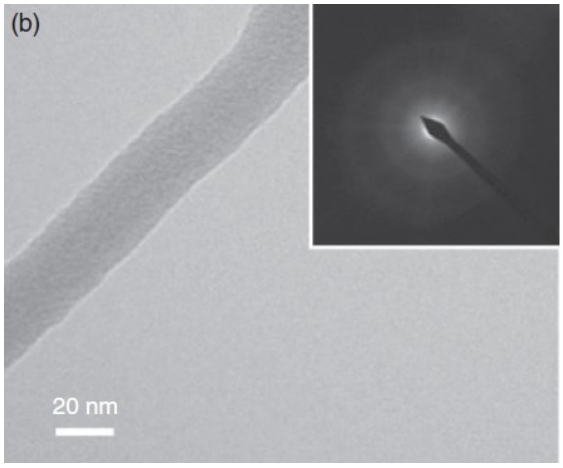

Fig. 4.3. TEM image of MWCNT irradiated with Ar^+.

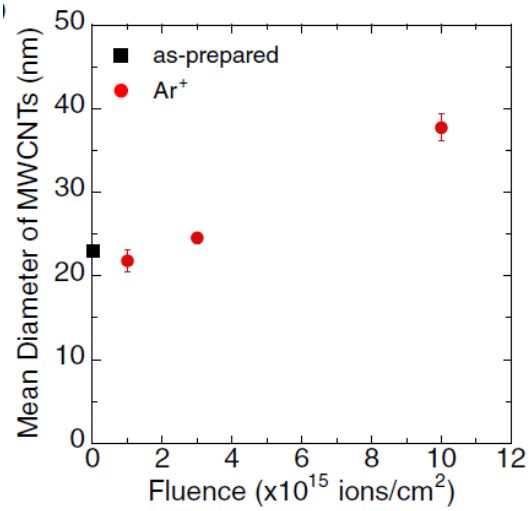

Fig. 4.4. Mean diameters of the MWCNTs as a function of Ar^+ ion fluence.

4.2 Experimental

In the present experiments, HCIs generated by Kobe EBIS were irradiated with the MWCNT created by the chemical vapor deposition (CVD) method. CVD is a method in which a carbon-containing gas such as methane or acetylene is thermally decomposed to produce CNTs. This is a method of synthesizing CNT by the action of a catalyst such as Fe, Co, or Ni. This method can grow CNTs directly on a solid substrate. In the present study the sample of MWCNT was grown by CVD on a SiO_2/Si substrate (Figs. 4.5 ~ 4.7) and bridged to a grid for the observation with transmission electron microscope (TEM). Figure 4.8 shows a scanning electron microscope (SEM) image of MWCNTs supported on a metal grid.

The purpose of the present experiment is to explore the method to control the structure and properties of MWCNTs that are cheaper than SWCNTs and to provide functionality in modified MWCNT. In addition, in the present experiments, it is a basic interest to know how much the surface of MWCNT is affected by the irradiation with HCIs.

TEM images and Raman spectroscopy were used to compare the structure of unirradiated MWCNTs with that of HCI irradiated samples.

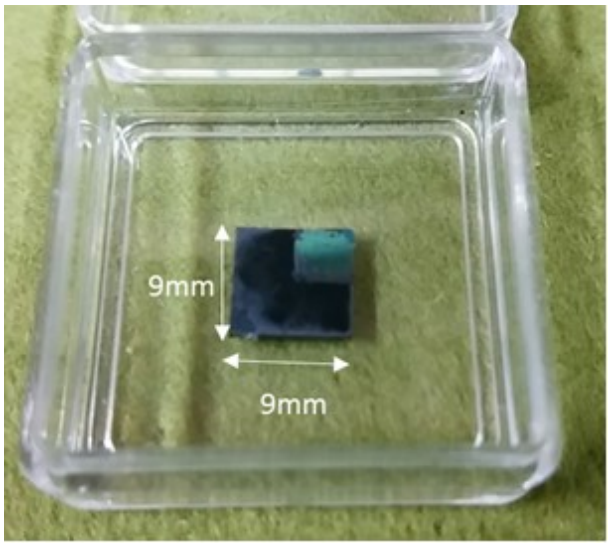

Fig. 4.5. MWCNT produced by CVD on a SiO_2/Si substrate.

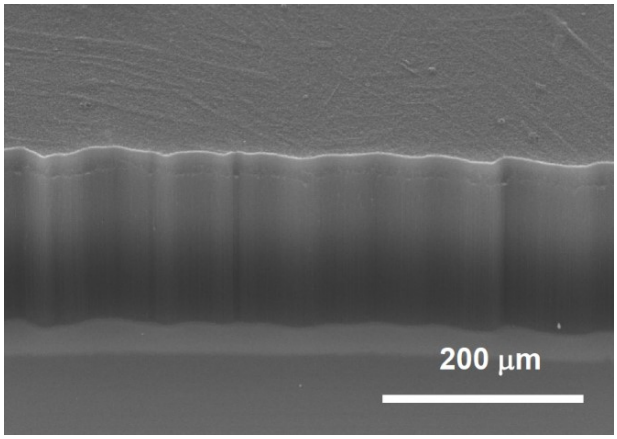

Fig. 4.6. SEM image of MWCNT on a SiO_2/Si substrate.

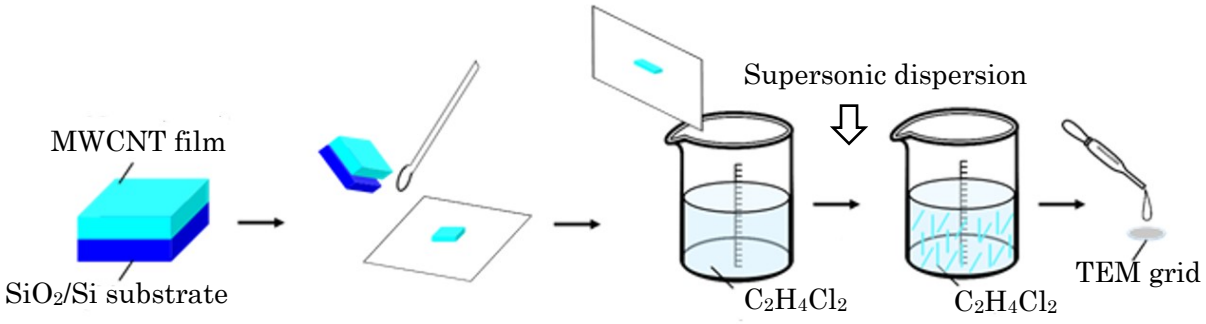

Fig. 4.7. Deposition method of MWCNT on a TEM grid.

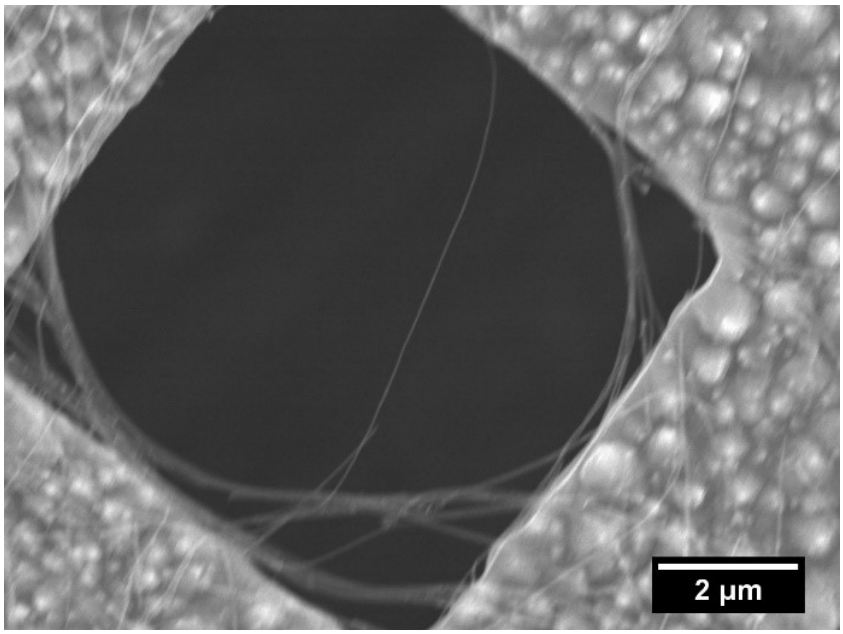

Fig. 4.8. SEM image of MWCNT supported on a metal grid.

TEM was used to observe the microscopic structure of MWCNTs. In TEM measurements, structural changes in atomic scale were observed from magnified images of single MWCNT before and after irradiation with HCIs. On the other hand, Raman spectroscopy provides the structural information by means of the excitation of lattice vibration modes, and the information is averaged one over micrometer area

The experiments consists of many runs with the different TEM apparatus and sample characteristics. We used two types of sample as listed in Table 4.1.

Table 4.1. MWCNT samples used in the present experiment.

	Sample A	Sample B
Diameter (nm)	10 ~ 20	30 ~ 50
Material gas	acetylene	xylene
Growth temperature (°C)	750	800 ~ 850
Growth time (min.)	20	5

First we used a TEM at the Osaka University for the observation of thinner MWCNT sample (10 ~ 20 nm in diameter, Sample A). In this run (Run A), observation area of about 50 nm square before irradiation is different from that of after irradiation.

After the second run we developed experimental technique to observe identical

area viewing single MWCNT on a TEM grid before and after irradiation. It is necessary to carry the sample between two apparatus of irradiation system and TEM which are installed in different buildings.

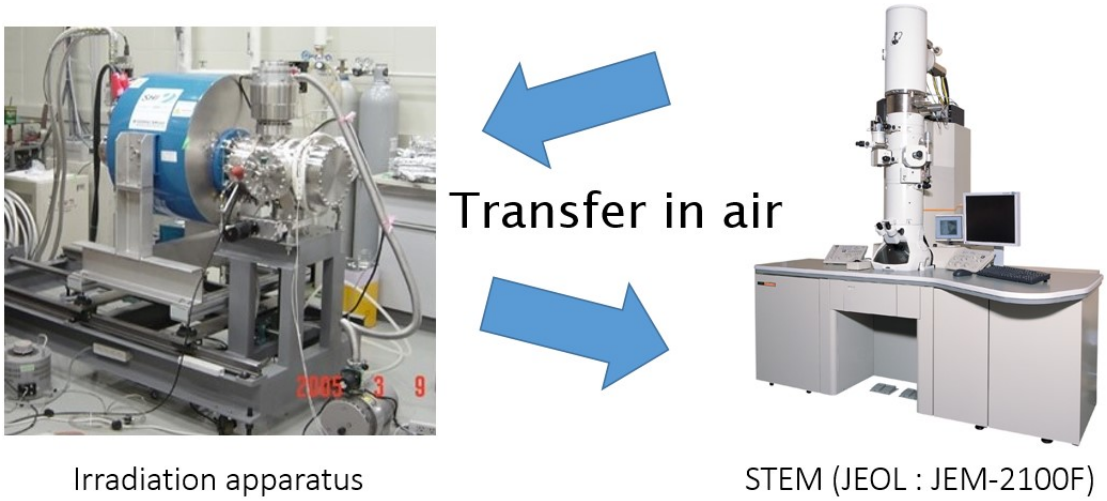

Fig. 4.9. Image of sample transfer.

Therefore it is necessary to register the position in the grid where the single MWCNT on which we focus exists. For the first step, we look for a grid cell which is easy to be addressed in the wide view of low magnification image as indicated with small, yellow square in Fig. 4.10.

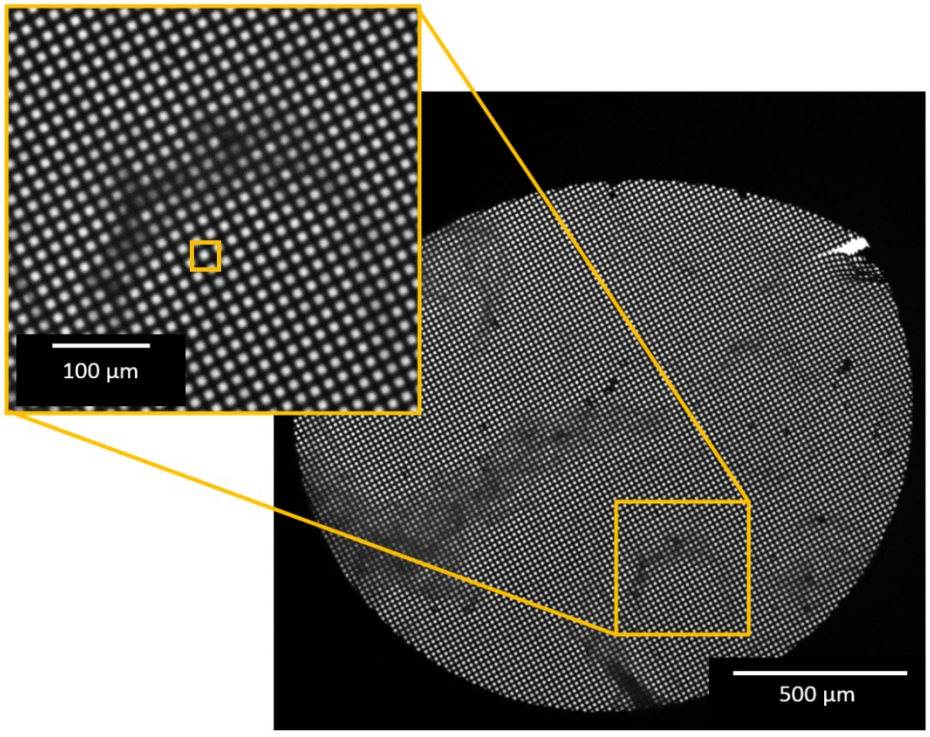

Fig. 4.10. TEM image at low magnification.

The magnified image of the single grid cell indicated in Fig. 4.10 corresponds to the upper right image in Fig. 4.11. Then it is not difficult to magnify further to recognize the layer structure of a specific single MWCNT as illustrated in Fig. 4.11. If the grid cell of interest could be found at the TEM observation after irradiation, TEM image of single MWCNT which is identical with that before irradiation could be obtained.

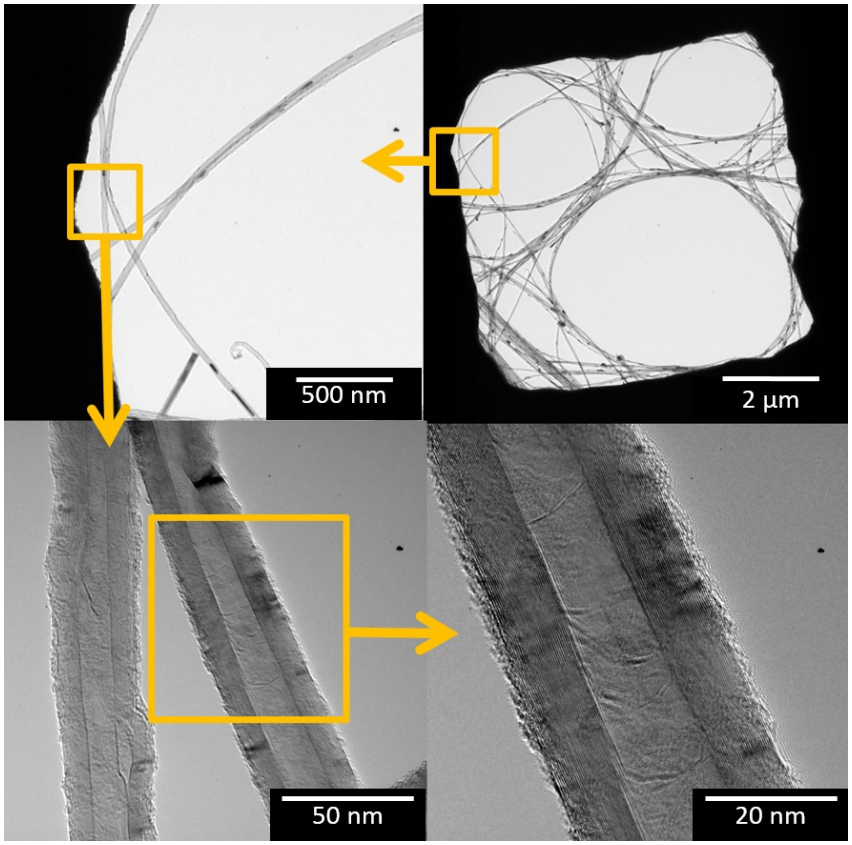

Fig. 4.11. TEM image with higher magnification.

As the second run (Run B), we observed TEM images of unirradiated and irradiated MWCNT [12, 13]. The sample is basically same as that used in Run A. For the next run (Run C), we observed sample B under similar irradiation condition as Run B. Finally we observed sample A again (Run D). Basically the sample used in Run D is same as that of Run A and Run B. However, structural modification induced by HCI irradiation was not remarkable in Run D compared to Run A and B. The reason of this difference is not clear but might be that the crystal structure of sample used in Run A and B had imperfection.

In order to investigate the effect of potential energy due to changes of charge state, irradiation was performed with a constant kinetic energy (16 keV) by applying a deceleration voltage to the sample stage.

4.3 Results and discussion

Run A

The TEM images of the unirradiated MWCNT is shown in Fig. 4.12. The sample irradiated with Ar^{8+} is shown in Fig. 4.13 to Fig. 4.15, and the one irradiated with Ar^{11+} is shown in Fig. 4.16 to 4.18, and Fig. 4.19 and Fig. 4.20 show the samples irradiated with Ar^{16+}.

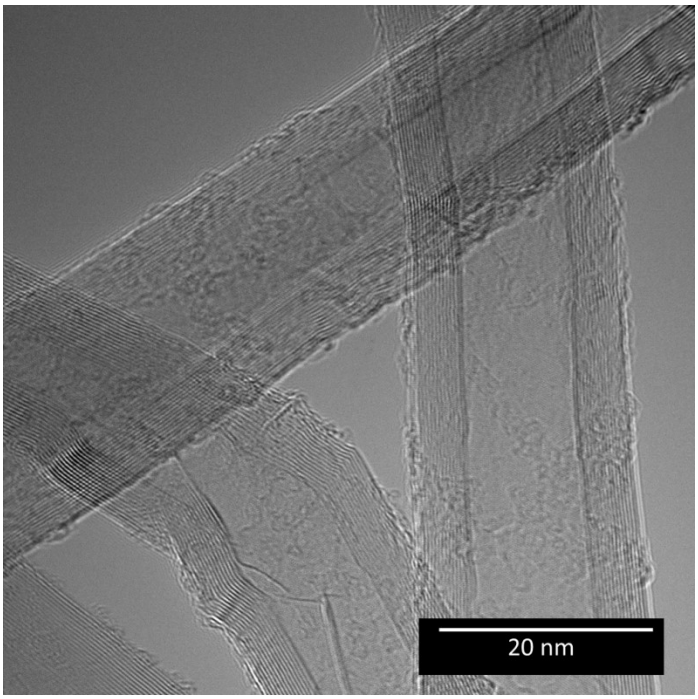

Fig. 4.12. TEM image of unirradiated MWCNTs.

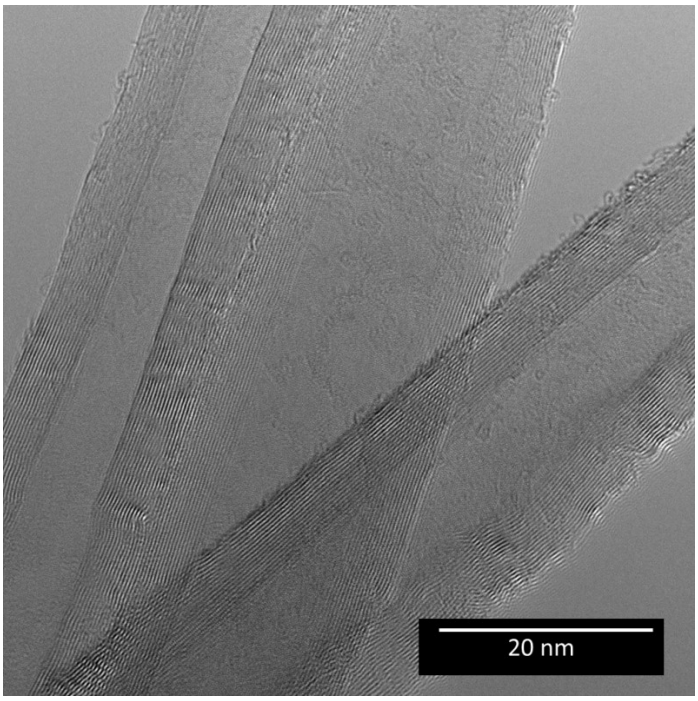

Fig. 4.13. TEM image of MWCNTs irradiated with Ar^{8+} at the fluence of 6×10^{12} ions/cm^2.

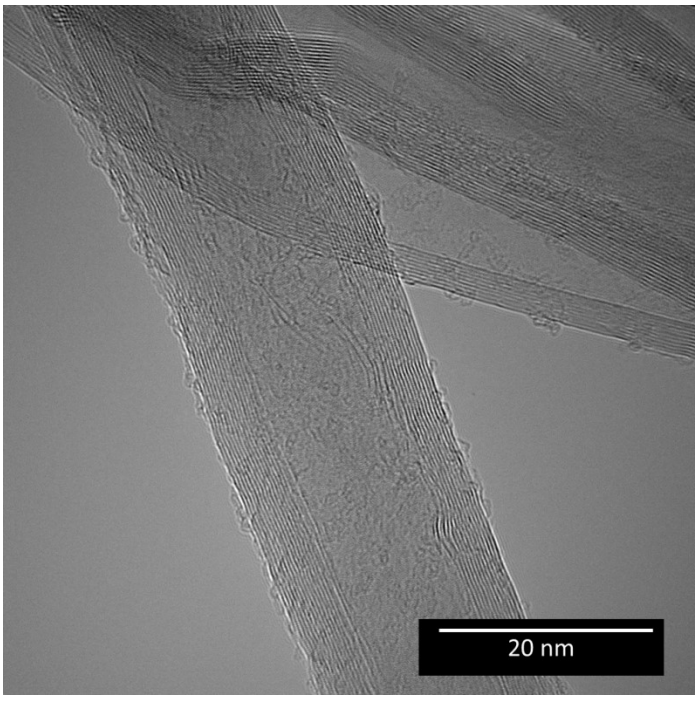

Fig. 4.14. TEM image of MWCNTs irradiated with Ar^{8+} at the fluence of 2×10^{13} ions/cm^2.

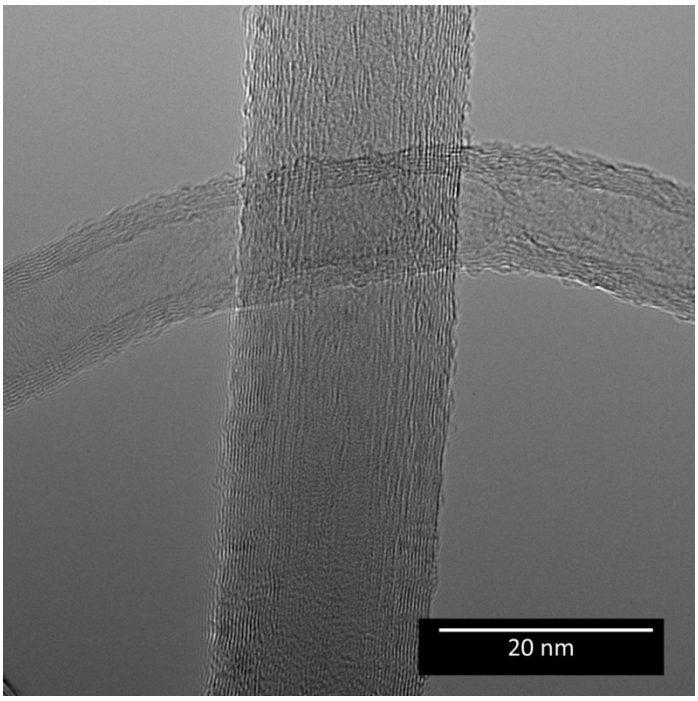

Fig. 4.15. TEM image of MWCNTs irradiated with Ar^{8+} at the fluence of 6×10^{13} ions/cm^2.

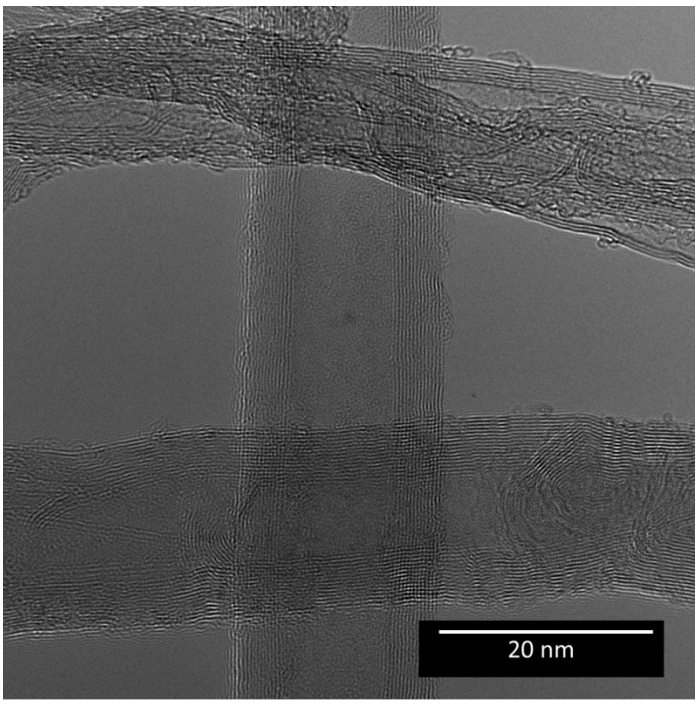

Fig. 4.16. TEM image of MWCNTs irradiated with Ar^{11+} at the fluence of 6×10^{12} ions/cm^2.

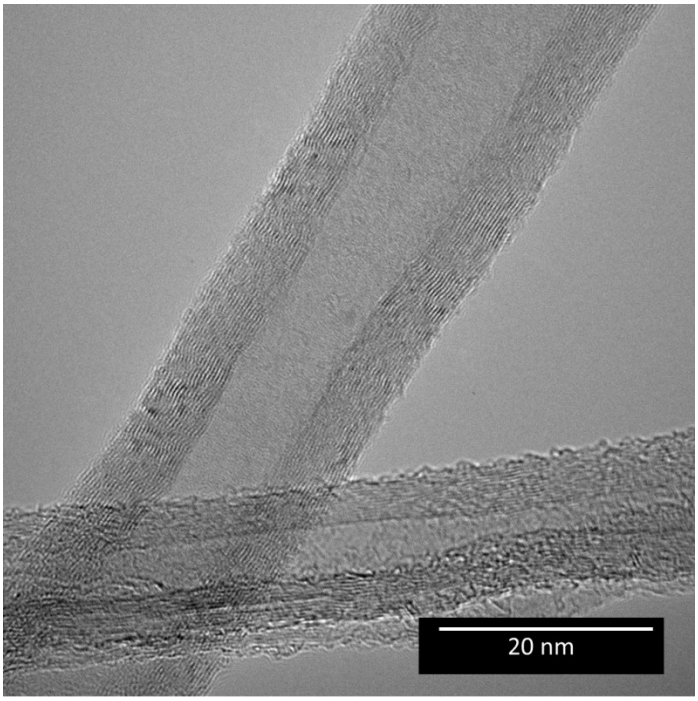

Fig. 4.17. TEM image of MWCNTs irradiated with Ar^{11+} at the fluence of 2×10^{13} ions/cm^2.

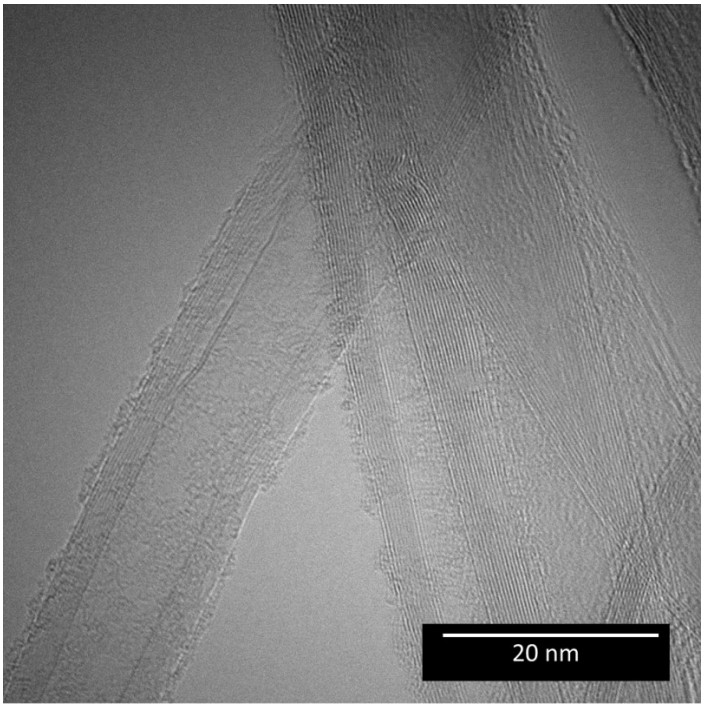

Fig. 4.18. TEM image of MWCNTs irradiated with Ar^{11+} at the fluence of 6×10^{13} ions/cm^2.

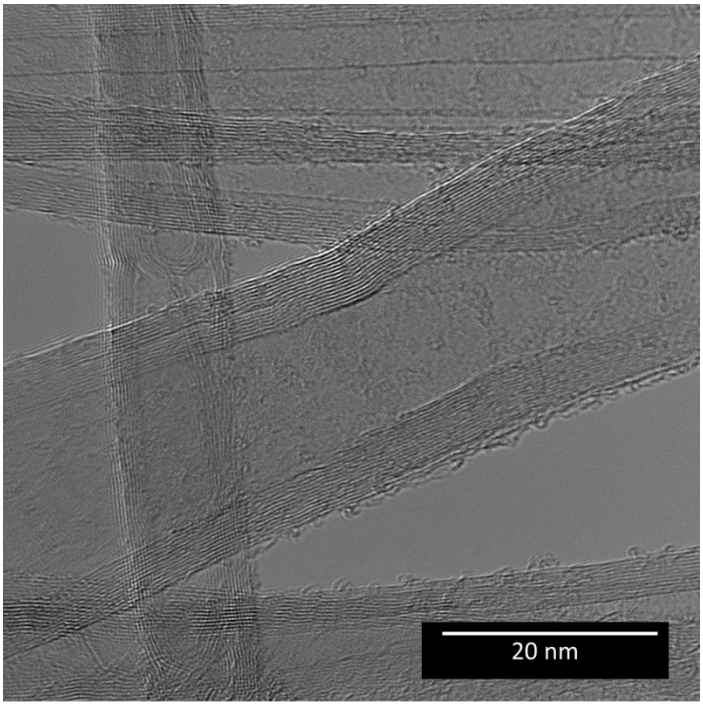

Fig. 4.19. TEM image of MWCNTs irradiated with Ar^{16+} at the fluence of 6×10^{12} ions/cm^2.

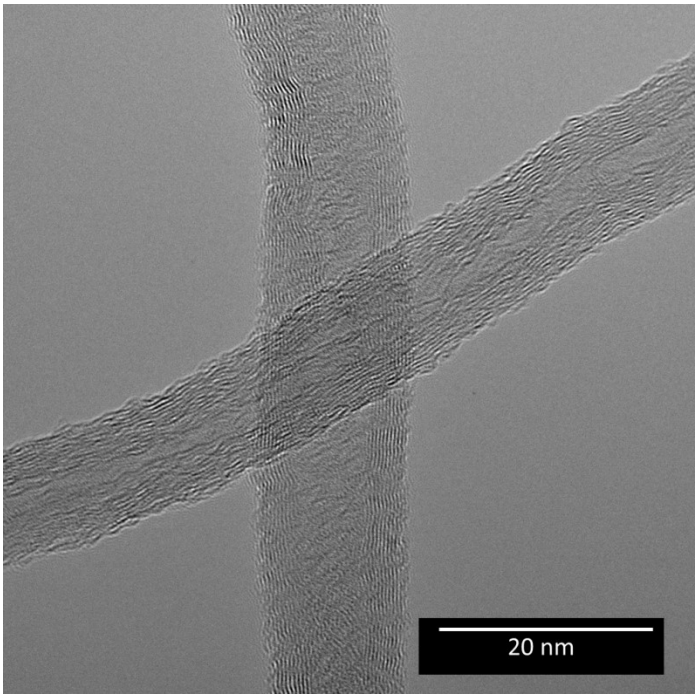

Fig. 4.20. TEM image of MWCNTs irradiated with Ar^{16+} at the fluence of 2×10^{13} ions/cm^2.

From the TEM images, the layer structure and hollow structure of the MWCNT are observed. When comparing the unirradiated samples with those irradiated with Ar^{16+}, uneven surfaces are observed on the MWCNTs. It is considered that defects are introduced in the irradiated samples. In order to investigate what kind of change occurred in the MWCNT, the outer diameter, inner diameter, and layer thickness were measured for each irradiation conditions. Figure 4.21, Fig. 4.22, and Fig. 4.23 show the relation of (outer) diameter, inner diameter, and layer thickness with the charge state of HCI and irradiation dose, respectively.

From Fig. 4.21 and Fig. 4.22, the diameter and inner diameter tend to decrease due to irradiation with HCIs. In particular, these decreases are remarkable in MWCNT irradiated with Ar^{16+}.

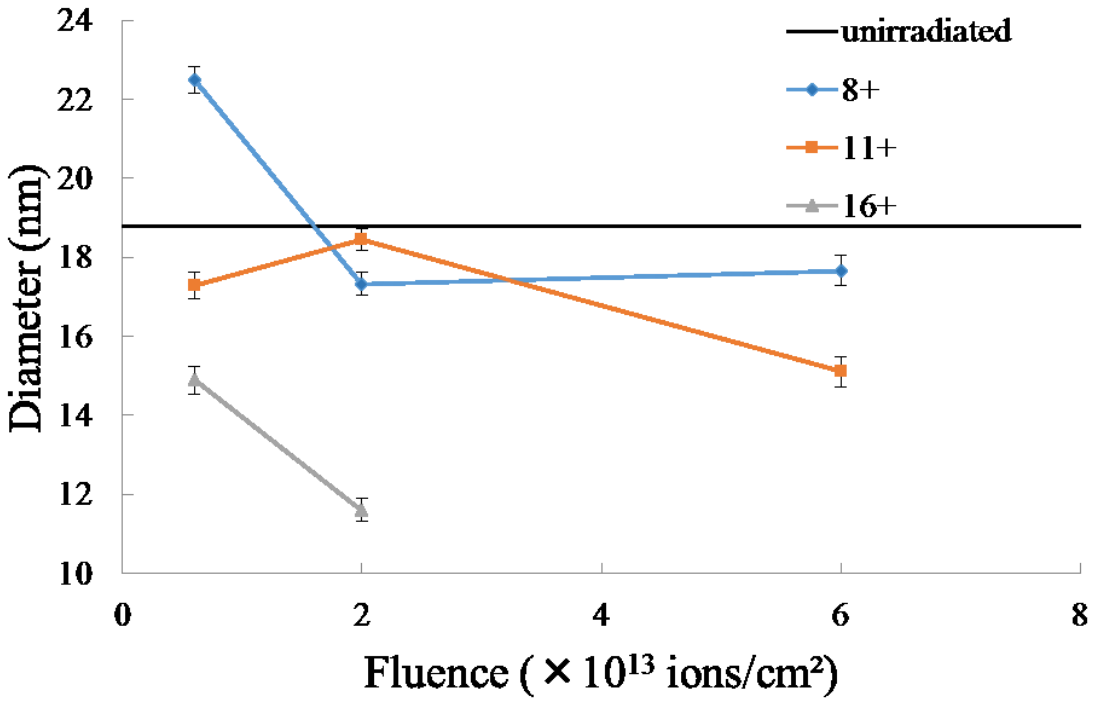

Fig. 4.21. Diameters of MWCNTs irradiated with Ar^{q+} (q = 8, 11, 16).

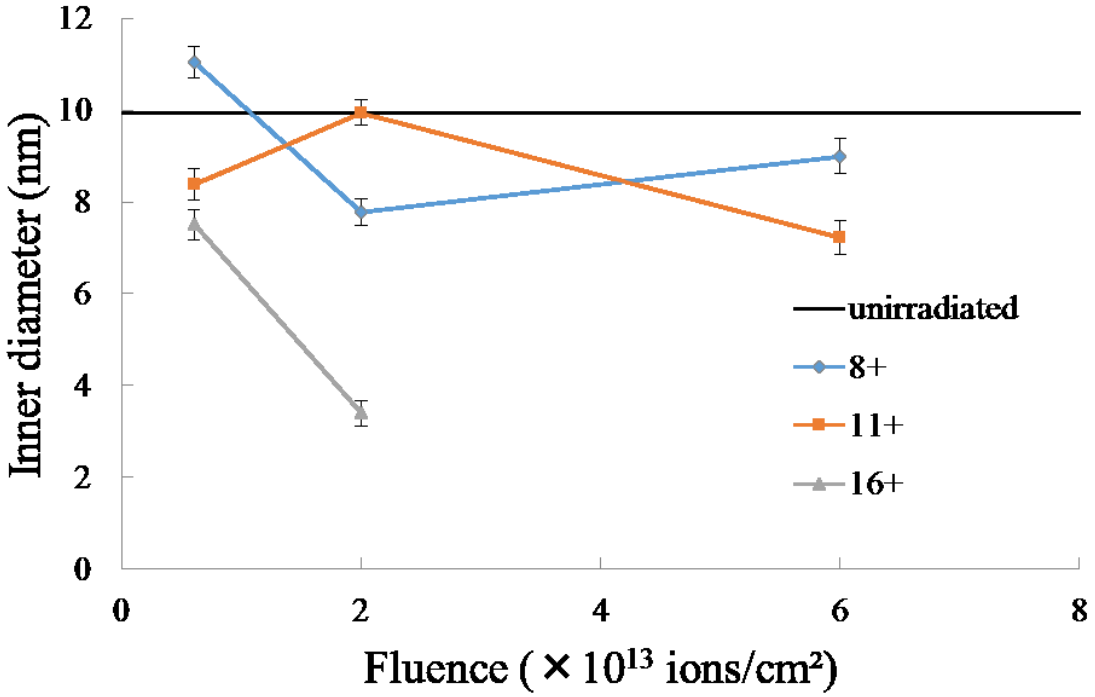

Fig. 4.22. Inner diameters of MWCNTs irradiated with Ar^{q+} (q = 8, 11, 16).

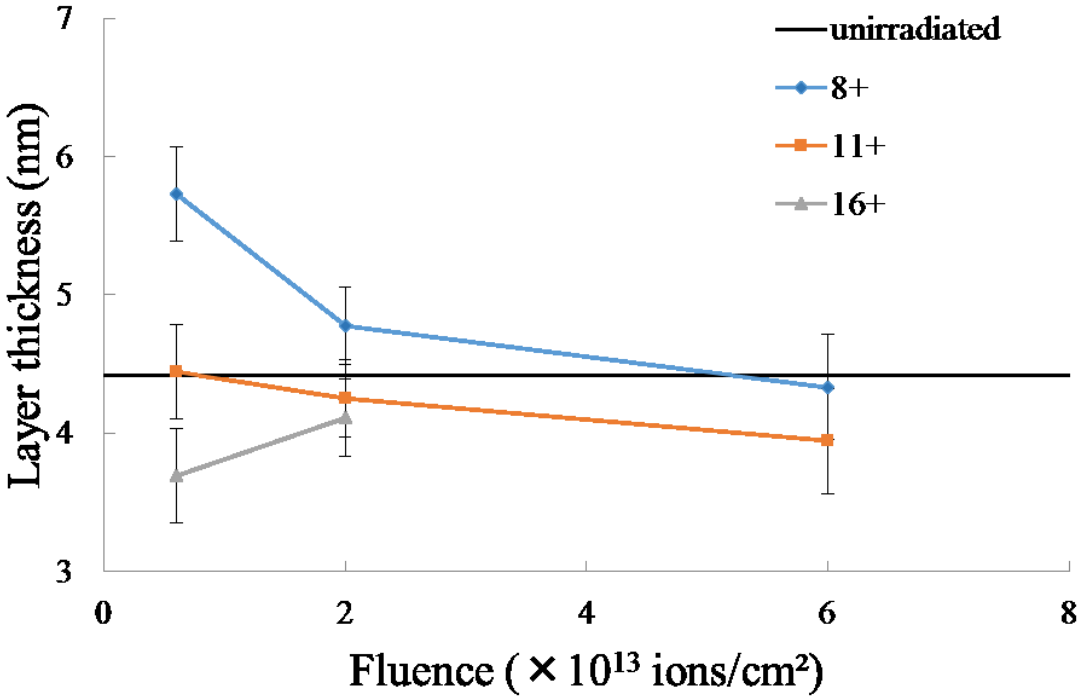

Fig. 4.23. Layer thickness of MWCNTs irradiated with Ar^{q+} (q = 8, 11, 16).

Figure 4.24 show electron diffraction pattern of a small part of the sample. Diffraction pattern is not spots but arcs since several MWCNTs affect the pattern.

From the diffraction pattern, it was found that the diffraction spots were blurred and the crystal structure was broken as charge state increased.

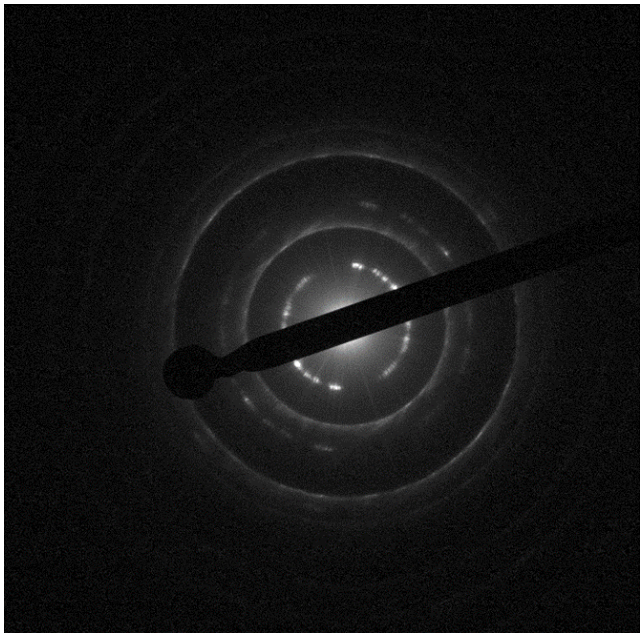

Fig. 4.24. Electron diffraction pattern of unirradiated MWCNT.

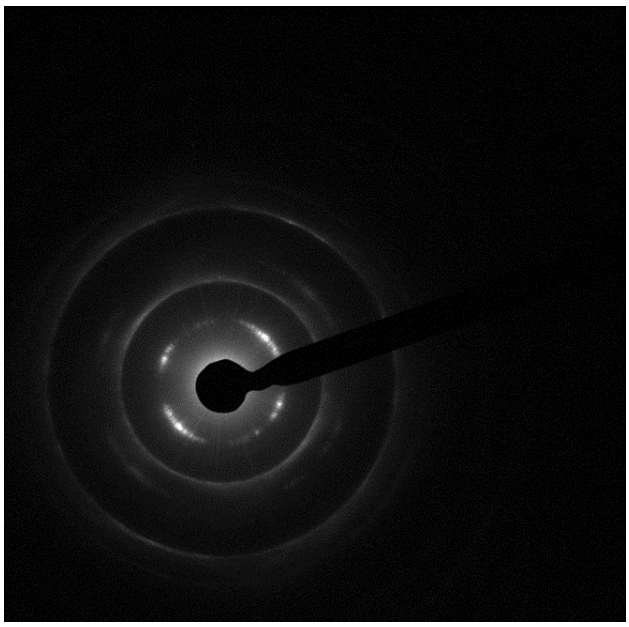

Fig. 4.25. Electron diffraction pattern of MWCNTs irradiated with Ar^{8+} at the fluence of 2×10^{13} ions/cm^2.

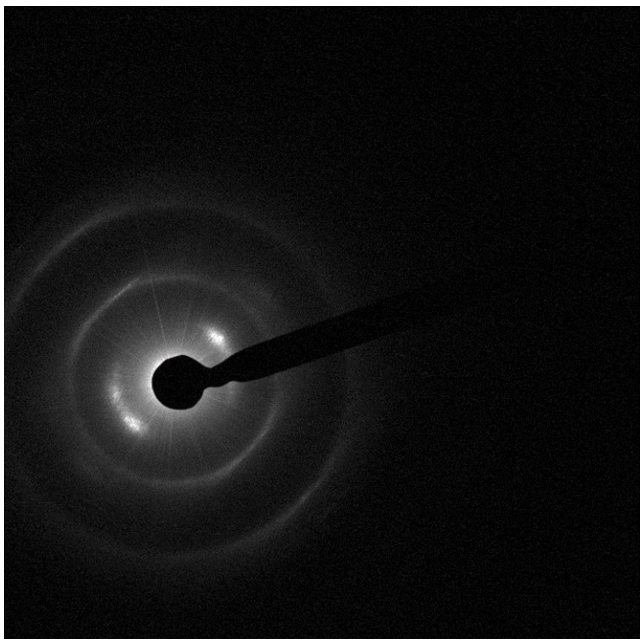

Fig. 4.26. Electron diffraction pattern of MWCNTs irradiated with Ar^{11+} at the fluence of 2×10^{13} ions/cm^2.

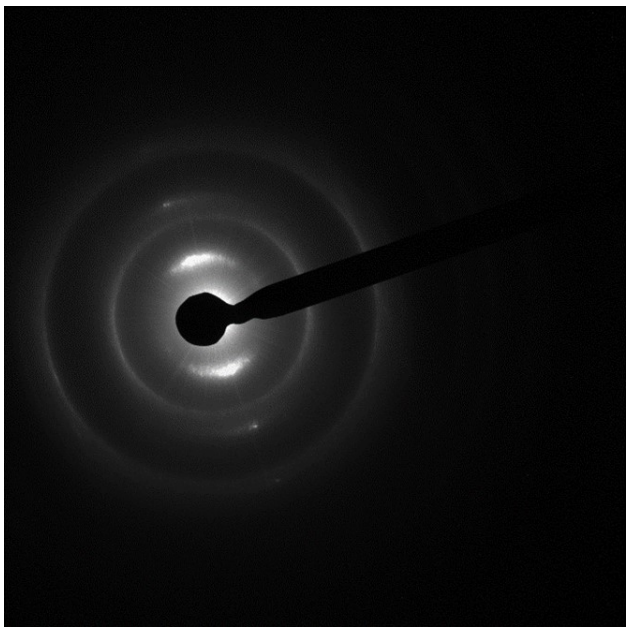

Fig. 4.27. Electron diffraction pattern of MWCNTs irradiated with Ar^{16+} at the fluence of 2×10^{13} ions/cm^2.

Raman spectra obtained by Raman spectroscopy are shown below. Figure 4.28 shows the unirradiated sample, Fig. 4.29 shows the results of irradiation with Ar^{8+}, Fig. 4.30 shows the results of irradiation with Ar^{11+}, and Fig. 4.31 shows the results of irradiation with Ar^{16+}. Each spectrum is normalized by the G peak (1580 cm^{-1}).

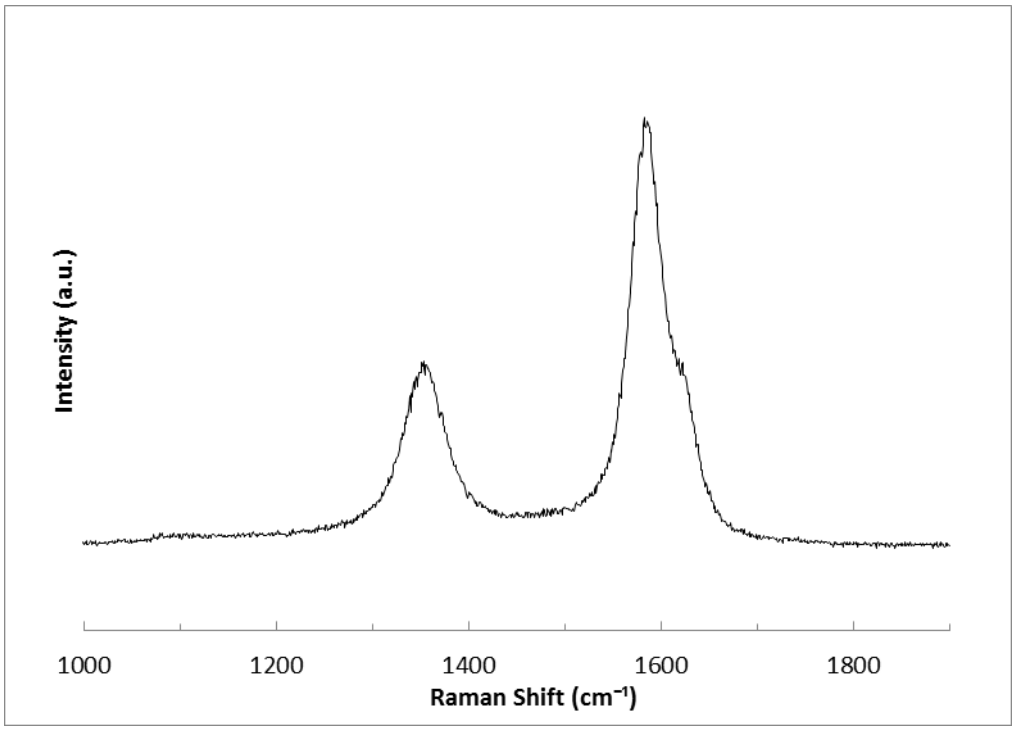

Fig. 4.28. Raman spectra of unirradiated MWCNTs.

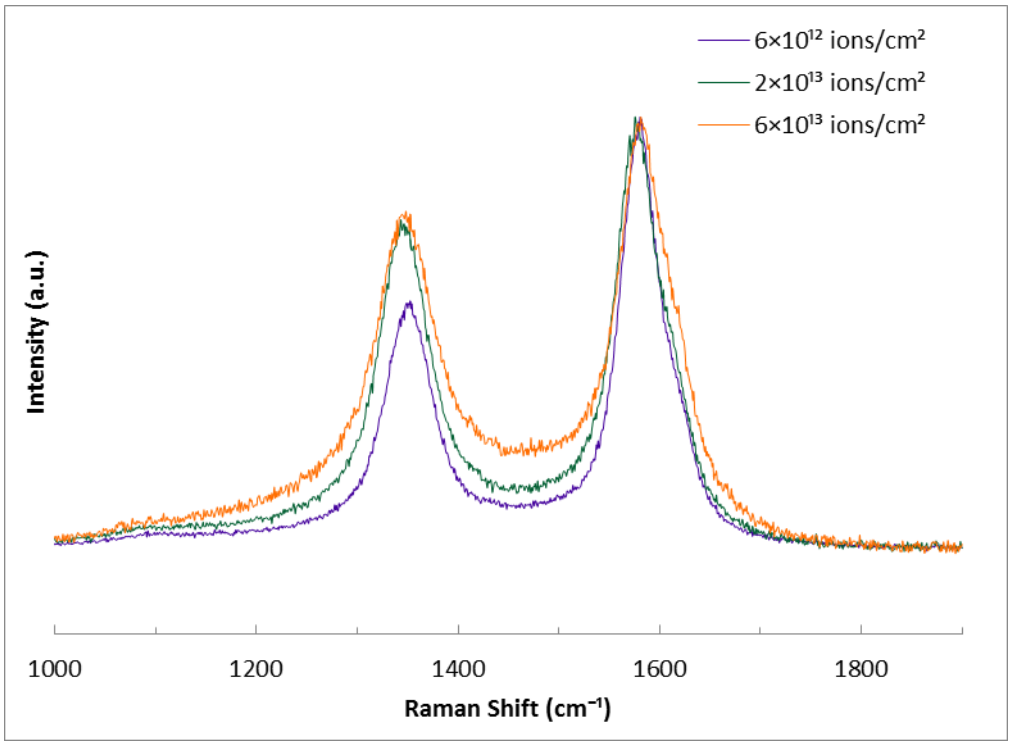

Fig. 4.29. Raman spectra of MWCNTs irradiated with Ar^{8+}.

.

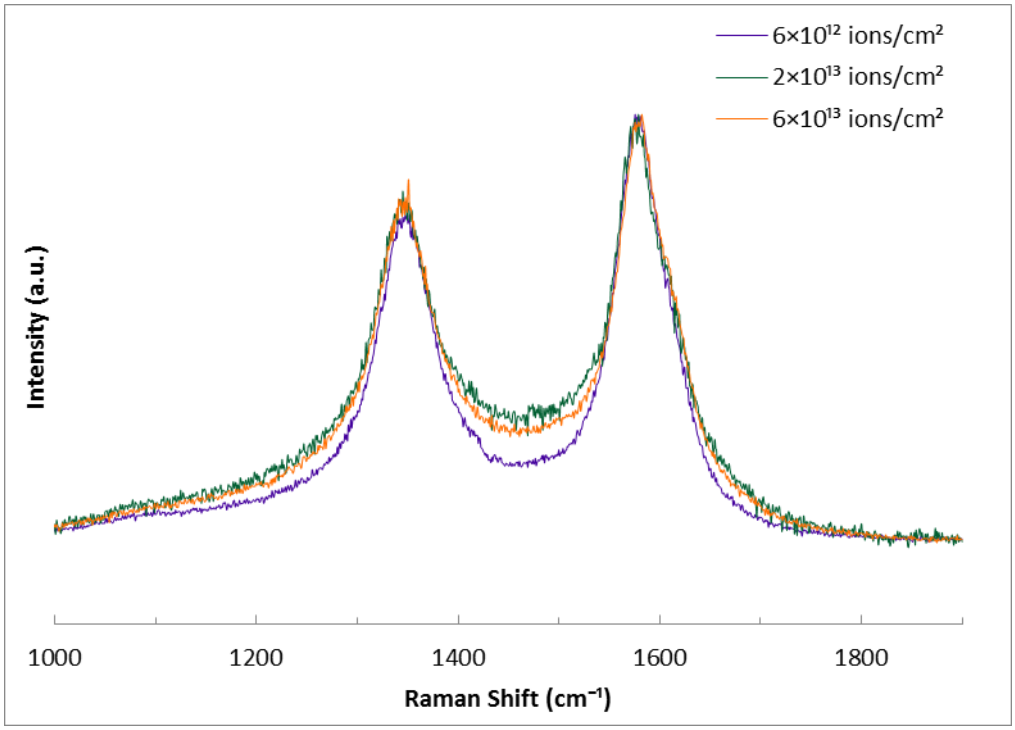

Fig. 4.30. Raman spectra of MWCNTs irradiated with Ar^{11+}.

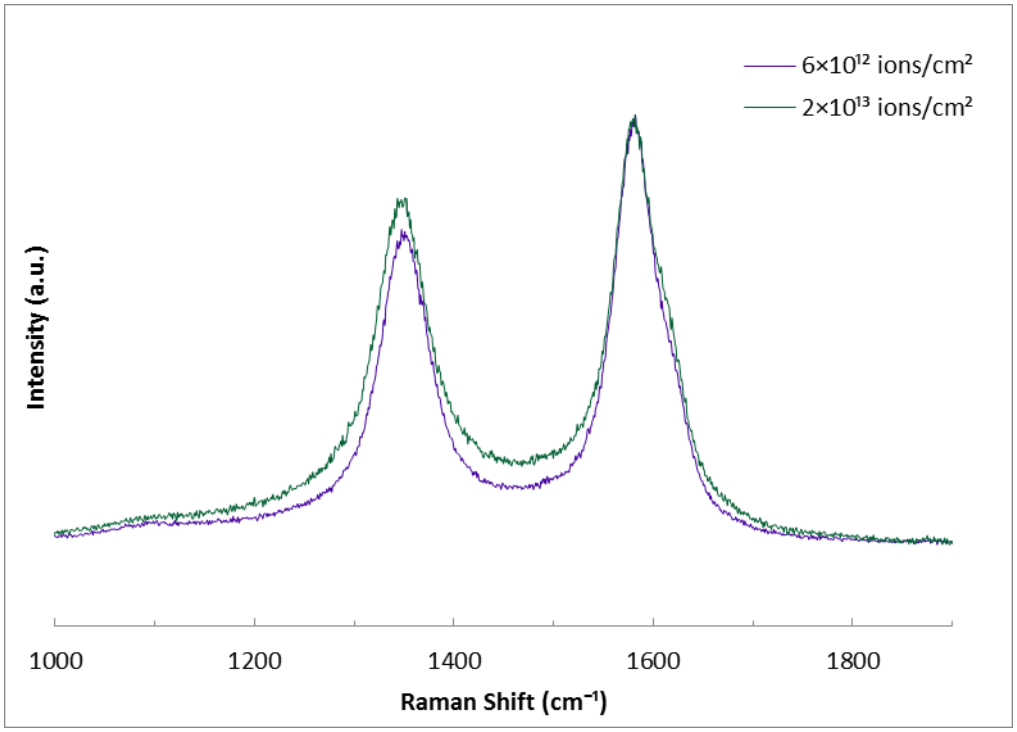

Fig. 4.31. Raman spectra of MWCNTs irradiated with Ar^{16+}.

From Fig. 4.28 to Fig. 4.31, the D peak (1350 cm^{-1}) is increased by irradiation with HCIs. It is considered that defects are introduced into MWCNTs by irradiation with HCIs.

Figure 4.32 shows the ratio of D peak to G peak and D/G ratio of Raman spectra. The higher D/G ratio, the more defects are introduced into MWCNTs. It is considered that the number of defects is increased by irradiation. There is no dependence on charge state. Since the D/G ratio increases as the fluence of HCIs increases, it is considered that many defects are introduced due to the kinetic energy of HCIs.

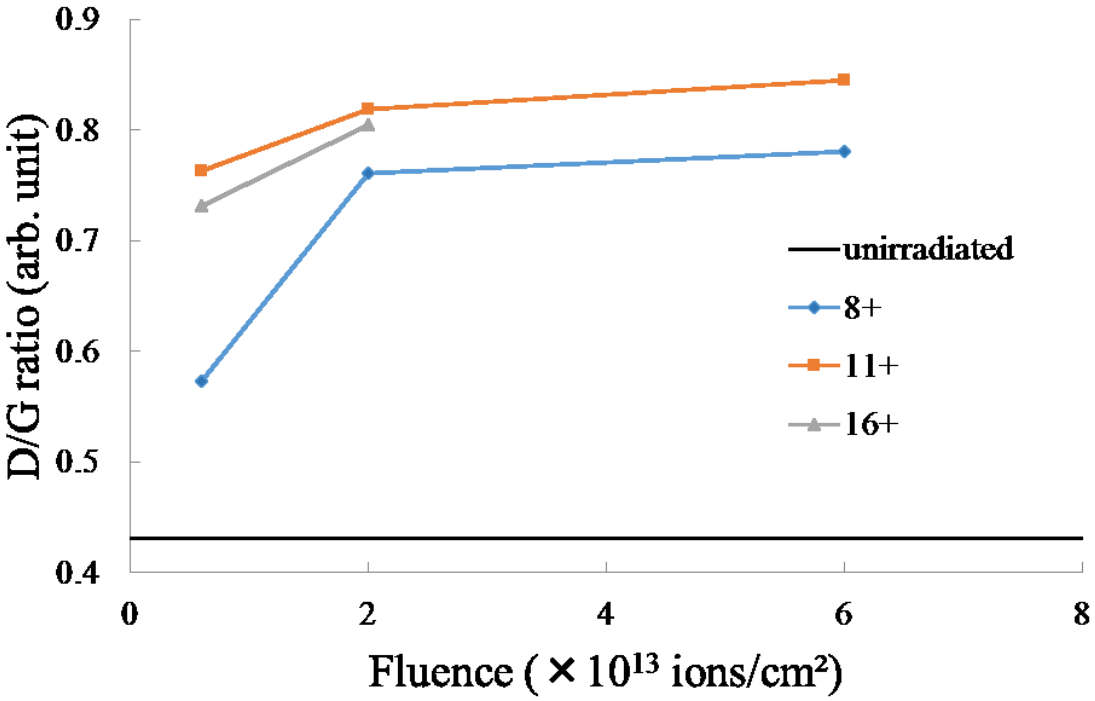

Fig. 4.32. D/G ratio of MWCNTs irradiated with Ar^{q+} (q = 8, 11, 16).

Run B

In the present experiments, we attempted to observe the structural change of the same position before and after the irradiation of HCIs using TEM. However, it has been thought to be difficult to observe the same position on the nanometer scale once the sample is removed from TEM apparatus. After scrupulous training of TEM operation it has become possible to compare the structure of identical nanometer region from a millimeter-sized sample before and after irradiation. This allows a more accurate comparison from TEM images of MWCNTs before and after irradiation.

In the case of irradiation with Ar^{14+}, the sample was irradiated at a rate of about 5×10^{12} ions/cm^2 per hour. The potential energy of Ar^{14+} is about 4 keV, and the kinetic energy is set to 16 keV. Also, as shown in Fig.4.33, the hollow structure disappears when the electron beam is focused strongly and applied for a long time. Therefore, in the present experiments, observation was performed as soon as possible in order to reduce the influence of the electron beam.

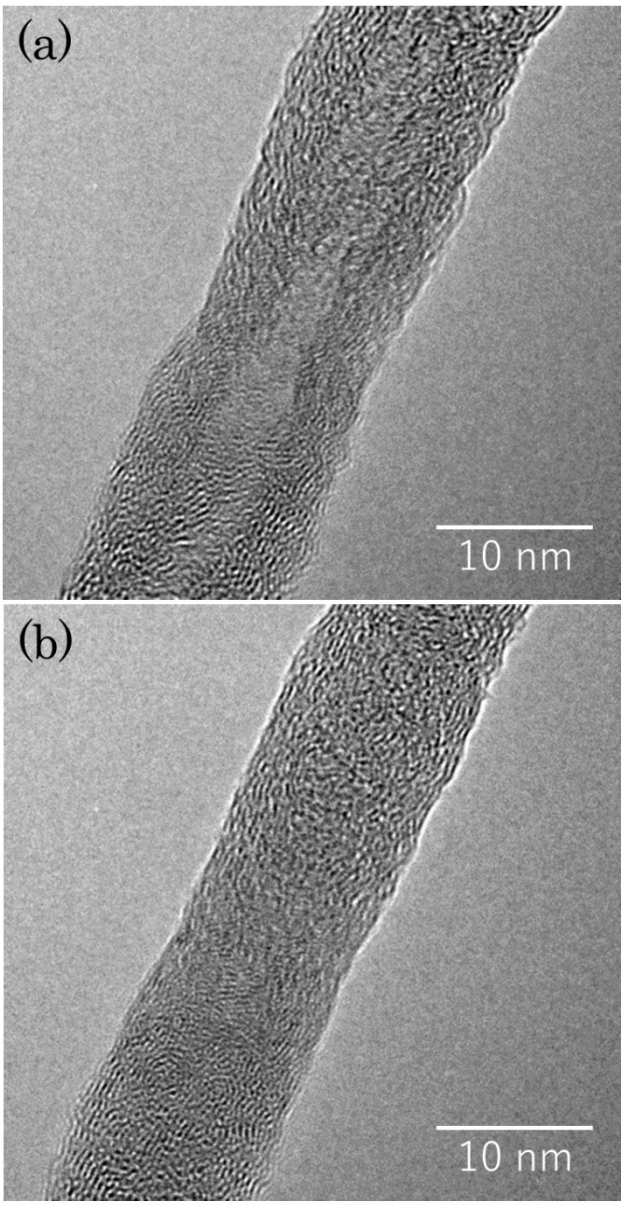

Fig. 4.33. Effect of electron beam on MWCNT. (a) shows initial state of the MWCNT and (b) shows the MWCNT after 10 min while observing by TEM.

Figure 4.34 and Fig. 4.35 show the TEM images before and after irradiation with HCIs. Comparing before and after irradiation with HCIs, the hollow structure of MWCNT disappeared, the diameter decreased, and uneven surface were observed.

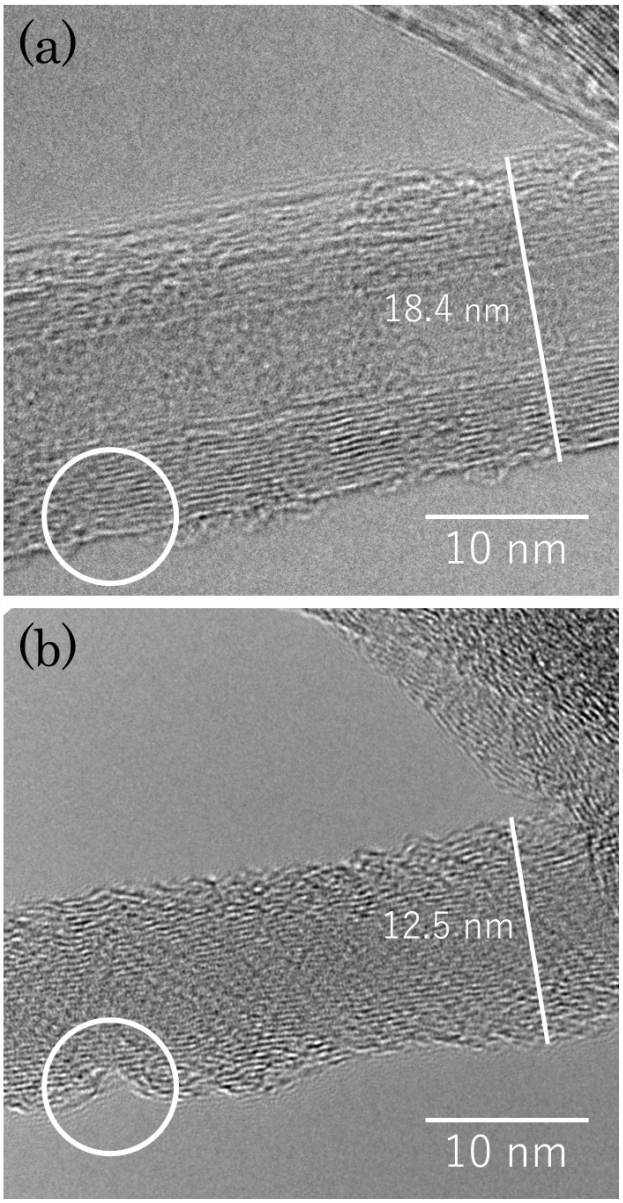

Fig. 4.34. TEM images at the identical position between samples (a) before and (b) after irradiation with Ar^{14+} at the fluence of 6×10^{13} ions/cm^2. Outer diameters are decreased, outlines of surfaces become uneven and hollow regions disappeared by the irradiation.

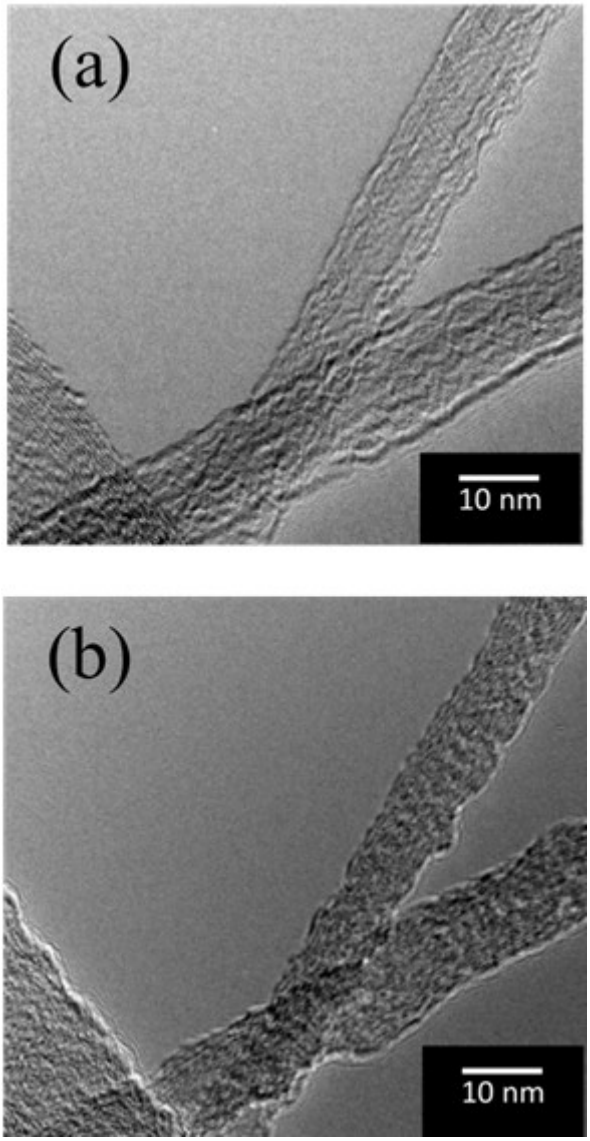

Fig. 4.35. TEM images at the identical position between samples (a) before and (b) after irradiation with Ar^{14+} at the fluence of 6×10^{13} ions/cm^2.

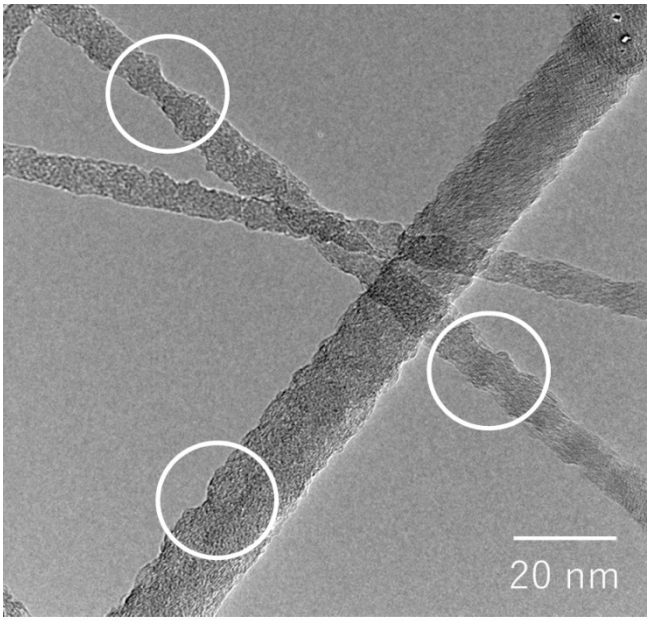

Fig. 4.36. TEM images of MWCNT after irradiation with Ar^{14+} at the fluence of 6×10^{13} ions/cm^2.

The difference between the result of MWCNTs irradiated with Ar^+ [10, 11] and the result of MWCNTs irradiated with Ar^{14+} is outer diameters and uneven surface. In the irradiation with Ar^+, the diameters tend to increase. However, the outer diameters of MWCNTs irradiated with Ar^{14+} decreases as shown in Fig. 4.34 and Fig. 4.35. In addition, uneven surfaces were observed that cannot be observed in Ar^+ in MWCNTs irradiated with Ar^{14+} as indicated with white circles in Fig. 4.36. The decrease in outer diameters and uneven surfaces caused by irradiation with HCIs (Ar^{14+}). It is considered that potential sputtering occurred due to irradiation with HCIs, and surface atoms were sputtered by potential sputtering. The potential effects of HCI, such as the appearance of uneven surfaces and a decrease in outer diameter, were clarified by observing the same location.

Run C

Next, experiments were performed using MWCNTs with a diameter of 30 nm to 50 nm. Comparisons were made at the same place before and after irradiation with HCIs using TEM. TEM images before and after irradiation with Ar^{8+} at the fluence of 6×10^{12} ions/cm^2 are shown at Fig. 4.37 and Fig. 4.38. Figure 4.39 and Fig. 4.40 show TEM images before and after irradiation with Ar^{8+} at the fluence of 2×10^{13} ions/cm^2, and Fig. 4.41 and Fig. 4.42 show TEM images before and after irradiation with 6×10^{13} ions/cm^2. TEM images before and after irradiation with Ar^{11+} are shown in Figures 4.43 to 4.48, and TEM images before and after irradiation with Ar^{14+} are shown in Figures 4.49 to 4.54.

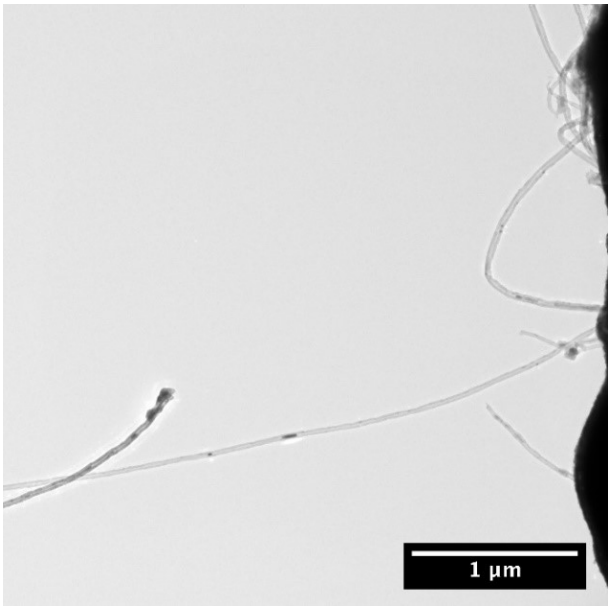

(a) Before irradiation ×5000

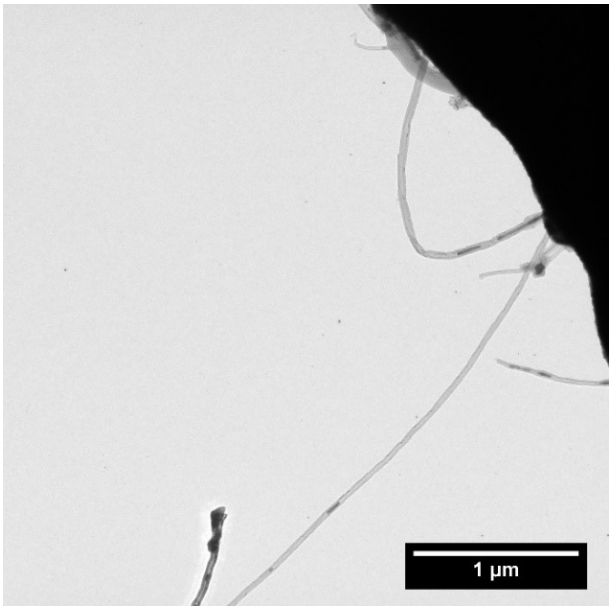

(b) After irradiation ×5000

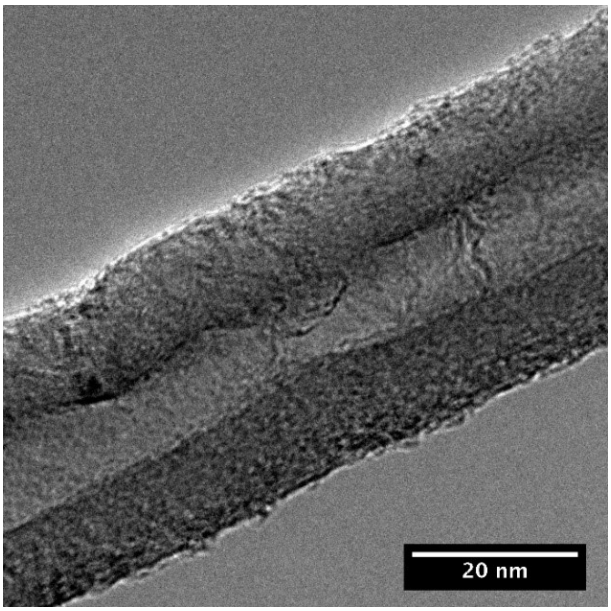

(c) Before irradiation ×250000

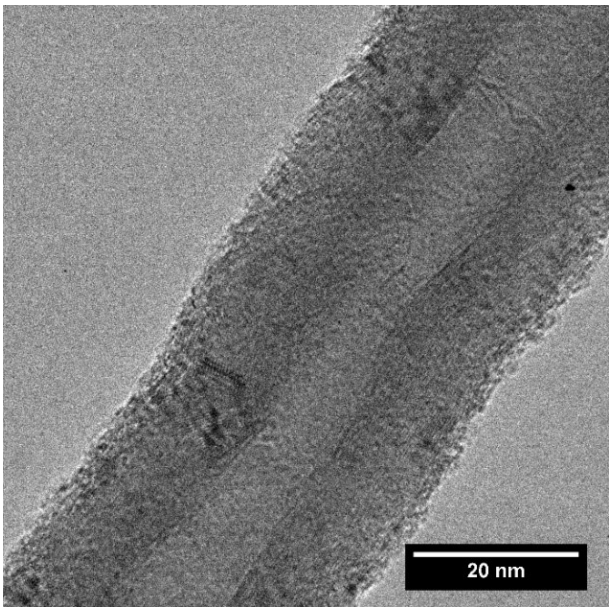

(d) After irradiation ×250000

Fig. 4.37. TEM images of MWCNTs irradiated with Ar^{8+} at the fluence of 6×10^{12} ions/cm^2.

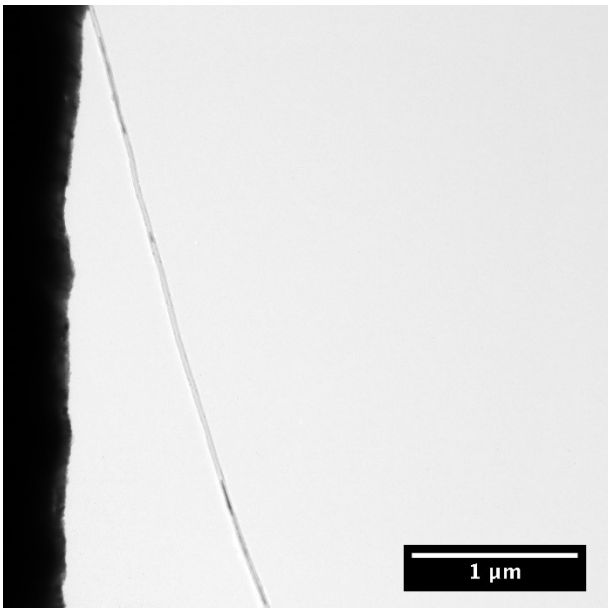

(a) Before irradiation ×5000

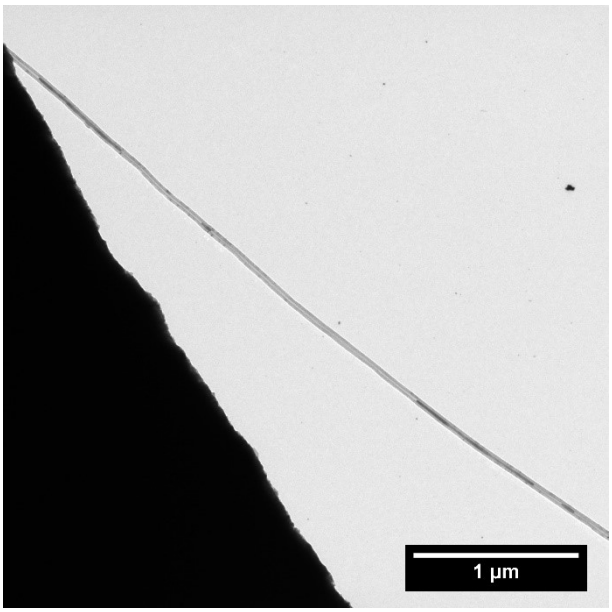

(b) After irradiation ×5000

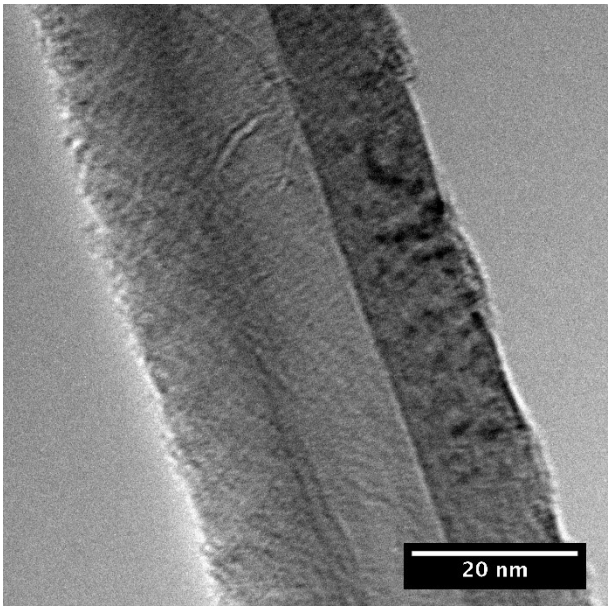

(c) Before irradiation ×250000

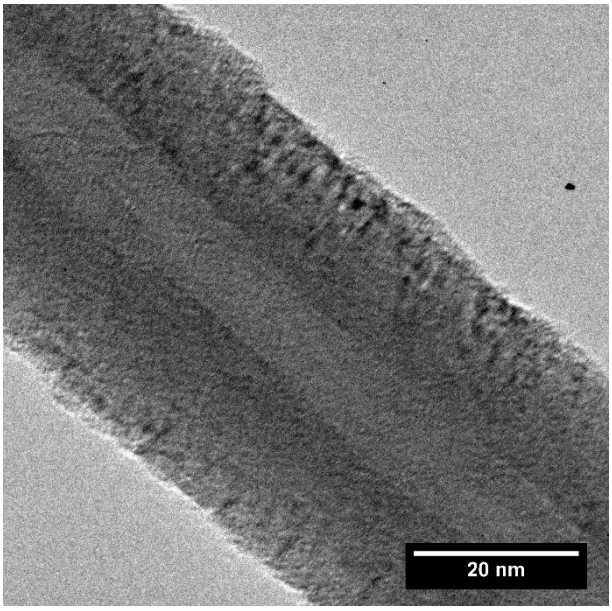

(d) After irradiation ×250000

Fig. 4.38. TEM images of MWCNTs irradiated with Ar^{8+} at the fluence of 6×10^{12} ions/cm^2.

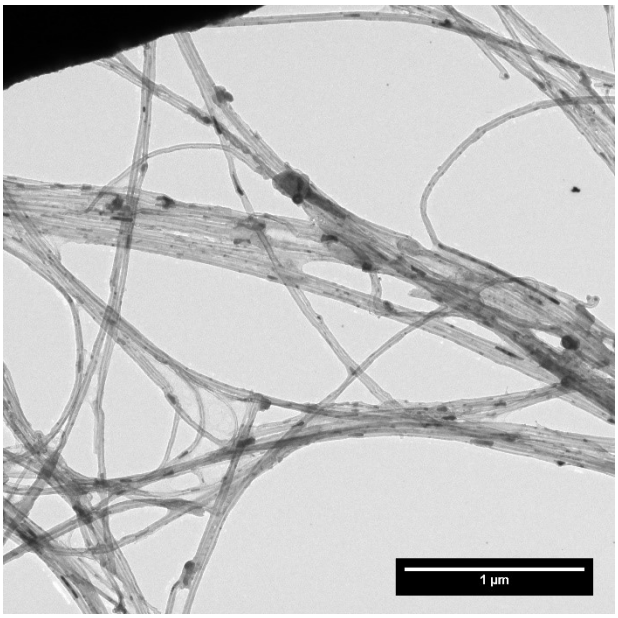

(a) Before irradiation ×5000

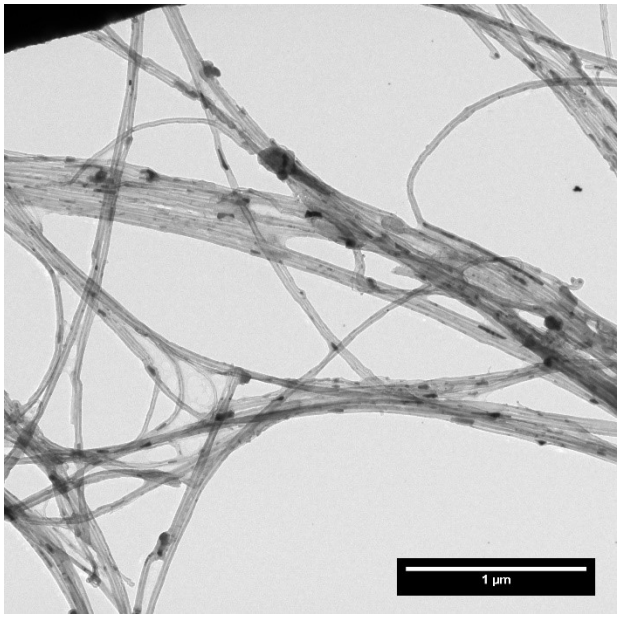

(b) After irradiation ×5000

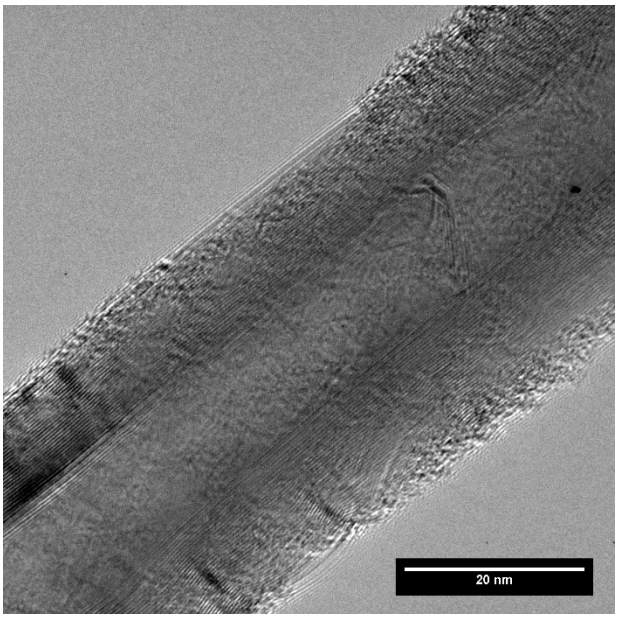

(c) Before irradiation ×250000

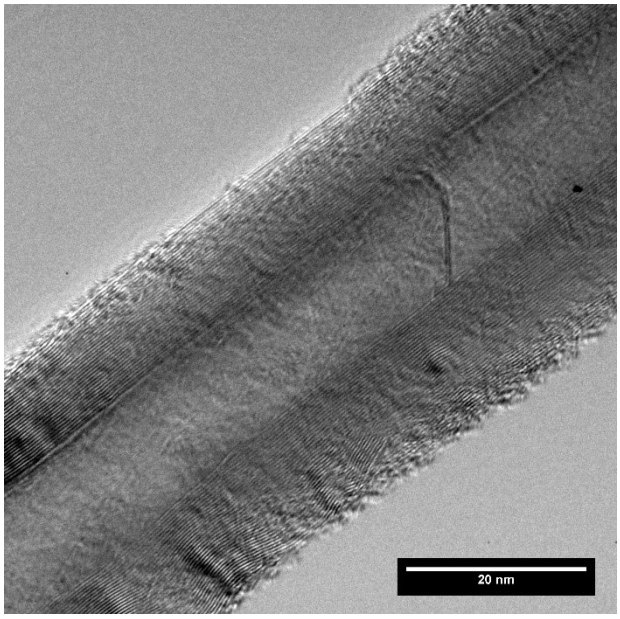

(d) After irradiation ×250000

Fig. 4.39. TEM images of MWCNTs irradiated with Ar^{8+} at the fluence of 2×10^{13} ions/cm^2.

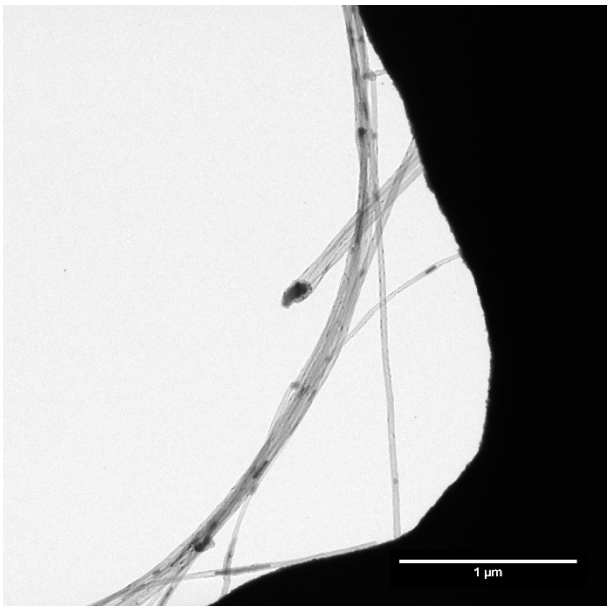

(a) Before irradiation ×5000

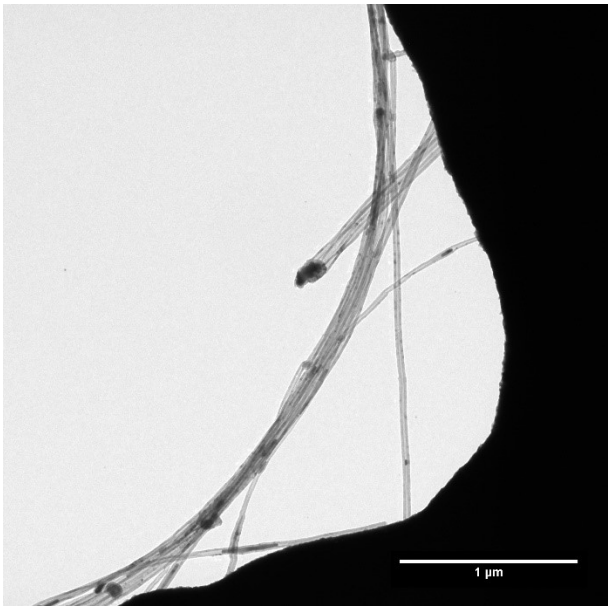

(b) After irradiation ×5000

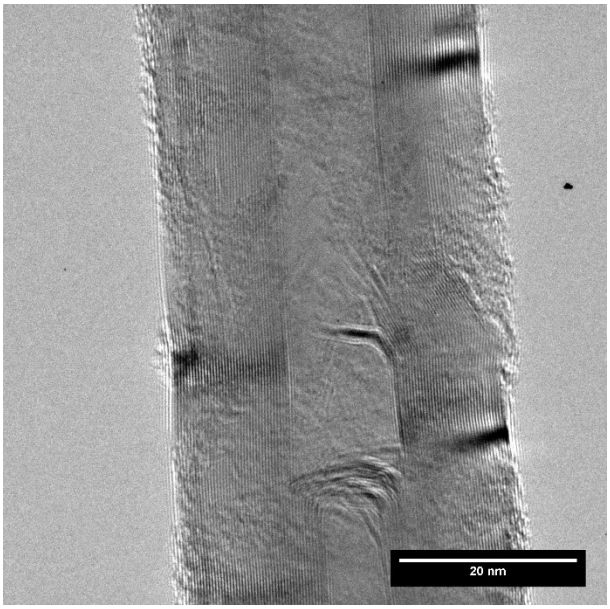

(c) Before irradiation ×250000

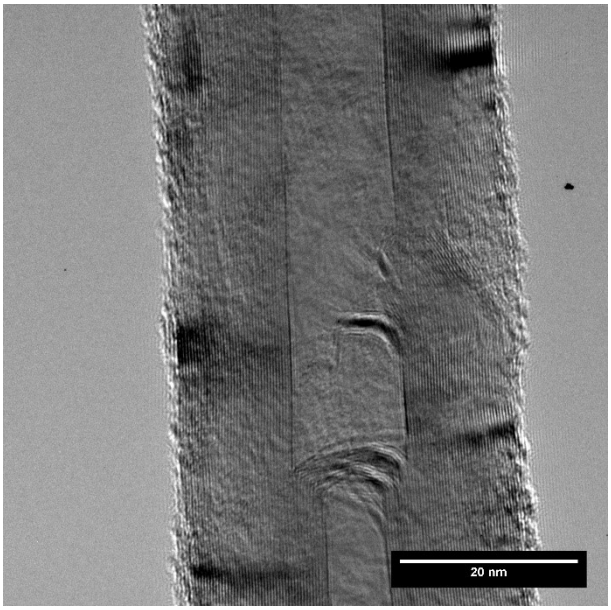

(d) After irradiation ×250000

Fig. 4.40. TEM images of MWCNTs irradiated with Ar^{8+} at the fluence of 2×10^{13} ions/cm^2.

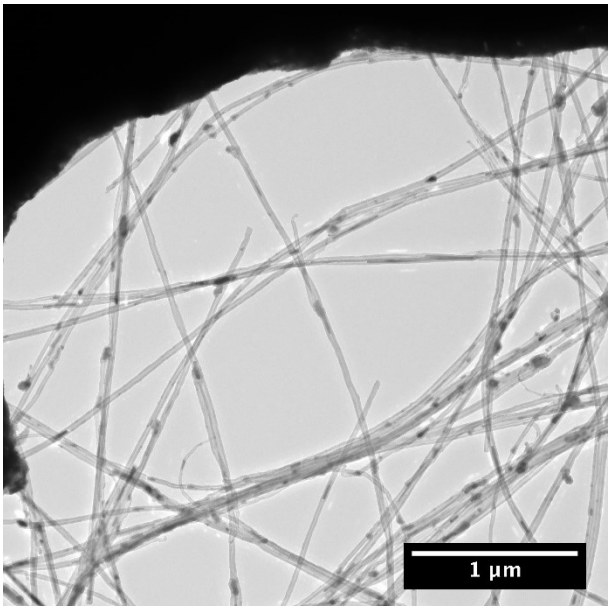

(a) Before irradiation ×5000

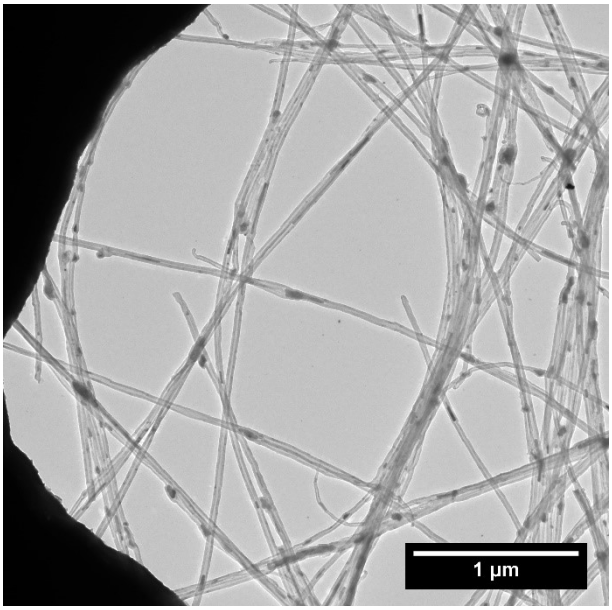

(b) After irradiation ×5000

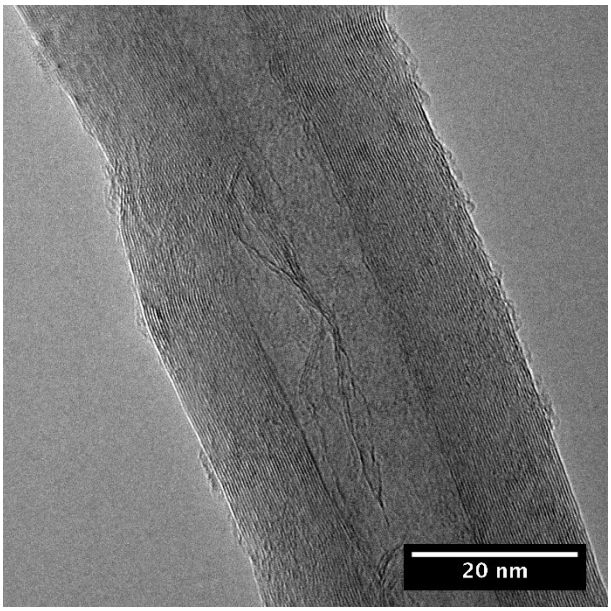

(c) Before irradiation ×250000

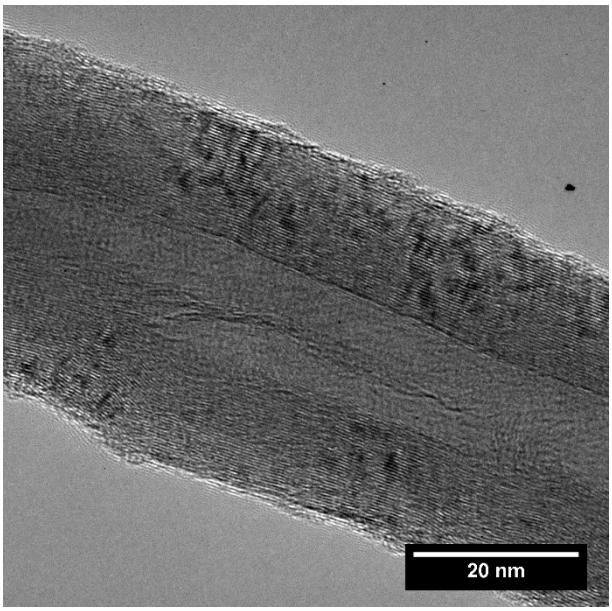

(d) After irradiation ×250000

Fig. 4.41. TEM images of MWCNTs irradiated with Ar^{8+} at the fluence of 6×10^{13} ions/cm^2.

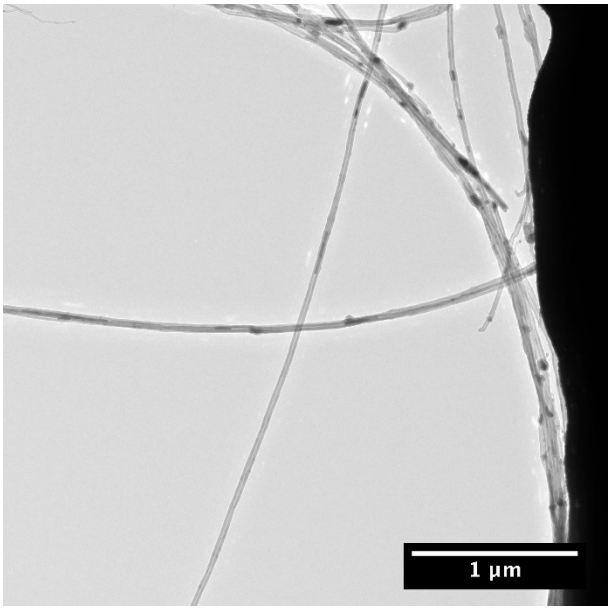

(a) Before irradiation ×5000

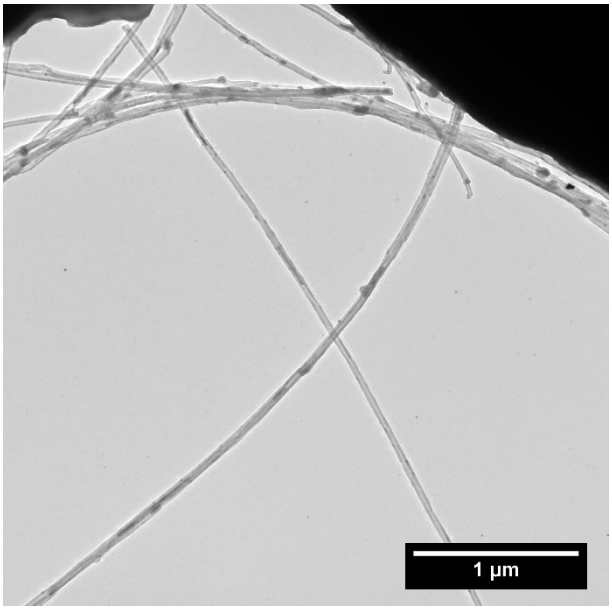

(b) After irradiation ×5000

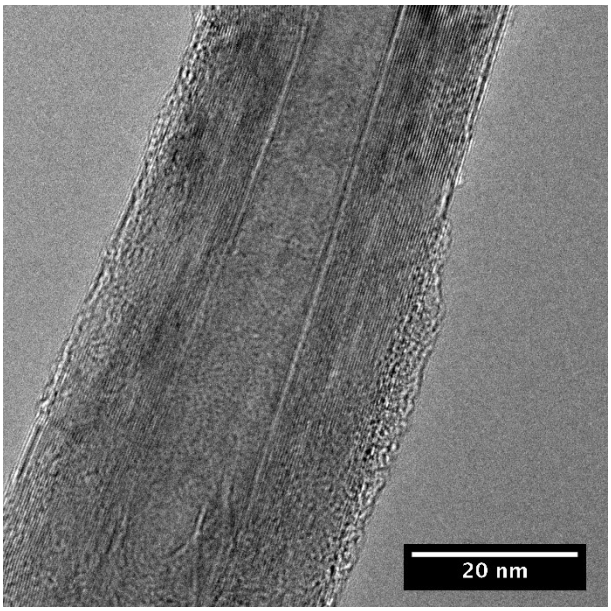

(c) Before irradiation ×250000

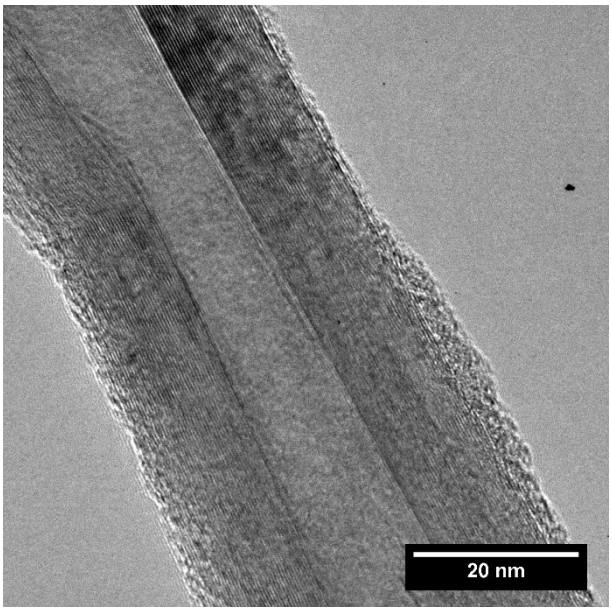

(d) After irradiation ×250000

Fig. 4.42. TEM images of MWCNTs irradiated with Ar^{8+} at the fluence of 6×10^{13} ions/cm^2.

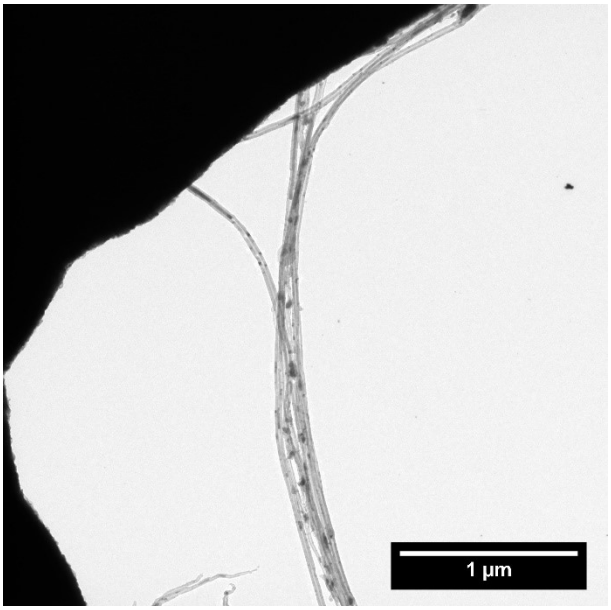

(a) Before irradiation ×5000

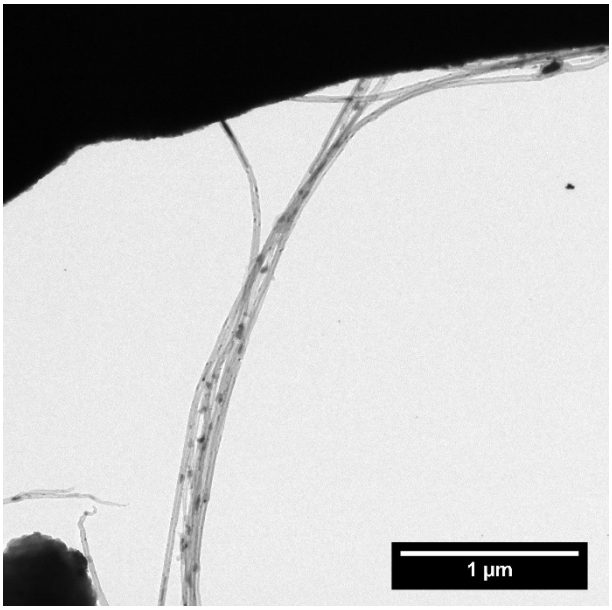

(b) After irradiation ×5000

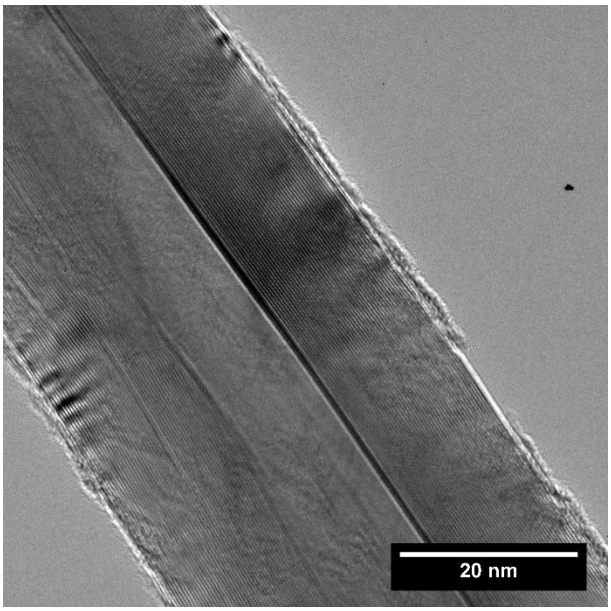

(c) Before irradiation ×250000

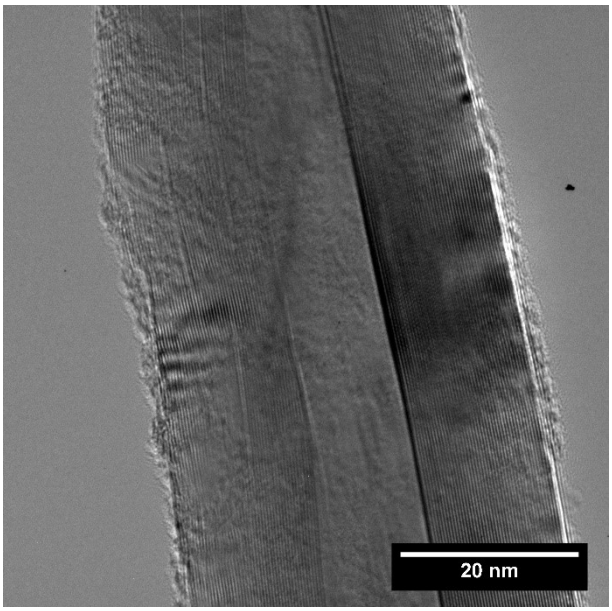

(d) After irradiation ×250000

Fig. 4.43. TEM images of MWCNTs irradiated with Ar^{11+} at the fluence of 6×10^{12} ions/cm^2.

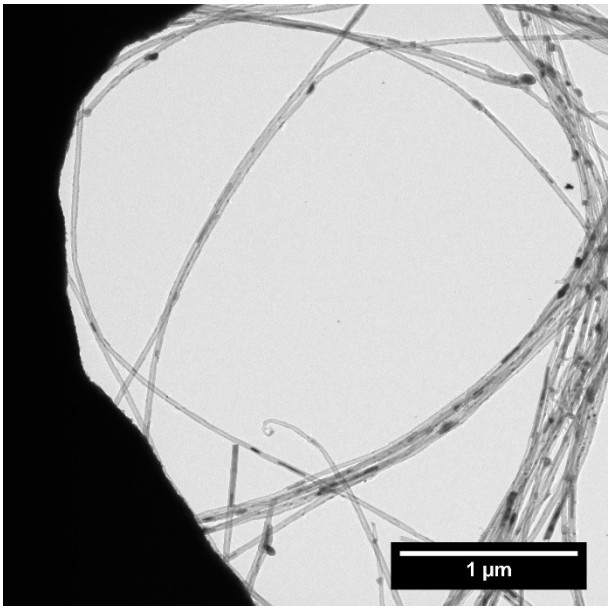

(a) Before irradiation ×5000

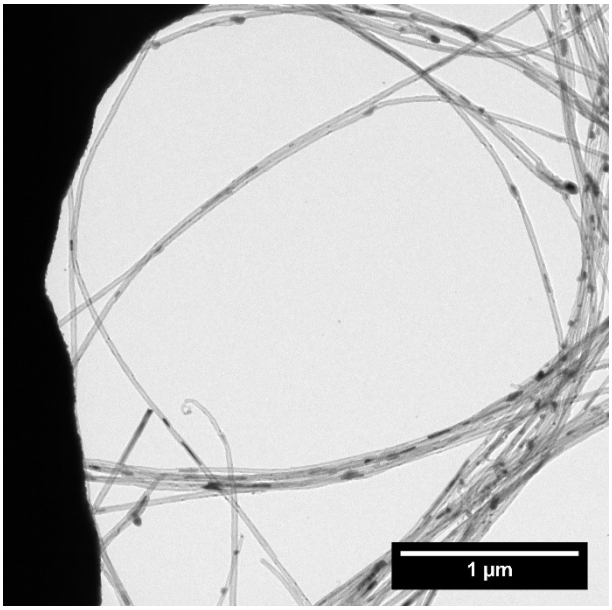

(b) After irradiation ×5000

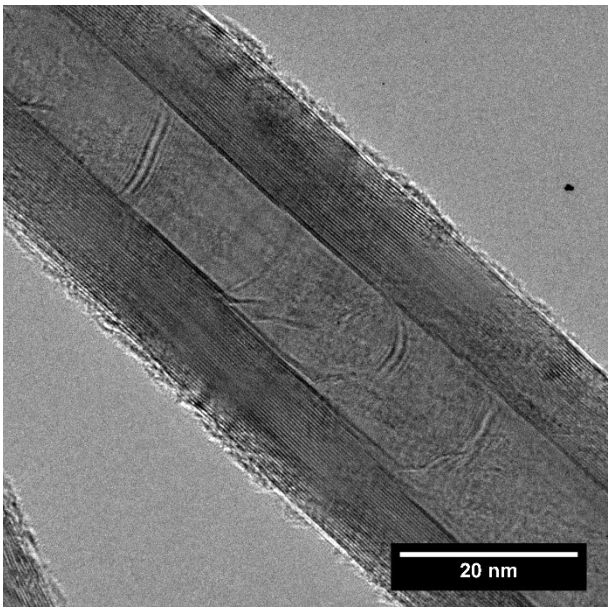

(c) Before irradiation ×250000

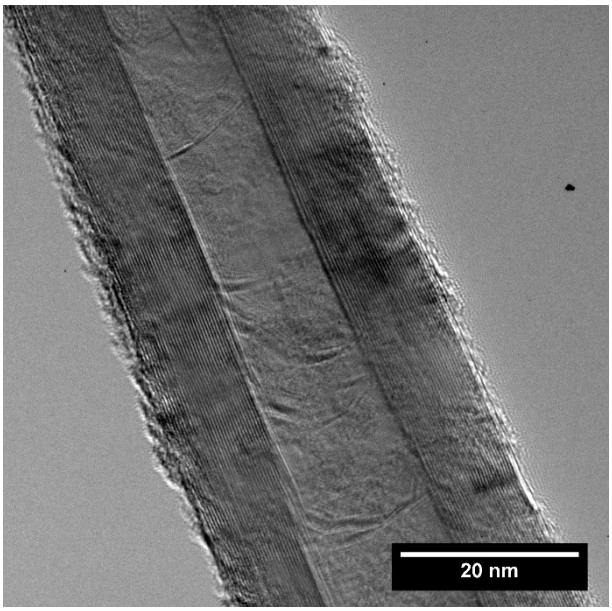

(d) After irradiation ×250000

Fig. 4.44. TEM images of MWCNTs irradiated with Ar^{11+} at the fluence of 6×10^{12} ions/cm^2.

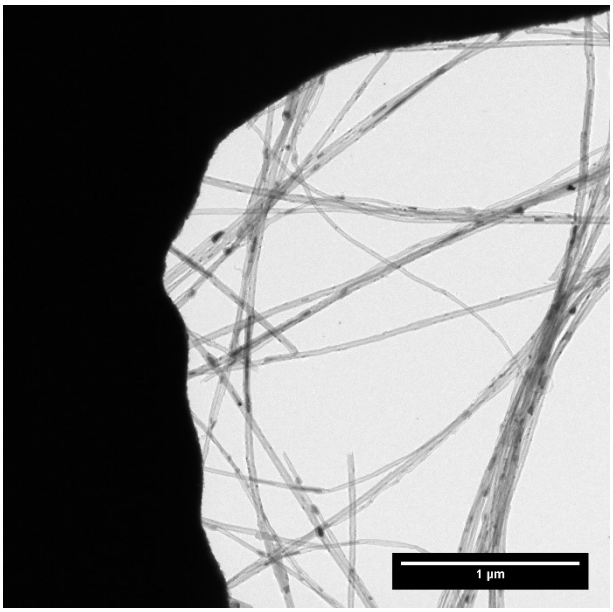

(a) Before irradiation ×5000

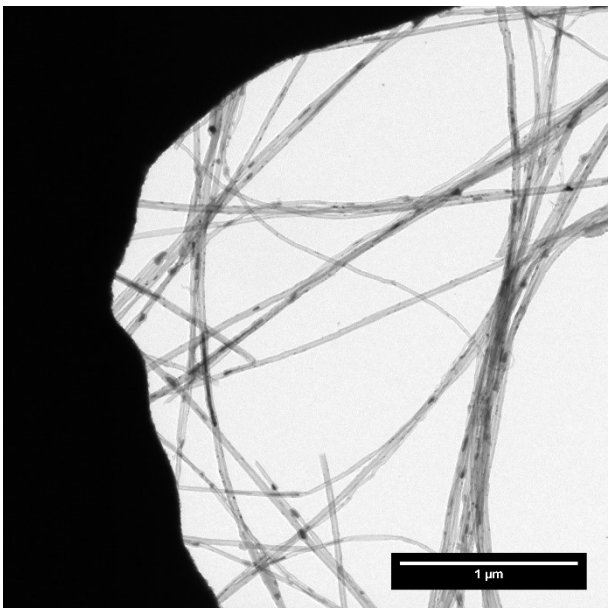

(b) After irradiation ×5000

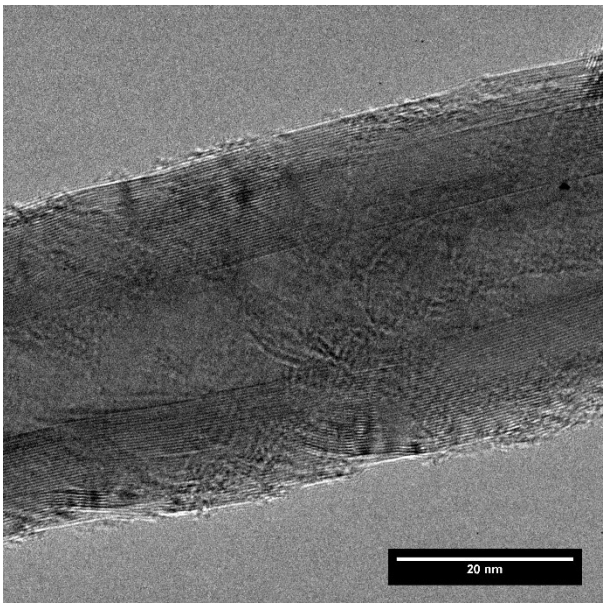

(c) Before irradiation ×250000

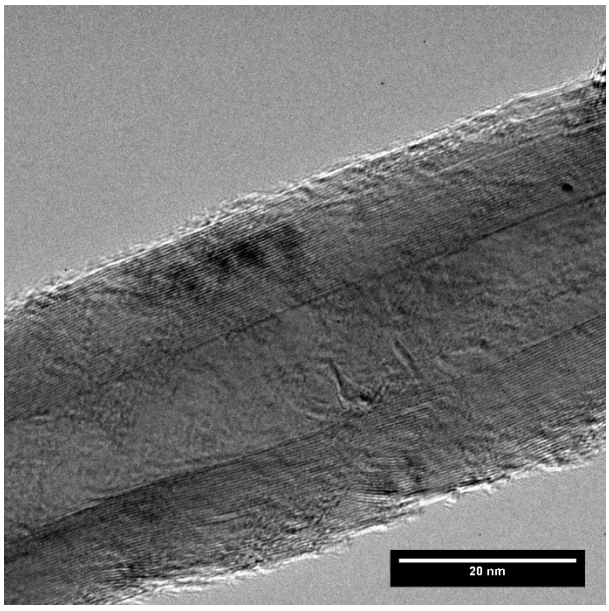

(d) After irradiation ×250000

Fig. 4.45. TEM images of MWCNTs irradiated with Ar^{11+} at the fluence of 2×10^{13} ions/cm^2.

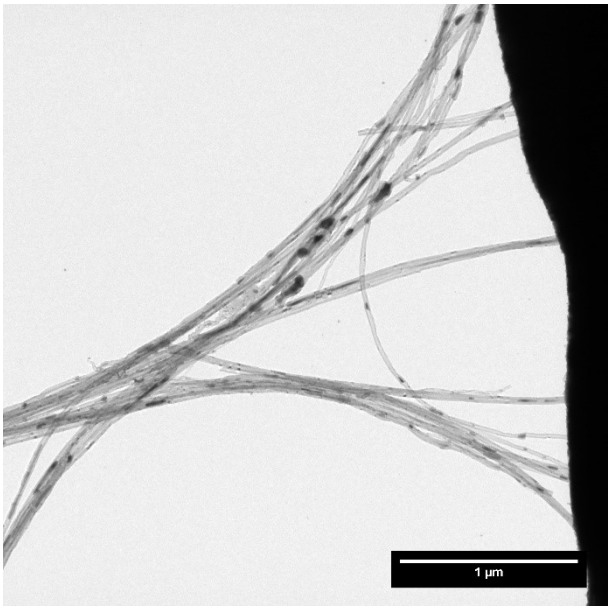

(a) Before irradiation ×5000

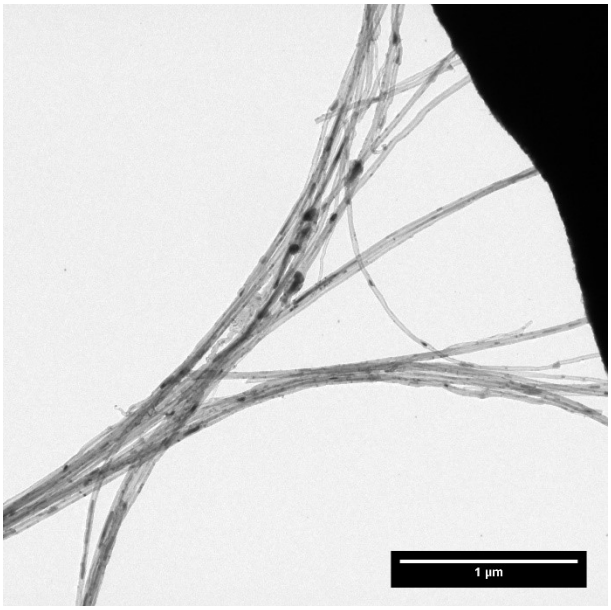

(b) After irradiation ×5000

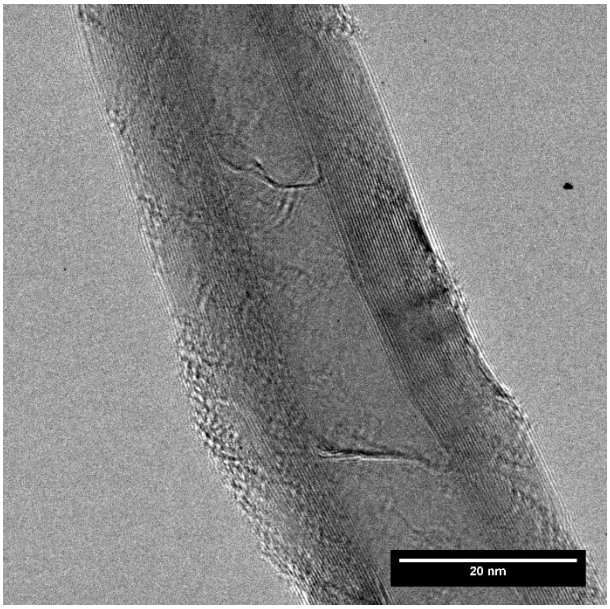

(c) Before irradiation ×250000

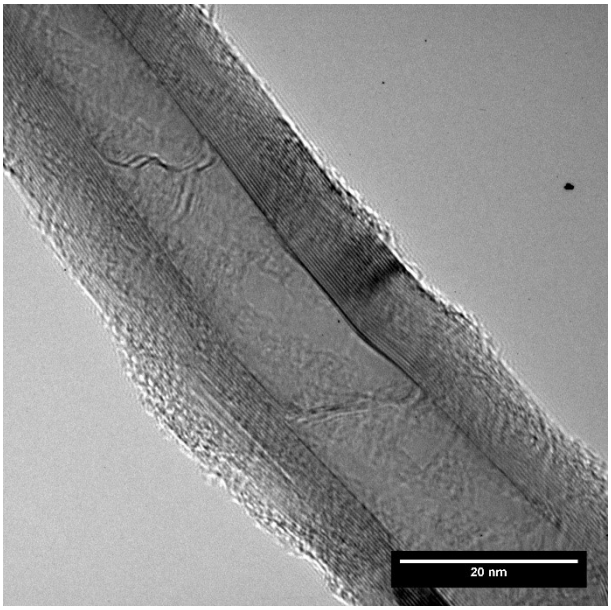

(d) After irradiation ×250000

Fig. 4.46. TEM images of MWCNTs irradiated with Ar^{11+} at the fluence of 2×10^{13} ions/cm^2.

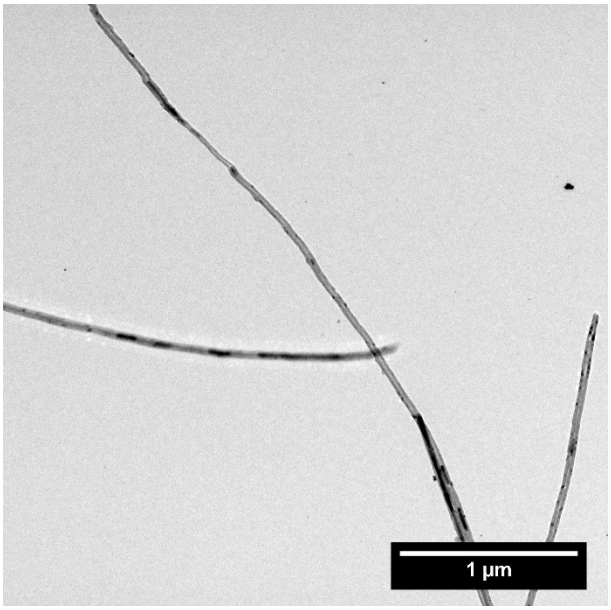

(a) Before irradiation ×5000

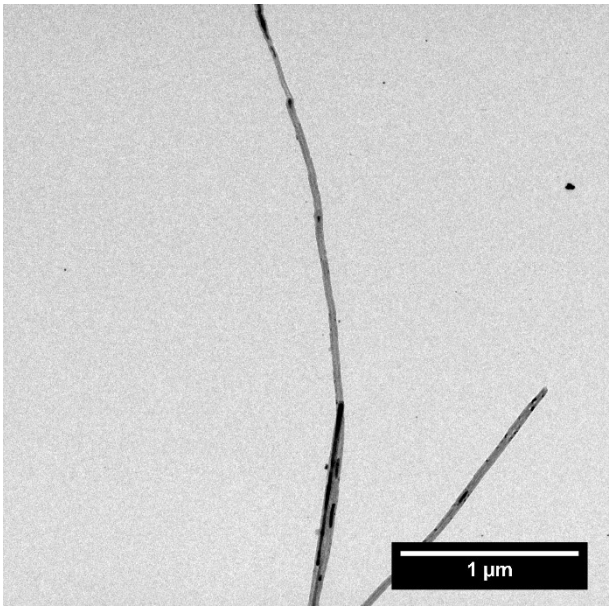

(b) After irradiation ×5000

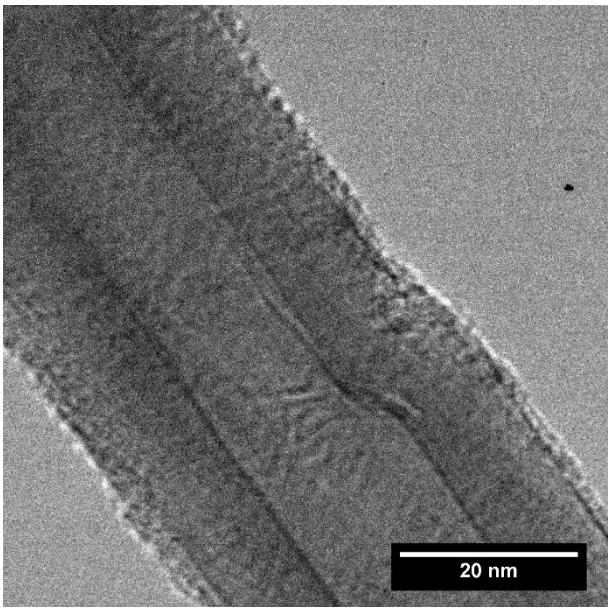

(c) Before irradiation ×250000

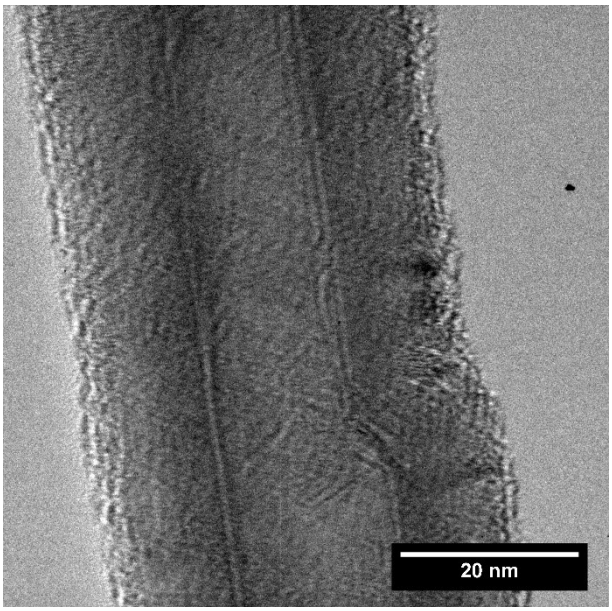

(d) After irradiation ×250000

Fig. 4.47. TEM images of MWCNTs irradiated with Ar^{11+} at the fluence of 6×10^{13} ions/cm^2.

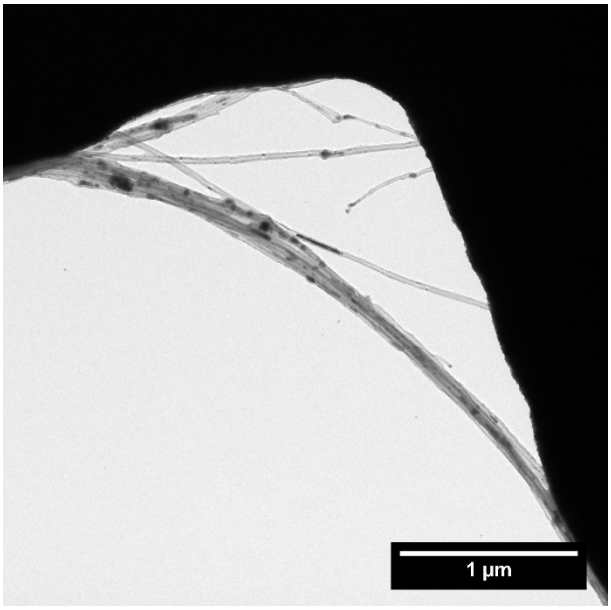

(a) Before irradiation ×5000

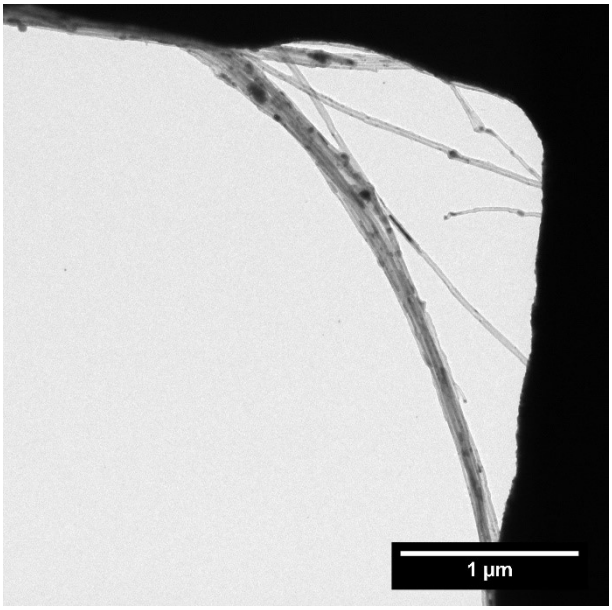

(b) After irradiation ×5000

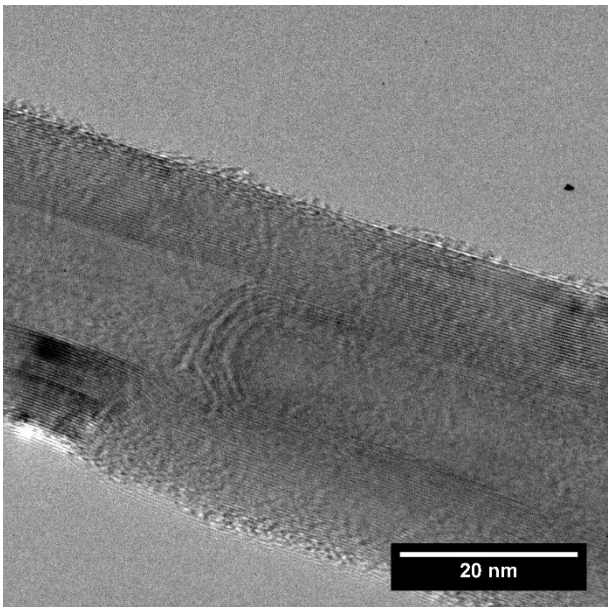

(c) Before irradiation ×250000

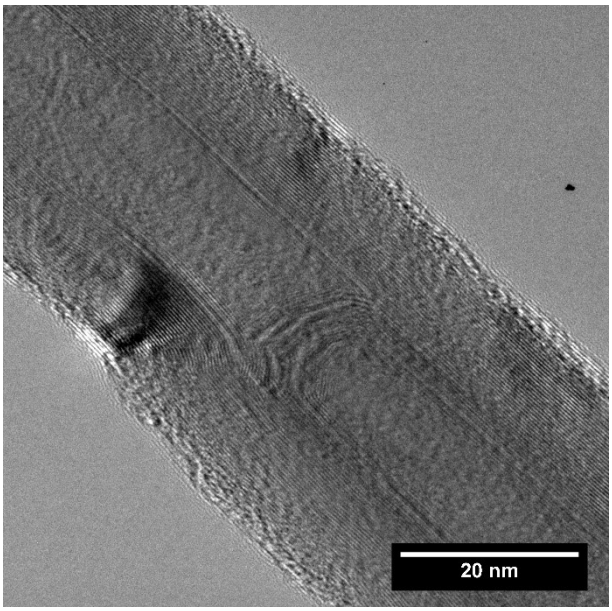

(d) After irradiation ×250000

Fig. 4.48. TEM images of MWCNTs irradiated with Ar^{11+} at the fluence of 6×10^{13} ions/cm^2.

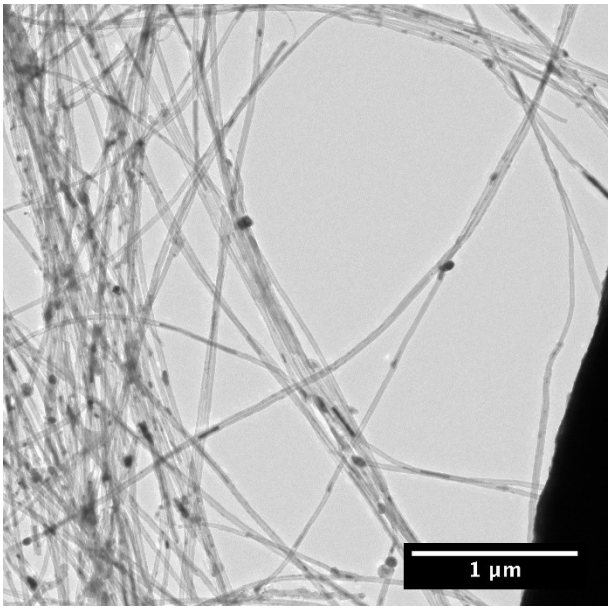

(a) Before irradiation ×5000

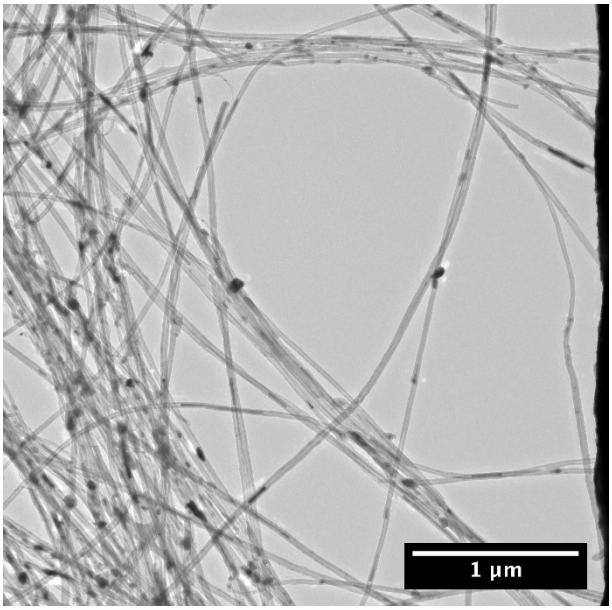

(b) After irradiation ×5000

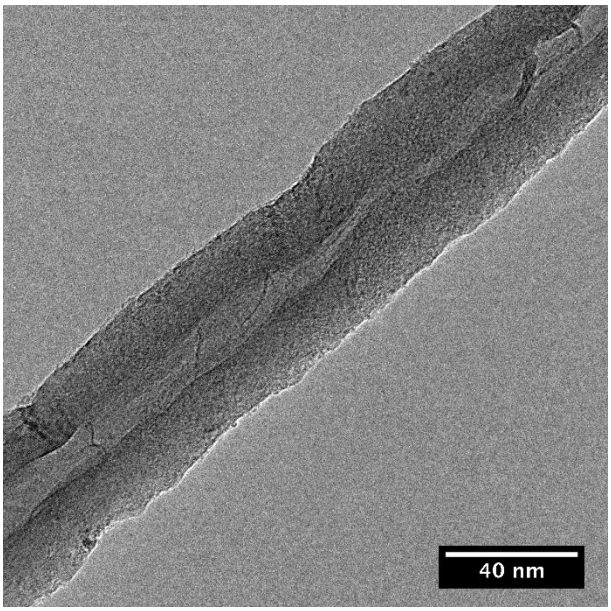

(c) Before irradiation ×250000

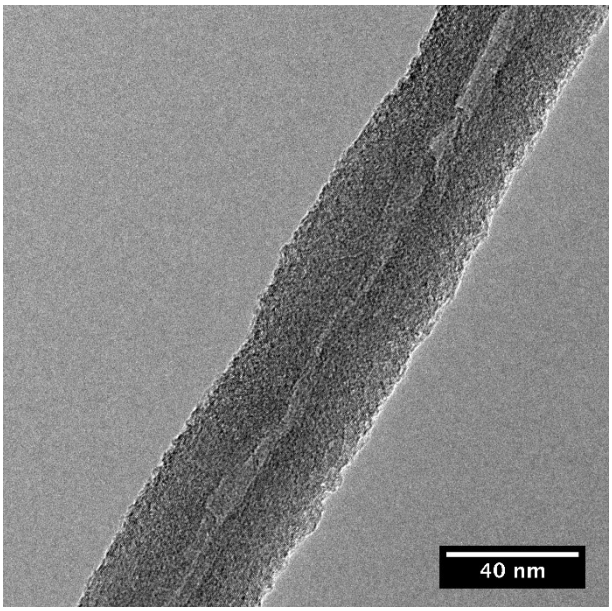

(d) After irradiation ×250000

Fig. 4.49. TEM images of MWCNTs irradiated with Ar^{14+} at the fluence of 6×10^{12} ions/cm^2.

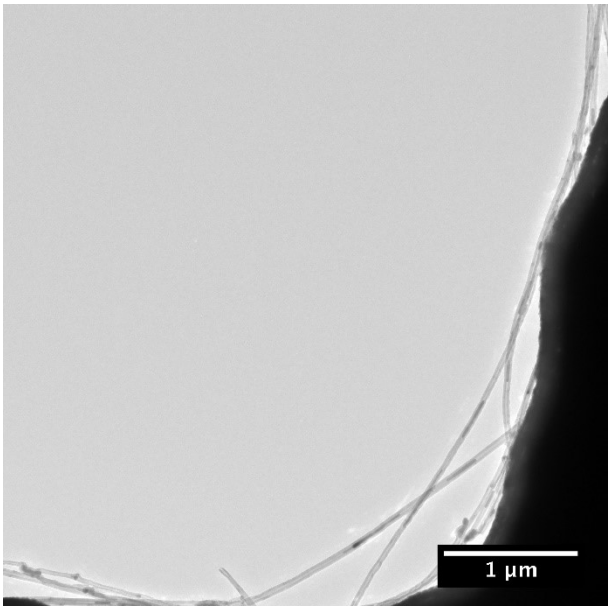

(a) Before irradiation ×5000

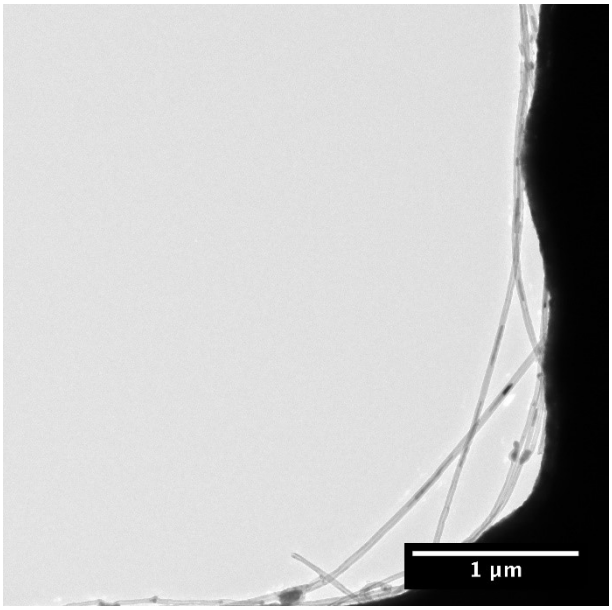

(b) After irradiation ×5000

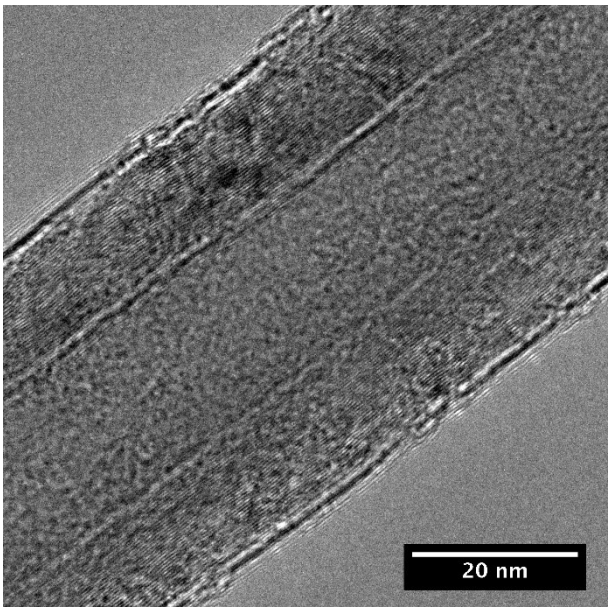

(c) Before irradiation ×250000

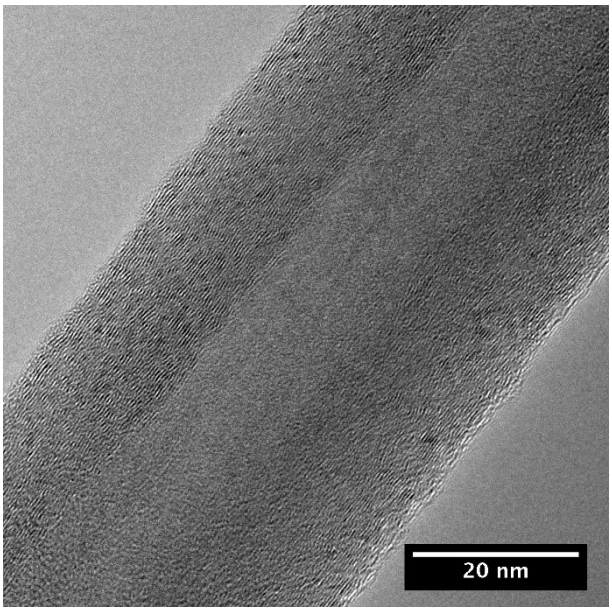

(d) After irradiation ×250000

Fig. 4.50. TEM images of MWCNTs irradiated with Ar^{14+} at the fluence of 6×10^{12} ions/cm^2.

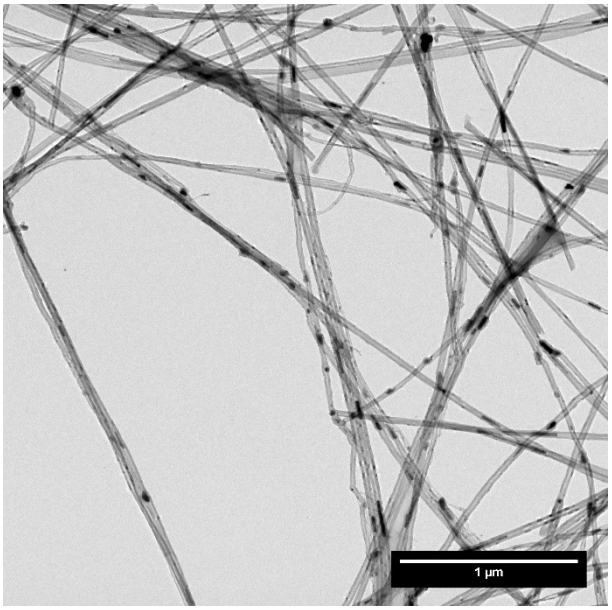

(a) Before irradiation ×5000

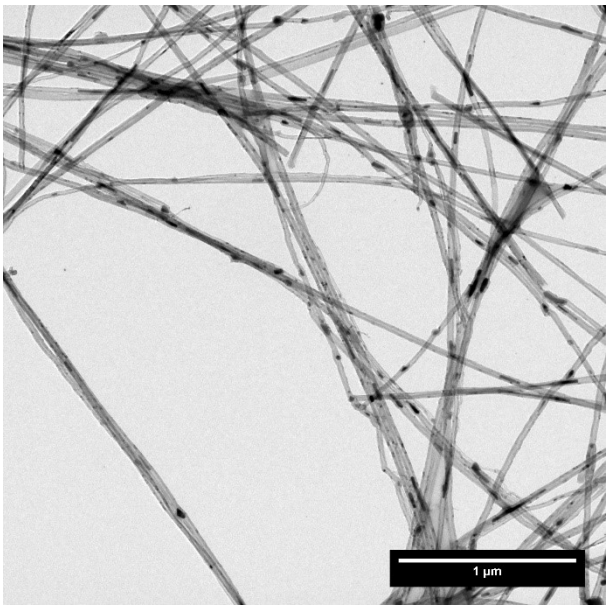

(b) After irradiation ×5000

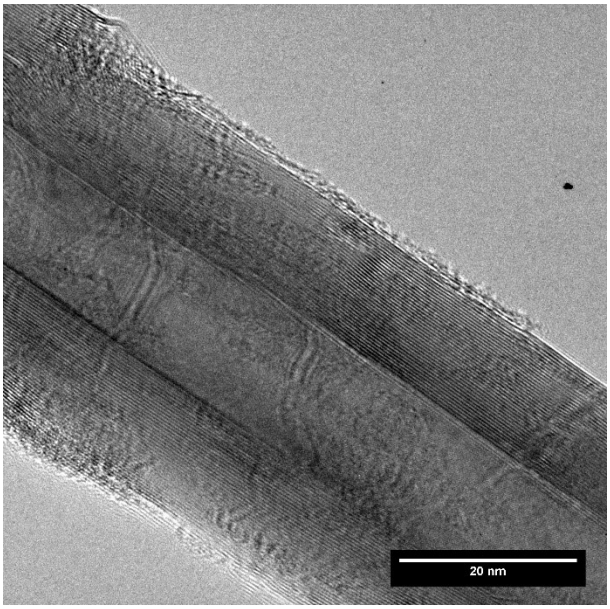

(c) Before irradiation ×250000

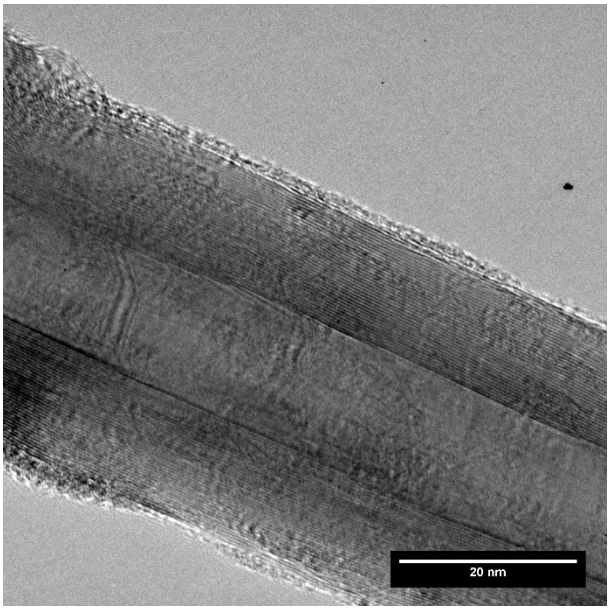

(d) After irradiation ×250000

Fig. 4.51. TEM images of MWCNTs irradiated with Ar^{14+} at the fluence of 2×10^{13} ions/cm^2.

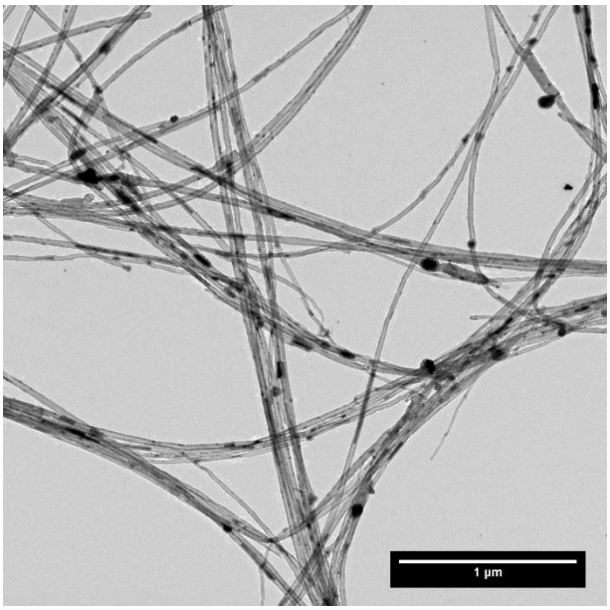

(a) Before irradiation ×5000

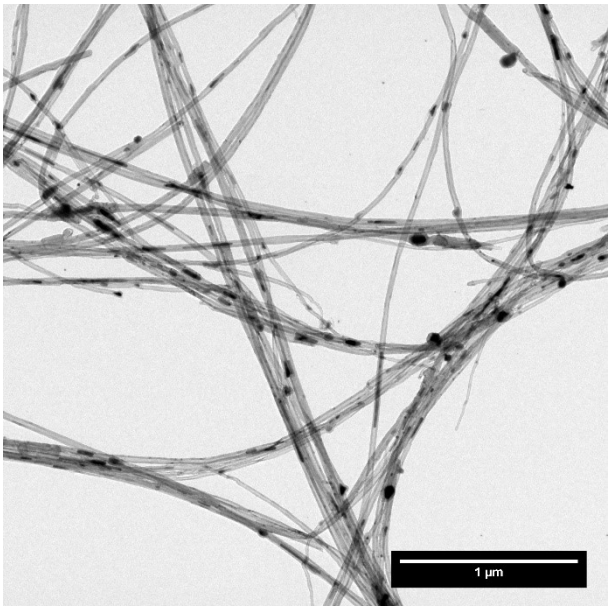

(b) After irradiation ×5000

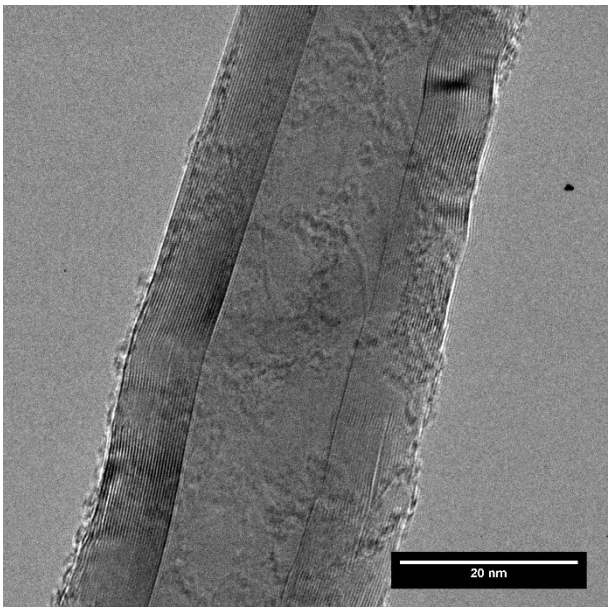

(c) Before irradiation ×250000

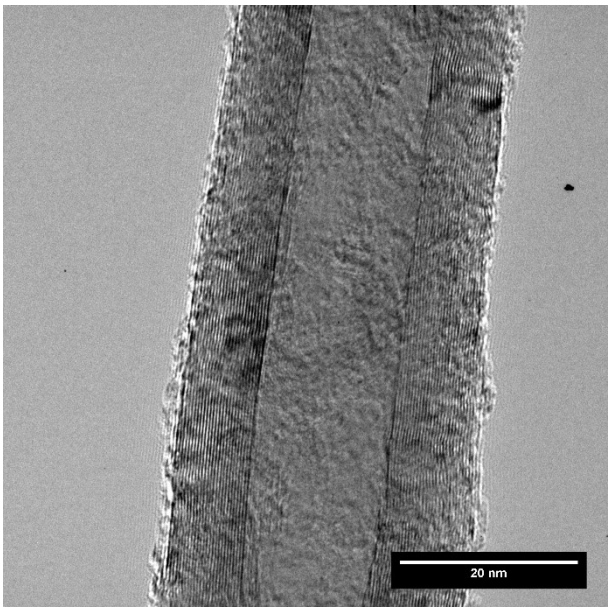

(d) After irradiation ×250000

Fig. 4.52. TEM images of MWCNTs irradiated with Ar^{14+} at the fluence of 2×10^{13} ions/cm^2.

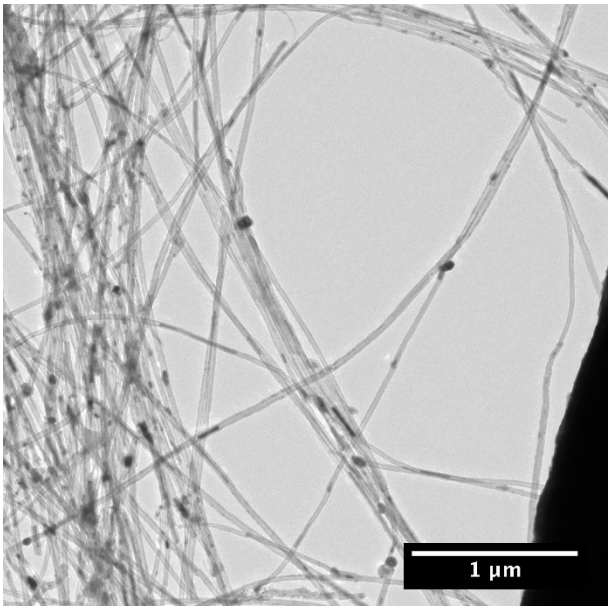

(a) Before irradiation ×5000

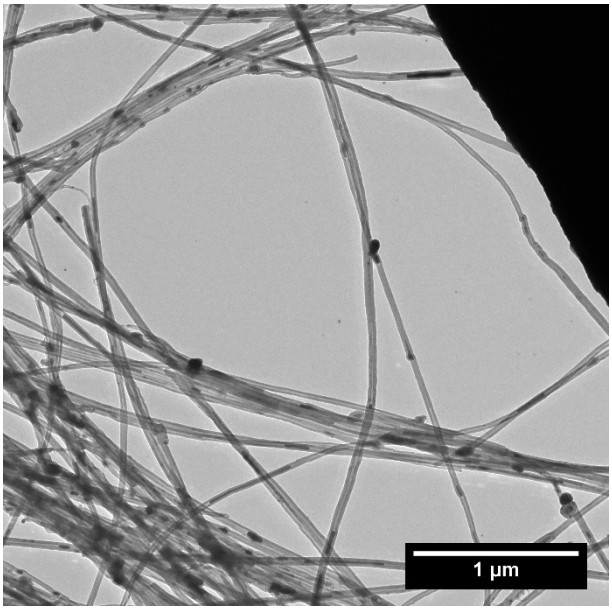

(b) After irradiation ×5000

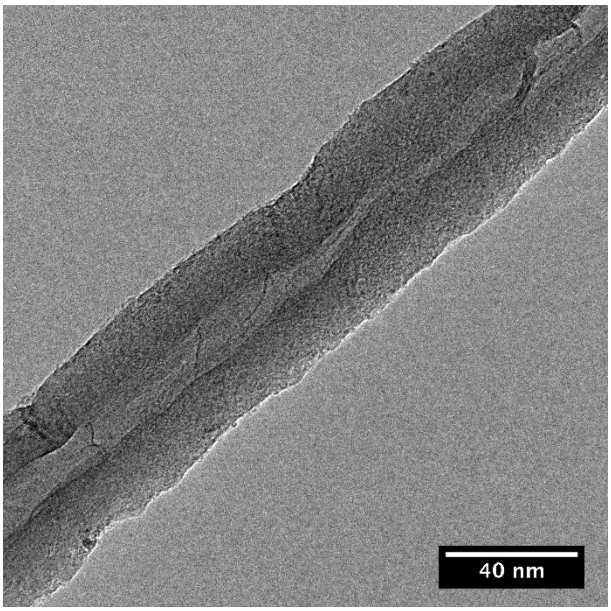

(c) Before irradiation ×250000

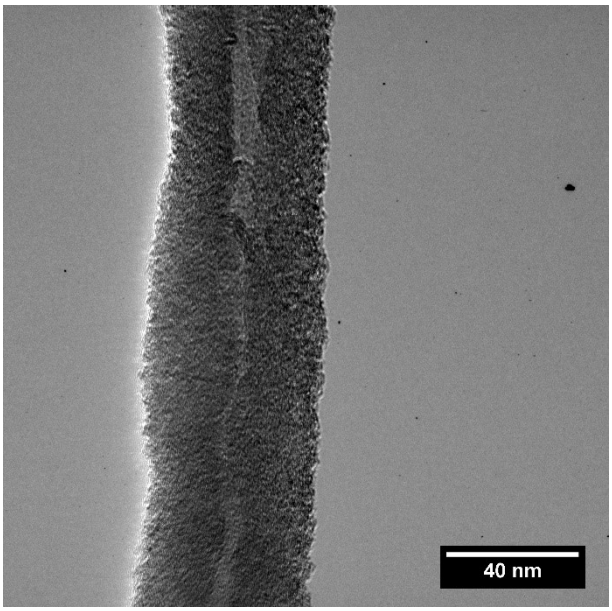

(d) After irradiation ×250000

Fig. 4.53. TEM images of MWCNTs irradiated with Ar^{14+} at the fluence of 6×10^{13} ions/cm^2.

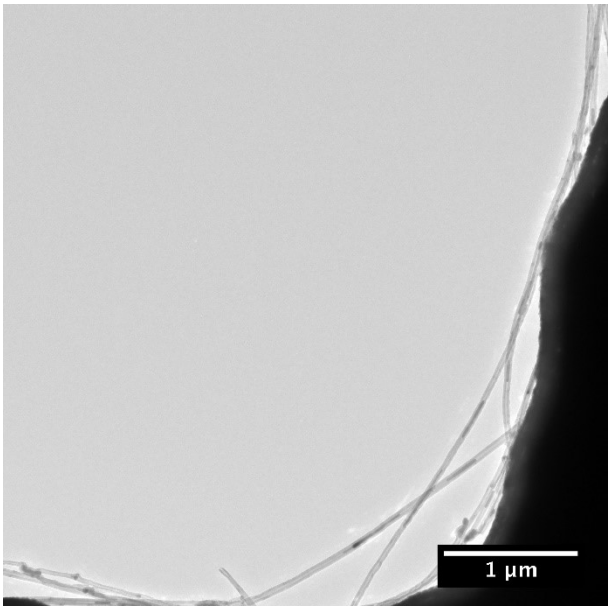

(a) Before irradiation ×5000

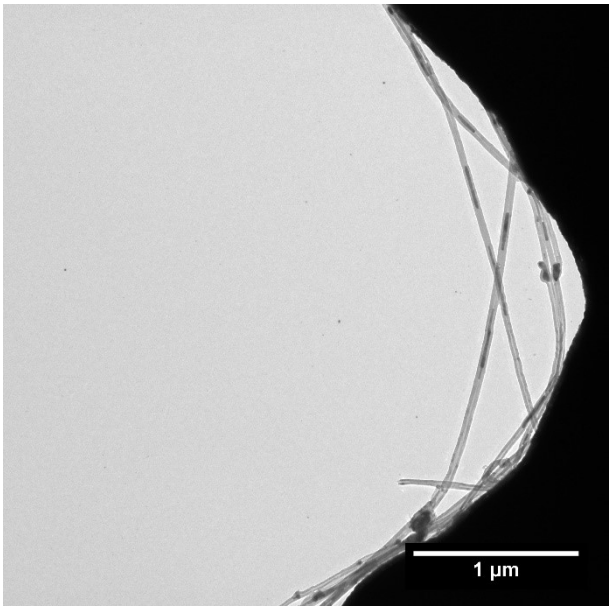

(b) After irradiation ×5000

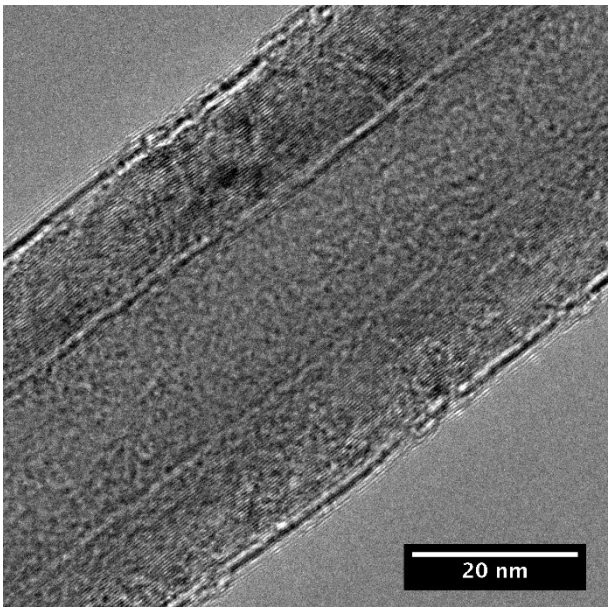

(c) Before irradiation ×250000

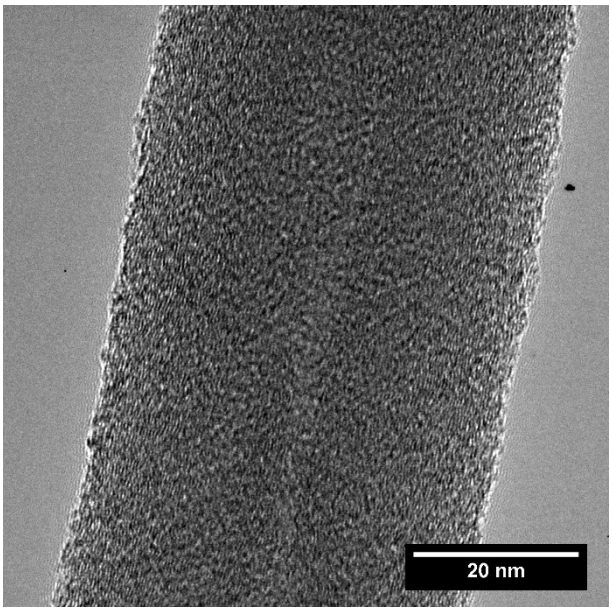

(d) After irradiation ×250000

Fig. 4.54. TEM images of MWCNTs irradiated with Ar^{14+} at the fluence of 6×10^{13} ions/cm^2.

In the MWCNTs irradiated with Ar^{14+} at the fluence of 6×10^{13} ions/cm^2, uneven surfaces that not seen in the samples without irradiation were observed. It is suggested that potential sputtering occurred.

The diameter, inner diameter, and layer thickness were compared before and after irradiation. The relations of the diameter, inner diameter, and layer thickness with charge state and fluence of irradiation are shown in Figures 4.55, 4.56, and 4.57, respectively. The inner diameter tends to decrease and the thickness of the layer tends to increase due to irradiation with HCIs. In particular, the change of MWCNT irradiated with Ar^{14+} is remarkable.

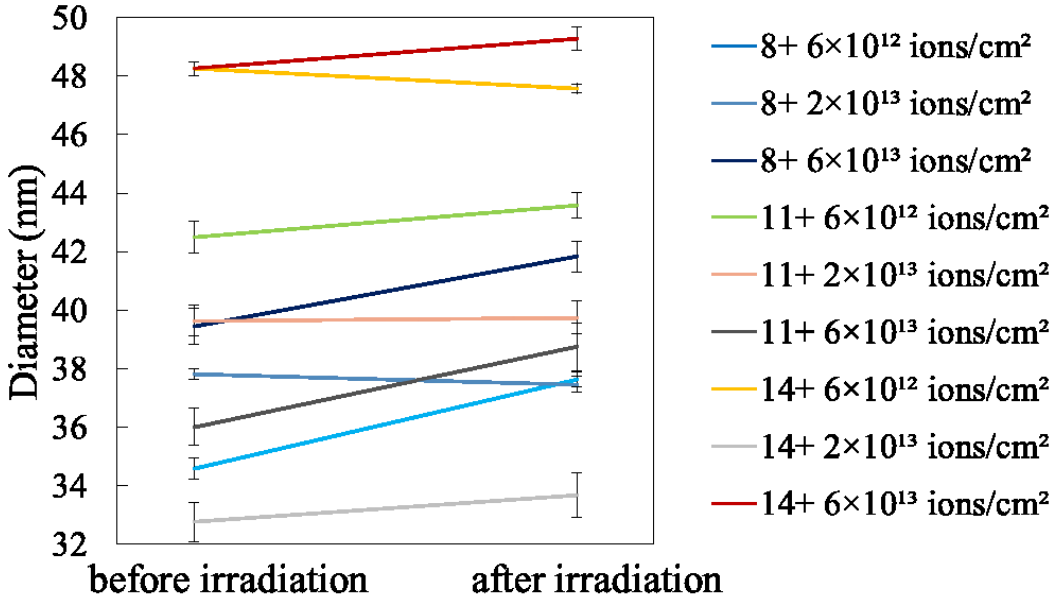

Fig. 4.55. Diameters of MWCNTs irradiated with Ar^{q+} (q = 8, 11, 14).

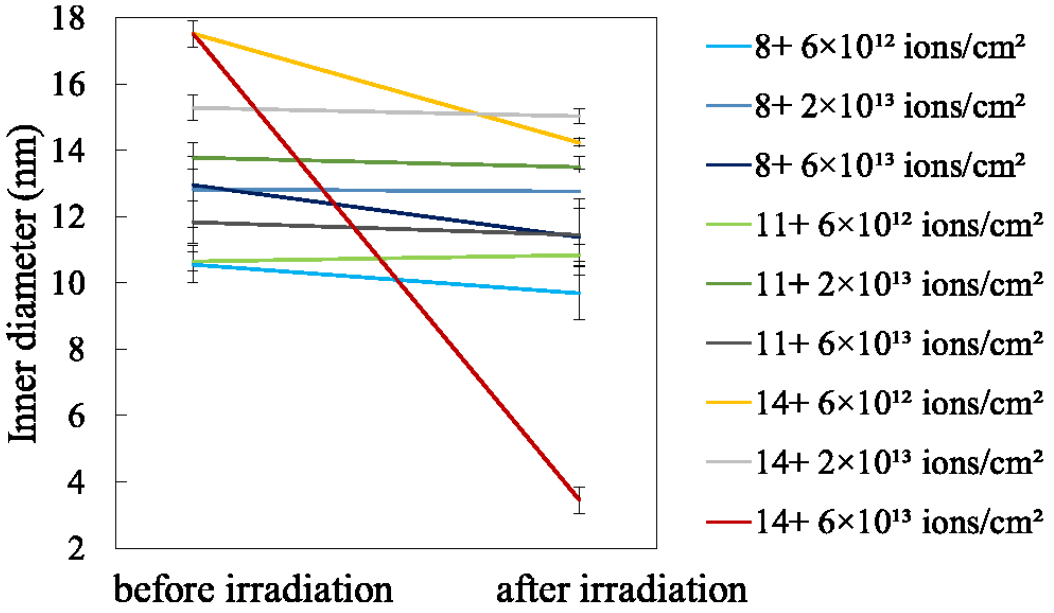

Fig. 4.56. Inner diameters of MWCNTs irradiated with Ar^{q+} (q = 8, 11, 14).

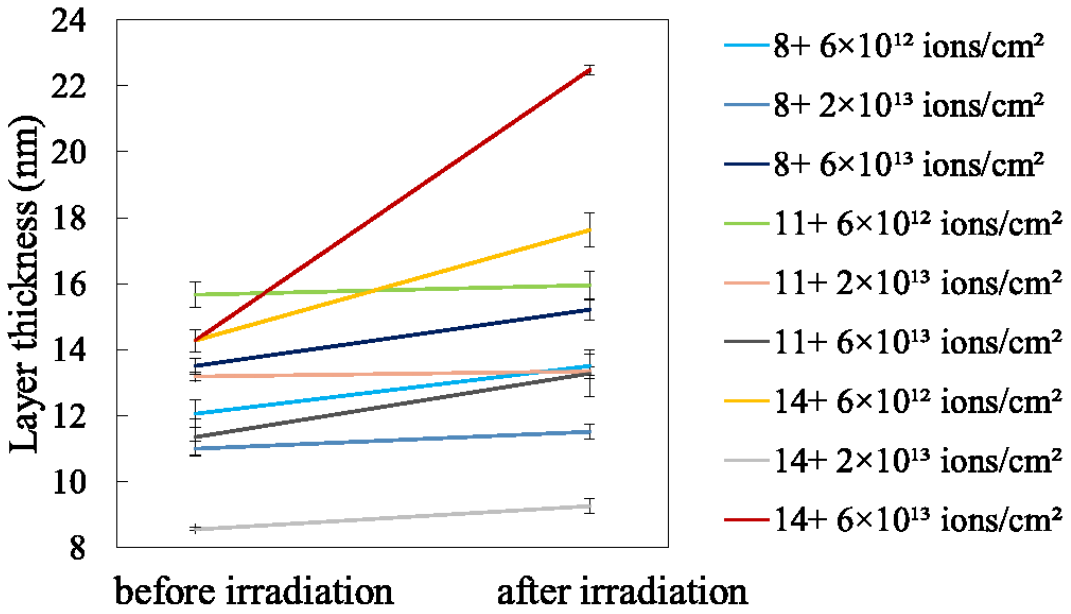

Fig. 4.57. Layer thickness of MWCNTs irradiated with Ar^{q+} (q = 8, 11, 14).

Figures 4.58 to 4.61 show electron diffraction patterns of single MWCNT. From the diffraction pattern, it was found that the diffraction spots are slightly blurred as

charge state increases. However, the change state dependence is not remarkable compared to the data obtained in Run A.

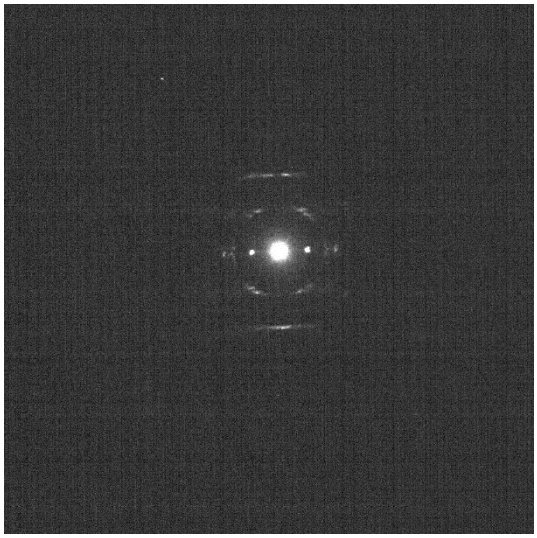

Fig. 4.58. Electron diffraction pattern of unirradiated MWCNTs.

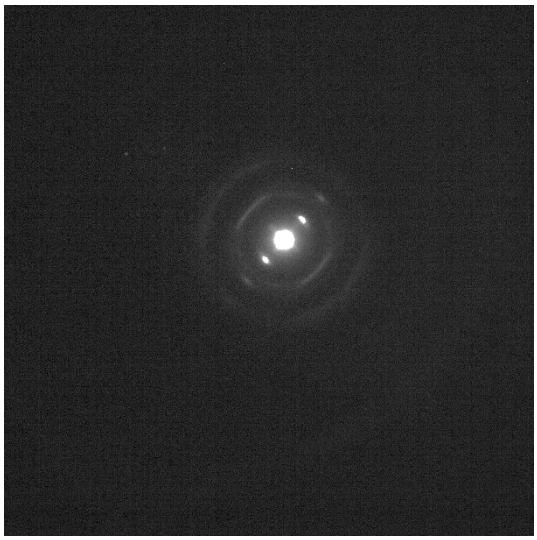

Fig. 4.59. Electron diffraction pattern of MWCNTs irradiated with Ar^{8+} at the fluence of 6×10^{13} ions/cm^2.

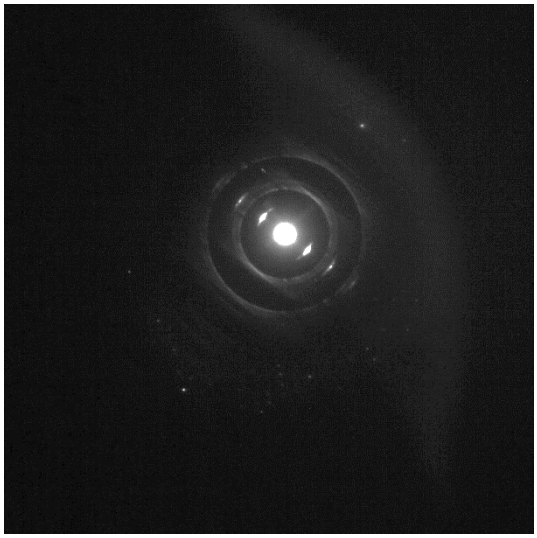

Fig. 4.60. Electron diffraction pattern of MWCNTs irradiated with Ar^{11+} at the fluence of 6×10^{13} ions/cm^2.

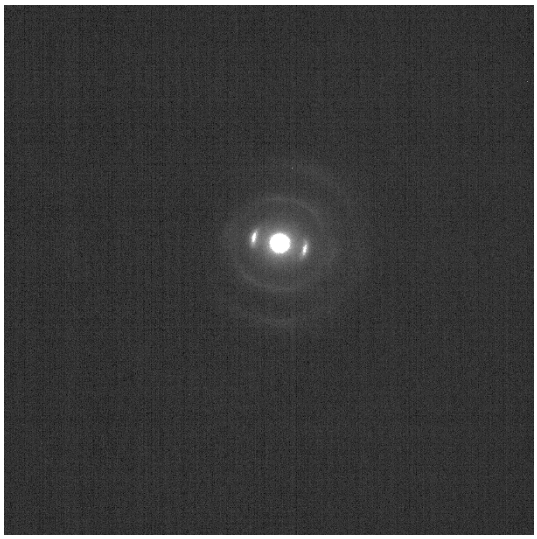

Fig. 4.61. Electron diffraction pattern of MWCNTs irradiated with Ar^{14+} at the fluence of 6×10^{13} ions/cm^2.

Figure 4.62 shows the ratio of D peak to G peak and D/G ratio of the Raman spectrum at each irradiation condition. From these results, it is seen that the D/G ratio increased by irradiation with HCIs and defects are introduced. There is not much difference in defects introduced by HCI injection between the results with different charge states, while the result shows that the defects increase with the fluence of irradiation.

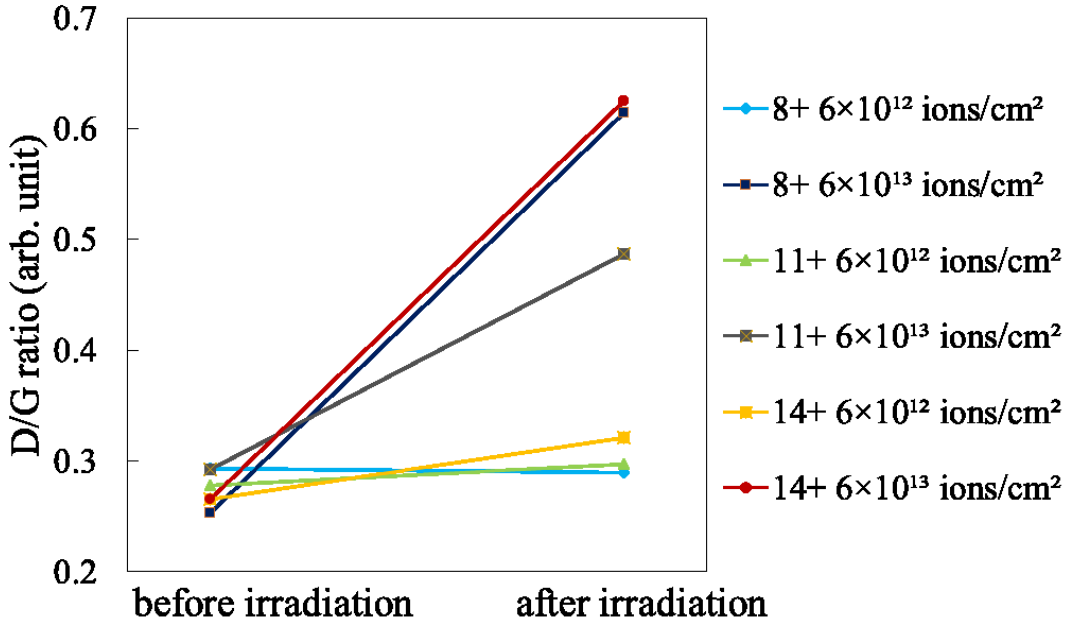

Fig. 4.62. D/G ratio of MWCNTs irradiated with Ar^{q+} (q = 8, 11, 14).

Run D

In these experiments, almost no significant change in the layer structure was observed. Apparent change in the outer diameter or layer thickness was not recognized. The reason of the absence of drastic change due to irradiation is assumed to be the difference in the completeness of crystal; perfect crystal with high electric conductivity does not allow potential sputtering. It is well known that potential sputtering is not observed on a metallic surface. The TEM observation of free-standing graphene irradiated with HCI (Xe^{30+}) also shows that no impact trace was recognized and the result is explained as ultrafast electron supply that prevents potential sputtering [14]. The detailed analysis of TEM images, however, provided findings in the irradiation effect. Irradiations with HCIs under different conditions stated below were performed to measure changes in the layer spacing. First, the layer spacing was evaluated for kinetic energies of 16 keV and 42 keV since the effect of kinetic energy is recognized in Raman spectroscopy results. Figure 4.63 shows the thickness of the four layers of MWCNTs for unirradiated and irradiated samples. The example of TEM images of four layers in a MWCNT are shown in Figs. 4.64 and 4.65.

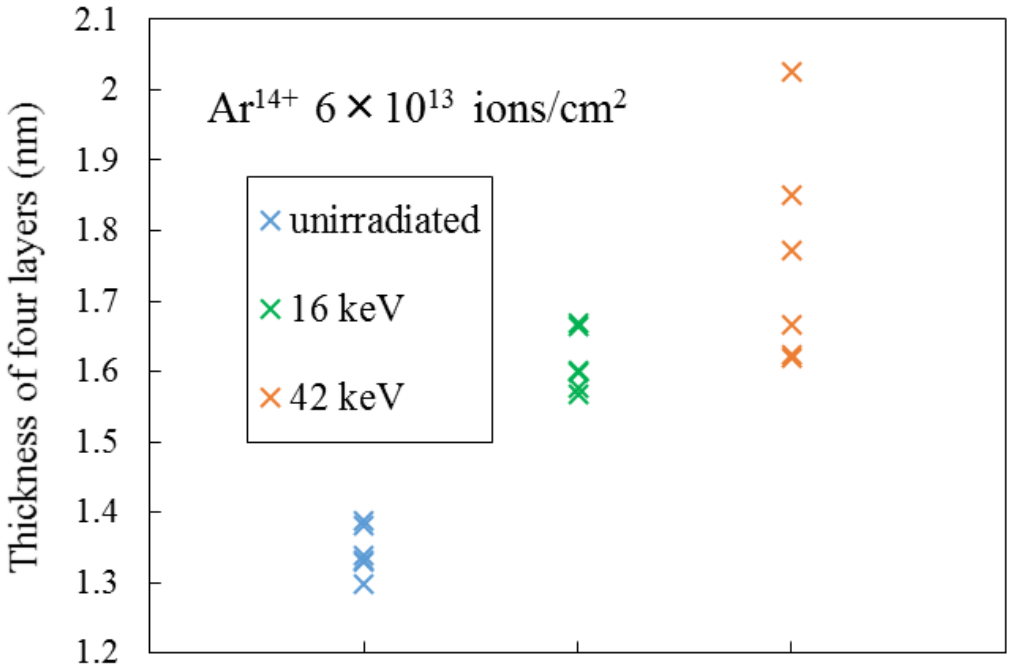

Fig. 4.63. Thickness of four layers of MWCNT irradiated with Ar^{14+}.

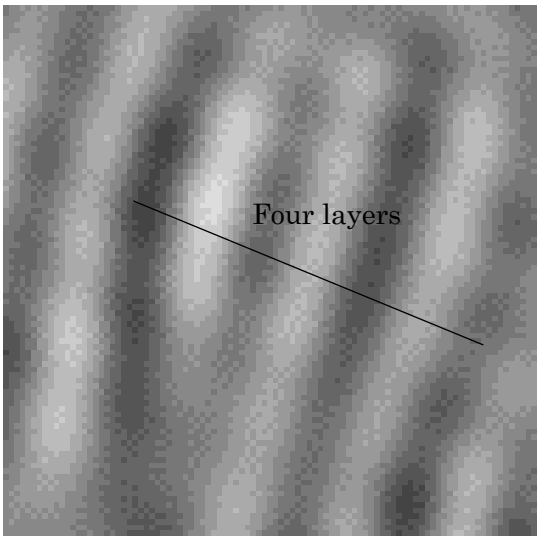

Fig. 4.64. TEM image of MWCNT irradiated with Ar^{14+} with kinetic energy of 16 keV.

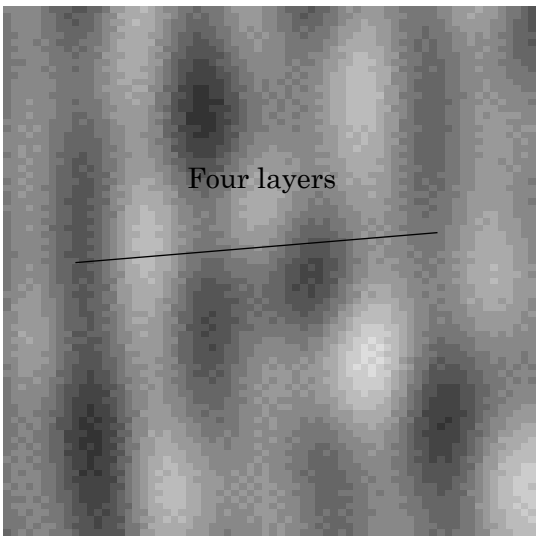

Fig. 4.65. TEM image of MWCNT irradiated with Ar^{14+} with kinetic energy of 42 keV.

As can be seen from the figure, the MWCNT irradiated with HCIs with larger kinetic energy tended to have a larger layer spacing. The average of the layer spacing was 0.34 nm for the sample without irradiation, 0.40 nm for the sample irradiated at 16 keV, and 0.44 nm for the sample irradiated at 42 keV. The results indicate that the increase of layer thickness by the irradiation is partly due to the effect of kinetic energy.

The potential energy of HCI is deposited on few layers near the topmost surface. On the other hand, structural modification by kinetic energy spreads over many layers. In the experimental condition of HCI irradiation and TEM observations so far, the direction of HCI incident to the grid plane and that of TEM observation (direction of electron beam) is the same. Since TEM observes right over the irradiated surface under this experimental condition, extraction of the information on structural modification characteristic to HCI such as potential sputtering is difficult for TEM observation with this geometry. Then in the following experiment, the sample was irradiated at an angle of 45° as shown in the Fig. 4.66, and the TEM observation was performed at an angle of 25° tilted to the other direction. As a result, the observation surface was tilted 70° compared to the case without tilt (Fig. 4.67). This makes it possible to observe the irradiated surface at nearly parallel direction to TEM observation, that is, irradiated surface is nearly perpendicular to the cross section of TEM observation.

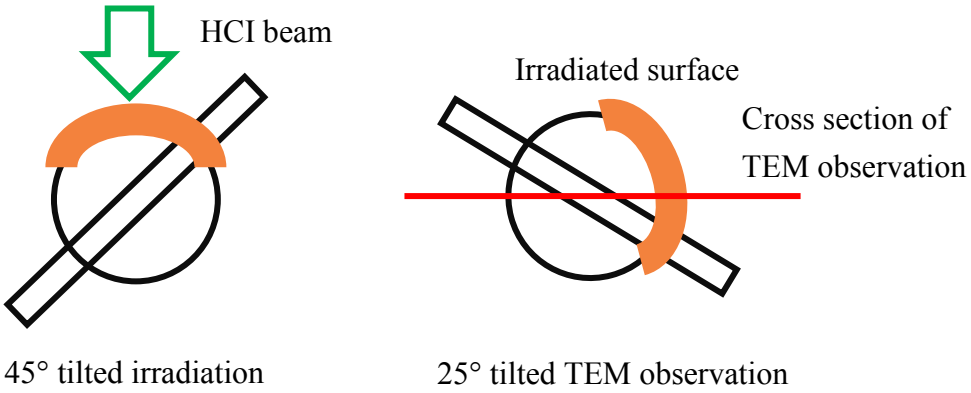

Fig. 4.66. Schematic diagram of tilted irradiation and TEM observation.

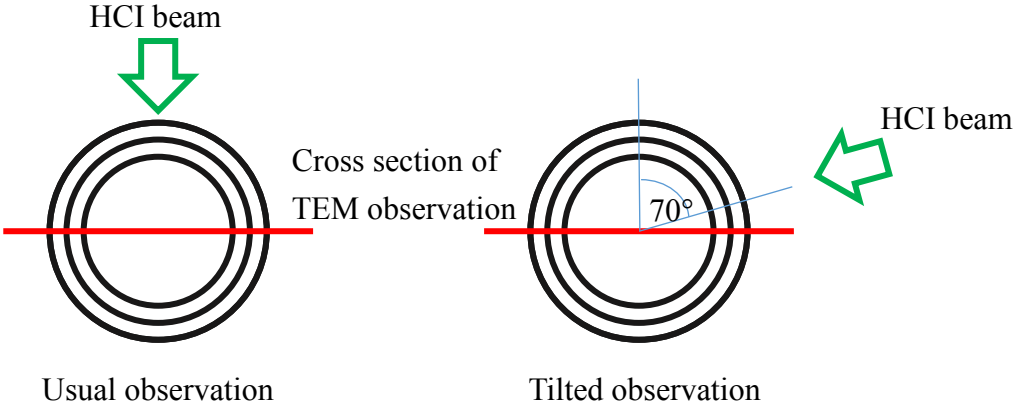

Fig. 4.67. Schematic diagram of tilted TEM observation.

Figure 4.68 shows TEM image obtained with tilted observation condition, and Fig. 4.69 shows the results of measurements of the thickness of the four layers on the surface side and the four layers on the inner side of each layer. The layer spacing tends to become wider in the layer near the surface to which the HCIs are irradiated. This illustrates the characteristic that the effect of the potential energy affects only a few nanometers.

The Raman spectrum is considered to show the result of the average defect of several MWCNTs because the laser beam of Raman apparatus spreads over several MWCNTs and the Raman spectrum includes the information of several MWCNTs. In the case of HOPG, the optical skin depth of Raman spectra of Ar ion radiation (514.5 nm radiation) is about 40 nm [15]. Assuming that MWCNTs also have the same skin depth as HOPG, it is considered that information over about 40 nm, that is, almost the size of diameter is obtained. Raman spectrum also reflects average information over many layers of MWCNT, this means that kinetic energy effect is stressed compared to potential energy effect in Raman spectrum. Therefore, the contribution of kinetic energy is large in Raman spectroscopy for the analysis of irradiation effect of HCI on MWCNT. On the other hand, since a fine structure with atomic resolution can be observed by TEM observation, it is considered that the potential effect of HCI is observable.

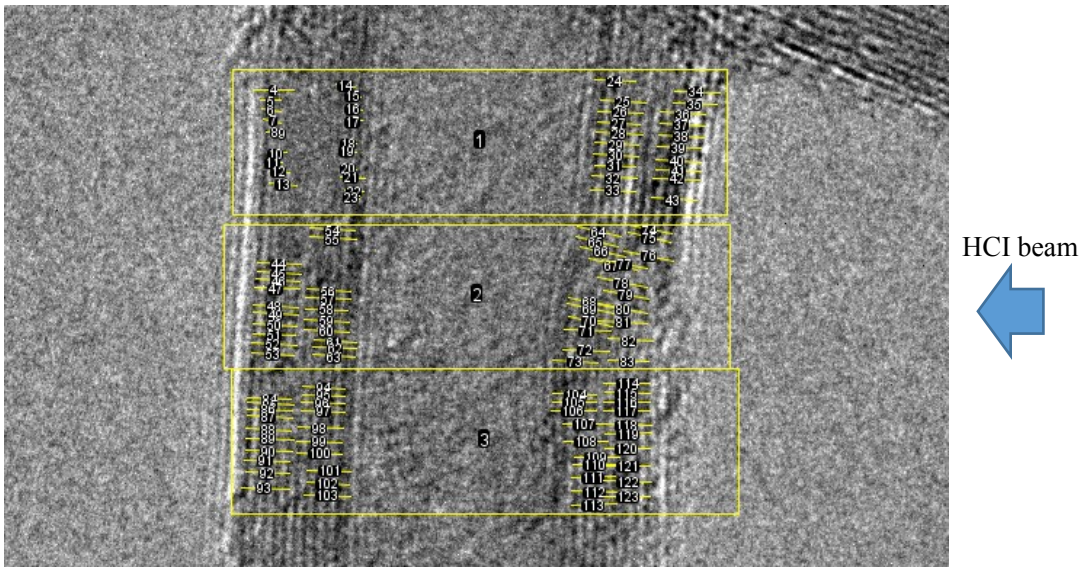

Fig. 4.68. TEM image of MWCNT irradiated with Ar^{14+} at the fluence of 6×10^{13} ions/cm^2 by tilted observation (70°).

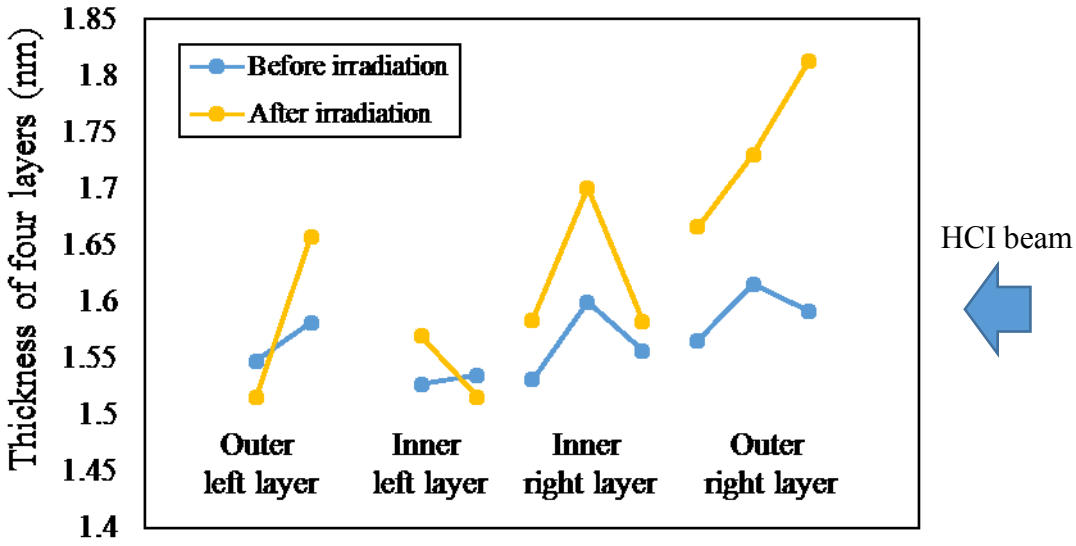

Fig. 4.69. Thickness of four layers of tilted MWCNT irradiated with Ar^{14+}. Three or two data spots connected with line mean the data extracted from corresponding windows indicated in Fig. 4.68.

Figure 4.70 shows the relation between the D/G ratio and the half width of the G peak. It was reported that the D/G ratio in the Raman spectra of HOPG increased as the in-plane defects increased due to the irradiation with Ar^+, and that after further ion dose the half-width of the G peak increased with the increase in the amorphousness as shown in Fig. 4.71 [16]. For the sample temperature less than 373 K, the plot of D/G ratio versus G peak FWHM follows the pass indicated with red numbers in circle. Comparing this figure with our results plotted in Fig. 4.70, where the plot shifts along similar pass as that of Fig. 4.71, it is considered that the effect of the irradiation dose is larger than that of the charge state, and the effect of kinetic energy is larger than that of potential energy, because the plot shifts with the fluence rather than charge state.

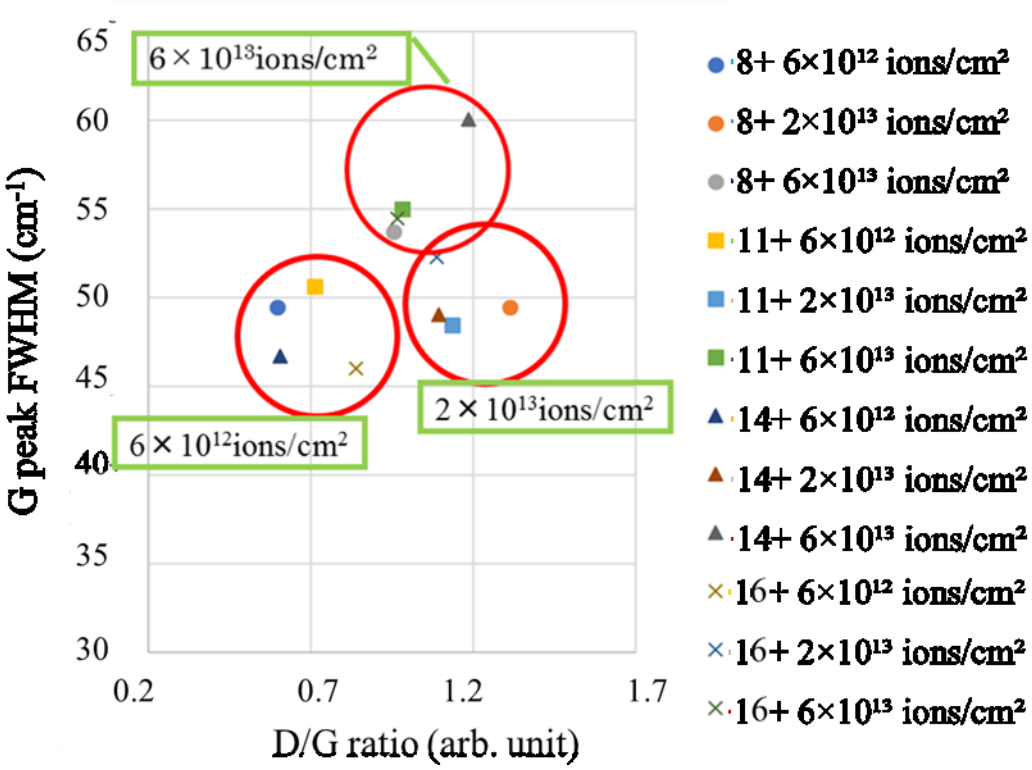

Fig. 4.70. Relation between D / G ratio, G peak half width and graphite structure.

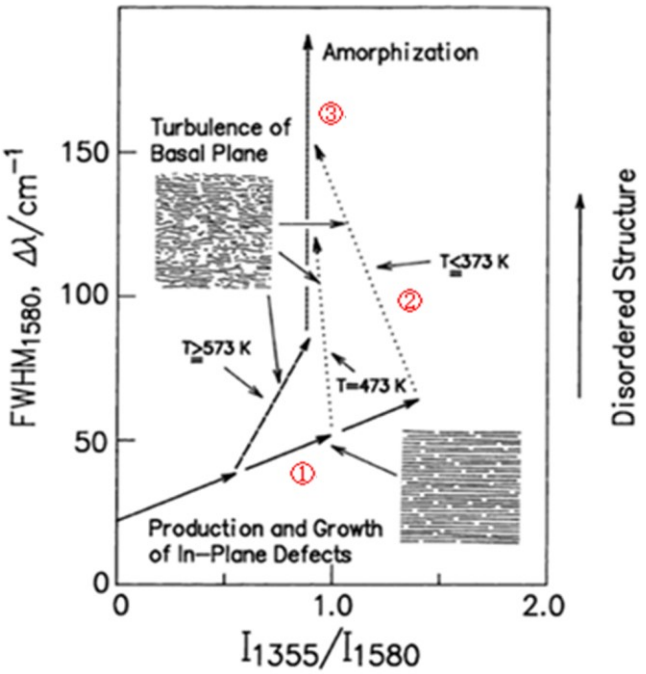

Fig. 4.71. Relation between D / G ratio, G peak half width and graphite structure [16].

4.4 Summary

Structural modifications of MWCNTs irradiated with HCIs have been analyzed TEM and Raman spectroscopy. Although it has been thought to be difficult to observe the same place on the nanometer scale because samples were transferred between irradiation at Kobe EBIS and observation with TEM, we established the procedure to make observation at an identical location in the sample before and after irradiation. By using this procedure it has become possible to compare a nanometer region in a millimeter-sized sample before and after irradiation. We investigated the difference of TEM images at the identical position between samples with the diameter of 10–20 nm before and after irradiation. TEM images of MWCNTs irradiated with Ar^{14+} exhibit uneven surfaces at the fluence of 6×10^{13} ions/cm^2. Outer diameters are decreased, outlines of surfaces become uneven and hollow regions disappeared by the irradiation. These results are different from the case of irradiation with SCIs. It is considered that potential sputtering occurred on the surfaces of MWCNTs. On the other hand, TEM observation of MWCNTs with the diameter of 30–50 nm irradiated with HCIs showed no significant changes such as uneven surface. From Raman spectroscopy, there is no significant dependence on charge state. Since the D/G ratio increases as the fluence of HCIs increases, it is considered that many defects are introduced due to the kinetic energy of HCIs. Raman spectrum reflects average information over many layers of multiple MWCNTs, this means that kinetic energy effect is stressed compared to potential energy effect. On the other hand, since a fine structure with atomic resolution can be observed by TEM observation, it is considered that the potential effect of HCI is observable. The layer spacing tends to become wider in the layer near the surface to which the HCIs are irradiated in the tilted TEM observation. This is considered to be a characteristic that the effect of the potential energy of the HCIs affects only a few nanometers. The potential effects of HCI, such as the appearance of uneven surfaces and a decrease in outer diameter, were clarified by observing the same location.

References

[1] M. S. Dresselhaus, G. Dresselhaus, and P. Avouris, Carbon Nanotubes; Synthesis, Structure, Properties, and Applications, Springer (2001).

[2] M. Nihei, A. Kawabata, Y. Awano, Jpn. J. Appl. Phys. 42 (2003) 721.

[3] W. Wongwiriyapan, S. Honda, H. Konishi, T. Mizuta, T. Ikuno, T. Ito, T. Maekawa, K. Suzuki, H. Ishikawa, K. Oura, and M. Katayama, Jpn. J. Appl. Phys. 44 (2005) L482.

[4] D.-H. Kim, H.-S. Jang, C.-D. Kim, D.-S. Cho, H.-D. Kang, and H.-R. Lee, Chem. Phys. Lett 378 (2003) 232.

[5] D. N. Futaba, K. Hata, T. Yamada, T. Hiraoka, Y. Hayamizu, Y. Kakudate, O. Tanaike, H. Hatori, M. Yumura, S. Iijima, Nature Mater. 5 (2006) 987

[6] S.-T. Kang, J.-Y. Seo, and S.-H. Park, Adv. Mater. Sci. End. 2015 (2015) 308725.

[7] A. V. Krasheninnikov, and F.Banhart, Nature Mater. 6 (2007) 723.

[8] A. V. Krasheninnikov and K. Nordlund, J. Appl. Phys. 107 (2010) 071301.

[9] A. V. Krasheninnikov, P. O. Lehtinen, A.S. Foster, and R.M. Nieminen, Chem. Phys. Let. 418 (2006) 132

[10] O. Lehtinen, T. Nikitin, A. V. Krasheninnikov, L. Sun, F. Banhart, L. Khriachtchev, and J. Keinonen, New J. Phys. 13 (2011) 073004.

[11] S. Honda, R. Tamura, Y. Nosho, A. Tsukagoshi, M. Niibe, M. Terasawa, R. Hirase, H. Izumi, H. Yoshioka, K. Niwase, E. Taguchi, K.-Y. Lee, and M. Oura, Jpn. J. Appl. Phys. 53 (2014) 02BD06.

[12] N. Nishida, M. Sakurai, K. Betsumiya, K. Suzuki, A. Yamauchi, M. Kato, Y. Hujiwara, S. Honda , M. Terasawa, K.-Y. Lee, and T. Terui, Vac. Surface Sci. 61 (2018) 162 (in Japanese).

[13] N. Nishida, Y. Hori, A. Yamauchi, H. Fujiwara, M. Sakurai, Y. Fujiwara, R. Tamura, S. Honda, H. A. Sakaue, D. Kato, T. Yamaguchi, K. Ishibashi, T. Terui, and K.-Y. Lee, X-Ray Spectrometry 49 (2020) 99.

[14] E. Gruber, R. A. Wilhelm, R. Petuya, V. Smejkal, R. Kozubek, A. Hierzenberger, B. C. Bayer, I. Aldazabal, A. K. Kazansky, F. Libisch, A. V. Krasheninnikov, A. Schleberger, S. Facsko, A. G. Borisov, A. Arnau, and F. Aumayr, Nature Comm. 7 (2016) 13948.

[15] K. Nakamura and M. Kitajima, Phys. Rev. B 45 (1992) 5672.

[16] K. Niwase and T. Tanabe, Mater. Trans. Jpn. Inst. Met. 34 (1993) 1111.

Chapter 5 Electric Properties of Multi-Walled Carbon Nanotube Irradiated by Highly Charged Ions

5.1 Introduction

A carbon nanotube (CNT) is a promising material for quantum dot (QD)-based nanodevices and circuits [1]. A multi-wall carbon nanotube (MWCNT) has advantages over single wall carbon nanotubes owing to its robustness against resist processes, metallic transport behavior, and low contact resistance at metal-MWCNT interfaces even at the liquid He temperature [2]. As it is necessary to create tunnel barriers in MWCNTs to realize QD-based devices, various experimental methods utilizing the beam irradiation technique have been employed; Ar atoms are injected on resist-covered MWCNTs with metal contacts [3], and MWCNTs are irradiated with singly charged Ga ions from a focused ion beam apparatus [4].

It is unknown how the injection of HCIs influences the electric properties of MWCNTs because the interaction of HCIs with materials is unique and essentially different from that of energetic neutrals and singly charged ions, where the kinetic energy of the primary particle plays a major role. In the present study, we present experiments on electric characteristics of MWCNT irradiated with HCIs [5].

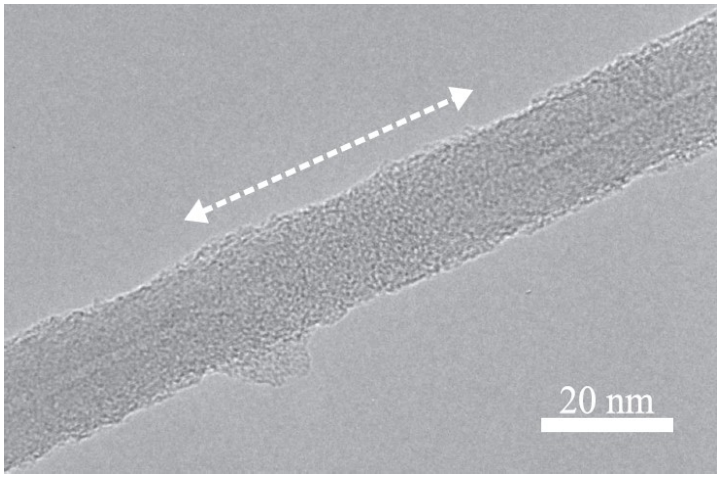

Fig. 5.1. TEM image of the irradiated region indicated by the arrow. The FIB irradiation was carried out for the MWCNTs dispersed on a TEM grid. A dose condition was 1.5×10^{16} ions cm^{-2} [4].

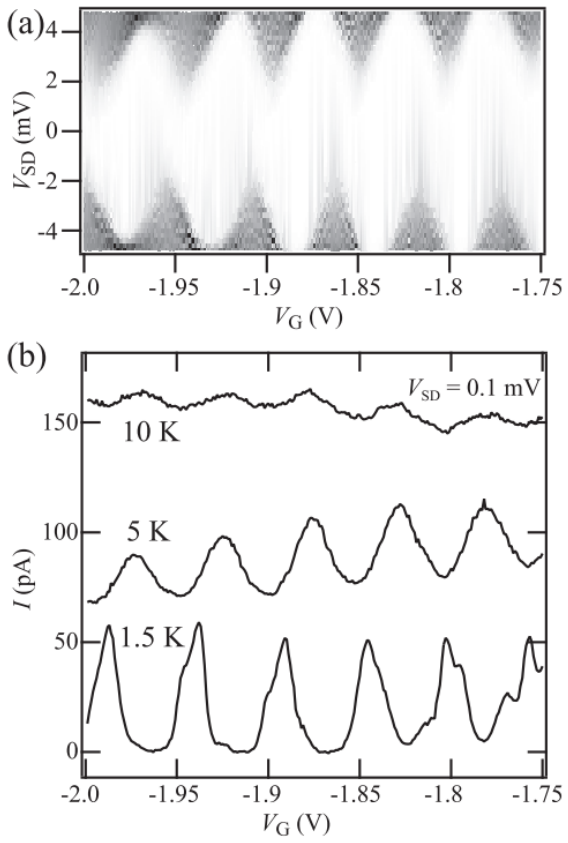

Fig. 5.2. (a) Grey scale plot of differential conductance as function of V_{SD} and V_G (Coulomb diamonds) at 1.5 K and (b) Coulomb oscillations of a double-barrier sample. The distance between the two barriers was 100 nm, and the dose condition was 1.2×10^{16} ions cm^{-2} for both barriers. Resistance increase at room temperature, which includes two barriers, was 124 kΩ. The oscillations have shifted during the temperature change between 1.5 and 5 K. This is sometimes observed in the single electron transistor [4].

5.2 Experimental

The MWCNTs were produced by an electric arc discharge method. The diameters were in the range 10–30 nm. The as-prepared MWCNTs were dispersed onto a Si substrate. The source/drain contacts were patterned by depositing 30 nm of Pd followed by 10 nm of Au. Figure 5.3(a) shows a SEM image of a pristine single MWCNT with metal contacts separated by 1 μm, constituting a back-gate FET configuration [Fig. 5.3(b)]. Such channel structures were multiply fabricated onto a Si chip of size 4×4 mm^2, as shown in Fig. 5.4. The resistance between the contacts was measured using a

DC two-terminal method. The resistance was ~10 kΩ at room temperature in most of the MWCNT channels before the irradiation.

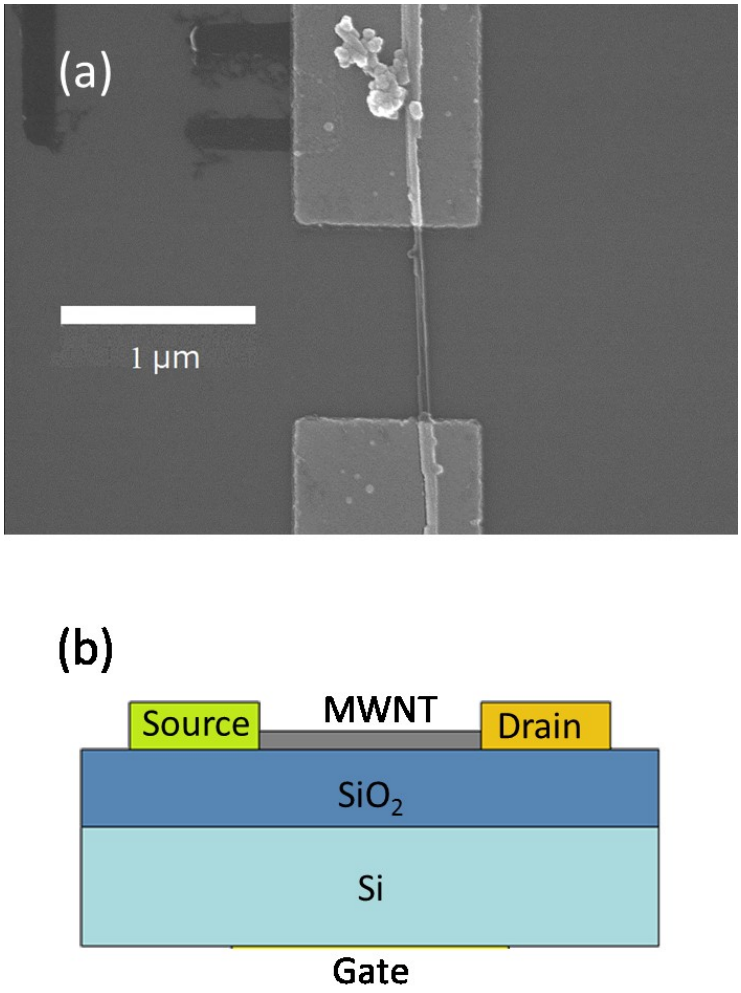

Fig. 5.3. (a) SEM image of a pristine single MWCNT with metal contacts separated by 1 μm. (b) Schematic picture of the substrate sample structure.

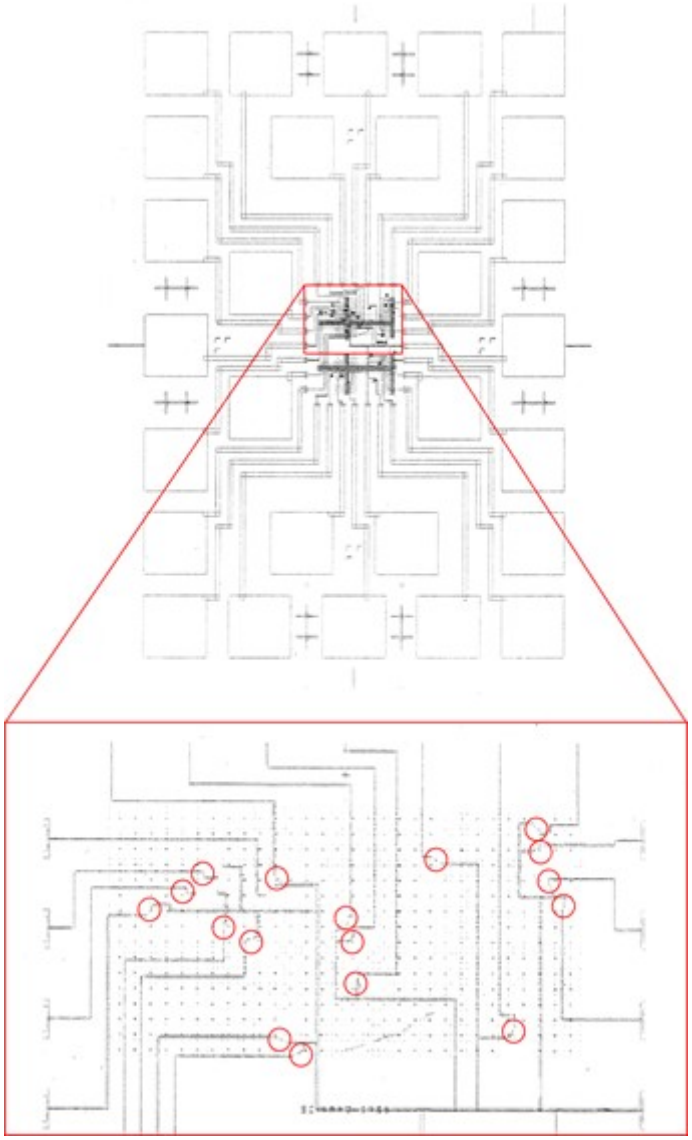

Fig. 5.4. Image of the MWCNT channel structures fabricated on a Si chip of size 4 × 4 mm^2. There is one MWCNT in each circle.

The Si chip with 26 MWCNT channel structures was mounted on a sample holder that was transferred to the sample stage in irradiation chamber A. The HCIs of Ar^{q+} (q = 6–16) with intensities of 0.1–1 nA were projected onto the sample with a constant kinetic energy (16 keV) by applying the retarding potentials to each sample, e.g., 1 kV for Ar^{8+} and 2 kV for Ar^{16+}. The room temperature current-voltage (I-V) curves were measured with a probe using a DC voltage/current generator (ADC Corp. 6240B) after extracting the sample from the irradiation chamber. This cycle was repeated to obtain the dependence of the I-V characteristics on fluence. To estimate the fluence, the

intensity and beam profile of the incident HCI beam were monitored, and the beam position was adjusted to the center where the chip would be located in advance, for the purpose of installing the sample on the sample stage. The beam size was first estimated, ~2–3 mm, before the beam density was estimated. To irradiate with Ar^{8+} at a current density of 0.2 nA/mm^2, 10 min was required to reach a fluence of 10^{13} ions/cm^2. The integrated fluence for the identical chip was in the range 10^{11} to 10^{13} ions/cm^2 for the present experiment.

Low temperature *I-V* measurements for a chip with a maximum fluence were carried out using a ^{4}He cryostat. The coulomb oscillation and Coulomb diamond characteristics were obtained by applying a gate voltage to the Si substrate of the chip.

5.3 Results and discussion

Figure 5.5 shows the dependence of the resistance of the MWCNTs, for many channels of a chip irradiated with Ar^{8+}, on the fluence at room temperature. The resistance tended to increase as the fluence increased. The irradiation with Ar^{8+} caused an increase in the resistivity at room temperature by 10% at a fluence as low as 6×10^{11} ions/cm^2. The resistivities at room temperature for the MWCNT samples with high fluences of the order of 10^{13} ions/cm^2 reached values greater than five times those of the original ones. Figure 5.6 shows the change in the electric resistance of the MWCNTs after irradiation with Ar^{q+} (q = 8, 11, and 14) at a fluence of 6×10^{11} ions/cm^2. Although there was only a slight difference between the samples irradiated with Ar^{8+} and those irradiated with Ar^{11+}, the resistance of the MWCNTs irradiated with Ar^{14+} increased more significantly than those of Ar^{8+} and Ar^{11+}. It was assumed that the HCIs with a larger potential energy caused more defects on the MWCNTs. Moreover, it is commonly observed that the degree of the potential effect caused by the interaction of the HCIs with surfaces is nonlinear, and in some cases is the fourth power of the charge state [6 - 9].

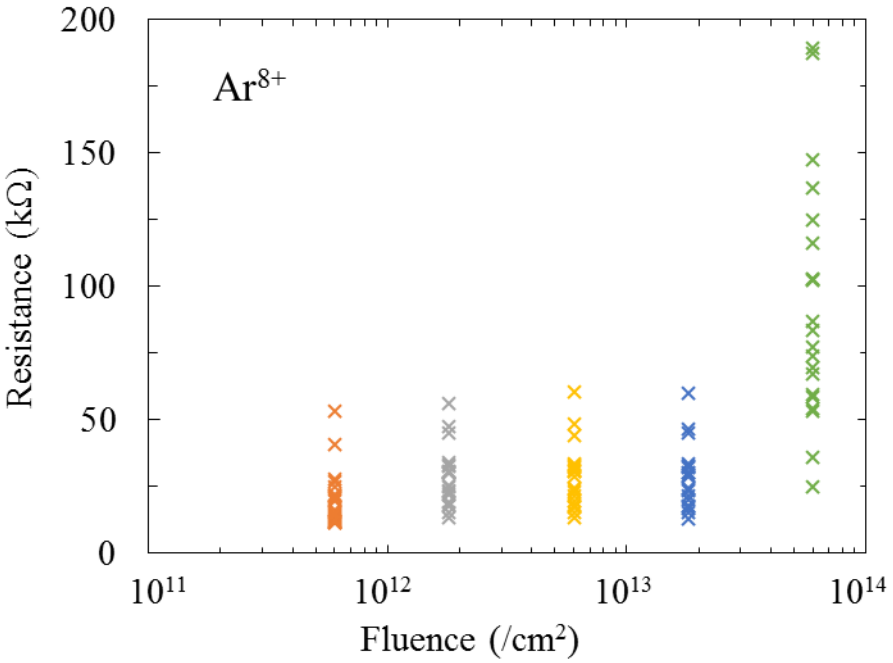

Fig. 5.5. Dependence of the resistance of the MWCNTs irradiated with Ar^{8+} on the fluence at room temperature.

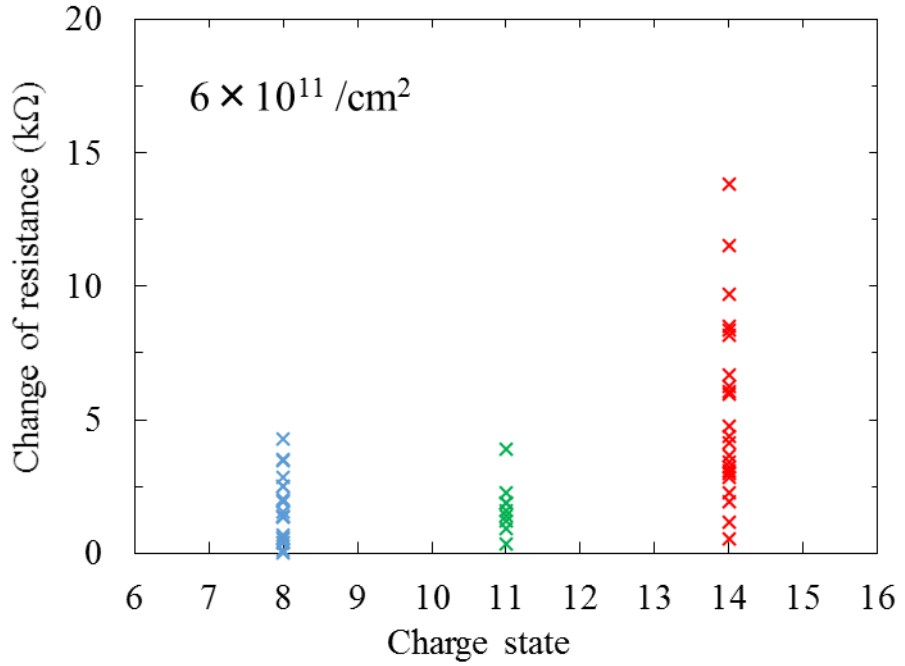

Fig. 5.6. Change in the electric resistance of the MWCNTs after irradiation with Ar^{q+} (q = 8, 11, and 14) at a fluence of 6×10^{11} ions/cm^2 at room temperature.

Figure 5.7 and Fig. 5.8 show the *I-V* curves and gate voltage dependences of the drain current of two different channels (chip number 18, and channel numbers 3 and 16) irradiated with Ar^{8+} at a fluence of 6×10^{13} ions/cm^2. The *I-V* curves became nonlinear at low temperatures. Coulomb oscillations can be observed in Fig.5.8, in contrast to Fig. 5.7. Table 5.1 shows a comparison of the resistances of 26 MWCNTs. Coulomb oscillations were observed in the MWCNTs for room temperature resistances of greater than 76 kΩ, as shown in Fig. 5.8. This was not the case in Fig. 5.7. However, the Coulomb blockade was not perfect (the current did not fall to zero at each dip in the oscillations), except for channel number 18. For channel number 18 with a room temperature resistance of 365 kΩ, Coulomb diamonds and periodic Coulomb oscillations were observed (Fig. 5.9) at 1.6 K. These results indicate that a single QD was formed by irradiation with Ar^{8+}. The estimated charging energy ($E_c = e^2/C_\Sigma$, where C_Σ is the self-capacitance) was E_c = 2.5 meV, and the gate capacitance ($C_g = e/\Delta V_g$, where ΔV_g is the period of the Coulomb diamonds) was C_g = 11 aF from Fig. 5.9 [10].

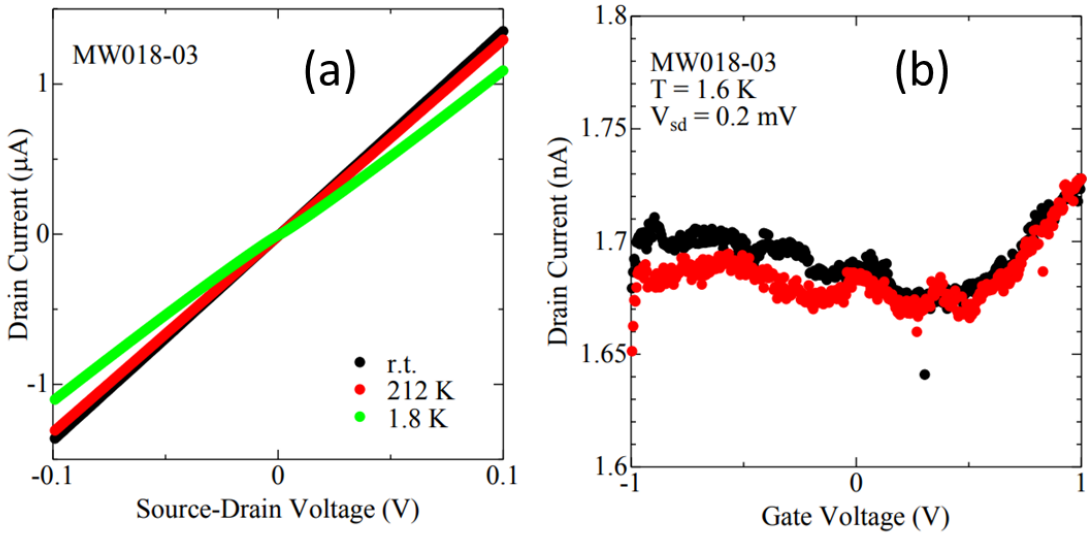

Fig. 5.7. (a) *I-V* curves and (b) gate voltage dependence of the drain current of the MWCNT samples irradiated with Ar^{8+} at a fluence of 6×10^{13} ions/cm^2. The resistance of the MWCNT was 75.9 kΩ at room temperature.

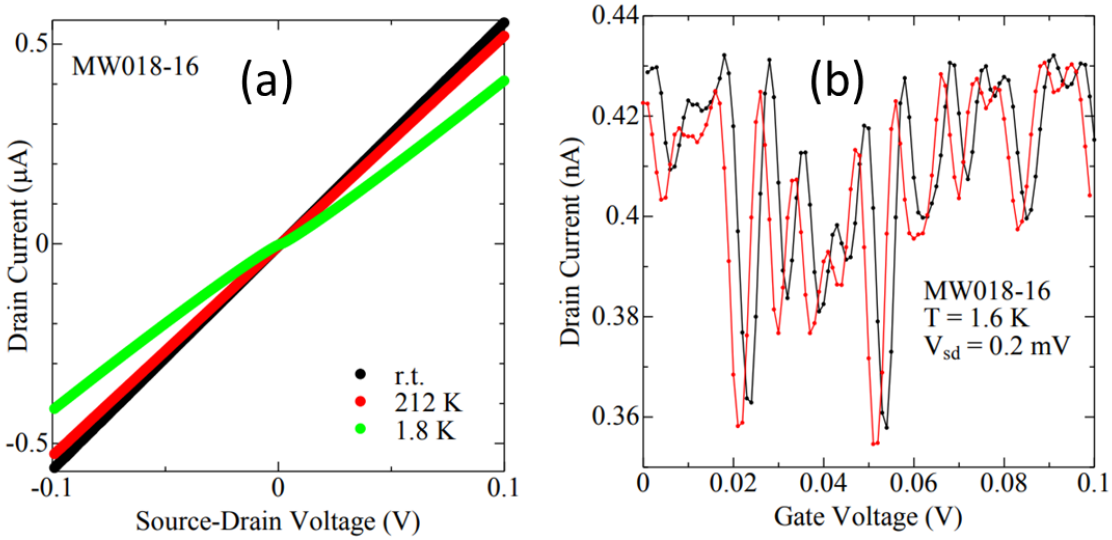

Fig. 5.8. (a) *I-V* curves and (b) gate voltage dependence of the drain current of the MWCNT samples irradiated with Ar^{8+} at a fluence of 6×10^{13} ions/cm^2. The resistance of the MWCNT was 179 kΩ at room temperature.

Table 5.1. Comparison of the resistances of 26 MWCNTs before and after irradiation with Ar^{8+} at a fluence of 6×10^{13} ions/cm^2 in the presence of Coulomb oscillations.

Channel number	Room temperature resistance (kΩ)		Coulomb oscillation
	before irradiation	Ar^{8+} 6×10^{13} ions/cm^2	
1	12.2	×	
2	19.4	×	
3	11.6	75.9	×
4	14.2	116	○
5	10.9	40.7	×
6	16.1	96.6	○
7	11.7	66.4	×
8	16.3	96.0	○
9	40.5	162	○
10	22.3	78.7	○
11	12.2	56.3	×
12	47.4	131	×
13	19.5	98.1	
14	24.9	73.5	×
15	9.87	34.5	×
16	21.9	179	○
17	12.3	92.4	○
18	17.6	365	○
19	×	×	
20	18.4	×	
21	18.7	64.2	×
22	16.8	118	
23	13.3	51.9	×
24	17.5	52.7	×
25	11.7	57.6	×
26	15.6	×	

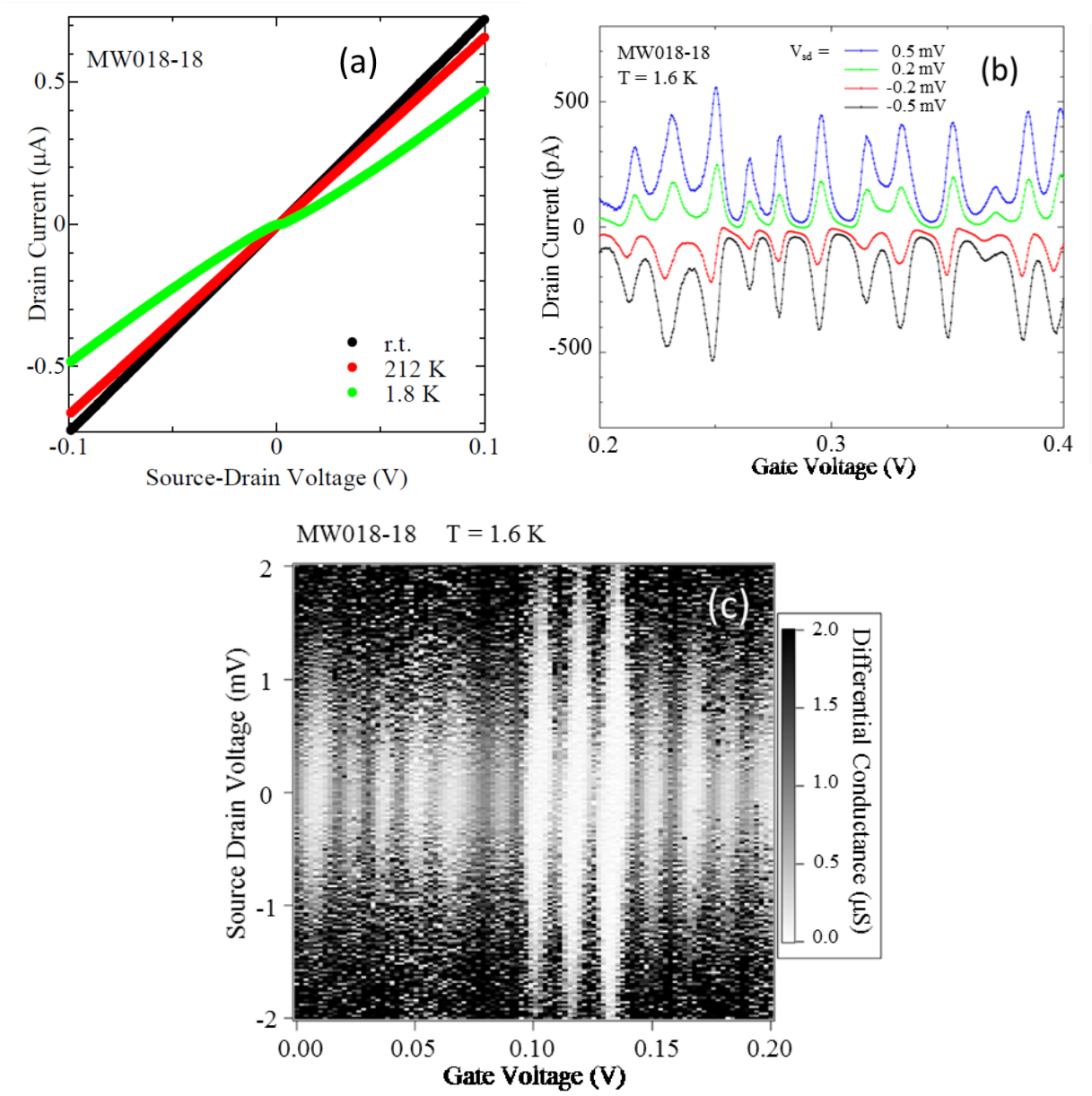

Fig. 5.9. (a) *I-V* curves, (b) gate voltage dependence on the drain current (Coulomb oscillations), and (c) plot of the differential conductance as a function of the source-drain and gate voltages (Coulomb diamonds) at 1.6 K of the MWCNT irradiated with Ar^{8+} at a fluence of 6×10^{13} ions/cm^2. The resistance of the MWCNT was 365 kΩ at room temperature.

It is suggested that the resistance of the irradiated HCIs depends on the charge state of the HCIs, since the kinetic energy of the HCIs was constant (16 keV) in these experiments. The single QD formed by irradiation of the whole surface of MWCNTs was

not previously reported for a double tunnel barrier where Ar atoms or Ga ions are injected on limited areas [3, 4]. As the Coulomb oscillations were periodic (not stochastic), it was considered that a single QD was produced [11, 12]. However, the mechanism may differ from that of the production of two tunnel barriers by irradiation. The area of the MWCNT between the electrodes was 30000 nm^2, assuming a diameter of 30 nm and length of 1000 nm. In the present experiment, ~18000 ions hit each MWCNT at a fluence of 6×10^{13} ions/cm^2. A simple calculation yields 0.6 ions incident per 1 nm^2. Therefore, it is unlikely that the HCIs are locally concentrated on only two places on a MWCNT. It is unknown how a single QD is formed under the irradiation without focusing the incident beam.

Coulomb oscillations were not observed for the MWCNTs with a resistance of 76 kΩ or less, and Coulomb diamond characteristics were observed at 365 kΩ. As a topic of future study, MWCNT samples will be produced with a high resistance and the formation of single QDs by irradiation with HCIs will be performed. TEM observations will also be required to evaluate the structure of the MWCNTs irradiated with the same fluence, as single QDs are formed. The fabrication of QD with HCI irradiation, that is an achievement of full-scale nanotechnology research using atomic physics techniques, has never been realized before the present study.

5.4 Summary

We evaluated the electric characteristics of MWCNTs irradiated with the HCIs of Ar^{8+}, Ar^{11+}, and Ar^{14+} extracted from an electron beam ion source (Kobe EBIS). Each MWCNT located on the high dope Si substrate had a source/drain contact, forming a back-gate FET configuration. The source to drain resistance of the MWCNT channel tended to increase with increasing fluence and charge state of the HCIs. The current-voltage curves were nonlinear at low temperatures for the irradiated samples, and Coulomb oscillations were observed in the gate voltage dependence of the drain current. At a cryogenic temperature (1.6 K), Coulomb diamonds and periodic Coulomb oscillations were observed, and it is suggested that a single QD was formed. We succeeded to achieve a full-scale nanotechnology research using atomic physics techniques such as HCI irradiation for the first time.

References

[1] Y. Kawano, T. Fuse, S. Toyokawa, T. Uchida, and K. Ishibashi, J. Appl. Phys. 103 (2008) 034307.

[2] M. R. Buitelaar, A. Bachtold, T. Nussbaumer, M. Iqbal, and C. Schönenberger, Phys. Rev. Lett. 88 (2002)156801.

[3] H. Tomizawa, T. Yamaguchi, S. Akita, and K. Ishibashi, J. Appl. Phys. 118 (2015) 044306.

[4] H. Tomizawa, K. Suzuki, T. Yamaguchi, S. Akita, and K. Ishibashi, Nanotechnology 28 (2017) 165302.

[5] N. Nishidai , Y. Hori, M. Sakurai, Y. Hujiwara, S. Honda, M. Terasawa, T. Yamaguchi, K. Ishibashi, and H. Izumi, Jpn. J. Appl. Phys. 58 (2019) SIIC01.

[6] M. Tona, K. Nagata, S. Takahashi, N. Nakamura, N. Yoshiyasu, M. Sakurai, C. Yamada, and S. Ohtani, Surface Sci. 600 (2006) 124.

[7] M. Sakurai, T. Miyamoto, K. Sasaki, D. Kato, and H. A. Sakaue, J. Vac. Soc. Jpn. 58 (2015) 147 (in Japanese).

[8] K. Kuroki, H. Torii, K. Komaki, and Y. Yamazaki, Nucl. Instr. Meth. Phys. Res. B 193 (2002) 804.

[9] M. Sakurai, K. Sasaki, T. Miyamoto, D. Kato, and H. A. Sakaue, e-J. Surf. Sci. Nanotech. 14 (2016) 1.

[10] K. Ishibashi, S. Moriyama, T. Fuse, and T. Yamaguchi, Physica E 35 (2006) 338.

[11] K. Ishibashi, S. Moriyama, T. Fuse, Y. Kawase, S, Toyokawa, and T. Yamaguchi, J. Vac. Soc. Jpn. 51 (2008) 445 (in Japanese).

[12] I. M. Ruzin, V. Chandrasekhar, E. I. Levin, and L. I. Glazman, Phys. Rev. B 45 (1992) 13469.

Chapter 6 Magnetization of HOPG Irradiated with Highly Charged Ions

6.1 Introduction

Highly oriented pyrolytic graphite (HOPG) samples irradiated with monovalent ions have been studied by electron spin resonance (ESR) and superconducting quantum interferometer device (SQUID) as a study of magnetism of HOPG irradiated with ions [1 - 4]. When a proton was injected, resonance peak due to the ion injection was observed at the fluence of 10^{16} ions /cm^2. ESR measurements of HOPG irradiated with Ar^{11+} were performed in the previous study using Kobe EBIS and ESR peak due to HCI irradiation was observed at the low temperature for the first time [5]. However, little is known about the dependence of ESR spectra on charge state and fluence. In the present study, HOPG samples irradiated with Ar^{q+} were measured by ESR in order to investigate the dependence of defect formation at the surfaces on charge state and fluence [6].

6.2 Experimental

In the present experiments, HOPG samples were irradiated with Ar^{8+} and Ar^{14+}. The fluence of Ar^{8+} per hour was about 6×10^{13} ions/cm^2 and that of Ar^{14+} was about 7×10^{12} ions/cm^2. When the charge state of HCIs is different, the kinetic energy of HCIs differs at same acceleration voltage. To avoid this, different deceleration voltages were applied to the sample for each charge state in order to unify the kinetic energy (16 keV). This makes it possible to purely evaluate the effect of the potential energy of HCIs. After irradiation, the HOPG samples were measured by an X-band ESR apparatus (BRUKER, EMX8/2.7). The sample extracted from the irradiation chamber to atmosphere was vacuum sealed in a quartz tube and cooled by liquid helium and its temperature was controlled by heater and flux of liquid helium. In these experiments, the samples were analyzed with the direction of microwave perpendicular to the *c* axis.

6.3 Results and discussion

Figure 6.1 shows the ESR spectra of the HOPG irradiated with Ar^{14+} at a fluence of 1×10^{14} ions/cm^2. These spectra were obtained at temperatures ranging from 10 to 260 K. There are two resonance lines in the spectra at low temperatures. A Dysonian line (D1 line) was observed in lower resonance field. A Lorentzian line (L1 line) appeared at low temperatures in higher resonance field. The L1 line decreases with increasing temperature and this line was not observed in measurement of unirradiated HOPG sample. Because unpaired electrons result in ESR signal, it is considered that the L1 line is originated from defects (dangling bonds) formed by Ar^{14+} irradiation.

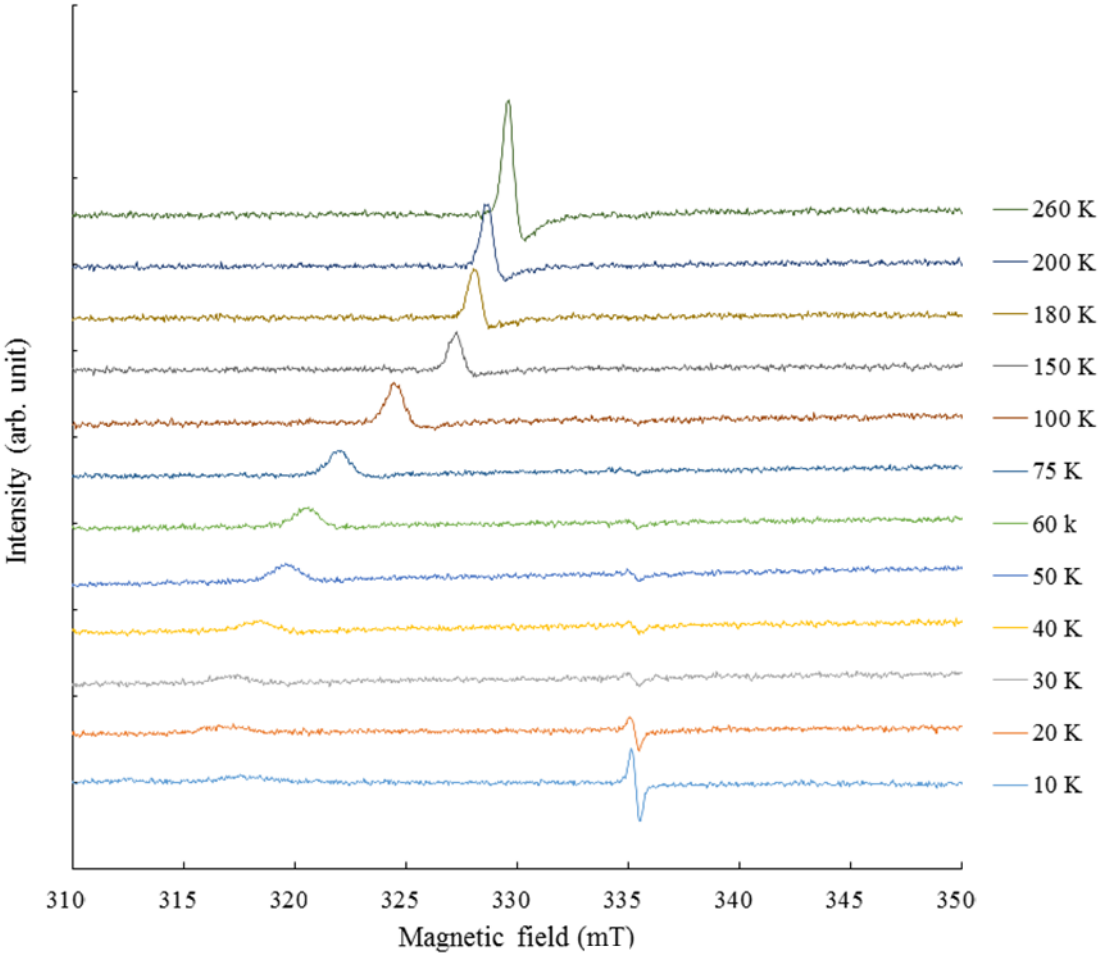

Fig. 6.1. ESR spectra of the HOPG sample irradiated with Ar^{14+} at the fluence of 1×10^{14} ions/cm^2.

Figure 6.2 shows ESR spectra and Fig.6.3 shows L1 line intensity observed in ESR spectra for four irradiation conditions at 10 K. The L1 line intensity for Ar^{14+} is larger than that for Ar^{8+} at the fluence of 1×10^{14} ions/cm^2. It is supposed that the difference in L1 line intensity of Ar^{8+} and Ar^{14+} was caused by that of potential energy of HCIs because the irradiation was performed with constant kinetic energy for different charge states. The L1 line of Ar^{14+} is about twice that of Ar^{8+} and it is suggested that the contribution of the potential energy is dominant over the kinetic energy for defect formation by irradiation of HCIs. Most of the potential energy of HCIs is dissipated at only some layers of topmost surface and forms irradiation traces on the HOPG surface [7, 8]. Since a single HCI injected in a HOPG surface makes one dot structure with 100 % probability [9], it is considered that dangling bonds are produced by the potential energy of HCIs on the sample surface with high efficiency.

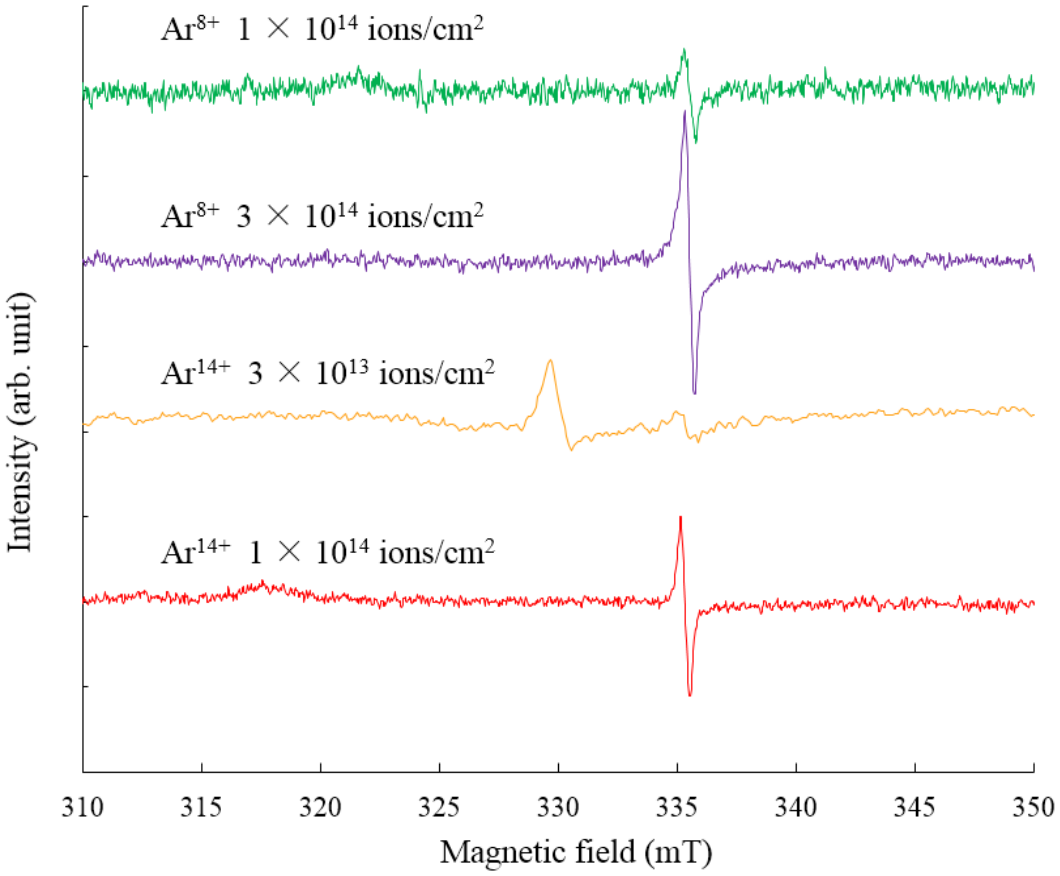

Fig. 6.2. ESR spectra of the HOPG samples irradiated with Ar^{8+} at the fluence of 1×10^{14} ions/cm^2 and 3×10^{14} ions/cm^2, with Ar^{14+} at the fluence of 3×10^{14} ions/cm^2 and 1×10^{14} ions/cm^2 at 10 K.

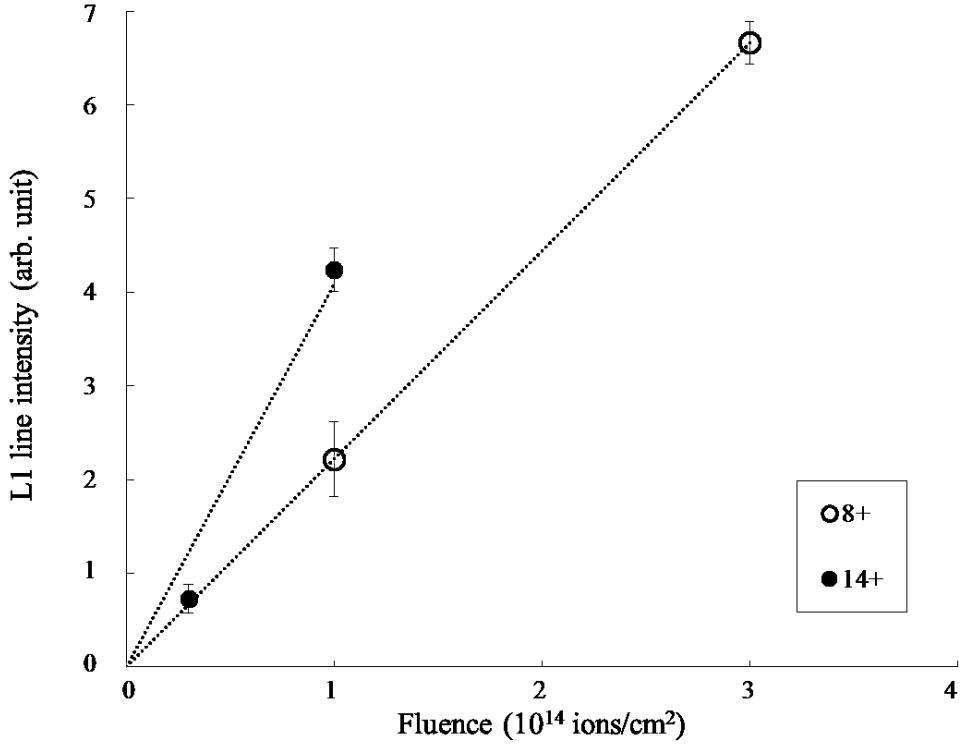

Fig. 6.3. L1 line intensity observed at ESR spectra of HOPG irradiated with HCIs (Ar^{8+} and Ar^{14+}) at 10 K as a function of the fluence of HCIs.

Comparing ESR spectra of HOPG samples irradiated with HCIs, L1 line intensities of Ar^{8+} and Ar^{14+} increase depending on the fluence. For the case of Ar^{8+}, the L1 line intensity of 1×10^{14} ions/cm^2 is about three times that of 3×10^{14} ions/cm^2. Based on these results, it is considered that the dangling bonds increase almost linearly with the fluence of HCIs. From these measurements, it is interpreted that dangling bonds, that is, existence of unpaired electrons that participated in the bonds between atoms, are created by the irradiation with HCIs. It is assumed that the number of defects is more for the irradiation with HCIs in larger charge state.

From the present experiment and the previous study [5], it is supposed that magnetic modification by HCIs appears in smaller fluence than by monovalent ions. Actually, SQUID measurements indicate that HOPG samples irradiated with Ar^{11+} at the fluence in the order of 10^{14} ions/cm^2 have greater magnetizations than samples irradiated with monovalent ions at the fluence of 1.875×10^{17} ions/cm^2 as in ref. 4.

It is necessary to perform measurements over various charge state and fluence

in order to reveal the effect of potential energy on magnetic modification of materials by HCI injection in detail.

By virtue of the high efficiency in magnetic modification and controllability of defect size using HCI injection while minimizing the contribution of kinetic energy, the single ion implantation of a HCI could be applied to microfabrication for spintronics applications.

6.4 Summary

In conclusion, we observed ESR spectra of HOPG samples irradiated with HCIs. The research to observe HCI-irradiation effect by ESR measurements is limited to our research group which uses Kobe EBIS. There are two resonance lines, D1 line and L1 line in the spectra at low temperatures. The L1 line was not observed in unirradiated HOPG sample. This line is considered to be caused by dangling bonds produced by irradiation with HCIs. The L1 line intensity of Ar^{14+} is larger than that of Ar^{8+} at the same fluence of 1×10^{14} ions/cm^2. This is because of the effect of the potential energy of HCIs. The L1 line intensity increases almost proportional to the fluence. Therefore, it is suggested that the defects of HOPG responsible for the magnetization is roughly proportional to the fluence of HCIs and increases with the charge state.

References

[1] K. W. Lee, H. Kweon, J. J. Kweon, and Cheol Eui Lee, J. Appl. Phys. 107 (2010) 044302.

[2] X. M. Yang, Z. T. He, W. F. Li, H. H. Xia, Y. Song, X. T. Zhou, X. D. Liu, M. W.Zhao, T. W. Wang, and K. Y. Hou, J. Appl. Phys. 109 (2011) 083933.

[3] M. Miyake, W. Daimon, P. Son, C. Miyake, and H. Ohya-Nishiguchi, J. Nucl. Mater. 187 (1992) 138.

[4] K. W. Lee and C. E. Lee, Phys. Rev. Lett. 97 (2006) 137206.

[5] S. Liu, M. Sakurai, W. Zhang, K. Asakura, N. Iida, T. Sakurai, H. Ohta, M. Tona, T. Terui, T. Wang, Y. Y. Wang, and G. Q. Xiao, e-J. Surf. Sci. Nanotech. 9 (2011) 241.

[6] N. Nishida, K. Betsumiya, M. Sakurai, T. Sakurai, T. Terui, and S. Honda, e-J. Surf. Sci. Nanotech. 16 (2018) 356.

[7] F. Aumayr and H. P. Winter, Nucl. Instrum. Methods. Phys. Res. B 233 (2005) 111.

[8] F. Aumayr, S. Facsko, A. S. El-Said, C. Trautmann, and M. Schleberger, J. Phys.: Cond. Matt. 23 (2011) 393001.

[9] N. Yoshiyasu S. Takahashi, M. Shibata, H. Shimizu, K. Nagata, N. Nakamura, M. Tona, M. Sakurai, C. Yamada, and S. Ohtani, Jpn. J. Appl. Phys. 45 (2006) 995.

Chapter 7 Luminescence near the Surface Irradiated with Highly Charged Ions

7.1 Introduction

Visible light emission from Er_2O_3 irradiated with Ar^+ has been studied, and luminescence band of Er_2O_3 at 640 ~ 690 nm was remarkable [1]. The intensity of this band decreases with the increase of ion dose, and it is speculated that oxygen atom is preferentially sputtered by the kinetic energy of incident ion and spectrum shifts to that of metallic Er where the luminescence band at 640 ~ 690 nm does not exist.

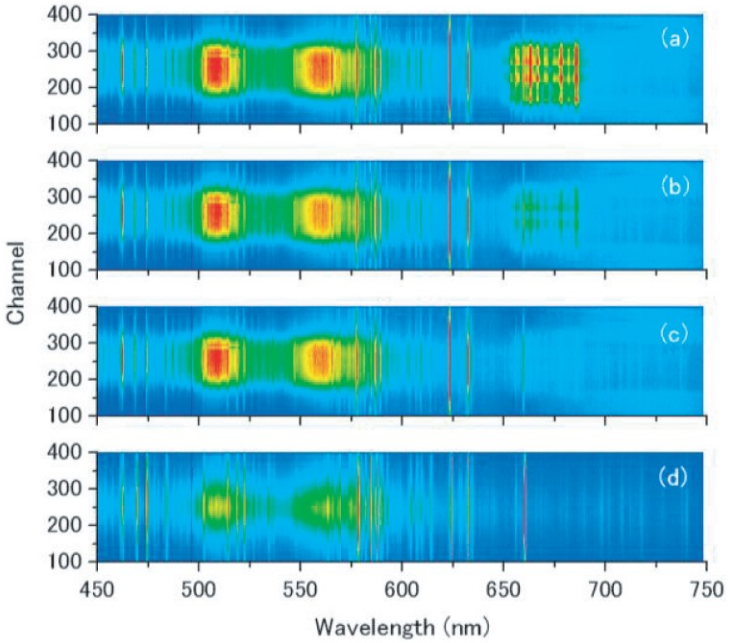

Fig. 7.1. 2D image of the ion-beam induced photon emission spectra. (a)-(c) are spectra for sintered Er_2O_3 samples irradiated by 33 keV Ar+ at 10μA in current, and (d) for Er disc at 50μA. These ion-beam currents were measured using the Faraday cup. The spectra (a)-(b)-(c) were measured successively with increment of the ion-beam dose by about 10^{21} m^{-2} [1].

In the previous experiments in Kobe University, measurement of luminescence of Er_2O_3 irradiated with HCIs had been performed to examine the difference of emission spectrum between HCI and singly charged ion (SCI) stimulated by the interest whether

the phenomena peculiar to potential sputtering induced by HCI impact will appear in the emission spectrum [2, 3].

In the luminescence from Er_2O_3 irradiated with HCIs, the emission intensity from the region of 607–680 nm strongly depended on charge state of HCIs. In addition, the emitted light was not dependent on kinetic energy. The luminescence caused by the potential effect of HCIs. The luminescence from Er_2O_3 irradiated with HCIs in above spectral range nonlinearly increased depending on the charge state of HCIs. According to the spatial distribution of emitted light which comes from vacuum in front of the surface, that is, the light does not come from the surface, the light emission of particles sputtered from the surface by HCIs is dominant. Finally it is concluded that the emission strongly dependent on the charge state is Balmer light. The origin of Balmer light is, however, not clear in the previous experiments.

In the present study, spectroscopic measurements and secondary ion mass spectrometry (SIMS) were performed in order to specify atoms participating in the luminescence. In addition, the characteristics of the Balmer light emission was investigated since the light emission from the adsorbed hydrogen atoms is remarkable at spectroscopic measurements. We investigated the dependence of Balmer light emission on charge state and temporal change of the emission intensity. Photon detection in HCI irradiation experiments has been limited to X-ray emitted from incident HCI [4 - 6]. The present study exhibits visible light measurement emitted via HCI impact on a surface, that is, observation of excited hydrogen atoms by the detection of Balmer lines, which has been never tried in the research field of interaction of HCI with surface [7].

7.2 Experimental

In the present measurement, several kinds of samples was irradiated with HCIs produced by Kobe EBIS and emitted light stimulated by the incidence of HCI on the sample surface was measured at the irradiation chamber connected to the Kobe EBIS [8 - 10]. Primary ion current is monitored by a Faraday cup and the ion beam shape and position are monitored by a micro-channel plate (MCP). Incident ion current to the sample during irradiation is also monitored. The diameter of HCI beam was about 3

mm for each experiment. The experimental setup common to the irradiation experiment is described in chapter 2.

The light emission caused by the interaction between HCIs and samples was measured with a liquid nitrogen cooled CCD. Spectroscopic measurements were conducted using a home-made polychromator. The polychromator consists of camera lens, entrance slit, mirror, flatfield concave grating and CCD detector as shown in Fig. 7.2.

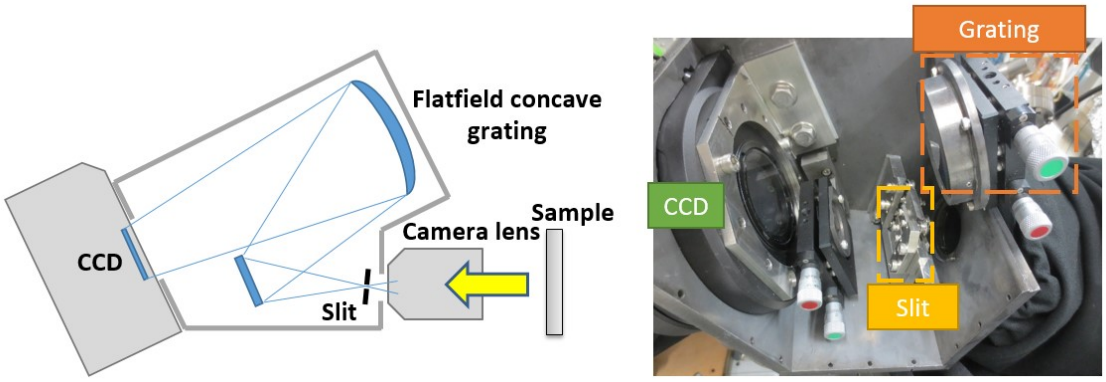

Fig. 7.2. Schematic diagram and photograph of polychromator.

The polychromator is installed near the view port of the irradiation chamber so that the grating disperses light vertically. Wavelength distribution for the range of 420–670 nm and spatial distribution of horizontal direction were measured from the two-dimensional CCD image (Fig. 7.3). An example of two-dimensional image measured with the CCD is shown in Fig. 7.4 [3]. Vertical position of incidence of a photon on the CCD detector corresponds the wavelength of the photon. We made calibration for the relation between vertical position and wavelength using a Balmer lamp.

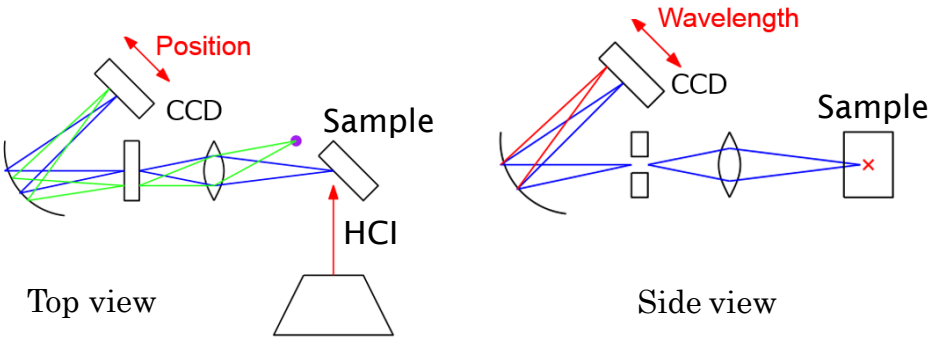

Fig. 7.3. Directions of wavelength and spatial dispersion of the polychromator.

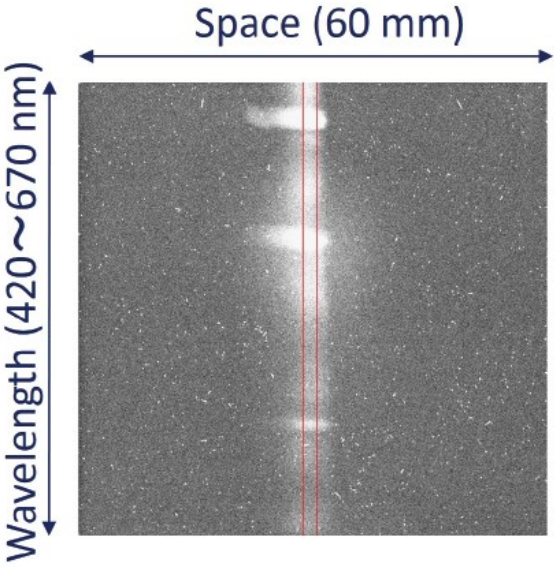

Fig. 7.4. CCD image of emitted light when the MOCVD film of Er_2O_3 is irradiated with Ar^{11+} ions at the exposure for 1 hour. Intensity distribution in horizontal direction corresponds to spatial distribution of emission around the impact site of HCI beam in the horizontal direction and vertical direction corresponds to wavelength distribution for the range of 420 to 670 nm (bottom to top direction) [3].

In the present experiment Er_2O_3, Si, highly oriented pyrolytic graphite (HOPG) and Cu were used as samples. We used commercially available Si wafer for Si sample. Because no cleaning or passivation procedure was done, the native oxide film was formed on the Si surface. These samples were stored in the atmosphere before each measurement, and were irradiated with HCIs (Ar^{q+} and Ne^{q+}). For HOPG, the surface was cleaned before introduction to the irradiation chamber by pealing-off procedure. In spectroscopic measurements, the exposure time was 2 hours. SIMS was performed using a quadruple mass spectrometer (QMS). In the Balmer light measurement, the distribution of light emission in two-dimensional space was obtained using a filter instead of a polychromator. The emission intensity in the 656 ± 5 nm region (H_α) was evaluated.

7.3 Results and discussion

Figure 7.5 shows the spectrum of Si irradiated with Ne^{6+}. The emission intensity is calculated as a summation of count at the pixels corresponding to each

wavelength. Since many noises appeared in the spectrum due to cosmic rays during measurement, data points which are remarkably stronger than that of adjacent pixels are replaced with average values of data on both sides in order to remove noises. In Fig. 7.5, emitted light lines are observed around 486 nm, 590 nm and 656 nm. These lines also appeared in the spectrum of Er_2O_3 irradiated with Ar^{11+} (Fig. 7.6). Similarly, peaks are observed around 485 nm, 590 nm and 656 nm in the emission spectrum of Cu irradiated with Ar^{11+} (Fig. 7.7). In addition, an emission signal of Cu appears around 520 nm. In Fig.7.8 which shows the emission spectrum of Er_2O_3 irradiated with Ne^{6+}, the peak with the shortest wavelength is not clear, but the other two appear at the same wavelength. From these results, it is suggested that these peaks are not derived from irradiated ions or samples since three emitted light lines appear in common.

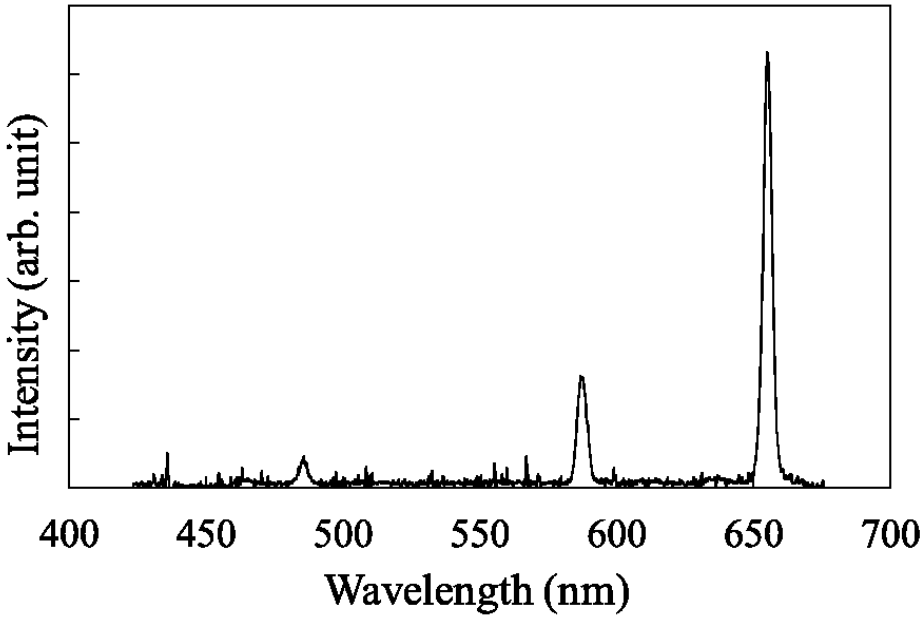

Fig. 7.5. The emission spectrum of Si irradiated with Ne^{6+}.

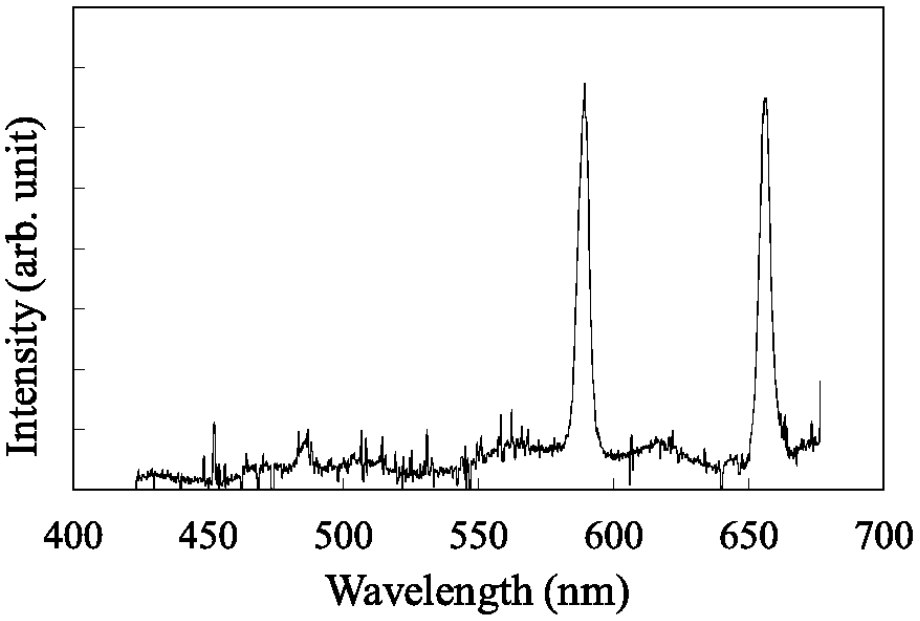

Fig. 7.6. The emission spectrum of Er_2O_3 irradiated with Ar^{11+}.

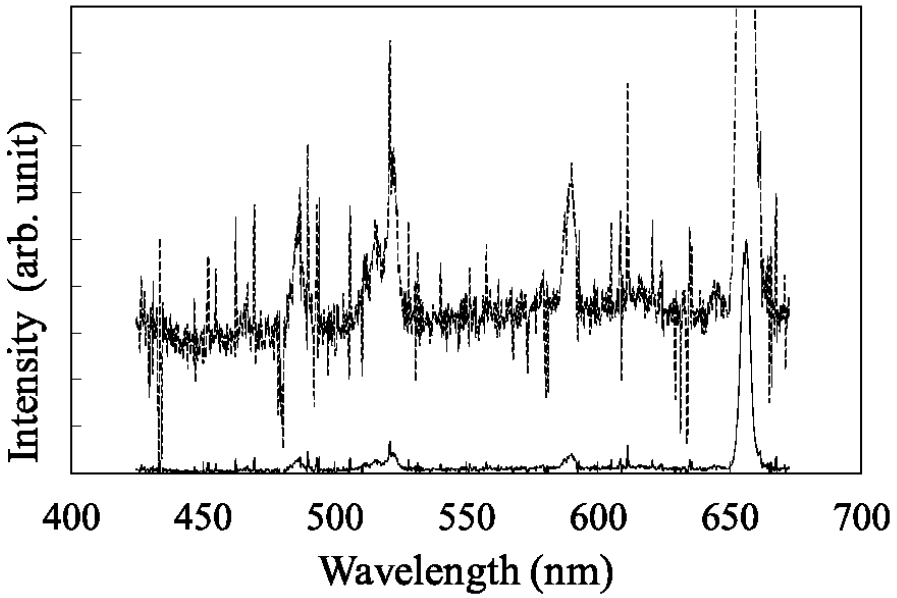

Fig. 7.7. The emission spectrum of Cu irradiated with Ar^{11+}.

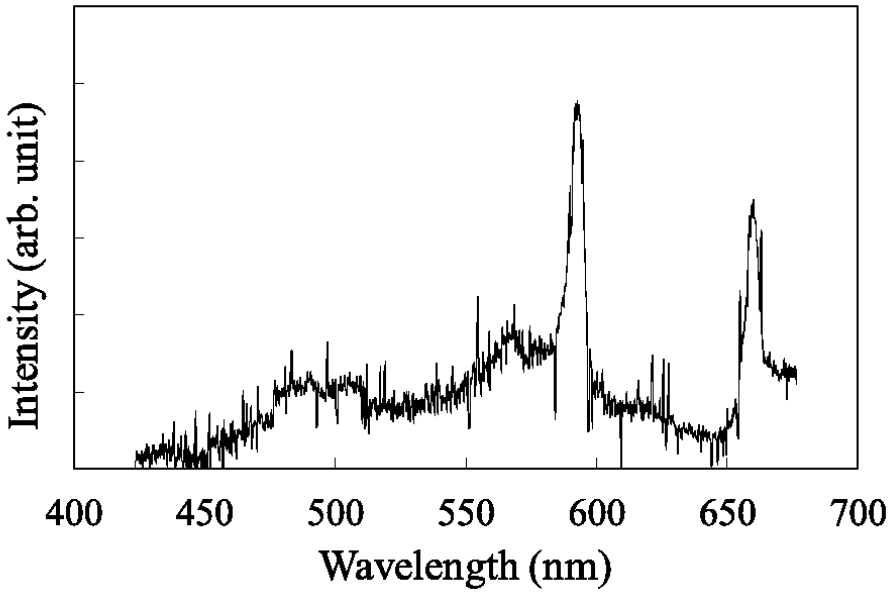

Fig. 7.8. The emission spectrum of Er_2O_3 irradiated with Ne^{6+}.

The analysis of ions produced by irradiation with HCIs was performed using a QMS to identify the origin of the light emission. Figure 7.9 shows a secondary ion mass spectrum of Si irradiated with Ar^{11+}. A very strong signal of H with a mass number of 1 and a signal of Na with a mass number of 23 are observed in the spectrum in addition to Si (28) as a sample and Ar (40) as a primary ion. It should be noted that the intensity of mass number of 1 (H^+) is overwhelmingly more than that of 2 (H_2^+) in the spectrum. This result is completely different from the quadruple mass spectrum of the residual gas [11]. These results indicate that hydrogen atoms contained in molecules on the surface are ionized and desorbed as an interaction of molecules with HCIs. From these results, it seems that emitted light lines observed by spectroscopic measurements come from H and Na, i.e. Balmer series (H_α and H_β) and the resonance line of Na (D line). It is considered that H is originated from either water or hydrogen adsorbed or occluded on the sample surface. The peak at 590 nm did not appear in the emission spectrum of HOPG, therefore the origin of Na is contamination.

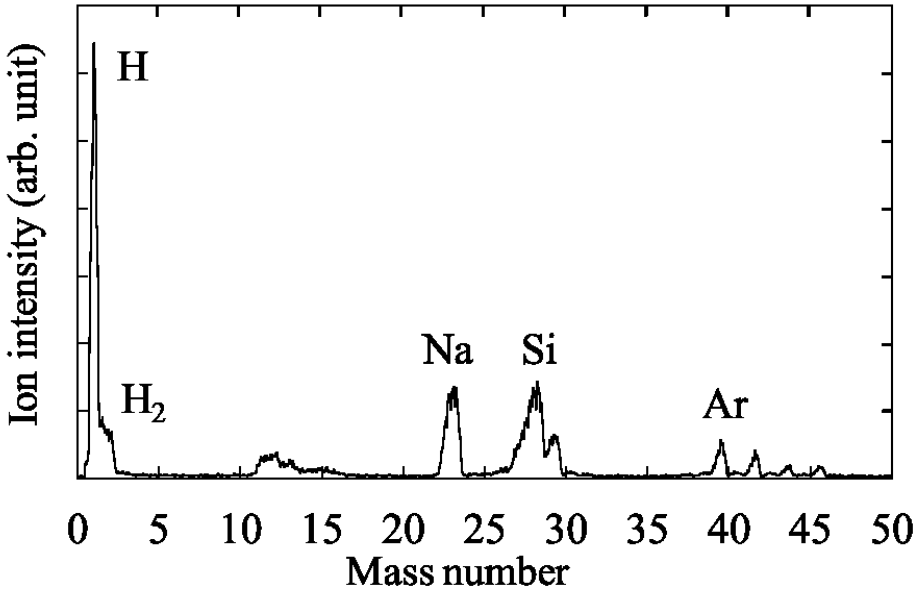

Fig. 7.9. The secondary ion mass spectrum of Si irradiated with Ar^{11+}.

To investigate the nature of Balmer light produced by the injection of HCIs, the emission intensities at the 656 ± 5 nm region (H_α) were evaluated for various experimental conditions. The emission intensity was obtained from the summation of data points at light emitting part subtracting background in the CCD image, and normalized by incident ion current divided by the charge state of HCIs. Finally, the intensity was converted to the emission intensity per single ion. Figure 7.10 shows the dependence of emission intensities per single HCI on the charge state of Ar^{q+} (q = 6, 8, 11, 14, 16). The intensities increase with charge state. It is considered that the transfer of electrons caused by large potential energy leads to the excitation of more hydrogen atoms. Figure 7.11 and Fig. 7.12 present temporal changes of emission intensities from Si and HOPG surfaces per the injection of single HCI. Here, the time is converted to the number of incident ions since the number of incident ions per unit time is different for each measurement. The intensities tend to decrease by continuous irradiation with HCIs. It is suggested that the number of hydrogen atoms on the surface decreased by the irradiation.

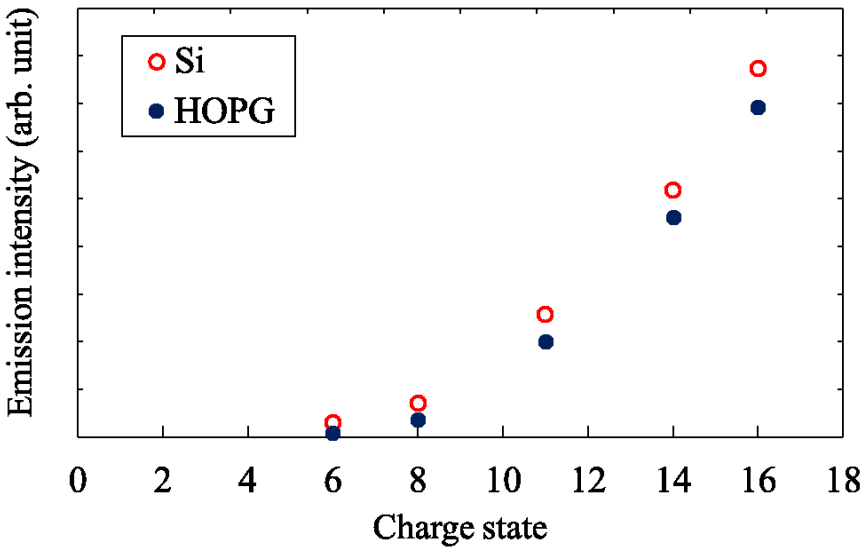

Fig. 7.10. Dependence of emission intensities per single ion on charge state of Ar^{q+} (q = 6, 8, 11, 14, 16).

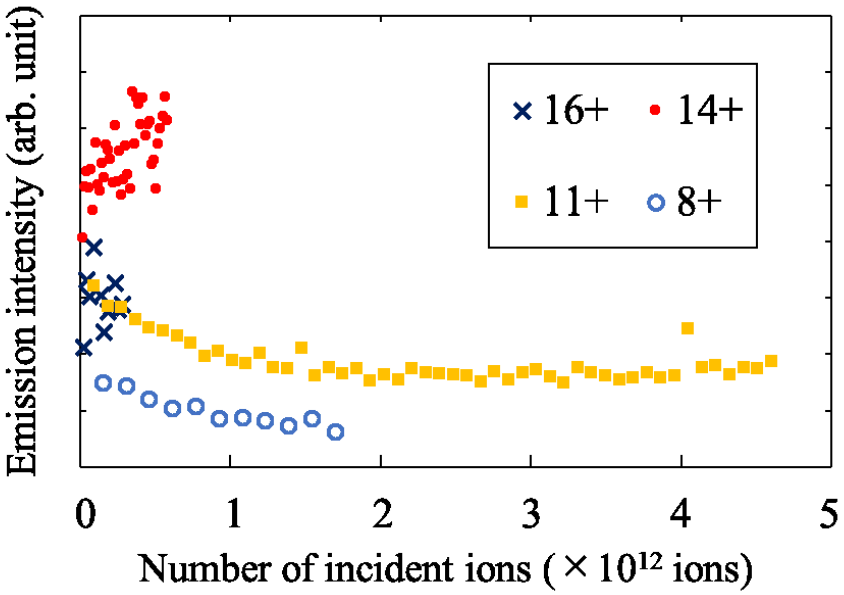

Fig. 7.11. Temporal changes of emission intensities of Si irradiated with Ar^{q+} (q = 6, 8, 14, 16).

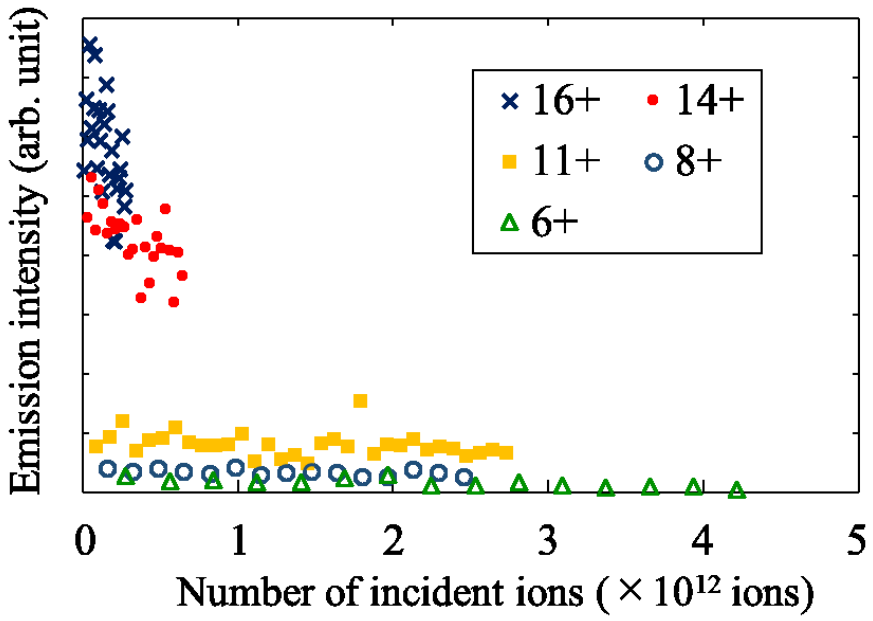

Fig. 7.12. Temporal changes of emission intensities of HOPG irradiated with Ar^{q+}.

It is suggested that water or hydrogen are desorbed and decreased from the surface by HCI injection, since the SIMS spectrum indicates that atomic hydrogen ions are produced by irradiation with HCIs. Comparing temporal changes of Si and HOPG, decrease of emission from HOPG is slower than that from Si. This is probably because the Si sample is stored in the atmosphere, while the HOPG surface was prepared a new surface for every measurement, so that exposure time of HOPG to air is shorter than that of Si. Therefore, it is considered that the origin of emission is both hydrogen attached to the sample in the irradiation chamber and water adsorbed in the atmosphere. However, the number of molecules present on the surface is unknown in these measurements due to the difference of exposure time to air. Figure 7.13 shows temporal changes of the emission from HOPG irradiated with Ar^{11+} for various exposure time to air after pealing-off procedure. Because the emission intensity of the sample exposed to air for 7 days is stronger than that of the sample exposed for 1 day, it is considered that water in air was adsorbed to the HOPG surface.

Water molecules seem to mostly contribute to the Balmer light emission. However, there remains a possibility of contribution from adsorbed hydrogen molecules which come from residual gas. It is essential to control the condition of the surface in order to identify the origin of Balmer light. As future prospects, in order to reduce the

influence of water, the sample surface will be cleaned using an ion gun in vacuum before measurement.

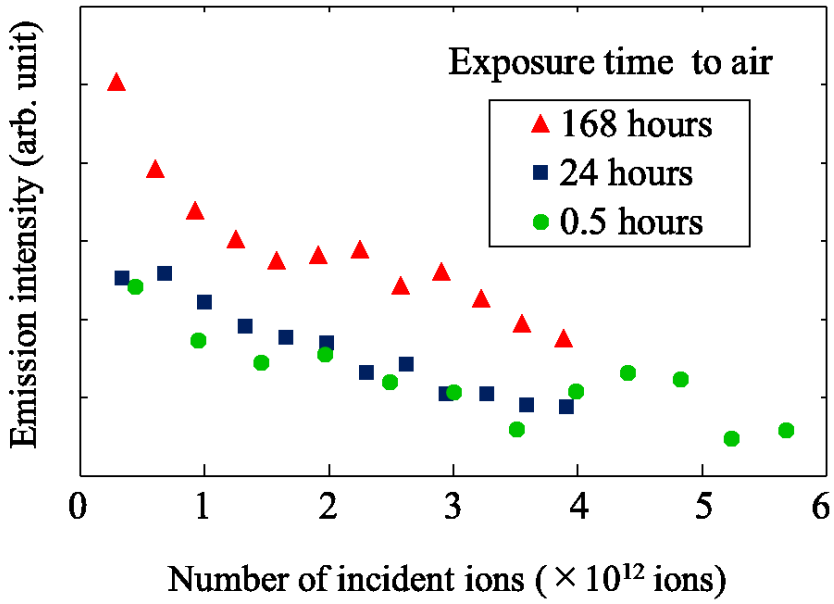

Fig. 7.13. Temporal changes of emission intensities of HOPG irradiated with Ar^{11+}. HOPG surfaces were exposed to air for 0.5 hours, 24 hours (1 day) and 168 hours (7 days).

The emission intensity of the Balmer light was measured using an ABS resin having a chemical composition containing a hydrogen atom, instead of a samples containing no hydrogen atom such as Si or HOPG. Figure 7.14 shows temporal changes of emission intensities of the Balmer light when the ABS resin is irradiated with HCIs. The emission intensity tends to decrease as irradiation with HCIs is continued. In the case of ABS resin, it is considered that hydrogen atom contained in the ABS resin is involved in light emission in addition to water and hydrogen existing on the surface as a source of light emission of the Balmer light emission. Here, when the initial and final emission intensity are compared, the intensity is reduced to almost half. The proportion of hydrogen contained in the composition of the ABS resin should not change significantly no matter how much HCIs are irradiated. If the hydrogen of the ABS resin greatly contributes to the light emission, it is considered that the light emission intensity does not decrease much. Therefore, it is suggested that the hydrogen and water molecules existing on the surface contribute greatly to the Balmer light emission, not the hydrogen atoms contained in the ABS resin.

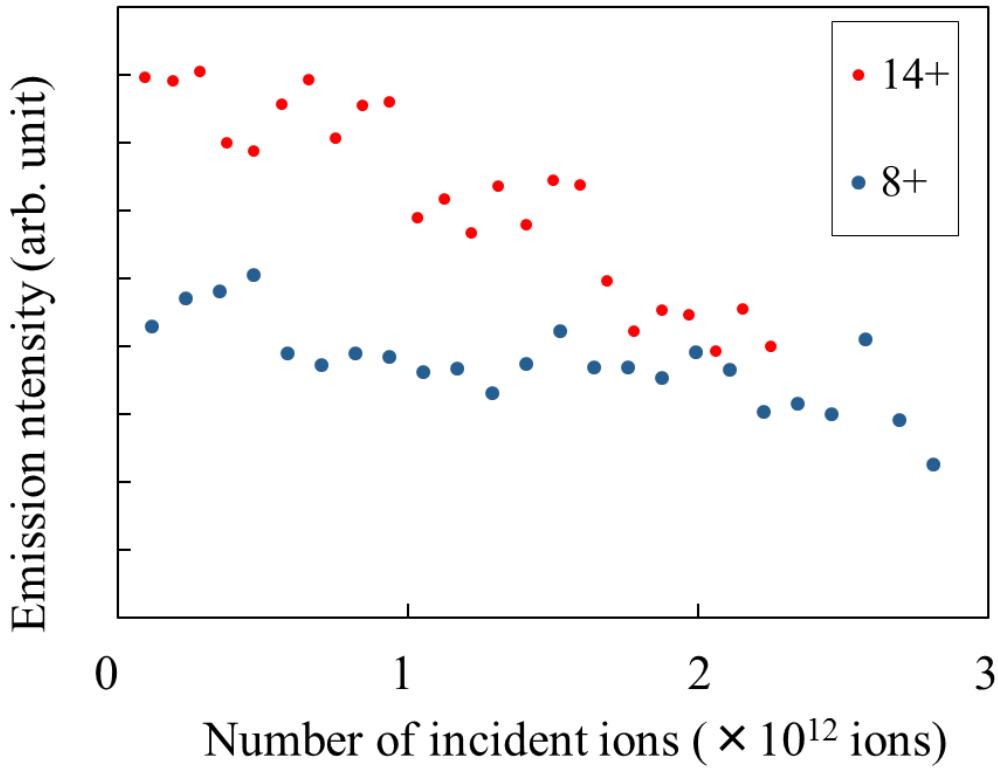

Fig. 7.14. Temporal changes of emission intensities of ABS risen irradiated with Ar^{q+} (q = 8, 14).

Next, the spatial distribution in the direction perpendicular to the HOPG sample irradiated with HCIs was measured. Figure 7.15 shows the spatial distribution of luminescence from HOPG surface irradiated with Ar^{q+} (q = 6, 8, 11, 14, 16). 0 mm on the horizontal axis of the graph indicates the position of the sample surface, and light spreads in the positive direction.

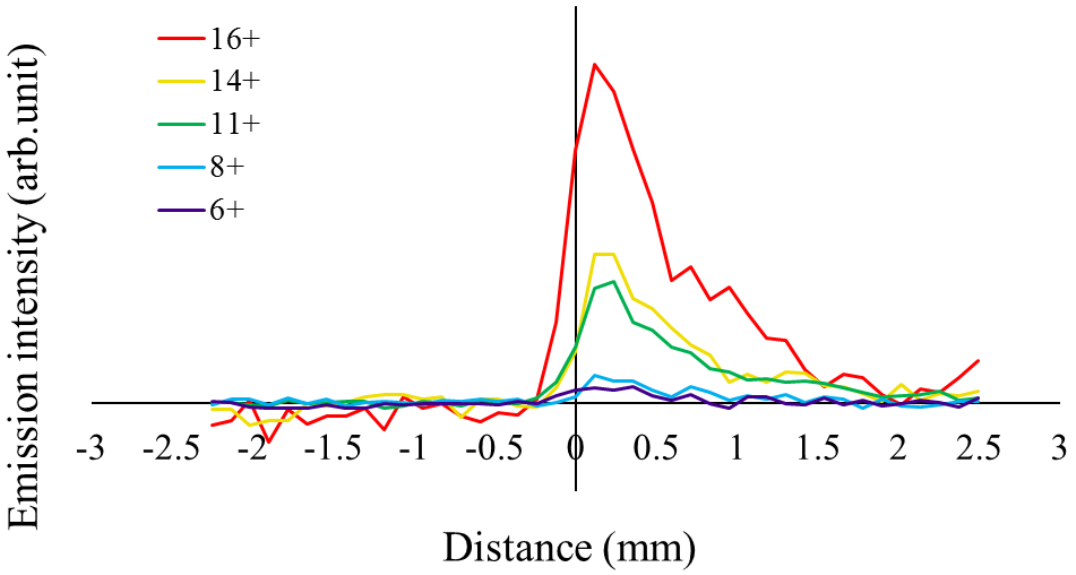

Fig. 7.15. Spatial distribution of luminescence from HOPG surface irradiated with Ar^{q+} (q = 6, 8, 11, 14, 16).

Light emission is the strongest at the sample surface, and seems to decay exponentially with distance from the surface. Since excited hydrogen is released to various directions, obtained distribution does not directly express density distribution normal to the surface. However, we conducted to roughly estimate the kinetic energy by fitting an exponential curve to the distribution of Fig. 7.15. Here, assuming that the reciprocal of Einstein's A coefficient of hydrogen atom $A_{32} = 0.96 \times 10^8$ /s at the electron transition from quantum number 3 to 2 becomes the lifetime of the excited level, the kinetic energy of the excited hydrogen released from the surface was estimated. When the distances at which the peak of the emission intensity decayed to 1/e times were obtained from the graph of each charge state in Fig. 7.15, no dependence due to the charge state was found, and the range was 0.56 to 0.71 mm. From this result, the kinetic energy of the excited hydrogen atom was found to be 14.9 to 24.4 eV, and was 19.3 eV on average. This value is much higher than that has been reported for secondary ion produced by HCI impact [12]. There might be an acceleration mechanism effective for the secondary ion which will capture an electron to the excited state of the hydrogen. Figure 7.16 shows the sum of the emission intensities of these results. Emission intensity is approximately proportional to $q^{3.5}$.

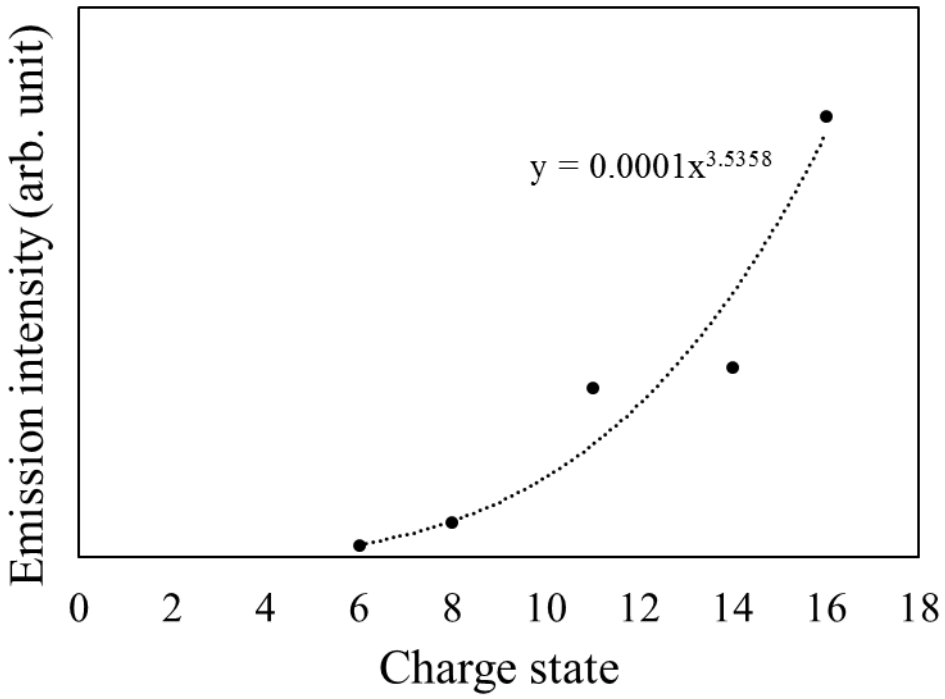

Fig. 7.16. Emission intensity of Balmer light as a function of the charge state of incident HCI.

Next, the dependence of the secondary ions to be sputtered and HCIs on the charge state was measured. When Si was irradiated with HCIs, signals of H (proton) with mass number of 1 and Na with mass number of 23 and Si with mass number of 28 were large, therefore, we focused on these three elements. Figure. 7.17 shows the signal intensity of sputtered H, Na, and Si ions when the Si sample was irradiated with HCIs.

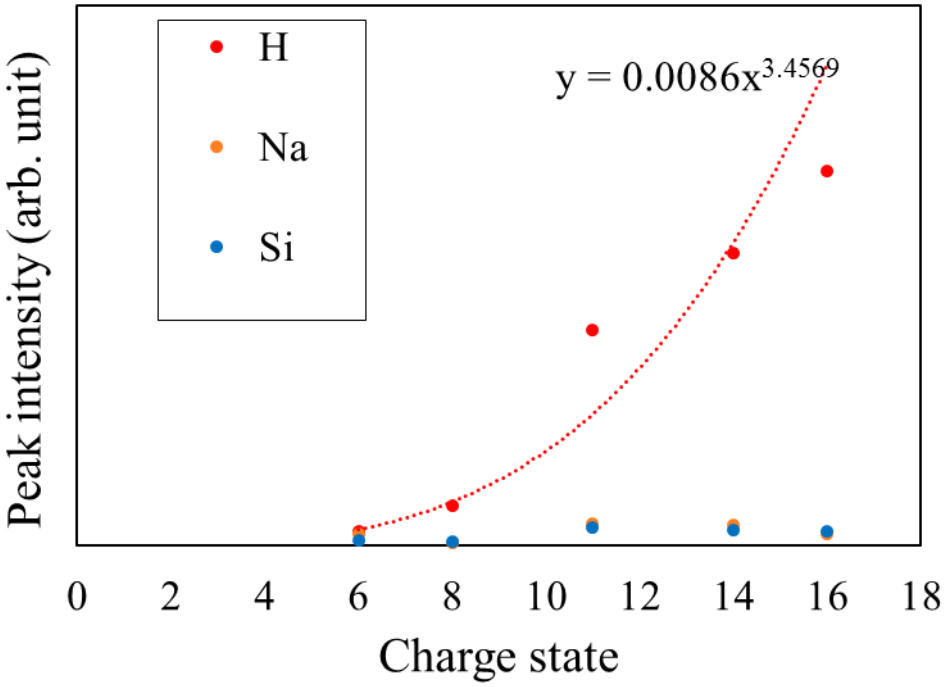

Fig. 7.17. The peak intensity of secondary ion sputtered from Si surface as a function of the charge state of incident HCI.

The H signal increases nonlinearly with the charge state, whereas the signal intensity of Na and Si hardly changes even when the charge state changes. This result indicates that the amount of H sputtered is greater than the amount of Na or Si sputtered by the potential energy of the HCI.

From these results, the charge state dependence of the intensity of Balmer emission generated by the irradiation with HCIs and the charge state dependence of H (proton) signal intensity in SIMS were compared. In both cases, the intensity was proportional to the charge state to the power of about 3.5. Since a Balmer light is emitted when an excited hydrogen atom is deexcited, it is considered that protons and excited hydrogen atoms generated by irradiation with HCIs are generated by a similar process. In other words, protons are generated by the electrons in surface atoms such as hydrogen atoms being captured by HCIs with a certain probability by the collision process of HCIs and hydrogen atoms on the surface, and protons are released by repulsion with other ions. Thereafter, it is considered that a Balmer light is emitted when the protons recapture electrons.

7.4 Summery

The emission light from the surface irradiated with HCIs was observed. The origin of luminescence was identified as H as the main light emission species from the spectroscopic measurement and SIMS. The emission intensity of Balmer light increases with the charge state of HCIs and decreases as the irradiation continues. The Balmer light emission is strongest near the surface irradiated with HCIs. In addition, temporal change in the Balmer light emission of the ABS resin irradiated with HCIs showed that H contained in the chemical composition of the ABS resin did not contribute significantly to the Balmer light than H derived from water or hydrogen. Because photon detection in HCI irradiation experiments has been limited to X-ray emitted from incident HCI, the present study is quite unique one to observe Balmer light emitted from excited hydrogen atoms produced through the interaction of HCI with surface.

References

[1] D. Kato, H. A. Sakaue, I. Murakami, T. Tanaka, T. Muroga, and A. Sagara, Plasma and Fusion Res. 7 (2012) 2405043.

[2] M. Sakurai, T. Miyamoto, K. Sasaki, D. Kato, and H. A. Sakaue, J. Vac. Soc. Jpn. 50 (2015) 147 (in Japanese).

[3] M. Sakurai, K. Sasaki, T. Miyamoto, D. Kato, and H.A. Sakaue, e-J. Surf. Sci. Nanotech. 14 (2016) 1.

[4] J. P. Briand, L. de Billy, P. Charles, S. Essabaa, P. Briand, R. Geller, J. P. Desclaux, S. Bliman, and C. Ristori, Phys. Rev. Lett. 65 (1990) 159.

[5] M. W. Clark, D. Schneider, D. Dewitt, J. W. McDonald, R. Bruch, U. I. Safronova, I. Yu. Tolstikhina, and R. Schuch, Phys. Rev. A 47 (1993) 3983.

[6] H. Watanabe, S. Takahashi, M. Tona, N. Yoshiyasu, H. Nakamura, M. Sakurai, C. Yamada, and S. Ohtani, Phys. Rev. A 74 (2006) 042901.

[7] N. Nishida, Y. Hori, A. Yamauchi, M. Sakurai, D. Kato, and H. A. Sakaue, J. Phys. Conf. Ser. 1220 (2019) 012037.

[8] M. Sakurai, F. Nakajama, T. Fukumoto, N. Nakamura, S. Ohtani, and S. Mashiko, Shinku 48 (2005) 317 (in Japanese).

[9] M. Sakurai, H. A. Sakaue, H. Watanabe, N. Nakamura, S. Ohtani, Y. Kawase, K Mitsumori, T. Terui, and S. Mashiko, Shinku 50 (2007) 390 (in Japanese).

[10] M. Sakurai, M. Tona, H. Watanabe, N. Nakamura, S. Ohtani, T. Terui, S. Mashiko, and H. A. Sakaue, J. Phys. Conf. Ser. 163 (2009) 012115.

[11] S. Inayoshi, Shinku 50 (2007) 228 (in Japanese).

[12] Okabayashi, K. Komaki, and Y. Yamazaki, Nucl. Instr. and Meth. in Phys. Res. B 235 (2005) 438.

Chapter 8 Conclusions

A highly charged ion (HCI) has large potential energy increasing with its charge state, and the potential energy of HCI is independent of its kinetic energy. The interaction between a HCI and the surface results in emission of photons in the range of visible to X-ray, hundreds of secondary electrons, sputtering of secondary ions and the modification of the surface structure at the nanometer scale. The effects of HCI on the surface are different from those of singly charged ion (SCI), since SCI deposits only its kinetic energy. The effect characteristic to the potential energy deposition is called as potential effect. Many kinds of experiments have been performed to exhibit various potential effects, such as the secondary ion emission with high efficiency, or production of nanostructure whose size increases with the potential energy of incident HCIs. For the structural observation of irradiation traces, which is the majority of research subject concerning the interaction of HCIs with the surface, the target material has been limited to bulk crystals, irradiation is conducted at relatively low fluence ($< 10^{12}$ ions/cm^2), and mostly measured using scanning tunneling microscopy (STM) and atomic force microscopy (AFM). In order to research unexplored fields, we have developed an electron beam ion source (EBIS) and observed surface structures irradiated with HCIs at relatively high fluence ($\sim 10^{14}$ ion/cm^2) using scanning electron microscopy (SEM) and Raman spectroscopy as well as STM and AFM. Observations of the photon emission from surfaces irradiated with HCIs and electron spin resonance (ESR) measurements of highly oriented pyrolytic graphite (HOPG) irradiated with HCIs have been conducted.

Carbon based materials such as carbon nanotube (CNT) are promising materials for nanodevices and circuits. Beam irradiation techniques using neutral atoms or SCIs have been employed in order to create tunnel barriers and realize the quantum dot function on a multi walled carbon nanotube (MWCNT). Investigations on the modification of structural and electric/magnetic properties of carbon based materials by the irradiation with HCIs are expected to provide valuable information for applying HCIs to such nanotechnology as well as understanding the interaction of HCIs with the materials. In the present thesis, we have described several experiments which exhibit the potential effect in various irradiation phenomena observed for carbon based materials; photon emission, modifications on structural, electric, and magnetic

properties.

Structural modifications of MWCNTs irradiated with HCIs have been analyzed TEM. We investigated the difference of TEM images at the identical position between samples before and after irradiation. It has become possible to compare a nanometer region from a millimeter-sized sample before and after irradiation by establishing the observation method before and after irradiation. This allows a more accurate comparison from TEM images of MWCNTs before and after irradiation. TEM images of MWCNTs irradiated with Ar^{14+} exhibit uneven surfaces at the fluence of 6×10^{13} ions/cm^2. Outer diameters are decreased, outlines of surfaces become uneven and hollow regions disappeared by the irradiation. These results are different from the case of irradiation with monovalent ions. It is considered that potential sputtering occurred on the surfaces of MWCNTs. The TEM images indicate that the larger the charge state is, the smaller the outer diameter is. The potential effects of HCI, such as the appearance of uneven surfaces and a decrease in outer diameter, were clarified by observing the same location.

We evaluated the electric characteristics of MWCNTs irradiated with the HCIs of Ar^{8+}, Ar^{11+}, and Ar^{14+} extracted from an electron beam ion source (Kobe EBIS). Each MWCNT located on the high dope Si substrate had a source/drain contact, forming a back-gate FET configuration. The source to drain resistance of the MWCNT channel tended to increase with increasing fluence and charge state of the HCIs. The current-voltage curves were nonlinear at low temperatures for the irradiated samples, and Coulomb oscillations were observed in the gate voltage dependence of the drain current. At a cryogenic temperature (1.6 K), Coulomb diamonds and periodic Coulomb oscillations were observed, and it is suggested that a single QD was formed. Production of QD using HCI irradiation worth one of full-scale nanotechnology research and this can be an epochal achievement because full-scale nanotechnology using atomic physics techniques such as HCI irradiation has never been realized to date.

We also observed ESR spectra of HOPG samples irradiated with HCIs. There are two resonance lines, D1 line and L1 line in the spectra at low temperatures. The L1 line was not observed in unirradiated HOPG sample. This line is considered to be caused by dangling bonds produced by irradiation with HCIs. The L1 line intensity of Ar^{14+} is larger than that of Ar^{8+} at the same fluence of 1×10^{14} ions/cm^2. This is because of the effect of the potential energy of HCIs. The L1 line intensity increases almost

proportional to the fluence. Therefore, it is suggested that the defects of HOPG is roughly proportional to the fluence of HCIs. The detection of ESR peak due to HCI irradiation is limited to our research group and potential effect in the interaction of HCI with surface is well illustrated also as ESR measurements in the present study.

For photon emission measurements, we observed spatial and spectral distribution of visible light emission from the surface during irradiation with HCIs. The origin of luminescence was identified as H as the main light emission species from the spectroscopic measurement and SIMS. To investigate the nature of Balmer light produced by the injection of HCIs, the emission intensities at the 656 ± 5 nm region (H_α) were evaluated for various experimental conditions. The emission intensity of Balmer light increases with the charge state of HCIs and decreases as the irradiation continues. The Balmer light emission is strongest near the surface irradiated with HCIs. In addition, temporal change in the Balmer light emission of the ABS resin irradiated with HCIs showed that H contained in the chemical composition of the ABS resin did not contribute significantly to the Balmer light than H derived from water or hydrogen. Our observation of Balmer light emitted from excited hydrogen atoms produced by the interaction of HCI with the surface is also a unique achievement in the world.

Acknowledgements

At Kobe University, my deepest gratitude goes first and foremost to thank my supervisor, associate Professor Sakurai, a modest and kindly scientist, for his constant encouragement and guidance.

I would like to thank Professor Kohmoto for their help and instruction when I came to quantum dynamics group.

I am also greatly indebted to the professors and staffs at the department of physics, who have instructed and help me a lot in the past three years.

I would like to thank staffs at Instrument Analysis Division and Cryogenic Division, Research Facility Center for Science and Technology for technical assistance with the experiments.

At University of Hyogo, I would like to give my deep thanks to Professor Honda at University of Hyogo, knowledgeable scientist. I got a lot of advice and guidance from him, including experiment, theory.

At Osaka University, I am would like to thank Professor Tanabe for TEM observations in early experiments.

At National Institute for Fusion Science, I am would like to thank associate Professor Kato and assistant Professor Sakaue for useful discussions.

At RIKEN, I am would like to thank Dr. Ishibashi and Dr. Yamaguchi for evaluation of electrical properties at cryogenic temperatures and knowledge support.

At Hyogo Prefectural Institute of Technology, I am would like to thank Dr. Izumi for the assistance with evaluation of electrical characteristics.

At National Institute of Information and Communications Technology, I am would like to thank Dr. Terui for his knowledge and technique for analytical instruments.

In addition, my thanks would go to my beloved family for their loving considerations and great confidence in me all through these years.

I certainly want to thank all other members of quantum dynamics group: Mr. Hori, Mr. K. Murakami, Mr. S. Murakami, Mr. Taniguchi, Mr. Kokogawa, Mr. Shaku, Mr. Fujimoto, Mr. Maeda, Mr. Iwasaki, Mr. Mushiaki, Mr. Oishi, Mr. Kita, Mr. Kawabata. I will remember ours happy time: studying, playing and, eating.